THE UNIVERSITY *of* EDINBURGH

Development of Stable and Efficient Visible-Light-Driven Photocatalysts through Heteroatom Doping Strategy

Mengyu Cao

THE UNIVERSITY *of* EDINBURGH

Thesis submitted for the degree of
Doctor of Philosophy

The University of Edinburgh

2020

Abstract

The photocatalysis is one of the most promising sustainable technologies to tackle the challenges of environmental pollutions. However, traditional photocatalysts such as TiO_2 exhibit the narrow light absorption range and low quantum efficiency. These drawbacks seriously limit their practical applications. The development of high-efficiency photocatalysts with large specific surface area and high photocatalytic activity has become the key to the photocatalysis technology. Doping heteroatoms into the crystal of photocatalyst is an effective way to improve its photocatalytic activity. With appropriate photocatalyst design, the dopants in moderate doping concentration can optimise the catalysts in the following multiple aspects: (i) with extra dopant energy level in the bandgap of semiconductor, dopants can reduce the bandgap to broaden the light absorption of the photocatalysts; (ii) dopants can intentionally shift the valence band position to improve the photooxidation capability of the catalysts; (iii) dopants can suppress the photo-excited electrons and holes recombination, which results in an enhanced quantum efficiency; (iv) in plasmonic photocatalysts, dopants can modify the electronic structure of the plasmonic crystal to enhance the photo-excited charge carrier generation and increase the energy of the excited charge carriers.

In this thesis, the heteroatom doping strategy has been used to enhance the dye photodegradation performance of photocatalysts. With the help of molecular and electronic structure analyses, the mechanisms underpinning the enhancement of photocatalytic performance are elucidated. In chapter 3, the Zn doped C_3N_4 has been successfully synthesized in eutectic $ZnCl_2$-KCl salts mixture for the first time. The low melting temperature of $ZnCl_2$-KCl promotes the dispersion of the organic precursors, therefore creating a specific surface area at least ~7.4 times larger than the bulk C_3N_4 synthesized via the conventional thermal polymerization method in air (C_3N_4-M-Air). The significant improvement in the photocatalytic activity is achieved through locating the melting point of the salt mixture within the temperature window between dicyandiamide and melamine oligomer formation steps in the polycondensation process. Using dicyandiamide as the precursor shifts the valence band maximum (VBM) of the prepared C_3N_4 (C_3N_4-D) positively, therefore enhancing the oxidation capability of the photocatalysts. The Zn dopants at the interstitial site of C_3N_4 in an appropriate concentration suppress the photo-excited electron-hole recombination, which significantly contributes to the high photocatalytic activity. The optimal sample C_3N_4-D shows ~4.2 times larger photocurrent density and ~1.46 times longer carrier lifetime than the C_3N_4-M-Air. In

photocatalytic methyl orange (MO) degradation, the pseudo-first reaction rate constant of C_3N_4-D is ~4.15 times higher than that of the C_3N_4-M-Air control group.

In chapter 4, the combined effects of Cl doping and agitation are used for the first time to improve the photocatalytic performance of C_3N_4 synthesized via solvothermal method. The enhanced photocatalytic RhB degradation activity is attributed to the optimized electronic structure, enlarged specific surface area and balanced interstitial/substitutional Cl doping. More importantly, it is found that the preferred doping site for Cl dopants is strongly controlled by the agitation rate. The atomic ratio of interstitial over substitutional Cl dopants shows a U-shape correlation with the agitation rate. Furthermore, the different effects of interstitial and substitutional Cl dopants on the photocatalytic activity are distinguished and elucidated. The optimal synthesis condition for Cl-doped C_3N_4 is associated with a moderate agitation rate of 60 rpm (60-C_3N_4). Under 60 rpm agitation during the synthesis, the 60-C_3N_4 exhibits remarkably larger specific surface area, stronger photo-oxidation capability, reduced bandgap and suppressed electron-hole recombination comparing with the control group g-C_3N_4 synthesized via conventional thermal polycondensation method. An outstanding photocatalytic RhB degradation performance is therefore observed for 60-C_3N_4 with ~37-fold higher pseudo-first reaction rate constant than the control group conventional g-C_3N_4 sample.

In chapter 5, the C doped TiN/ultrathin carbon layer has been synthesized via the calcination of $TiCl_4$/urea mixture and shows the prominent plasmonic photocatalytic RhB degradation performance under visible light irradiation. Based on the systematic investigations on the preparation conditions, it is found that the urea amount and calcination temperature are the two critical factors determining the chemical composition and crystal size of TiN nanoparticles. In the optimal condition with 3.0g urea and 1100 ºC synthesis temperature, the TiN nanocrystals with the mean size of ~37 nm are formed and well-dispersed on N doped ultrathin carbon layer layers. The larger amount of urea and higher synthesis temperature result in the increase of TiN nanoparticle size. Moreover, it is proven that the appropriate amount of C doping can enhance the plasmonic photocatalytic activity of TiN. Based on DFT calculation, the C sp band introduced into TiN band structure can enhance the interband excitation of electrons, which results in the excited holes with higher quantity and energy. In visible light driven RhB photodegradation, the optimal C doped TiN/ultrathin carbon layer sample shows the higher first-order reaction rate constant than the benchmark rutile TiO_2 and C_3N_4/TiO_2 by ~34.2 and 6.5 times, respectively.

Lay Summary of Thesis

Photocatalysis has gained considerable attentions for its potential to utilize solar energy as a driving force to carry out the degradation of organic pollutants and renewable energy production. The advantages of photocatalytic degradation of pollutants are the capability to fully convert the toxic organic dyes to unharmful inorganic compounds such as CO_2 and H_2O. Many photocatalysts have been reported in literature. However, the shortcomings for these photcatalysts are their low absorption capacity of solar light, low catalytic efficiency, limited surface area and poor stability, which largely restrict the application of photocatalytic process.

The key to the success of the photocatalytic technique in pollutant degradation and renewable energy production is to develop high-performance photocatalysts to address the issues mentioned above. This thesis focuses on the development of effective synthesis methods based on heteroatom doping strategy to improve the activity and stability of photocatalysts. The work starts from modifying graphic carbon nitride (g-C_3N_4 or C_3N_4), as graphic carbon nitride has been considered as the next-generation photocatalyst, due to its transition metal-free chemical composition, good visible light response and appealing electronic band structure. This thesis is formed by four sections. The first section of this thesis presents a systematic review on photoactalysis theory, photocatalytic materials, strategies, its history and the recent developments. The second section of this thesis presents the molten salt method that we developed to improve the specific surface area and photocatalytic activity of C_3N_4. The organic precursors were annealed inside the melted KCl-$ZnCl_2$ salts mixture, resulting in a significant increase in the specific surface area. The results also show that the Zn atoms doped into the crystal of C_3N_4 can improve its photocatalytic activity for dye degradation. Since visible and infrared light constitute 95% of total solar light power and UV light only accounts for ~5%, the third section of this thesis aimed to modify C_3N_4 to efficiently degrade the dyes under visible light irradiation. The improvement achieved by optimizing the doping sites of Cl dopants via the combined effect of Cl contraction and agitation rate during the solvothermal synthesis. With proper amount of Cl dopants and balance of the doping sites, the photocatalytic performance was remarkably improved by Cl-doped C_3N_4. The fourth section of this thesis reports the synthesis of the C doped TiN/ultrathin carbon layer. This newly developed C_3N_4/TiO_2 heterostructure has a superior photocatalytic activity than commercial rutile TiO_2 under visible light irradiation. The C dopants are proven to be able to promote the generation and energy of hot carriers.

List of Abbreviations

0D	**Zero-dimensional**
1D	**One-dimensional**
2D	**Two-dimensional**
3D	**Three-dimensional**
A/A^-	**Acceptors**
BET	**Brunauer–Emmett–Teller**
CB	**Conduction band**
CBM	**Conduction band minimum**
CBE	**Conduction band edge**
D/D^+	**Donators**
DFT	**Density functional theory**
DI	**Deionized**
DRS	**Diffuse reflectance spectroscopy**
DSC	**Differential scanning calorimetry**
e^-	**Electron**
EDS	**X-ray energy dispersive spectrometer**
E_g	**Band gap**

ESI-MS	**Electrospray ionization mass spectrometry**
FTIR	**Fourier transform infrared**
FWHM	**Full width at half maximum**
h^+	**Hole**
HOMO	**Highest occupied molecular orbital**
HPLC-MS	**High-performance liquid chromatography-Mass Spectrometry**
IR	**Infrared**
ITO	**Indium tin oxide**
K-M	**Kubelka-Munk**
L-H	**Langmuir-Hinshelwood**
LSPR	**Localized surface plasmon resonance**
LUMO	**Lowest unoccupied molecular orbital**
MO	**Methyl orange**
NHE	**Normal hydrogen electrode**
NIR	**Near infrared**
PDOS	**Projected density of states**
PID	**Proportional–integral–derivative**
PL	**Photoluminescence**

PSPP	**Propagation surface plasmon polaritons**
RhB	**Rhodamine B**
rpm	**Revolution per Minute**
SEM	**Scanning electron microscopy**
SHE	**Standard hydrogen electrode**
SSA	**Specific surface area**
STA	**Simultaneous thermal analyses**
STEM	**Scanning transmission electron microscope**
TDOS	**Total density of states**
TEM	**Transmission electron microscopy**
TGA	**Thermogravimetric analysis**
TOC	**Total organic carbon**
UPLC-MS	**Ultra-performance liquid chromatography-mass spectrometry**
UV	**Ultraviolet**
UV-Vis	**Ultraviolet–visible**
VB	**Valence band**
VBE	**Valence band edge**
VBM	**Valence band maximum**

XPS	**X-ray photoelectron spectroscopy**
XRD	**X-ray diffraction**

Acknowledgments

First of all, I would like to express my deepest gratitude to my supervisor, Professor Xianfeng Fan for his continuous support throughout this study and research and his guidance, motivation and advice. His patience, prudence and enthusiasm for scientific truth have had a great impact on me.

I would also like to thank the staff at the University of Edinburgh who aided in so many ways to the completion of this work. In particular, I would like to acknowledge Dr Ke Wang; this research could not be possible without his constant help and encouragement. I would like to express my appreciations to Mr Fergus Dingwall, Dr Ignacio Tudela-Montes, Dr Francisco García García, Dr Cher Hon Lau, Dr Chenggong Sun, Dr Nicola Cayzer, Dr Andrei Gromov, Dr Gary S. Nichol and Steve Mitchell for all their help and supporting of facilities. I would like to thank team members and lab mates who were always open to chat with me and help me with my questions; my sincere thanks go to Jialin Yu, Shibo Shao, Cong Chao and Dr Francis Bougie. To all my friends in IMP, thank you for all the support and good times, in particular I would like to thank Ammara Akram, Winifred Obande, Hairan and Nancy Wang for their encouragement and advice.

Finally yet importantly, I would like to give thanks to those friends and family members who supported me at times of difficulties and rejoiced with me at times of happiness. A special thanks to Mr Xiaodong Liu and Ms Hong Su, they take care of me like family here in Edinburgh. I would like to thank my friends in China; they give me unfailing confidence and company. My foremost and greatest thanks should be given to my dear parents, for their enormous support and encouragements throughout the time. I dedicate this thesis to their love, patience and belief in my capabilities.

Declaration

I declare that this thesis has been composed solely by myself and that it has not been submitted, in whole or in part, in any previous application for a degree. Except where states otherwise by reference or acknowledgment, the work presented is entirely my own.

Contents

List of Figures

List of Tables

Chapter 1 Literature review

1.1 Introduction

1.1.1 Backgrounds and motivations

Environmental pollution has been one of the major international concerns, due to its harmful impact on human health, the sustainable development of society and economy, and ecosystems in the world. Various emerging pollutants are increasingly accumulated in the environment due to the accelerated industrialization, urbanization and agricultural intensification, such as persistence organic pollutants, nanomaterials pollutants, microplastics, radioactive pollutants, and heavy metals. Among them, organic pollutants have drawn significant attention because of their bio-accumulative and harmful nature. Utilization of sustainable energy has received great interest, particularly the use of solar energy, as the amount of solar energy striking the earth surface is 1.3×10^5 TW per year, which is much greater than the energy consumed by humanity [1]. The challenges in the utilization of solar energy is mainly related to the effective harvest, storage and efficient utilization due to its intermittent nature [2]. Photocatalysis is believed as a promising technology to address and the environmental challenge through the utilization of solar energy, and it has been intensively investigated in the past two decades [1, 3]. Development of new semiconductors as highly efficient photocatalysts has been considered as the key to achieve the practical implementation of photocatalytic technology in real world.

To date, in the industry the most widely used method of water treatment is adsorption based: membrane operations, activated carbon, coagulation by chemical agents etc. [4]. However, only adsorption cannot effectively remove the dye in wastewater, and the subsequent processing is still complicated and expensive [5]. Biological method (biodegradation [6]) and chemical methods (eg. chlorination, ozonation [7]) have shown efficient dye degradation capability in the laboratory. However, these new methods show higher operating costs and have a limited impact on carbon content, which limits their practical usage in industry.

The emerging photocatalytic technology can take advantage of solar light to drive the catalytic degradation and mineralization of environmental pollutants. After absorbing solar light, the photocatalysts can produce highly reactive substances, such as hydroxyl radicals, which can rapidly and non-selectively oxidize a variety of contaminants. Additionally, the photocatalytic environmental remediation only requires a relatively mild reaction condition. After

photochemical treatment of wastewater, the pollutants can be completely mineralized into CO_2 and H_2O. The photocatalytic remediation has the advantages of zero energy consumption, low cost, and high efficiency in organic pollutants degradation. Therefore, it is believed as one of the most promising strategies for environmental pollution control. A series of studies have proven that the photocatalytic removal of hazardous compounds from water is efficient and versatile [8-10]. Hundreds of organic or inorganic pollutants can be degraded by photocatalytic oxidation, therefore the photocatalysis shows promising applications in atmospheric and water pollution remediation.

Although the photocatalytic technology has gone through a rapid development in recent decades, the photocatalytic technology still shows critical shortcomings such as low utilization of visible light and poor efficiency of photo-generated electron-hole separation, which seriously restricts its photocatalytic performance for dye degradation. Therefore, it is of great importance to conduct the fundamental researches to develop new photocatalysts with high photocatalytic dye degradation performance. The focus of this thesis is to develop new synthesis methods for high-performance photocatalysts, strategy to enhance the activity of photocatalysts and most importantly, unravelling the mechanism underpinning activity improvement.

1.1.2 Structure of thesis

This thesis is formed by six main chapters.

The first chapter is the literature review and the fundamental theory. The background of the research project is discussed in detail. It includes the history, basic principle and current knowledge gaps in photocatalysis. The introduction of major factors affecting photocatalytic performance and typical modification methods to improve the photocatalytic performance were discussed in this chapter too.

The second chapter focuses on the experimental methodologies, which were employed in this thesis. The synthetic methods, materials, equipment specifications and analytical techniques have been described in detail.

The following three chapters are constructed by my original research works. The third chapter presents the improvements of C_3N_4 photocatalytic performance through a unique synthesis method in KCl-$ZnCl_2$ molten salts. The photocatalytic activities of the prepared C_3N_4 samples were tested under simulated solar light irradiation. The sample with moderate Zn doping

showed outstanding photocatalytic properties. Moreover, there was a temperature window in the thermal polycondensation for C_3N_4 proven critical to successfully improve the photocatalytic activity of the C_3N_4. However, the prepared Zn-doped C_3N_4 can only absorb UV light, though visible light constitutes as the main part of solar energy. To achieve an enhanced solar energy utilisation, improving the photocatalytic performance of C_3N_4 under visible light irradiation was conducted. In the fourth chapter, Cl-doped C_3N_4 was synthesized via a novel agitation-assisted solvothermal method. The structural analyses evidenced that Cl could dope into both interstitial and substitutional sites in C_3N_4 and the preferred doping site was controlled by the agitation rates. Furthermore, it was found the Cl dopants at different sites function very differently on improving the photocatalytic performances. In this chapter, the photodegradation performance was evaluated under visible light irradiation. The prepared Cl doped C_3N_4 with high SSA achieved high photocatalytic activity and excellent stability. In order to further optimize C_3N_4, combining C_3N_4 with other semiconductors to form a heterojunction was the initial intention of subsequent research. However, it was found that the C-doped TiN/ultrathin carbon layer produced during the optimization of synthesis condition outperformed the classical design of C_3N_4/TiO_2 heterostructure. In the fifth chapter, the C doped TiN/ultrathin carbon layer catalysts were prepared via a facile one-pot calcination method and proven to be an efficient noble-metal free plasmonic photocatalyst. The experimental and theoretical results proved that the C doped TiN/ultrathin carbon layer had shown enhanced photocatalytic activity due to the photo-excited holes with both higher energy and quantity.

The final chapter concludes the thesis and summarizes the key findings. Additionally, potential improvements and future investigations are proposed at the end of the sixth chapter.

1.2 Principles of photocatalysis

Photocatalysis is inspired by the natural process that plants converts CO_2 and H_2O into carbohydrates under solar light irradiation [11]. In general, photocatalysis involves both the utilization of light to thermodynamically drive the reaction as well as the catalytic process to overcome the kinetic activation barrier of the reaction [2, 12]. These light-driven thermodynamic uphill reactions are not spontaneous, therefore the energy converted from solar light is indispensable to make them thermodynamically feasible. In addition, the introduction of a catalyst is to increase the reaction rate by lowering the kinetic energy barrier. Many different types of reactions can be classified into the category of photocatalysis.

1.2.1 History of photocatalysis

The chemist, Giacomo Ciamician was one of the first to experimentally study whether "light" would promote chemical reactions in 1908 [13]. In 1911, scientists discovered the bleaching effect of ZnO on Prussian blue under external illumination, and "Photocatalysis", then for the first time, appeared in the scientific literature [14]. This discovery inspired subsequent experiments in the use of ZnO as a photocatalyst for other reactions. For example, in 1924, Baur and Perret [15] discovered that ZnO could catalyse the reduction of silver salts to metal silver under the irradiation of light. From the perspective of the reduction reaction, its photocatalytic mechanism was speculated. Subsequently, in 1938, Goodeve et al. [16] studied the photocatalytic decomposition of dyes by TiO_2 powders and found that TiO_2 powders could accelerate the photochemical oxidation. In 1972, Fujishima and Honda [17] reported on the journal *Nature* the very first research on photocatalytic H_2 production through water splitting by exposing TiO_2 electrodes under UV light irradiation. This work soon drew the attention of the researchers worldwide. Pioneering researches on the application of photocatalytic technology to convert solar energy into clean energy such as hydrogen increased significantly afterwards. In 1976, Carey et al. [18] found that TiO_2 could decompose organic pollutants (polychlorinated biphenyls, PCBs) in water under the irradiation of UV light. Later in 1977, Bard et al. [19] also reported that TiO_2 could be excited by UV light to boost the degradation of cyanide and sulfite in water. These two studies proved the feasibility of implementing photocatalytic technology in the field of environmental pollution treatment. Due to the excellent results in the development of photocatalytic environmental restoration, it has attracted widespread attention from researchers in the environmental research fields around the world. Photocatalytic technology has also rapidly moved from the basic theoretical research in laboratories to the practical applications of solving the problems of environmental pollution in the real-life [20].

1.2.2 Mechanism of semiconductor photocatalysis

The modern photocatalysts are mainly composed by semiconductors and semiconductor photocatalysts are usually referred as photocatalysts in short. Compared with metal conductors, semiconductors have discontinuous energy bands. In the crystal of semiconductor materials at ground state, highest band occupied by electrons is called that valence band (VB). The lowest unoccupied band is called the conduction band (CB). The region without electrons between

the top of the semiconductor valence band and the bottom of conduction band is called the forbidden band. The width of this region is called the band gap width, which is expressed by E_g. Generally, the band gap width for a semiconductor is about 1~4 eV. Titanium dioxide (TiO_2) [21] has proven to be one of the excellent photocatalysts for water splitting and the oxidative decomposition of many organic compounds. It is featured by its relatively narrow band gap, long lifetime of the photo-excited charge carriers, nontoxicity, environmental friendliness and low cost. Other common semiconductors such as ZnO, CdS, MoS_2, Fe_2O_3, WO_3 are also excellent candidates for photocatalysis [22-26].

From the perspective of semiconductor photochemistry, the photocatalysts have two roles: (1) absorbing the solar light and convert the energy from light to electron-hole pairs; (2) providing active sites to catalyse the reaction. The basic mechanism of photocatalytic process involves five key stages, as outlined in **Figure 1.1**:

(i) The energy that is equal to or greater than the band-gap energy of the semiconductor can be absorbed. An electron (e^-) is excited from the VB into the CB, leaving a hole (h^+) in the VB;

(ii) The excited holes migrate to the surface of the photocatalyst as an oxidant to react with the electron donors (D);

(iii) The excited electrons move to the surface and act as the reductant to react with the electron acceptors (A). The products of the initial steps are active radicals and capable of degrading organic pollutants;

(iv) e^- and h^+ recombination on the surface;

(v) e^- and h^+ recombination in bulk and dissipate energy in the form of heat or photon.

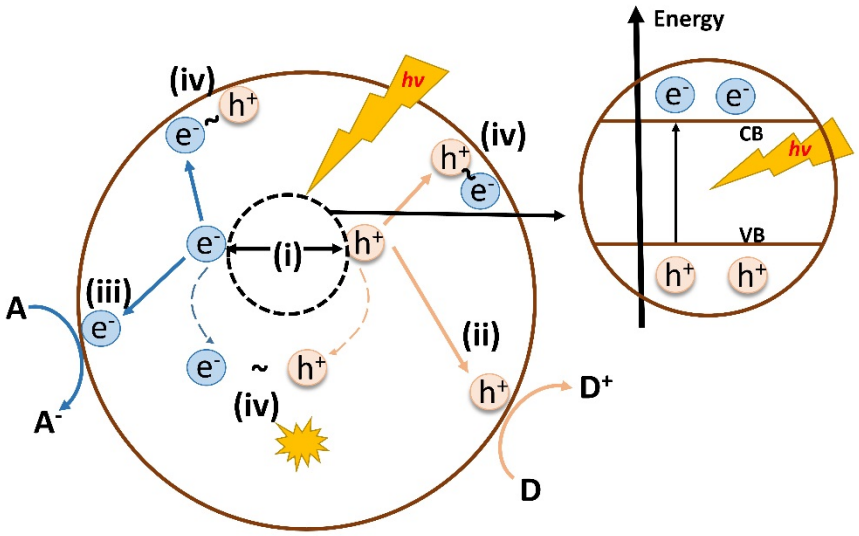

Figure 1.1. The scheme of the photocatalysis mechanism

To date, the typical applications of photocatalytic redox technology includes water splitting for H_2 production, photodegradation of pollutants and CO_2 reduction to hydrocarbon fuels. In the following paragraph, a brief introduction is presented to describe these 3 processes.

Thermodynamically, the overall water splitting reaction has a positive ΔG, indicating that it is an uphill reaction and requires energy of 1.23eV (Eq.(1.1)) [27, 28].

$$H_2O \xrightarrow{light+photocatalyst} \frac{1}{2}O_2 + H_2;\ \Delta G = +237.35\ \text{kJ mol}^{-1} \quad (1.1)$$

Different from water splitting, the pollutant decomposition is a downhill reaction, indicating that such a reaction is a spontaneous process. Once the photo-induced e^- and h^+ reach the photoactive sites on the surface of the catalyst, electrons will react with the electron acceptor; usually the dissolved oxygen in the solution, producing $\cdot O_2^-$ radical anions, while holes can react with electron donors such as H_2O or OH^- to generate oxidant ·OH [29]. The strong oxidizing and reducing abilities of these highly active species can cause direct oxidisation of organic compounds to CO_2 and H_2O as the final products. However, in more cases, the intermediates of the organic compounds oxidation rather than CO_2/H_2O are the products due to the incomplete oxidation. Therefore, to enable the full oxidation of pollutants, the photocatalyst should have a positive enough VBM. Simultaneously, a sufficiently small bandgap of the photocatalyst is also necessary for an enhanced light absorption [27]. In summary, the chain reaction involves in the photocatalytic organic pollution degradation process are described by the following equations (Eq. (1.2) to Eq. (1.11)).

(i) Generation of electron-hole pairs:

$$\text{Photocatalyst} + h\nu \rightarrow h^+ + e^- \quad (1.2)$$

(ii) Reactions triggered by the holes

$$h^+ + \text{RH(pollutant)} \rightarrow \text{RH}^+ \quad (1.3)$$

$$h^+ + \text{H}_2\text{O} \rightarrow \cdot\text{OH} + \text{H}^+ \quad (1.4)$$

$$h^+ + \text{OH}^- \rightarrow \cdot\text{OH} \quad (1.5)$$

(iii) Reaction triggered by the electrons and the following chain reactions:

$$e^- + \text{O}_2 \rightarrow \cdot\text{O}_2^- \quad (1.6)$$

$$\cdot\text{O}_2^- + \text{H}^+ \rightarrow \cdot\text{OOH} \quad (1.7)$$

$$2\cdot\text{OOH} \rightarrow \text{O}_2 + \text{H}_2\text{O}_2 \quad (1.8)$$

$$\text{H}_2\text{O}_2 + \cdot\text{O}_2^- \rightarrow \cdot\text{OH} + \text{OH}^- + \text{O}_2 \quad (1.9)$$

$$\text{H}_2\text{O}_2 + h\nu \rightarrow 2\cdot\text{OH} \quad (1.10)$$

(iv) Organic pollutant degradation:

$$\text{Pollutant} + \text{active species } (\cdot\text{OH}, \text{h}^+, \cdot\text{OOH or } \cdot\text{O}_2^-) \rightarrow \text{degradation product} \quad (1.11)$$

The three main radicals involved in the redox reaction are proton (H^+), superoxide radical ($\cdot O_2^-$) and hydroxyl radical ($\cdot$OH). Usually, $\cdot$OH is the main oxidant for pollutants oxidation in the aqueous solution [29].

Inoue et al. [30] firstly reported the photocatalytic reduction of carbon dioxide in 1979 with the formation of organic compounds such as formic acid, formaldehyde, methanol and methane. Photocatalytic reduction of CO_2 with H_2O, which is known as the artificial photosynthesis, is considered as an ideal way to produce solar fuels and high-value chemicals. However, due to the high energy of the LUMO of CO_2 and linear molecular structure, almost no semiconductor can provide sufficient potential to transfer a single photo-generated electron to a free CO_2 molecule. The first step of direct reduction of CO_2 to CO_2^- requires the energy of -1.90 V (*vs* SHE) [31]. In fact, the CO_2 photoreduction process is not a one-step reaction but involves multiple steps of proton-coupled electron transfer. By obtaining two, four, six or eight electrons and protons, the CO_2 is reduced to HCOOH (liquid phase, E^0=-0.61 V)/CO

(gas phase, E^0=-0.53 V), HCHO (liquid phase, E^0=-0.48 V), CH_3OH (liquid phase, E^0 = -0.38) and CH_4 (gas phase, E^0=-0.24 V), respectively (the reduction potentials are relative to the RHE at pH 7) [32].

1.2.3 Factors affecting the efficiency of photocatalysis

It should be noted that the photo-excited CB electrons and VB holes can recombine and release another photon or heat (as described in **Figure 1.1**). The recombination is believed to be the main factor detrimental to the activity of photocatalysts [33]. Besides the photo-excited electron/hole pairs recombination, many other factors can affect the photocatalytic reaction rate too. The influential factors include bandgap, electronic structure, crystal structure, morphology and SSA. Besides the effects of photocatalyst properties, external reaction condition factors mainly include the intensity of illumination, the organic concentration for degradation, temperature and pH of the solution, etc.

1.2.3.1 Semiconductor photocatalyst bandgap and the influence of band edge position

Semiconductor adsorbs light below a threshold wavelength λ_g, which is related to the bandgap energy E_g by:

$$E_g = h\frac{c}{\lambda_g} \tag{1.12}$$

where h is the Planck's constant (6.626×10^{-34} J s), c the speed of light (3.0×10^8 m s^{-1}). Considering the constitution of the solar spectrum (shown in **Figure 1.2**), UV light (200-400 nm) accounts for only about 5% of the entire solar energy, while visible light (400-700 nm) and IR light (700-2500 nm) accounted for 47% and 48% of the total solar energy [34]. It can be seen that visible light and IR light are considered as the main components of sunlight. In general, few semiconductor photocatalyst can be excited by infrared light with a longer wavelength, due to its very low energy. Therefore, it is of great research value and practical significance to develop the photocatalysts that can be excited by visible light. According to the Eq. (1.12) , when λ_g = 400 nm, E_g = 3.1 eV. Therefore, to adsorb visible light, the bandgap (E_g) of the semiconductor need to be lower than 3.1 eV.

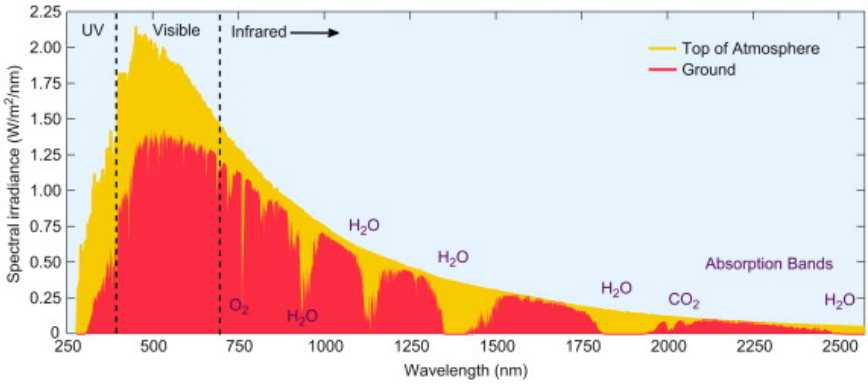

Figure 1.2. Solar spectra as a function of wavelength. Reproduced from Ref. [35] with permission.

However, as photocatalysts, the bandgap of semiconductor needs to be moderate. Because the positions of the CBM and VBM in semiconductor determine the reducing ability of photo-generated electrons and the oxidizing ability of photo-generated holes, respectively. The more negative of the CB edge, the stronger the reduction ability the photo-generated electrons possess; the more positive of the VB position, the stronger the oxidizing ability the photo-generated holes exhibit. The thermodynamically feasible photocatalytic reaction must meet two conditions: (1) the electron acceptor potential is more positive than the semiconductor CBM potential; and (2) the electron donor potential is more negative than the semiconductor VBM potential. **Figure 1.3** shows the bandgap energy and band edge positions of common semiconductors with selected redox potentials.

Taking photodegradation of pollutants as an example, if the photocatalyst CBM potential is more negative than the potential of E^0 ($O_2/\cdot O_2^-$) = -0.33 eV (*vs.* NHE at pH=7), oxygen will be reduced as an electron acceptor to generate superoxide radicals ($\cdot O_2^-$) [36]. If the VBM potential of semiconductor photocatalyst is more positive than the potential of E^0 ($\cdot OH/OH^-$) = +2.38 eV or E^0 ($\cdot OH, H^+, H_2O$) = +2.72 eV, photogenerated holes (h^+) can oxidize OH^- or H_2O adsorbed on the surface of a photocatalyst to ·OH [37]. As already mentioned, the generated $\cdot O_2^-$, ·OH and photogenerated h^+ are the main participators in the degradation of environmental pollutants.

From the above description, it can be seen that the redox capabilities of semiconductor photocatalysts compete with their light absorption ability. If the light absorption ability increases, the redox capabilities of its photo-induced electrons/holes decrease. On the contrary, with redox capability increasing, the light absorption ability decreases. Therefore, it is important to balance these parameters and find the optimal electronic structure for photocatalysts.

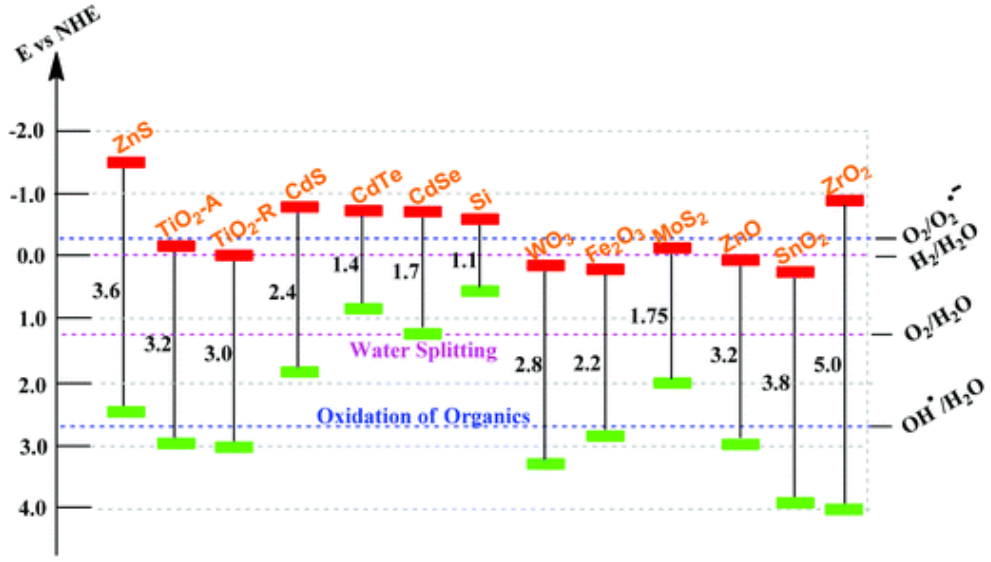

Figure 1.3. Band gap energy, VB and CB for a range of semiconductors on a potential scale (V) versus the normal hydrogen electrode (NHE). Reproduced from ref. [38] with permission.

1.2.3.2 The lifetime of photogenerated carriers

As emphasized in the previous section, the recombination of photo-induced electron/hole pairs is the main reason retarding the photocatalytic activity. Therefore, the key to the development of high-performance photocatalysts is to suppress the recombination. It has been proven that the charge carrier separation efficiency is closely related to the crystal structure of the semiconductor, the existence of co-catalysts and the microscopic surface structure of the catalyst. But the detailed mechanisms underpinning the strategies to promote the electron-hole pairs separation are still ambiguous. To date, in order to maximise the usage of photo-generated carriers and enhance the photocatalytic reaction rate, an additional trapping agent is often added during the photocatalytic reaction. The trapping agent is used to quench one kind of the charge carriers, as the result, the other kind of charge carriers can survive with longer lifetime. The most commonly used scavengers are presented as following: h^+ scavengers including EDTA-2Na, ammonium oxalate (AO), potassium iodide, light aliphatic alcohol, triethanolammonium, citric acid, etc.; e^- scavengers including silver nitrate, hydrogen peroxide, ozone, SF6 and potassium bromate. In addition, to investigate the pathway of the photocatalytic reaction, trapping agents to fast consume a specific kind of photo-reaction radicals are often used. For example, ·OH capture agents mainly include isopropyl alcohol (IPA), Tert-butanol (TBA), etc.; O_2^- capture agent is p-benzoquinone (BQ).

1.2.3.3 Effect of crystal structure

It is generally believed that the degree of crystallization of the semiconductor catalyst strongly affects the rate of charge carriers migration. The higher the degree of crystallization, the faster the charge carriers migrate in the catalyst, and the chances for the recombination become low. Samples with higher crystallinity with fewer defects and less scattering to the electron transport process, leading to a higher transfer rate. Besides the crystallization degree, the crystal structure is also one of the factors affecting the photocatalytic activity of the photocatalyst. For example, the most widely used n-type semiconductor photocatalyst, TiO_2, has two common crystal phases: anatase and rutile. Both rutile and anatase TiO_2 belong to the tetragonal system, but their electronic structures are different. The researches show that the band gap width of the rutile type is 3.0 eV, which is slightly smaller than 3.2 eV of the anatase type [39, 40]. In terms of band gap width, the corresponding light adsorption range of rutile TiO_2 is slightly larger than that of anatase. However, under UV light irradiation, the anatase exhibits higher photocatalytic activity than the rutile. It is because the anatase and rutile TiO_2 exhibit indirect and direct bandgap electronic structures, respectively [41]. Since the recombination of e^- and h^+ in the indirect bandgap structure needs extra assistance from phonon, the photo-induced charge carriers lifetime in anatase is significantly longer than in rutile [42, 43]. In addition, studies have shown that different crystal planes have different photocatalytic activities, even in the same crystal phase. If the proportion of crystal planes with high photocatalytic activity is increased, the catalytic activity of semiconductor photocatalysts can be improved. For example, the photocatalytic activity of the (001) crystal plane of bismuth oxychloride (BiOCl) is higher than that of other crystal planes. Increasing the proportion of the (001) crystal plane also significantly improves its photocatalytic activity. Similar phenomena exist in other semiconductor photocatalysts too [44-46].

1.2.3.4 Particle size and specific surface area

Particle size and SSA are also important factors affecting the photocatalytic activity of semiconductor photocatalysts. When the semiconductor photocatalyst particle size becomes smaller, its photocatalytic activity usually becomes higher. The main reasons are summarized as the following:

(1) Comparing with bulk semiconductor materials, nanoscale semiconductor materials have a widened band gap [47, 48]. Because the less atoms in the nanoscale crystal will narrow every electronic band and result in an enlarged gap between bands [49]. The VB and CB are more separated and the absorption band edge undergoes a "blue shift" (the absorption band moves

in the short-wave direction). As a result, the redox capacity of the photogenerated carriers is enhanced.

(2) The nanoscale semiconductor particles can promote the transport of photogenerated carriers from the bulk to the surface due to the shorter transport distance [50]. Therefore, the improved photocatalytic activity can be achieved by lowering the probability of photo-generated e^-/h^+ pairs recombination [51, 52].

(3) The nanoscale nanoparticles are expected to have enlarged SSA. A significantly large SSA will result in the enhanced pollutants adsorption and the increases of active sites on the photocatalyst surface. Therefore, the catalytic activity of the nano-semiconductor photocatalyst is increased [53].

1.2.3.5 External influence factor

The activity of photocatalyst is not only related to itself but also to many external reaction conditions [29]. Firstly, according to the Arrhenius equation (Eq.(1.13)), the reaction temperature is an important factor affecting the photocatalytic reaction rate [54].

$$k = Ae^{-E_a/RT} \tag{1.13}$$

Secondly, the pH of the system mainly affects the photocatalytic activity of the photocatalyst in the following two aspects: on the one hand, changing the pH of the system can change the surface charge of the semiconductor and affect its ability to adsorb reactants [55]; on the other hand, the pH of the system also has a significant impact on the molecular configuration of some organic pollutants adsorbed on the active sites [56]. Therefore, changes in pH will have different effects on the degradation of different pollutants from case to case. Thirdly, an external field such as an electric field can promote the photocatalytic degradation of pollutants. For example, an external electric field can be built by adsorbing polarized molecules on the semiconductor surface, and the enhancement is attributed to the promoted directional separation of photogenerated carriers under the external electric field [57, 58]. Fourthly, the additives (H_2O_2, Fenton, $S_2O_8^{2-}$, etc.) can also promote the photocatalytic degradation of pollutants [59-61]. In addition to their capability of directly oxidizing some organic pollutants, these additives can also interact with photo-generated carriers to form more strongly oxidizing active species. Therefore, they can improve the photocatalytic activity of the system. The last point, the concentration of organic pollutant also significantly affects the degradation rate [62].

1.2.4 Materials design strategy to improve photocatalytic activity

1.2.4.1 Doping

Doping has been proven as an effective way to improve the photocatalytic performance of catalysts by modifying the electronic structure [63, 64]. The promotion effects of doping on photocatalytic activity can be summarized as the following aspects.

Firstly, the doping can reduce the bandgap of the semiconductor and enhance the utilization of the solar light. Many promising photocatalysts are relatively wide-bandgap semiconductors such as TiO_2, ZnO and their UV range adsorption band hampers the full utilization of the solar spectrum. By adding the dopants into the crystal of the semiconductor, additional energy level derived from dopants can effectively reduce the bandgap. For example, Zhang et al. [65] reported the C doping into the monolayer of WS_2 via the plasma-assisted method. The bandgap of WS_2 reduced from 1.98 to 1.93 eV and a p-type conductivity was achieved. In addition to the single kind of dopants, the co-doping techniques have been proven successful too. Na Phattalung et al. [66] doped V-N pairs into the lattice of anatase-TiO_2 and reduced the bandgap by ~0.5 eV. The doping atoms are not limited to be heteroatoms different from the formula of the semiconductor. The self-doping strategy has also been proven effective. Ti^{3+} self-doped TiO_2 has been reported by Mao et al. [67] and the enhanced performance of photocatalytic N_2H_4 reduction is attributed to the increased solar light adsorption.

Secondly, the doping could adjust the band edge positions to meet the requirement of interested reaction. For instance, the CBM is often lifted by doping to enhance the CO_2 reduction capability and VBM is often reduced to enhance the performance of pollutants oxidation. There is a general relation between the dopants and energy band edge position adjustment. Here, the TiO_2 is taken as an example for explanation. The VB and CB of TiO_2 are usually composed by 2p-orbitals of O atoms and d-orbitals of Ti atoms, respectively. Therefore, when anion dopants have 2p orbitals more negative than the O 2p orbital in the energy, the VBM will be lifted to the negative direction with a decrease in the oxidation capability. It is because the p orbital of anion dopants having energy levels higher than the O 2p-orbital energy will hybridize with O 2p-orbitals forming a more negative O 2p-orbitals as the VB. On the contrary, if the 2p-orbital energy of anion dopants is lower than O 2p, the VB will be shifted to the positive direction. The cation doping follows the same rule. When doping cations (usually transition metal elements) into the TiO_2 with higher energy d-orbital than Ti, the hybridization will move the CB of TiO_2 to the negative direction, which enhances the

reducibility of the TiO_2. The cation dopants with lower d-band energy than Ti will make the VB more positive.

The last important effect of doping is the suppression of the recombination of photo-induced charge carriers. The mechanism of the recombination suppression is due to the trapping effects of dopant energy level in the electronic structure. The photogenerated charge carriers can be temporarily trapped by these dopant energy levels before recombination, which results in a remarkably longer carrier lifetime [68, 69]. However, an over-doped semiconductor can show more severe recombination since the dopants can also play the role as the recombination centre.

1.2.4.2 Vacancies engineering

Besides doping, introducing atom vacancies in the semiconductor is another effective way to improve the photocatalytic performance. In oxides, the O vacancies are usually the intrinsic defect. For instance, the TiO_2 and ZnO are intrinsic n-type semiconductors due to the existence of O vacancies in the lattice [70, 71]. The oxygen vacancies can introduce extra electrons localized at the defects and acting as the active sites for photocatalytic reaction. Recently, O vacancies with concentration much higher than the intrinsic concentration are introduced to the oxides, which has been proven as an effective way to improve the photocatalytic performance. Chen et al. [72] for the first time reported the H_2 treatment method to synthesize TiO_2 in black colour. Comparing with pristine TiO_2 only absorbing UV light, the black-TiO_2 shows the broad light absorption from UV to IR. The huge amounts of surface defects are ascribed to the significantly enhanced photocatalytic water splitting performance. Following this pioneering work, Wang et al. [73] reported a similar phenomenon that the TiO_2 nanotubes can turn to blackish after H_2 treatment. The abundance of V_O was ascribed to explain the remarkably narrowed bandgap. The detailed effects of abundant V_O on the electronic structure were investigated by Naldoni et al. [74] via the combination of experiments and DFT calculations. Their results indicated that the black-TiO_2 shows the structure constituted by a crystalline but reduced core and disordered but stoichiometric shell. It is generally believed that the oxygen vacancies in bulk and on the disordered surface contribute together to the narrowed bandgap and black-colour appearance: the disordered surface causes the tailing of the VBE and the oxygen vacancies introduce mid-gap defect energy level.

Although less common than the anion vacancies [75, 76], the transition metal vacancies introduction is also effective to tune the electronic structure and optimize the photocatalytic performance. The Ti vacancies engineering was firstly reported by Wang et al. [77] in TiO_2 to enhance the photocatalytic performance. The $Ti_{0.905}O_2$ was synthesized via the solvothermal

method under the assistance of glycerol. A p-type conductivity feature was observed and the photocatalytic degradation activity increased by 7 times. The same group also reported the p-type ZnO with abundant Zn vacancies using the same synthesis strategy [78]. The transition metal vacancies are formed easier in low-dimensional materials than conventional nanoparticles. Guan et al. [79] reported a triple-vacancy-associates: $V_{Bi}'''V_O^{\bullet\bullet}V_{Bi}'''$ formed on ultrathin BiOCl, which exhibited significant improvement on visible-light-driven RhB degradation. Bi vacancies engineering was also reported by Zhu et al. [80] in $BiPO_4$ nanorods. A mechanical vacancies creation mechanism was proven by the introduction of Bi vacancies via ball milling method with controllable concentrations.

1.2.4.3 Dye sensitization

Photosensitization is an effective strategy to expand the absorption of visible light of semiconductors. The dye added to the surface of the semiconductor can absorb visible light and reach an excited state. The presence of photosensitizers can effectively expand light usage by semiconductors [81, 82]. In the photocatalytic reaction, the photosensitizer needs to meet the following condition in order to function properly: the HOMO position of the photosensitizer is more negative than the CBE of the modified semiconductor. In this case, the electrons generated under photoexcitation can be injected to the CB of the semiconductor and participates in the photocatalytic reaction.

Commonly used photosensitizers include phthalocyanine dyes [83-85], fluorescent pigment derivatives [86, 87], and pyridine complexes of ruthenium [88]. Li et al.[82] showed that ISQ-sensitized TiO_2 nanoparticles significantly expanded the light response in the visible light region, and their photocatalytic activity was significantly enhanced under visible light irradiation. In such system, the ISQ dye on the TiO_2 photosensitive surface can be easily excited from the ground state (D) to the excited state (D*) with the help of visible light. Following the injection of electrons into the CB of TiO_2, this excited state dye material can be converted into a semi-oxidized free radical cation ($^{\cdot}D^{+}$) because the LUMO energy level of the ISQ dye and the IQ dye matched well. The CB of TiO_2 is therefore conducive to charge transfer. Free radicals are then generated through a series of protonation and reduction steps. As reported by Shang et al.[89], the enhanced photocatalytic activity of dye-sensitized TiO_2 can be attributed to the wider light absorption spectral range and the direct transfer of electrons from the excited state of the dye molecule to the CB of TiO_2.

1.2.4.4 Heterostructure

The heterojunction is one of the hottest topics in the photocatalysis research field in recent years. The main purpose to build up the heterostructure is to efficiently separate the photogenerated electron-hole pairs and suppress the recombination. The construction of heterostructure is to combine semiconductors with a secondary substance (metal, other semiconductors, etc.) with good contact. The better electron-hole separation efficiency ensures the heterostructured catalyst exhibiting better catalytic performance than the single-component catalyst.

Heterostructure built between two kinds of semiconductors has been proven as a successful design for high-performance photocatalysts. Classification by semiconductors band alignment situation, the coupled composites can be categorized to three types: Type I with a straddling gap, Type II with a staggered gap and Type III with a broken gap (illustrated in **Figure 1.4**) [90]. In detail, for the type I band alignment, the VB and CB potentials of the smaller band gap semiconductor 2 are both confined within the larger band gap of semiconductor 1, forming a straddling style alignment. Therefore, under light irradiation with sufficient energy equal to or greater than the band gap of the semiconductor 1, photo-generation of electron-hole pairs can be generated. Due to the more negative CB and more positive VB of semiconductor 1 than semiconductor 2, both the photo-induced electrons and holes will transport into the CB and VB of semiconductor 2. Because charge carriers accumulate in the semiconductor 2, there is no significant overall enhancement of charge separation, which results in no enhancement on the photocatalytic activity. Moreover, the oxidizing and reducing abilities of the photocatalyst decrease too. Therefore, type I heterojunction should be avoided. As for the type II heterojunction, the chemical potential between semiconductor 1 and semiconductor 2 forms an upwards and downward band bend. The band edge potential is staggered between the two semiconductors, causing photogenerated charge carriers migrate to the opposite directions [91], which preventing recombination and extending the lifetime of the electrons and holes. Oxidation and reduction reactions occur independently on semiconductor 1 and semiconductor 2, respectively. Type II heterojunction is the most popular heterojunction because of the significantly enhanced electron-hole spatial separation. As for the type III heterojunction, obviously, both VB and CB edges of a semiconductor 2 are located above the CB potential of semiconductor 1 without crossing each other. There is no charge carrier transport between the heterojunctions, and it is equal to two independent semiconductors.

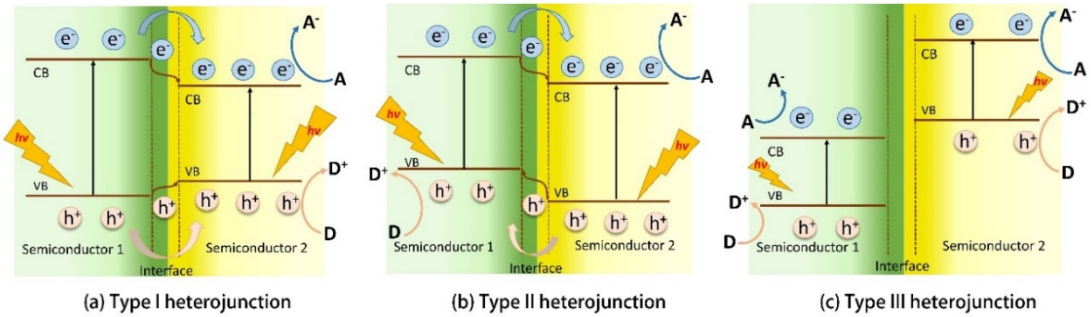

Figure 1.4. Schematic energy band diagram of three different types of heterojunctions in a typical semiconductor hybrid nanocomposite: (a) Type I heterojunction, (b) Type II heterojunction, and (c) Type III heterojunction. A and D denote electron acceptor and donor

The p-n heterojunction is the heterostructure formed by combining the p and n-type semiconductors together (as shown in **Figure 1.5** (a)). The p-n heterojunction attracts a lot of interests in this research field due to its inner electric field crossing the interface, which effectively promotes charge carriers separation [92]. According to the relative positions of the VB and CB band of each semiconductor, photogenerated electrons are transferred from the CB of the p-type semiconductor to the n-type semiconductor CB. At the same time, the holes in the n-type semiconductor VB will transport to the p-type semiconductor. As the built-in electric field points from n-type to p-type, which is opposite to the photo-induced electron transport direction and same with photo-induced hole transport direction, the separation and transport of photo-generated carriers are accelerated and high efficiency is achieved. The build-in electric field has shown a remarkable effect on improving the photocatalytic performances [93-95].

Another emerging heterostructure design is called the Z-scheme heterostructure (as shown in **Figure 1.5** (b)). As described in the former paragraph, though the conventional type II can achieve an enhanced electron/hole separation between the interface, the improvement comes with a compromise with decreased reducing and oxidizing ability. Aiming to address this issue, the characteristic feature of the Z-scheme heterostructure is the recombination between the hole in VB of semiconductor 1 and electron in CB of semiconductor 2. This design not only ensures a high charge carrier separation efficiency but also retains the high oxidizing and reducing potentials. To date, the Z-scheme design has been developed into the 3rd generation, the direct Z-scheme. Different from the 1st generation Z-scheme using redox ions in aqueous solution to transport charges and 2nd generation using a conductive interface between semiconductors, the 3rd generation Z-scheme is featured by a direct charge transport across the interface [96-98]. The success of direct Z-scheme heterostructure is based on the careful selection of semiconductor materials to achieve a proper band alignment and inner electric field.

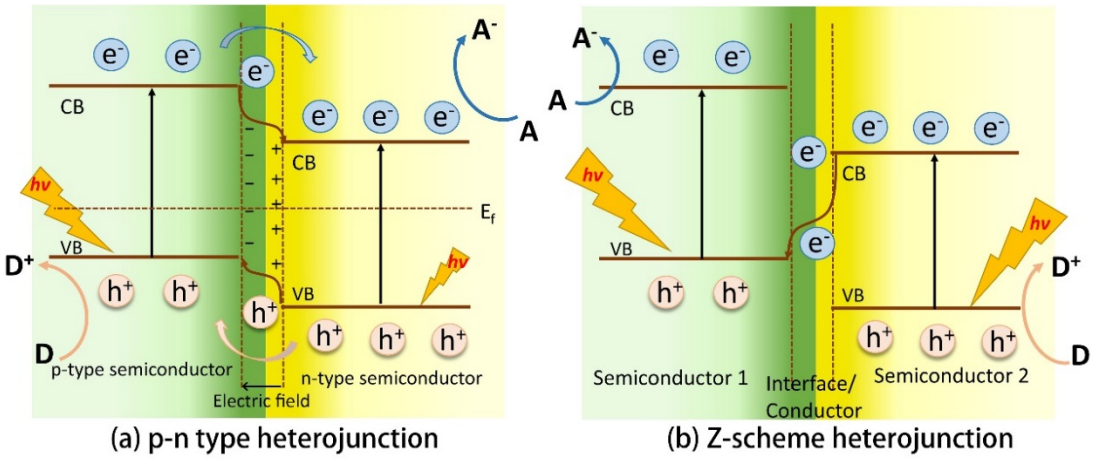

Figure 1.5. Scheme of (a) p-n type heterojunction and (b) Z-scheme heterojunction.

1.2.4.5 Coupling with π-conjugation materials

Establishing heterostructure with π-conjugated materials is an effective method for the modification of wide band gap semiconductors. The π conjugated structural materials including g-C_3N_4, graphene, C_{60}, polyaniline and polypyrrole (PPy) have been proven as effective co-catalysts for semiconductor. The main feature of π-conjugated electronic structures is the efficient transportation of charge carriers. Some π-conjugated materials can also be excited by incident light, which further enhances the photocatalytic performance of the system [99].

In Ni et al.'s work [100], graphene was strongly wrapped on the TiO_2 surface by hydrothermal method. A strong interaction between the carbon atoms and TiO_2 surface was built up with the formation of Ti–O–C chemical bonds. As the result, graphene-TiO_2 showed a strong redshift of the light absorption band and good photocatalytic performance even under visible light irradiation. C_{60} with unique electronic configuration and performance has been extensively investigated as co-catalysts, too. C_{60} has a closed-shell configuration consisting of 30 bonded molecular orbitals constituted by 60 π-electrons, which can effectively cause fast photogenerated charge separation and relatively slow charge recombination [101]. Fu et al.[102] proved that C_{60} hybridized ZnO could extend the light absorption of ZnO to the visible light range. The C_{60} also showed the ability to inhibit the photo-corrosion of ZnO. The authors claimed that it was because the C_{60} as co-catalysts could lower the activation energy of surface oxygen molecules. Due to the conjugated π electronic structure of C_{60}, a higher photoelectron migration efficiency was achieved at the interface between C_{60} and ZnO, which led to high efficiency in photo-induced electron/hole separation.

1.2.4.6 Other modification techniques

Besides all the strategies mentioned above, another method being able to enhance the photocatalytic activity of a semiconductor is to control its size, shape and crystalline degree. Altering the crystal shape with most active facets allows for a more efficient photocatalyst [103]. In addition, the photocatalytic activity can also be enhanced by achieving a highly crystalline structure as it increases the mobility of the excited charge carriers in comparison with an amorphous structure. Modification of surface functional group is another method to improve the photocatalytic performance [104-106]. For example, He et al. [107] reported an investigation on sulphuric acid modified TiO_2 nanosheets. It was concluded that the enhanced performance was due to the formation of oxygen vacancies, improved absorption capacity and promoted ·OH oxidation on the surface. Acid modifications were also found to lead to surface protonation, which was thought to increase the lifetime of the charge carriers.

1.3 Recent developments of g-C_3N_4 as photocatalysts

1.3.1 Introduction

In the past few decades, the most studied photocatalysts are mainly oxide semiconductor photocatalysts, but these oxides have the disadvantages of relatively high cost and poor acid and alkali resistance, which severely limits their practical application. The metal-free polymer graphite carbon nitride (g-C_3N_4), reported by Wang et al. [108], has become an attractive candidate in the visible-light-driven photocatalytic field for its unique properties. g-C_3N_4 is featured by its metal-free composition, non-toxicity, narrow bandgap (~2.7 eV and varies slightly due to different preparation method), proper CBE position, environmental friendliness and high chemical stability.

The researches on carbon nitride materials can be traced back to 1834. Berzelius synthesised a polymer derivative composed of carbon and nitrogen. This yellow, amorphous, and insoluble product was later named "melon" by Liebig et al. [109]. Liebig discovered melamine, melam, melem, and melon, which were recognized as heptazine- and triazine-based molecular compounds. In the following century, many types of researches have been done on the synthesis, design and application of these carbonitride polymers. In 1922, Franklin et al. [110] used mercury thiocyanate as a precursor to synthesize an amorphous carbon nitride by pyrolysis. The preliminary verification proved the polymer was chemically composited by "melon", and also found that such polymers contained about 1.1% -2.0% hydrogen. In 1937, Pauling and Sturdivant demonstrated coplanar tri-triazine units as basic elementary structural

patterns of various polymer derivatives through X-ray crystallographic studies [111]. Subsequently, Redemaim et al. [112] found that "melon" was not composed of a single structural unit, but a carbon-nitrogen polymer derivative composed of different polymers. Later, researchers tried to synthesize carbon nitride with a well-defined crystal structure through various efforts but failed. Because of the chemical inertness and insolubility of such polymers, researchers had not been able to determine their chemical structures. These polymers then were forgotten in the following decades. Until the end of the 1993, Liu and Cohen [113] replaced the Si atoms in sp^3-hybridized Si_3N_4 (denoted as β-C_3N_4) crystals with C atoms to construct the β-C_3N_4 model in the *ab initio* calculations. As a result, they predicted the β-C_3N_4 exhibited excellent thermal conductivity and hardness, which was even higher than diamond. This prediction made a large number of works focus on the design and synthesis of high hardness β-C_3N_4. In 1996, Teter and Hemley proposed through theoretical calculations that there were generally seven phases of C_3N_4, which are α-C_3N_4, β-C_3N_4, cubic C_3N_4 (c-C_3N_4), pseudo-cubic C_3N_4 (p-C_3N_4), g-h-triazine with band gaps of around 5.49, 4.85, 4.30, 4.13, and 2.97eV, respectively. The g-C_3N_4 was the only soft phase among these super hard phases, but it was the most stable one at room temperature [114]. The utilization of g-C_3N_4 in the heterogeneous catalysis research field started more than 10 years ago in 2006 [115]. In 2009, Wang et al. [108] found that g-C_3N_4 exhibited a high activity of water splitting to produce hydrogen under the excitation of visible light with Pt as the co-catalyst. Since then, the researches on the photocatalytic performance of g-C_3N_4, the polymeric conjugated semiconductor booms.

g-C_3N_4 has a layered structure similar to graphite, and the layers are held together by van der Waals force. The structure of a single layer is a hexagonal structure composed of σ bonds formed by sp^2 hybridisation between C and N atoms [116, 117]. At the same time, the lone electron pairs in the p_z orbits of the C and N atoms form a large π-bond aromatic conjugate structure similar to the benzene ring. The researchers further analysed the structure through theoretical calculations and found that the HOMO of g-C_3N_4 was composed of the p_z orbit of the N atom, and the LUMO was composed of the p_z orbit of the C atoms hybridized with p orbital of N atoms. The electronic structure that N atom contributed to both the HOMO and LUMO leading to the weak delocalization of the large π-bond. The high photocarrier recombination rate can be attributed to this structure, which was deemed as the main reason retarding the photocatalytic activity of pristine g-C_3N_4 [118, 119]. In addition, theoretical calculations showed that the VB position of g-C_3N_4 was approximately at 1.40 eV and the CB position was at approximately -1.30 eV vs. SHE [120]. The proper positions of the VB and CB enable g-C_3N_4 to drive the hydrogen and oxygen evolution reactions of water under light

irradiation. The relatively narrow bandgap of 2.7 eV ensures g-C_3N_4 responsible to visible light up to 460 nm.

Generally, there are two arguments about the elementary structural motif of g-C_3N_4: one is triazine (C_3N_3) and the other is tis-s-triazine/heptazine (C_6N_7), as shown in **Figure 1.6** [121]. Kroke et al. [122] used density functional theory (DFT) to perform theoretical calculations for the above two units. The results showed that the heptazine structural unit was more stable than the triazine structural unit. At present, the basic structural unit of g-C_3N_4 is considered to be a tis-s-triazine structure in most of the reported works.

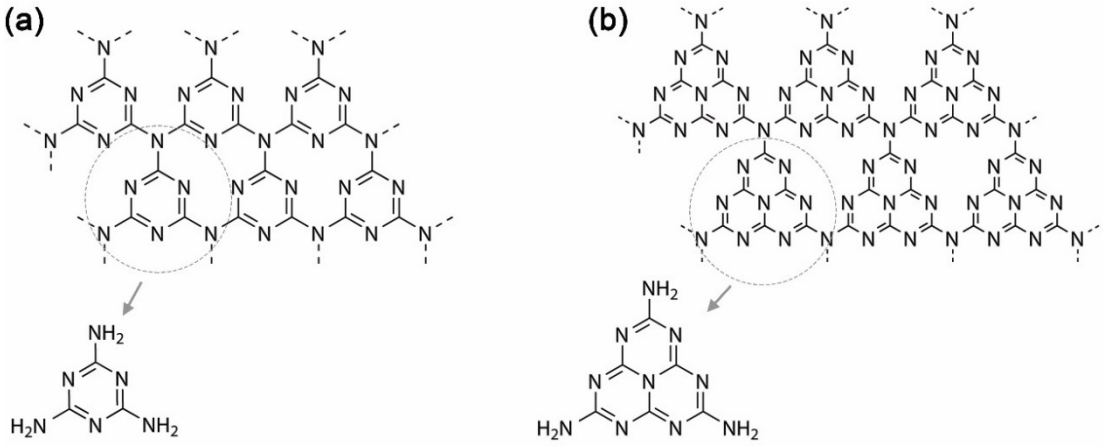

Figure 1.6. (a) Triazine and (b) tri-s-triazine (heptazine) structures of g-C_3N_4.

The preparation of g-C_3N_4 can be easily achieved by using a low-cost thermal condensation of nitrogen-rich precursors such as cyanamide, melamine, urea, and so forth. However, the g-C_3N_4 synthesized via this conventional method shows very limited SSA. And the fast recombination of photo-generated electron-hole pairs causes severe detrimental effects on the photocatalytic activity of g-C_3N_4. To address these challenges, many attempts have been carried out to optimise the synthesis of g-C_3N_4. Additionally, designing heterostructures by forming semiconductor/semiconductor interface or loading co-catalysts (e.g. metal cluster, carbon quantum dots, graphene) on g-C_3N_4 has also been proven effective to improve the lifetime of photo-induced charge carriers. Two categories of elemental doping, mainly non-metal doping and metal doping have been extensively investigated too. In the following paragraphs, the synthesis methods and strategies to improve the photocatalytic performance of g-C_3N_4 are summarized and reviewed.

1.3.2 Synthesis methods of g-C_3N_4

1.3.2.1 Thermal polymerization method

As the most conventional method for g-C_3N_4 synthesis, the thermal condensation method is to thermally induce a series of polycondensation reactions of precursors of C and N sources to form g-C_3N_4. Due to its simple pathway, low-cost and the good g-C_3N_4 crystallinity, it has become the most prevailing method for the preparation of g-C_3N_4 as photocatalysts in the literature.

Although the thermal polymerization experiment is simple to conduct, the molecular level understanding of the reaction is quite complicated. Thomas et al. [123] have used the first principle calculation and differential scanning calorimetry to carry out a detailed study on the thermal condensation of cyanamide to g-C_3N_4. As shown in **Figure 1.7**, according to the experimental results, it is inferred that cyanamide polymerizes to form cyanoguanidine at about 150 °C. When the temperature rises to about 240 °C, dicyandiamide or cyanamide can be polycondensed to melamine. With further increase in temperature to about 350 °C, melamine or dicyandiamide undergoes thermal polycondensation to melamine dimer (melam) and emits gaseous ammonia. The melamine dimer will undergo further thermal polycondensation and deamination to form the g-C_3N_4 structural unit 3-s-triazine (melem) at ~390 °C. When the temperature reaches 500 °C, melem will further undergo thermal decomposition, polycondensation and deamination to yield a carbon-nitrogen polymer compound melon with a higher degree of polymerization. These polymer compounds undergo further polycondensation and deamination at a temperature above 520 °C to produce g-C_3N_4 with a high degree of polymerization. This kind of structure can stay stable below 600 °C. Above 600 °C, g-C_3N_4 will start to decompose to generate nitrogen and cyano fragments. When the temperature reaches 750 °C, g-C_3N_4 will completely decompose.

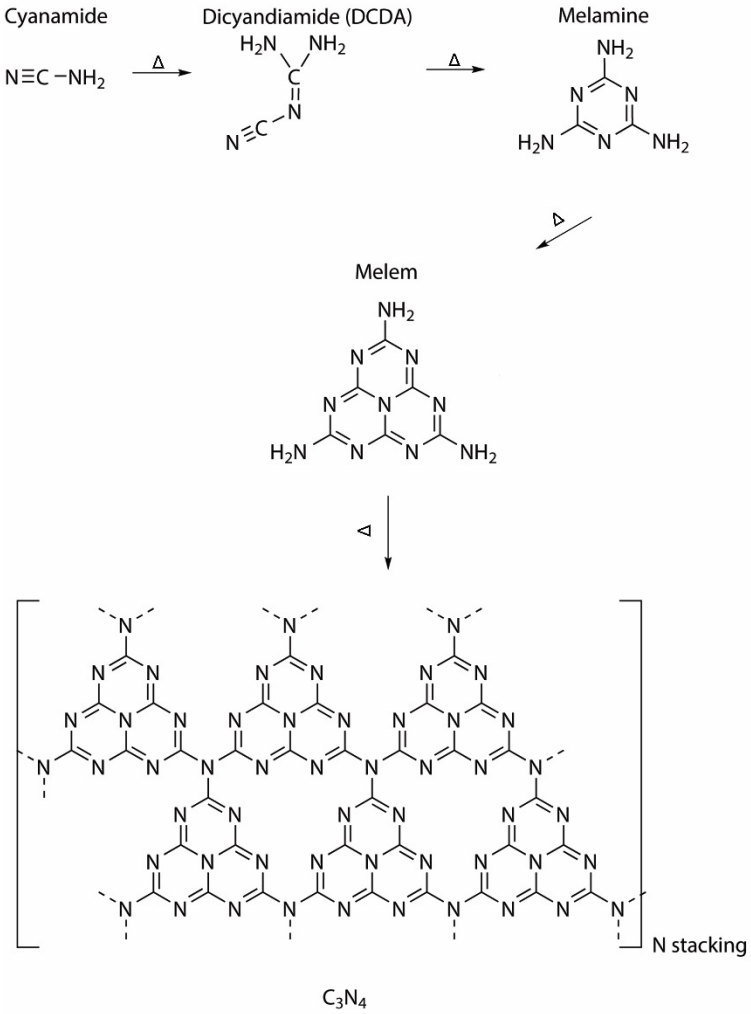

Figure 1.7. Reaction pathway for the formation of g-C_3N_4 starting from cyanamide

Besides cyanamide, dicyandiamide, and melamine as the conventional precursors for the g-C_3N_4 synthesis, urea and thiourea, which are oxygen or sulphur-containing compounds, have also been thermally transformed into g-C_3N_4 [124, 125]. After analysing and summarizing the results, the proposed thermal polycondensation of urea and thiourea are shown in **Figure 1.8**. Urea and thiourea are all polycondensed to g-C_3N_4 through the melamine as the intermediate. Due to more gases eluted during the synthesis, the prepared g-C_3N_4 using urea or thiourea shows larger SSA than melamine (or cyanamide, dicyanamide)-derived g-C_3N_4. However, the SSA of urea or thiourea derived g-C_3N_4 is still lower than 100 m^2 g^{-1}.

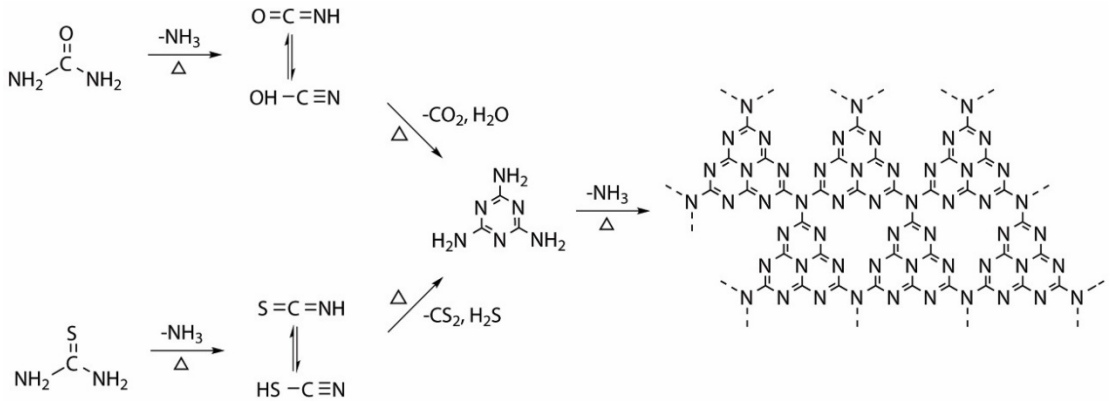

Figure 1.8. The scheme of self-polymerization of urea and thiourea into a g-C_3N_4

Due to different precursors used as C/N sources and slight differences in preparation conditions, generally g-C_3N_4 can be divided into C-rich g-C_3N_4 (C/N: 1-5) and N-rich g-C_3N_4 (C/N: 0.6-1) according to the C/N ratio in the polymer. Using carbon tetrachloride and ethylenediamine as precursors, C-rich g-C_3N_4 was obtained after low-temperature polycondensation at about 90 °C and then high-temperature polycondensation at about 600 °C. It was found that graphitic carbon was obtained in this experiment. The degree of crystallinity was low according to XRD results [126, 127]. If urea, cyanamide, dicyandiamide, melamine, thiocyanic acid or other N-rich precursors pre-polycondensed into a triazine structure at low temperature and further subjected to high-temperature polycondensation above 500 °C, N-rich g-C_3N_4 with higher polymerization degree and crystallization degree was obtained [128-130]. Nowadays, g-C_3N_4 is generally referred to as N-rich g-C_3N_4, which is close to the ideal, fully condensed g-C_3N_4 with C/N ratio of 0.75.

1.3.2.2 Solvothermal synthesis method

In addition to synthesizing g-C_3N_4 by thermal polycondensation, g-C_3N_4 can also be prepared by solvothermal reaction. Moreover, the solvothermal method has the characteristics of good uniformity of products and controllable synthesis condition. And the reaction can be carried out at a relatively low temperature. As the result, the morphology, size and structure of the prepared g-C_3N_4 are controllable.

At first, the solvothermal method was mainly used to explore the synthesis of β-phase super hard C_3N_4. For example, in 1999, Zhu et al. [131] prepared a series of β-phase and α-phase C_3N_4 by using benzene as the solvent, cyanuric chloride ($C_3N_3Cl_3$), and lithium nitride (Li_3N) as raw materials at different reaction temperatures and soaking time. Subsequently, Montigaud et al. [132] prepared g-C_3N_4 using hydrazine (N_2H_4) as solvent and melamine as raw material under high pressure of 3 GPa and high temperature above 850 °C. In 2003, Bai Y.J. et al. [133]

used simple carbon tetrachloride and ammonium chloride as raw materials. The raw materials reacted at 400 °C for 20 hours under solvothermal condition to successfully obtain g-C_3N_4 with good crystallinity at the reduced reaction temperature. Gao et al. [134] further reduced the synthesis temperature by using benzene as the solvent, melamine chloride and sodium amine as the raw materials. It is reported after the solvothermal synthesis at 180-220 °C for 8-12 hours, g-C_3N_4 hollow spheres and hollow tetragonal crystals with high crystallinity were successfully prepared. Later on, Guo et al. [135] replaced sodium amide with sodium azide in the solvothermal synthesis at 220 °C for 15 hours and achieved a better morphology selection to hollow sphere. In 2012, Wang et al. [136] reported the successful synthesis of g-C_3N_4 in uniform nanorod shape by using acetonitrile as the solvent, melamine and cyanuric chloride as the reactants at 180 °C. The SSA and light absorption of g-C_3N_4 nanorods are significantly higher than those of bulk g-C_3N_4. The band gap width of the prepared g-C_3N_4 nanorods was also reduced. Photocatalytic performance experiments also suggested that the performance of g-C_3N_4 nanorods under visible light for photocatalytic hydrogen production and photocatalytic degradation of 4-chlorophenol was higher than that of bulk g-C_3N_4. Gu et al. [137] prepared g-C_3N_4 microspheres by a template-free solvothermal method followed by post-calcination in Ar atmosphere. The prepared porous microspheres exhibited larger SSA, stronger visible light absorption and suppressed electron-hole recombination. The prepared g-C_3N_4 porous microspheres showed 2.3 times apparent quantum efficiency of bulk g-C_3N_4 in photocatalytic H_2 production.

1.3.2.3 Molten salts method

Different from the conventional thermal polymerization method that the thermal condensation process takes places at static air atmosphere, molten salts synthesis method conducts this process in eutectic salts mixture in the liquid phase. Due to the enhanced dispersion of reactants, modification effects of salts, the g-C_3N_4 synthesized via molten salts method shows unique properties. The molten salts have a long history being used as solvents in research and industry. For example, molten salts have been used as reaction media for various organic and inorganic reactions [138, 139] as well as media for crystal growth. Various melted salt systems have also been widely used as high-temperature liquid electrolytes in batteries [140] and electrolytic metals refractory [141, 142]. Since many salts are soluble in water by their nature, molten salts have the advantage of being easily separated from the solid products. In the specific case of g-C_3N_4 synthesis, Bojdy et al. [143] reported the synthesis of crystalline g-C_3N_4 using eutectic LiCl-KCl mixture in 2008. The salts mixture was identified as a good medium for dicyandiamide condensation owing to its thermal stability, non-corrosive

properties and its melting point below the polycondensation temperature of tri-s-triazine. Besides providing a unique inert atmosphere for the reaction, Zhao et al. [144] used KCl-LiCl eutectic mixture to prepare bandgap tunable, K-Na co-doped g-C_3N_4 from melamine. The authors also mentioned that molten salt could be used as a soft template to introduce micro-meso pores into the bulk g-C_3N_4. In recent years, researchers also mixed hard-templates (such as silica [145], Al_2O_3 [146]) with various precursors (3,5-diamino-1,2,4-triazole and 3-amino-1,2,4-triazole-5-thiol [147]), and secondary semiconductors [148-150] to synthesize g-C_3N_4 via molten salt method.

In addition to direct synthesis of g-C_3N_4 in melted salts mixture, the eutectic molten salts are also used as the media for post-treatment of preliminary polymerized g-C_3N_4. Zhang et al. [151] synthesized highly crystalline g-C_3N_4 by post-annealing co-condensed urea and oxamide in molten salts. The optimal sample reaches 57% apparent quantum yield for H_2 production at 420 nm. Similarly, Lin et al. [152, 153] reported that the post-treatment in molten salts can increase the crystalline degree of prepared g-C_3N_4. The increased crystalline degree will enhance the photo-induced charge carriers transportation and suppress the recombination. Additionally, Liu et al. [154] took advantage of LiCl-KCl eutectic mixtures to introduce N vacancies into the g-C_3N_4.

1.3.3 g-C_3N_4 based heterojunction photocatalysts

The strategy to build semiconductor heterostructures is an effective way to increase the photocatalytic performance. The mechanism underpins this strategy includes the broadening light absorption range, suppressing the recombination of electrons and holes etc. In this section, the recent progresses on g-C_3N_4 based heterostructure design are summarized and reviewed.

1.3.3.1 The heterostructure between g-C_3N_4 and semiconductors

As briefly introduced in section 1.2.4.4, the heterostructure between two semiconductors can be generally classified into 3 types. Since only the type II heterostructure benefits to the photocatalytic performance, most of the researches working on the heterostructure between g-C_3N_4 and another semiconductor on pollutant photodegradation are based on this type II design. Dong et al. [155] reported the in-situ synthesis of type II g-C_3N_4/g-C_3N_4 heterostructure and its photocatalytic NO degradation performance. By co-calcination of urea and dicyandiamide, the type II heterostructure was achieved. Since the dicyandiamide-derived g-C_3N_4 possessed the more negative CBE and VBE than the urea-derived g-C_3N_4, the CBE and VBE between these two g-C_3N_4 showed the discrepancies of 0.04 and 0.36 eV respectively. TiO_2/g-C_3N_4 is

another well-documented type II heterostructure with photo-induced electrons flowing from g-C_3N_4 to TiO_2 and photo-induced holes flowing inversely [155-158]. Recently, Wang et al. [159] investigated the g-C_3N_4/TiO_2 interface with both experimental and theoretical methods. It was found that the charge separation efficiency was g-C_3N_4 layer thickness dependent. The optimal heterostructure showed the 7.2 times phenol photodegradation performance of the bulk g-C_3N_4. ZnO/g-C_3N_4 is another typical type II heterostructure design [160-164] for pollutants photodegradation. Wang et al. [165] further expanded the understanding of the electronic structure between ZnO and g-C_3N_4. It was found by the authors that a direct Z-scheme heterostructure could be formed when ZnO possessed abundant oxygen vacancies.

The p-n junction is a special kind of heterostructure showing outstanding photocatalytic activity due to the built-in electric field that further promotes the photo-induced electron/hole separation. The g-C_3N_4 synthesized via the conventional thermal polymerization method is an intrinsic n-type semiconductor due to the intrinsic defects [166]. Therefore, other p-type semiconductors such like Cu_2O [167], NiO [168], CoO [169], Co_3O_4 [170], Ag_2O [171], BiOI [172] etc. have been used to build the p-n heterostructure with g-C_3N_4. For example, Guo et al. [169] reported the p-n heterojunction of CoO/g-C_3N_4 synthesized by solvothermal method. The optimal CoO/g-C_3N_4 with 30%wt CoO showed ~5 times enhanced tetracycline photodegradation performance comparing with the pristine g-C_3N_4. As a typical p-type semiconductor, $NiCo_2O_4$ has been used to build the p-n junction with g-C_3N_4 by Chang et al. [173]. The enhanced RhB photodegradation performance had been achieved and the photo-induced hole had been proven as the active radical. The p-n junction between Ag_2O and g-C_3N_4 was reported by Fan et al. [174] for the photocatalytic algae removal. The key to achieving successful heterostructure construction was the negatively charged surface of g-C_3N_4. The algae growth was reported to be efficiently prohibited and the photocatalytic process could significantly cause the death to the algae cells. Liang et al. [171] constructed the p-n junction between Ag_2O and g-C_3N_4. Ascribed to the broad-band light absorption of Ag_2O, the Ag_2O/g-C_3N_4 exhibited the 26 and 343 times RhB photodegradation performance of pristine g-C_3N_4 under visible and NIR light irradiation, respectively. Doping [175-177] can change the conductivity type of the C_3N_4 semiconductor. Therefore, it provides more versatility in p-n junction construction. The heteroatom dopants such as B [178], P [179], K [180] and Fe [180] etc. have been reported to change g-C_3N_4 to p-type conductivity. In addition, it has been reported that the vacancy introduction [181, 182] can change the conductivity type of the g-C_3N_4 too. Therefore, the p-n heterostructure can be built within the stoichiometric and defected parts of the g-C_3N_4 photocatalysts. For instance, Cao et al. [182] introduced N-vacancies into g-C_3N_4 and claimed a p-type conductivity was achieved. The proposed reason

was the trapping of electrons at the defect site, which increased the local concentration of holes. The p-n junction was claimed to be constructed between N-deficient g-C_3N_4 and pristine g-C_3N_4. And the RhB photodegradation performance was enhanced. Liu et al. [183] suggested the p-type conductivity could be achieved by replacing the -NH/-NH_2 terminal with cyano terminal (−C≡N) in the molecules of g-C_3N_4. The theoretical basis was that the -NH/-NH_2 (amino) group was the electron donner while −C≡N (cyano) group was the electron accepter. The Mott-Schottky plot suggested the co-existence of p-type and n-type conductivity behaviours in the prepared catalysts.

Z-scheme is another kind of heterostructure can successfully improve the photocatalytic performance [179, 184]. The key feature of the Z-scheme is the direct recombination of low-energy photo-induced electrons and holes from two sides of the heterostructure interface and the high-energy photo-induced electrons and holes are efficiently separated. Katsumata et al. [185] reported the construction of Z-scheme heterostructure between g-C_3N_4 and Ag_3PO_4 and an improved visible-light-driven MO degradation performance was achieved. The Z-scheme electronic structure relied on the Ag nanoparticle formed between the g-C_3N_4/Ag_3PO_4 as the charge bridge. Wu et al. [186] synthesized the $LaFeO_3$/g-C_3N_4 heterojunction and the composite exhibited the Z-scheme electronic structure. The unique electronic structure was ascribed to the enhanced brilliant blue dye degradation performance with h^+, •OH and $\bullet O_2^-$ identified as the reaction radicals.

1.3.3.2 The heterostructure between g-C_3N_4 and other co-catalysts

Heterostructure built between g-C_3N_4 and cocatalysts can effectively improve its photocatalytic performance. Besides the promoted photo-induced electron/hole separation between the interface, the cocatalysts themselves possess unique property catalysing targeted reactions. In the specific g-C_3N_4 photocatalysts, metallic nanoparticles such as Pt, Pb, Au, Ag and Rh are the most common co-catalysts for heterostructure construction [187, 188]. For example, Shiraishi et al. [189] loaded Pt nanoparticles onto g-C_3N_4 by high-temperature reduction of Pt-precursors. The authors focused on strengthening the interaction between g-C_3N_4 and Pt nanoparticles. With the Pt nanoparticles in close contact with the g-C_3N_4 surface, the photo-excited electrons could easily migrate to the Pt nanoparticles. Therefore, Pt/g-C_3N_4 exhibited excellent photocatalytic hydrogen production activity. For comparison, the Pt/g-C_3N_4 composites prepared at low temperature had loose interfacial contact and thus exhibited lower photocatalytic activity. The effects of Pt nanoparticles sizes and morphologies have different effects on the photocatalytic performance of g-C_3N_4/Pt too. Cao et al. [190] conducted a detailed study on this issue through a colloidal adsorption-deposition method to

synthesize Pt particles with different morphologies supported on g-C_3N_4 surface. These Pt nanoparticles supported on the g-C_3N_4 surface had similar sizes, but their photocatalytic performances increased in the following order: cubic Pt/g-C_3N_4, octahedral Pt/g-C_3N_4, and spherical Pt/g-C_3N_4. The results indicated that different exposed surfaces of Pt nanoparticles had different surface atomic structures, resulting in different active sites and different adsorption energies for intermediates in the photocatalytic reaction, and thus exhibited different photocatalytic performance. In addition to Pt, other noble metals including Pd [191, 192], Ru [193] etc. have also been loaded onto g-C_3N_4 too.

However, considering the high cost and scarcity of precious metals, it is of great importance to find non-precious metals of low cost and high abundance for preparing the photocatalysts,. The non-precious metals such as Ni, Mn, and Co have been used to modify g-C_3N_4 photocatalytic materials and improve their photocatalytic performance [29, 194, 195]. For example, Bi et al. [195] used melamine and nickel acetylacetonate as precursors to synthesize a series of Ni@g-C_3N_4 composites using a simple solvothermal method. Compared with pristine g-C_3N_4, Ni supported on the surface of g-C_3N_4 greatly improved its photocatalytic hydrogen production efficiency. When the Ni loading was ~ 10%wt, the corresponding photocatalytic hydrogen production rate reached a maximum of 8.41 μmol h^{-1}. Due to the different work functions between g-C_3N_4 and Ni, when they were in contact with each other, a deeper band bend was formed, which led to the efficient separation of photo-generated carriers. Recently, Kong et al. [196] proposed a facile photo-assisted method for the preparation of stable Ni/g-C_3N_4 magnetic composite photocatalysts. The uniformly dispersed metallic Ni nanoparticles with a diameter of 30-80 nm was deposited on the g-C_3N_4 surface. Under full-spectrum light irradiation, the optimized g-C_3N_4 system containing 7.4%wt Ni showed a very high photocatalytic hydrogen production rate of 4318 μmol g^{-1} h^{-1}. The apparent quantum efficiency at 400 nm was 2.01%.

Besides metallic nanoparticles, the non-metal co-catalysts have also been loaded onto the g-C_3N_4 to build up the heterostructure. For example, Liu et al. [197] built the heterostructure between g-C_3N_4 with C quantum dots. The prepared C quantum dots showed the average diameters of ~ 10 nm. The optimal sample exhibited ~15 times higher diclofenac degradation rate than the pristine g-C_3N_4. Yang et al. [198] synthesized the BN quantum dots and ultrathin g-C_3N_4 heterostructure. It was claimed by the authors that the BN quantum dots attracted the photo-induced holes under excitation state. An enhanced O_2^- radical production ability was ascribed to the facilitated photodegradation of oxytetracycline hydrochloride.

In summary, apart from the different elements used and different reaction targeted, the mechanism underpinning the photocatalytic activity enhancement is the same. The co-catalysts act as the photo-induced electrons or hole sinks depending on the relative fermi energy levels. The schottky barrier formed between the metallic co-catalyst and g-C_3N_4 semiconductor can hinder the back-flow of the photo-induced charge carriers. Therefore, the facilitated separation of photo-induced charge carriers is achieved.

1.3.4 Electronic structure modification of g-C_3N_4

1.3.4.1 Metal and non-metal doping

Metal or non-metal elemental doping is one of the most effective strategies for material modification. By doping a small amount of non-metal or metal impurity into the C_3N_4 crystal lattice, the electronic structure and corresponding physiochemical properties of the C_3N_4 photocatalyst can be changed accordingly. The main advantages of doping to g-C_3N_4 include following aspects: (i) reducing the bandgap and enhancing the light absorption; (ii) trapping the charge carriers and retarding the electron/hole recombination; (iii) tuning the positions of CBM and VBM to improve the photo-reducing and oxidising capability.

For g-C_3N_4 photocatalysts, non-metal elemental doping such as O [199-202], C [119, 203, 204], N [205], S [206-208], P [209-211], Br [212] etc. have been extensively reported. Huang et al. [199] reported O-doped C_3N_4, which was synthesized by thermal calcination of H_2O_2 treated melamine at 550 °C under N_2 flow. The H_2O_2 treatment could produce hydrogen bond-induced supramolecular aggregates, which further converted to O-doped g-C_3N_4 after calcination. Based on their work, the bandgap of the O-doped g-C_3N_4 became smaller and an internal electric field was created due to the drastically decreased electron density at the adjacent parts of O dopants and significantly increased electron density near the N atoms. As a result, the visible light response range was extended and the internal electric field promoted the electron-hole separation. Dong et al. [119] developed a mild method for synthesizing C self-doped C_3N_4, with C substituting the bridging N atoms. After replacing the N with C, the intrinsic electronic structure and band structure of C_3N_4 was changed. According to the theoretical calculation results, C substitution resulted in the formation of a delocalized π-bond between the doped C atom and the aromatic ring, thereby increasing the conductivity of g-C_3N_4 and facilitating the electron transfer. The self-doping of carbon reduced the band gap from 2.72 eV to 2.65 eV, which ensured the more visible light harvest. Zhou et al. [205] reported the synthesis of N-doped C_3N_4 through a simple one-pot thermal polymerization route.

During the thermal calcination process of urea and citric acid mixture, urea created an amine-rich environment that could react with the carbon source, citric acid, to finally achieve the N-doped C_3N_4. Liu et al. [206] pointed out that the doping of S could raise the position of CBE due to the electron-rich property of S. Under the light of $\lambda > 320$ nm and 420 nm, $C_3N_{4-x}S_x$ showed the 7.2 times and 8.0 times hydrogen evolution rates of the undoped g-C_3N_4, respectively. More importantly, the S-doped C_3N_4 could completely oxidize phenol under $\lambda >$ 420 nm light, while the un-doped C_3N_4 could not achieve even under the irradiation of $\lambda > 320$ nm light. Hu et al. [210] prepared P-doped g-C_3N_4 by utilizing dicyandiamide and $(NH_4)_2HPO_4$ as the P source. P atoms were interstitially doped into the g-C_3N_4 lattice with the generation of the P–N bonds, which acted as the bridge between C_3N_4 layers. As a result, the band gap of g-C_3N_4 was reduced and the charge separation efficiency of C_3N_4 was improved. Besides doping at interstitial site, Zhou et al. [209] used the thermal polymerization of the mixture of tripolyphosphazene chloride and guanidine hydrochloride to synthesize the g-C_3N_4 with substitutional P dopants. The P dopants were found to favourably replace the corner carbon and bay-carbon sites. The obtained P-doped C_3N_4 exhibited outstanding photocatalytic performance on both photocatalytic H_2 production and rhodamine B decomposition. This was mainly because the doping of P increased the electron density in C_3N_4 and the dopants could suppress the recombination of photo-excited carriers. Halogen atoms are also common dopants for g-C_3N_4. For instance, Wang et al. [212] compared Br-doped g-C_3N_4 derived from several different nitrogen-rich materials and ammonia bromine (NH_4Br) as the Br sources via one-pot thermal co-condensation method. Photocatalytic H_2 evolution rate of Br-doped C_3N_4 under visible light irradiation and the photocatalysts stability were greatly enhanced.

In addition to non-metal doping, transition metal dopants have also been proven successfully improving the g-C_3N_4 activity. The g-C_3N_4 constituted by heptazine units possesses repeated in-plane interstitial sites, which are filled with six N lone electron pairs. Those are generally regarded as ideal sites for the inclusion of transition metal cations through an ion coordination. The introduction of metal cations into the g-C_3N_4 lattice can accelerate charge migration and reduce the energy band gap. Therefore, the light absorption capacity and electron/hole separation are enhanced. Moreover, the transition metals are featured of empty states in d-orbitals, which provides the high catalytic activity for target photocatalytic reaction. For example, Wang et al. [213] reported that a simple soft chemical synthesis method could be used to introduce iron cations (Fe^{3+}) at the "nitrogen pore" position in the g-C_3N_4 crystal without destroying the graphitic crystal structure. Fe-doped C_3N_4 was found to be able to photo-activate hydrogen peroxide in a mild reaction condition for the direct oxidation of benzene to phenol. The introduction of iron ions regulated the electronic structure of C_3N_4 and

reduced the band gap, but still maintained a sufficient potential for driving oxidation reactions. With increasing metal contents, the light absorption range expanded and moved towards long wavelengths with lower photon energies. Gao et al. [214] prepared a novel Fe-doped C_3N_4 polymer using a mild one-pot method with formamide and citric acid as the precursors. It exhibited an efficient hydrogen production rate (~16.2 mmol g^{-1} h^{-1}) under visible light with a quantum efficiency of 0.8%. The doped Fe cations enhanced the coupling between the metal and carbon nitride electrons, and the unique electronic structure formed was conducive to the migration of electrons in the 2D plane, which was very effective to promote the electron transport and leads to the improvement of photocatalytic hydrogen production efficiency. Yue et al. [215] developed a simple soft chemical method to prepare a Zn-doped C_3N_4. Under visible light (λ > 420 nm) irradiation, the Zn-doped C_3N_4 hybrid system showed high photocatalytic activity and stability in hydrogen production with methanol as the hole scavenger. Its hydrogen production rate (59.5 μmol $h^{-1}g^{-1}$) was ~10 times that of pristine g-C_3N_4, and the maximum quantum yield at 420 nm was 3.2%. The enhancement of photocatalytic hydrogen production performance of the Zn-doped C_3N_4 was mainly due to the increased light absorption caused by the doping of Zn ions, which led to the generation of more photo-excited electrons and holes. The doping of Zn ions also facilitated the separation of these photo-excited electron-hole pairs, allowing more electrons to be used for the photocatalytic H_2O splitting. Furthermore, similar observations and phenomena were found in other transition metals such as Ni and Mn doping, as reported by Ding et al. [216]. In summary, the transition metal dopants intend to be positioned at the interstitial sites of the g-C_3N_4 due to the relatively large atomic diameters. The enhanced photocatalytic efficiency of transition metal doped C_3N_4 has been reported in the literature [214, 215, 217-219].

In addition to transition metal dopants, alkali metal ions are another kind of effective dopants [144, 220-222]. For instance, Xiong et al. [223] synthesized a K and Na doped C_3N_4 system and found that the K-doped g-C_3N_4 system showed a unique electronic structure and excellent performance in visible-light-driven catalytic elimination of nitric oxide. The performance was superior to Na-doped C_3N_4 system. This was mainly because K ions were situated in-between the layers of the C_3N_4 system, forming a bridge between the adjacent layers of the g-C_3N_4 system. The introduced tunnels for electron/hole transfer could reduce the recombination of photogenerated carriers and an enhancement in photocatalytic performance. However, Na was mainly doped in-plane, which could only facilitate the in-plane charge transfer and contributed less to the recombination suppression.

In addition to doping g-C_3N_4 with single kind of dopants, co-doping g-C_3N_4 with metal ions and non-metal ions are emerging as a more sophisticated and effective way to improve the performance of g-C_3N_4. For example, by using dicyandiamide monomer, diammonium hydrogen phosphate, and ferric nitrate as precursors, Fe/P co-doped g-C_3N_4 system was successfully prepared [224]. P dopants substituted the N atoms at the corner sites and the Fe dopants were coordinated to the N atoms at the interstitial position in the nitrogen pots of g-C_3N_4. The results indicated that the doped ions inhibited the continuous growth of the g-C_3N_4 crystals, which increased the specific surface area of C_3N_4. Locating at different sites, the N, Fe collaborated to reduce the optical band gap and suppress the recombination of photo-excited electrons and holes. Therefore, comparing with the singly doped and undoped g-C_3N_4, the Fe/P co-doped g-C_3N_4 has been demonstrated showing higher photocatalytic efficiency on both photodecomposition of RhB and water splitting. Zhang et al. [225] prepared the co-doped g-C_3N_4 system with Fe/C by a simple thermal co-condensation method. The experimental results indicated that under visible light ($\lambda > 420$ nm) irradiation, the Fe/C co-doped g-C_3N_4 decomposed RhB more efficiently than the undoped g-C_3N_4 by ~14 times. The synergistic effect of Fe and C dopants narrowed the band gap of co-doped C_3N_4 system and shifted the VB downwards, which led to the expansion of the light absorption range and promotes the photo-oxidation capability. Guo et al. [226] prepared the g-C_3N_4 co-doped with K and I through the co-polycondensation of dicyandiamide and KI. Compared with undoped g-C_3N_4, the K-I-co-doped g-C_3N_4 showed a noticeable redshift in the light absorption edge and the enhancement of visible light absorption. The decrease in photogenerated carrier recombination rate derived from the improvement of charge transport efficiency was mainly attributed to the K dopants.

Although there are a lot of successful demonstrations of doping strategy in improving the photocatalytic activity of g-C_3N_4, the intrinsic shortcomings of doping strategies need to be taken into consideration. After the introduction of dopants to g-C_3N_4, its band gap can be reduced to a certain degree with the compromising in photo-reducing or phot-oxidising capabilities. Moreover, excessive dopants can easily act as the recombination centres and facilitate the phot-induced electron/hole recombination.

1.3.4.2 C/N vacancies

Besides atom doping, the vacancies engineering is another effective method to improve the photocatalytic activity of g-C_3N_4. Niu et al. [227] reported the g-C_3N_4 with N vacancies synthesized by increasing the thermal polycondensation temperature to 600 °C. The lost N atoms left additional electrons redistributed to their nearest C atoms, which were reduced from

C^{4+} to C^{3+}. Presence of C^{3+} were responsible for the enhanced light absorption of the nitrogen-deficient g-C_3N_4 with the band gap narrowed from 2.74 to 2.66 eV. The same group also reported the improved method for introducing N vacancies into g-C_3N_4 [228]. After polycondensation of dicyandiamide at 550 ºC, the as-prepared g-C_3N_4 was further annealed in flowing H_2 atmosphere to create the N vacancies. Due to the layered structure of g-C_3N_4, the H_2 could diffuse into the bulk of g-C_3N_4 and the N vacancies were homogeneously created inside the g-C_3N_4 crystal. Impressively, the retarded electron/hole recombination was achieved by N vacancies introduction as claimed by the authors. Similarly, Tay et al. [229] reported a slightly different method to introduce N vacancies into g-C_3N_4. By conducting the thermal polycondensation of dicyandiamide directly under H_2 atmosphere at 550 ºC, the N vacancies introduction, as well as H doping, could be facilely achieved. It was reported that this N-deficient g-C_3N_4 showed the reduced bandgap from 2.7 eV to 2.0 eV and the photocatalytic H_2 production rate increased by 4.8 times comparing with the pristine g-C_3N_4. Besides the high-temperature N vacancies creation method, Li et al. [230] developed a method being able to introduce N vacancies to g-C_3N_4 at the mild condition. The N deficient g-C_3N_4 was prepared at room temperature inside a plasma reactor under H_2 atmosphere. In addition to the researches on developing N vacancies creation methods, the investigations on the role of N vacancies in the catalytic reaction are more important. The specific role of N vacancies on NO_x photocatalytic removal has been investigated by Wang et al. [231]. The controllable amounts of N vacancies were introduced by post-calcinating solvothermally prepared g-C_3N_4 microtubes. The 2.6 times enhanced NO removal rate of N-deficient g-C_3N_4 microtubes was attributed to the new active sites and enhanced electron/hole separation attributed to the N vacancies. In addition to the cases reporting the positive effects of N vacancies, Lan et al. [232] investigated the effects of the N vacancies on the simultaneous photocatalytic H_2 production and aqueous pollutants degradation and the negative effects of N vacancies were presented. The authors claimed that the photocatalytic activity of g-C_3N_4 with N vacancies was inferior to the g-C_3N_4 with less defects, though the bandgap of the N-deficient g-C_3N_4 was narrower.

Although less investigated than N vacancies, the C vacancies engineering is also an important method to improve the photocatalytic activity. Li et al. [181] successfully prepared C vacancies on the surface of g-C_3N_4 by calcinating g-C_3N_4 in Ar gas atmosphere. The photocatalytic activity of H_2O_2 production of C-deficient g-C_3N_4 was significantly improved. It was because the g-C_3N_4 with C vacancies could produce more photo-induced electrons/hole with the reduced band gap width. Similarly, the C vacancies were created by calcinating g-C_3N_4 in CO_2 atmosphere [233]. Dong et al. [234] reported the synthesis of C-deficient g-C_3N_4 via co-polycondensation of cyanuric acid and melamine mixture. The improvement of

photocatalytic NO removal on C-deficient g-C_3N_4 was demonstrated. The authors ascribed the enhanced activity to the C vacancies-induced bandgap narrowing, recombination retarding and enhanced NO adsorption at the defect sites.

In summary, the mechanism of the C vacancies enhancing the photocatalytic activity of g-C_3N_4 is similar is similar to that of N: narrowing bandgap, retarding electron/hole recombination and creating active sites. At the same time, it is important to emphasize the difference between the C and N vacancies. Since the N and C contribute the most of the VB and CB of the g-C_3N_4, respectively, the created N and C defect states locate at different positions inside the bandgap [235]. More importantly, the N defect energy level shows the N sites dependence [236]. The tailing of the CBM and VBM will have different effects on the reducing and oxidizing potentials of the vacancies-engineered g-C_3N_4. Therefore, these differences are needed to be considered when conducting vacancy engineering to g-C_3N_4 for interested reactions.

1.3.5 Morphology modification of g-C_3N_4

g-C_3N_4 prepared via conventional thermal polycondensation method usually possesses very limited SSA and no dominated morphology. Therefore, synthesis with controllable morphology and enlarged SSA becomes an attractive aspect to improve the photocatalytic activity of g-C_3N_4. Two strategies can be applied to increase the SSA of g-C_3N_4: reducing the dimension of g-C_3N_4 to increase the outer surface area; creating 3-D porous structure to increase the inner surface area. At present, the methods for modifying the morphology of g-C_3N_4 can be classified to following two types: approaches with templates; approaches without templates.

1.3.5.1 Hard-template and soft-template approaches

The hard-template approach is almost identical to the conventional casting process. This approach can be considered as a flexible technique for the development of g-C_3N_4 materials with varying morphology or hierarchical porous architectures. In 2005, Groenewolt et al. [237] loaded cyanamide on a mesoporous silicon material for thermal polycondensation, and then removed the mesoporous silicon material template with a 5% HF solution to obtain the porous g-C_3N_4. Its SSA increased significantly to 100.0 m^2/g. Vinu et al. also used silica as the template and cyanamide as the precursor to synthesize the mesoporous g-C_3N_4. After high temperature thermal polycondensation and removal of the silica template, g-C_3N_4 with uniform mesopores in ~12 nm were obtained and the SSA reached 505.0 $m^2\ g^{-1}$ [238, 239].

In addition to 3D porous structure design, the morphology engineering has also drawn a lot of interests from researchers. For instance, Wang's group [240] successfully synthesized hollow g-C_3N_4 nanospheres using silica nanoparticles as the template (**Figure 1.9**). By carefully controlling the thickness of the polymer hollow spherical shell, deformation of the soft hollow structure could be effectively prevented even at 400 °C. These monodispersed hollow g-C_3N_4 nanospheres showed prominent photocatalytic hydrogen production performance. The unique hollow nanosphere morphology could cause internal light reflection and increase the light utilisation. The apparent quantum yield of hydrogen evolution reached 7.5%.

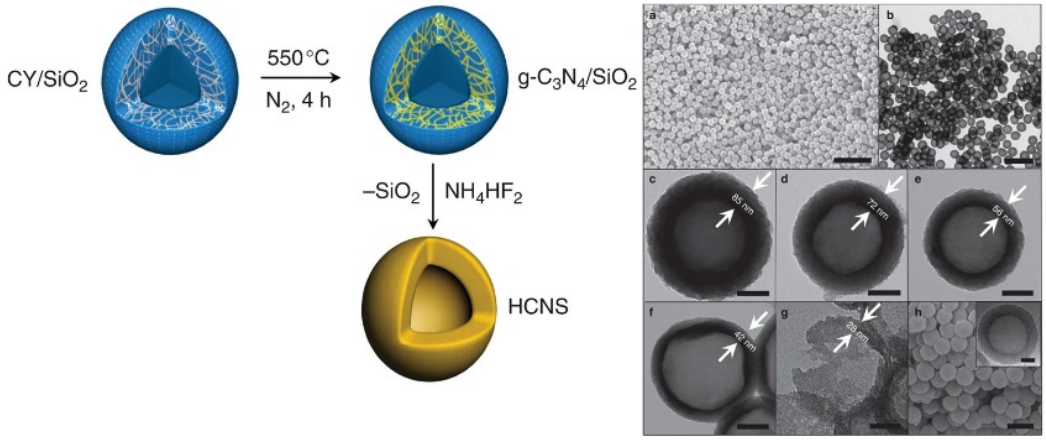

Figure 1.9. Steps to synthesize hollow graphite phase carbon nitride nanospheres. CY stands for cyanamide. (a-h) TEM image of hollow graphite phase carbon nitride nanospheres. Reproduced from ref. [240] with permission.

The one-dimensional photocatalysts (nanorods, nanotubes, nanowires, nanoribbons, and nanoribbons) possess unique properties such as enlarged SSA and enhanced axial charge carrier transport. And the properties can be optimized by tuning the diameter, length, and aspect ratio of one-dimensional materials [241-243]. Li et al. [244] used SBA-15 nanorods as a hard template to synthesize mesoporous g-C_3N_4 nanorods with an open channel. The prepared g-C_3N_4 nanorods had a large SSA of 110-200 m^2 g^{-1}, a length of ca. 650 nm and a diameter of ca. 100 nm. This structure can play a robust role as the substrate for ultrafine metal nanoparticles (Au, Pt and Pd NPs), which can be further used in various photocatalytic redox reactions. The g-C_3N_4 nanorods enhance light absorption and charge transportation along the axial dimension. In addition, the short transport path of the photoinduced carriers at the radial dimension can enhance the electron/hole separation. Moreover, the electronic structure is affected by the 1D morphology too. The HOMO position of the obtained g-C_3N_4 nanorods is shifted to the positive direction, which provides a stronger oxidizing ability to drive the oxygen evolution reaction. Other silica templates such as SBA-15, SBA-16 [245, 246] and KCC-1[247, 248] have also been used to develop g-C_3N_4 in highly ordered morphology. Traditional hard

template materials need to be removed by fluorine-containing etchants such as HF and NH_4HF_2, which is highly toxic and inevitably introduces F ions into the g-C_3N_4 crystal. Therefore, it is attractive to use an alternative template more friendly to the environment. Wang et al. [249] used calcium carbonate instead, which was proven as a safer and environmentally friendly way to synthesize porous g-C_3N_4. $CaCO_3$ as a template can be easily removed by diluted HCl and costs significantly less than zeolite templates. After direct co-condensation of the nitrogen-rich precursor dicyandiamide and $CaCO_3$ particles at 550 ° C, the prepared porous g-C_3N_4 exhibited not only enlarged surface areas, but also enhanced photocurrents of up to ∼4.2 and 7.5 times that of the bulk counterpart.

The soft template approach is to use the soft polymers, surfactants and ionic liquids etc. as the template during the g-C_3N_4 synthesis. Due to the low thermal stability of the soft template, the polycondensation process in g-C_3N_4 needs to be conducted at a relatively low temperature. For example, bulk polymers P123 and Triton X-100 have been used as soft templates to obtain mesoporous g-C_3N_4 nanoparticles. Compared with conventional bulk g-C_3N_4, the SSA of mesoporous g-C_3N_4 nanoparticles prepared under the assistance of the soft templates was significantly increased to 299 $m^2 g^{-1}$ comparing to 8 $m^2 g^{-1}$ in bulk g-C_3N_4 and its maximum absorption wavelength exhibited a "redshift". Its visible light photocatalytic performance on hydrogen production was also significantly improved, the H_2 evolution rate of the porous g-C_3N_4 increased to 148.2 μmol h^{-1} [250, 251].

Synthesis of g-C_3N_4 with controllable morphology and mesoporous structure is an effective technique to promote the photocatalytic performance through the efficient charge transport and enhanced mass transfer during the photocatalytic reaction. In general, g-C_3N_4 nanostructure modifications based on the hard template and soft template will continue to grow rapidly. However, finding a low-cost, environmentally friendly and effective template is still an unresolved challenge.

1.3.5.2 Template free approaches

In addition to the synthesis of g-C_3N_4 with large SSA under the assistance of templates, it is more desired to develop the methods without using templates due to the environmental and economic concerns. In recent years, some non-template methods have also been used to enlarge the SSA of g-C_3N_4, such as post-heat treatment, chemical stripping, acid etching and hydrothermal treatment.

Wang et al. [252] prepared C_3N_4 quantum dots through the thermal–chemical etching in the hydrothermal treatment. The acid etching by concentrated HNO_3 and H_2SO_4 resulted in the direct cleavage of bulk g-C_3N_4 to nanosheets, nanoribbons and 0D quantum dots. The g-C_3N_4 quantum dots structure showed unique up-conversion characteristics, and the hydrogen production efficiency of g-C_3N_4 quantum dots was 2.87 times of bulk g-C_3N_4. Tahir et al. [253] developed a green and facile method without templates to successfully prepare g-C_3N_4 nanofibers, which had a large SSA of ~165 m^2 g^{-1}. The rate of degradation of rhodamine B by the synthesized 1D g-C_3N_4 nanofibers was 4 times of g-C_3N_4 bulk structure. Its enhanced photocatalytic activity was mainly due to the higher SSA, reduced band gap, and fewer defects. They also synthesized graphitic-C_3N_4 microtubes [254] and micro-strings [255] using HNO_3-pretreated melamine as feedstock and annealed at 550 ºC and 400 ºC, respectively. All the 1D nanostructure g-C_3N_4 exhibited good photocatalytic activity and enhanced stability compared to bulk g-C_3N_4. Gong et al. [256] prepared g-C_3N_4 nanotubes by calcining melamine in a designed programme. The nanotube morphology was formed due to using the *in-situ* formed NH_3 gases as the template. Under the irradiation of visible light ($\lambda \geq 420$ nm), the prepared g-C_3N_4 nanotube structure could degrade MB at the rate of 0.43 times and 1.56 times of bulk g-C_3N_4 and P25-TiO_2, respectively. The bulk g-C_3N_4 is a van der Waals crystal with 2D layers interacting with each other via van der Waals force. Therefore, it is natural to try to exfoliate the layers from the bulk to synthesize the 2D g-C_3N_4 nanosheets. The 2D g-C_3N_4 nanosheets with atomic-thickness have a larger SSA and higher carrier mobility due to the quantum confinement effects in the thickness direction. Therefore, g-C_3N_4 nanosheets have become a research hotspot in the photocatalysis research field. For example, Zhu et al. [257] successfully prepared the g-C_3N_4 nanosheets with single atomic layer thickness using a simple chemical stripping method. The thickness of the prepared nanosheets was only ~0.4 nm, which was the thickness of the monoatomic layer. Compared with g-C_3N_4 with bulk structure, g-C_3N_4 nanosheets with monoatomic layer thickness have excellent transport rate and separation of photo-generated carriers. Therefore, the g-C_3N_4 nanosheets with single-atomic thickness exhibited higher efficiency than the bulk g-C_3N_4 in photocatalytic water splitting and photodegradation of pollutants. Liang et al. [258] successfully prepared single-layered g-C_3N_4 nanosheets with a thickness of only 0.38 nm by a typical liquid phase exfoliation method. Compared with bulk g-C_3N_4, the prepared single-layered g-C_3N_4 nanosheets showed excellent photocatalytic activity in selective oxidation of benzyl alcohol and photodegradation of RhB under visible light irradiation. The improvement in photocatalytic performance was attributed to the high SSA, low surface defects, and more active sites in single-layer g-C_3N_4 nanosheets.

In summary, by changing the morphology of g-C_3N_4, the SSA of nanostructured g-C_3N_4 is greatly improved compared to the bulk g-C_3N_4. It results in the increase of photocatalytic active sites and the suppression of photo-excited carrier recombination rate. Therefore, the photocatalytic activity of g-C_3N_4 is effectively enhanced.

1.3.6 Dye photodegradation reaction pathway

Photocatalytic degradation and environmental remediation of pollutants have become one of the most promising strategies to address the challenges of pollution. Among all the photocatalyst candidates, g-C_3N_4 as a kind of visible-light photocatalyst has attracted continuous research interests due to its unique advantages. Generally, the photocatalytic pollutant degradations on g-C_3N_4 reported in the literature can be divided into two categories: degradation of gaseous pollutants (e.g. NO_x [259]) and removal of pollutants in aqueous solution. In this section, the two most widely employed pollutants in aqueous solution, MO and RhB are used as examples. Since the general photodegradation mechanism has already been reviewed in section 1.2.2, this section focuses on the investigations on the detailed photocatalytic degradation reaction pathway.

Figure 1.10 depicts a schematic diagram of the photocatalytic degradation of pollutants on g-C_3N_4. Under light irradiation, highly reactive electrons and holes initiate the oxidation and reduction reactions on the surface of g-C_3N_4. The photoinduced electron reacts with the adsorbed molecular O_2 to generate $\bullet O_2^-$ superoxide anion radical, which helps to further generate •OH and •OOH radicals. It is believed that the reaction between •OH radicals and organic pollutants will eventually lead to the mineralization of these compounds [260]. At the same time, in aqueous systems, photogenerated holes react with the surface OH^- groups to form •OH radicals.

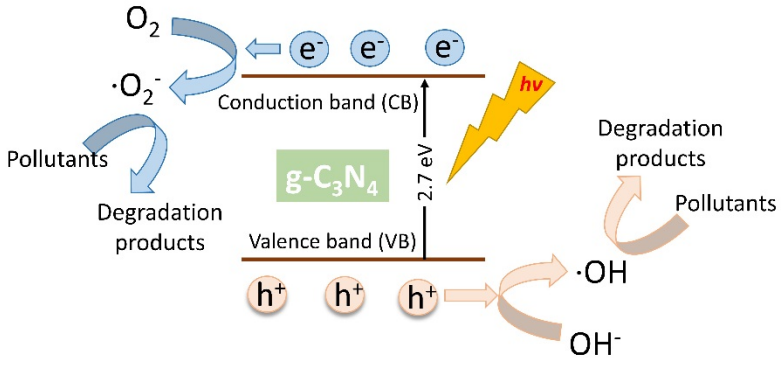

Figure 1.10. Schematic illustration of photocatalytic degradation of pollutants under light irradiation using g-C_3N_4 as photocatalyst.

MO dissolved in water shows two absorption peaks in the ultraviolet-visible spectrum [62]. The first peak is at ~270 nm and the stronger second one is at ~465 nm. The evolution of absorption peak at 465 nm can be used to monitor the concentration changes of MO based on the Beer's law. As an azo dye, MO's oxidative degradation usually initialises with the attack of hydroxyl radicals. The chromophore structure of an azo dye consists of two aryl rings connected via an azo -N=N- bridge [261]. The main reaction between a •OH radical with an azo compound is the addition of •OH to the N=N double bond of the chromophore, which causes the rapid disappearance of the colour. At the same time, hydroxyl radicals will also be added to the aromatic ring [262, 263].

As shown in **Figure 1.11**, Ökte and Yilmaz [264] proposed that during the degradation process, •OH radicals firstly attacked the azo bond in MO molecules, which generated dimethylaniline benzyl sulfonate and N_2. Hydroxyl radicals attacked the ring with an amino group and formed aniline and 4-hydroxyaniline. Further •OH radicals attacks resulted in the formation of more intermediate products. They believed that during the degradation process, small molecules and inorganic ions were formed gradually. Although the bleaching reaction was very fast, it took longer for the dye to completely mineralize to CO_2, H_2O and inorganic anions.

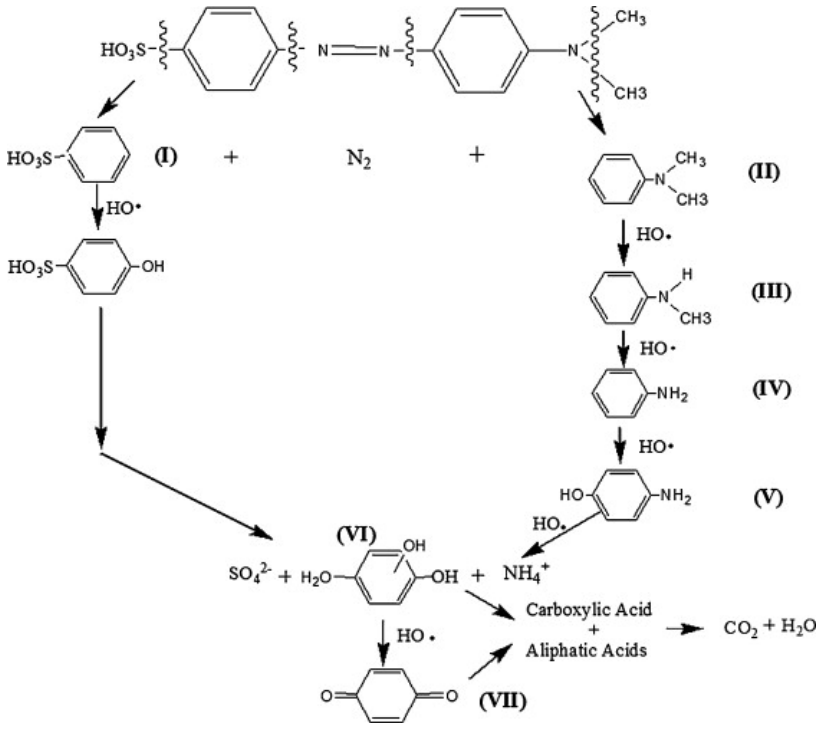

Figure 1.11. Postulated photocatalytic degradation pathway of MO by Ökte and Yilmaz. Reproduced from ref. [264] with permission.

Adding more details to the pathway proposed by Ökte and Yilmaz [264], Xu et al. [265] believed that •OH radicals attacking on azo bonds in MO molecule formed the -HN-NH- first.

Then further •OH radical attacks caused the N-N bond cleavage. This was because the conjugate degree of π–π bonds in the molecules generated during degradation was lower than that of MO. They pointed out that the absorption peak of the hydrogenated MO molecules after the first-step degradation was shorter than that of the original MO molecules. This was reflected by the blue shift of the absorption peak during the photodegradation. In 2018, Zhong et al. [266] observed symmetric cleavage of MO with the formation of N, N-dimethyl-p-phenylenediamine and sulfanilic acid as the main intermediates based on the ultraviolet-visible (UV-Vis) spectroscopy, electrospray ionization mass spectrometry (ESI-MS) and high-performance liquid chromatography (HPLC) analyses.

RhB is a bright red dye with a complex structure that makes it chemically stable and difficult to biodegrade. RhB has the main absorption peak at 554 nm in the visible light region and a characteristic absorption band at 259 nm in the UV region. The absorption of RhB at 554 nm mainly comes from C=N and C=O in its conjugate structure [267] and its absorption in the UV region mainly comes from the benzene ring structure of RhB. As shown in **Figure 1.12**, Yu et al. [268] pointed out that there were two competitive reaction pathways for photocatalytic degradation of RhB, in which the cleavage of the dye chromophore structure dominated over the N-de-ethylation. By using HPLC and liquid chromatography electrospray ionization tandem mass spectroscopy (LC-ESI-MS/MS) method, they observed that as RhB disappeared, the concentration of the four N-de-ethylated intermediates firstly increased and then decreased. The phenomenon indicated the N-de-ethylation of RhB was a stepwise process. On the other hand, the cleavage of the entire conjugate chromophore structure of RhB dominated the photoreaction. Hydroxyl radicals or photo-generated holes could directly attack the central carbon of RhB, therefore rapidly decolouring the dye. The proven main intermediates of the decolourization process included adipic acid, phthalic acid, isophthalic acid and terephthalic acid, which were further degraded into ethane-1,2-diol, butane-1,3-diol, propane-1,2,3-triol etc.. These two competitive pathways occurred simultaneously and the RhB molecules were eventually degraded into water, carbon dioxide and inorganic ions.

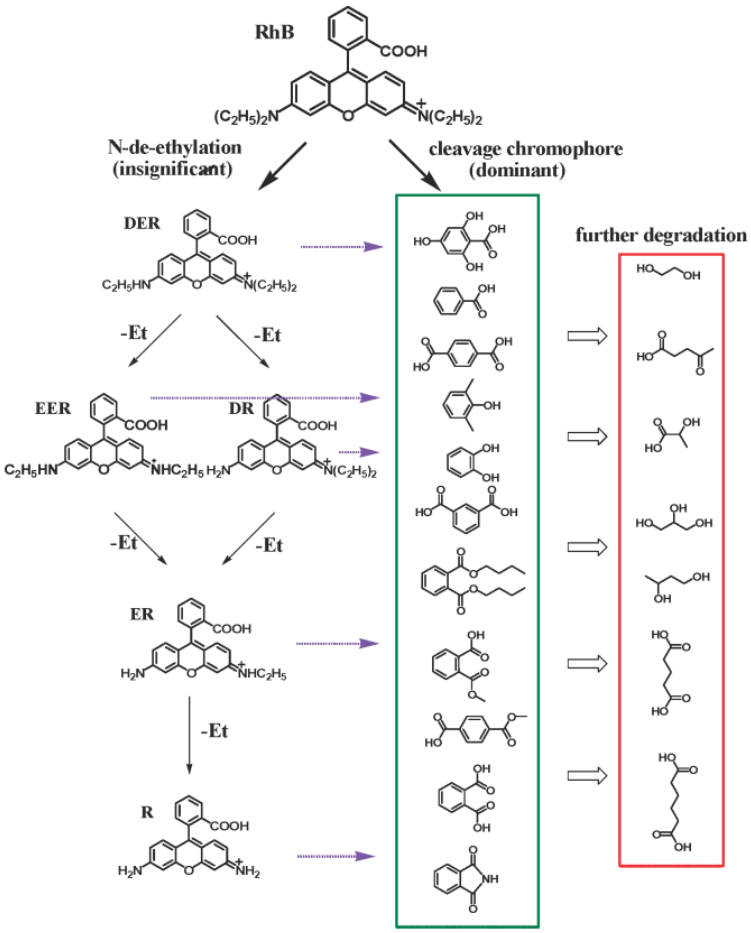

Figure 1.12. RhB photodegradation pathway under visible light irradiation. Reproduced from ref. [268] with permission.

Tahir et al. [269] also tried to identify the degradation products of RhB by ultra-performance liquid chromatography-mass spectrometry (UPLC-MS). It was deducted from the analyses that RhB was firstly degraded into several smaller compounds by the cleavage of the azo (C-N) bond. Fragmented compounds do not have any chromophores, such as azo bonds, and are therefore colourless. RhB dye was completely mineralized after photocatalytic degradation under ultraviolet light irradiation. The products of RhB photodegradation were non-toxic, colourless organic acids which were further mineralized to water and carbon dioxide.

In order to identify the photo-induced active species (e.g. hydroxyl radicals (•OH) and superoxide (•O_2 or •OOH)) responsible for the photodegradation process, some works have investigated the photodegradation rate changes in the presence of different scavengers [270]. The triethanolamine (TEOA) is an effective hole scavenger and tert-Butyl alcohol (TBA) is chosen as the •OH scavenger for the g-C_3N_4 photocatalysis system. The hydrogen peroxide (H_2O_2) test strip was used to check the formation of H_2O_2 on the g-C_3N_4 via the multi-step reduction (Eqs. (1.6) to (1.8)) of O_2 during the photocatalytic reaction. When 10%vol TEOA

was added into the aqueous solution of MO or RhB during the photodegradation, the degrading rate of RhB decreased significantly while the MO photodegradation rate was only slightly decreased. When TBA was added into the reaction solution, there was no degradation rate change of RhB and only a slight drop of MO degradation rate was observed. These results indicated that the photogenerated holes (h^+) were the main oxidation species for the RhB photodegradation. In order to further investigate whether O_2 was a key factor in the generation of $\bullet O_2$ and •OH radicals during photoreduction (Eq. (1.6) to (1.10)), photodegradations of RhB and MO were performed in Ar atmosphere. As a result, O_2 barely affected the degradation rate of RhB, but the degradation rate of MO was remarkably depressed. These results indicated that MO photodegradation on g-C_3N_4 mainly happened through the following pathway: O_2 firstly formed superoxide ($\bullet O_2$ or •OOH) from direct coupling with photo-induced e^-; then the formed radicals further oxidized the MO. The proposed reaction pathways for MO and RhB photodegradation are summarized in **Table 1.1**.

Table 1.1. Summary of reaction mechanisms of RhB and MO photodegradation on g-C_3N_4.

Dye	Class	Chemical structure	Active Species	Dominate process	Ref.
Methyl Orange	Anionic dye	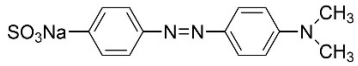	$\cdot O_2^-$(main process) h^+(minor process)	Photoreduction	[270, 271]
Rhodamine B	Cationic dye	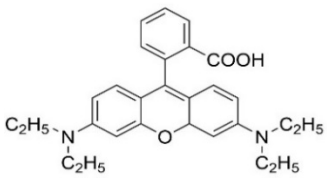	h^+	Photooxidation	[270]

1.4 Plasmonic photocatalysts

1.4.1 The light excitation on metallic nanoparticles: plasmon

In addition to the conventional photo-induced bandgap electron/hole excitation in the semiconductor, the plasmonic excitation mechanism is another emerging hot carrier excitation mechanism. Unlike the bandgap excitation mechanism in semiconductor, the conductive electrons in metals and semi-metals are 'free' to move and able to exhibit a collective oscillation under interaction with an external electromagnetic wave, which is known as the plasmonic resonance. Due to its well-defined behaviour, the oscillation of electrons is quantized into a quasiparticle, *plasmon*. For bulk metals, the lattice can be treated as infinitely

large and the conductive electrons can be described by the Drude-Sommerfeld model. The collective oscillation frequency (ω_p) of the electrons, the plasma frequency, is an intrinsic property of the metal and described by the following equation:

$$\omega_p^2 = \frac{ne^2}{\varepsilon_0 m_e} \tag{1.14}$$

where n is the free electron density, e the charge of an electron, ε_0 the dielectric constant of vacuum and the m_e is the effective mass of the electron in the lattice [49, 272]. Any light with a frequency lower than the plasma frequency will be reflected by the metal. Most the metals possess the plasma frequency at the deep UV region, which is the reason why metals have a shiny appearance and are good reflector materials. When considering the plasmon excitation by photon, only the interaction with the surface of the metal is practical due to the limited penetration depth of the light. As shown in **Figure 1.13**(a), the excited plasmon propagates on the metal surface, which is called the propagation surface plasmon polaritons (PSPP). In the research field of photocatalysis, the interaction between light and nanoparticles with a diameter much smaller than the light wavelength becomes more important. It is because most of the photocatalysts are nanoparticles to ensure a high surface area. Therefore, in the following section, we focus on the review of the interaction between light and nanoparticles. Different from PSPP, the excited plasmon in nanoparticles is localized at the surroundings of the nanoparticle (**Figure 1.13**(b)). The corresponding phenomenon is known as the localized surface plasmon resonance (LSPR).

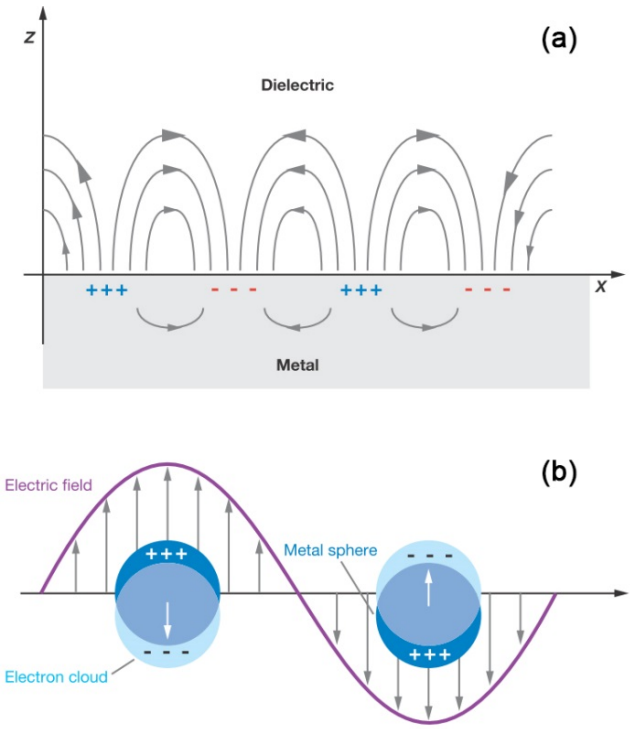

Figure 1.13. Scheme of (a) propagating surface plasmons and (b) localized surface plasmon. Reproduced with permission from ref. [273].

1.4.2 The generation and the transfer of hot carriers in nanoparticles

Then it is necessary to focus on the electron excitation process, which generates the 'hot carriers' driving the photocatalytic reaction. After the generation of LSPR, it quickly decays in both radiative (Γ_{rad}) and non-radiative ways. The latter can be further classified into bulk-like decay (Γ_b) and surface-assisted decay (Γ_{sur}), which becomes more prominent on nanoparticles with small radium (r) due to its high surface to bulk ratio [274]:

$$\Gamma_{total} = \Gamma_{rad} + \Gamma_b + \Gamma_{sur} \tag{1.15}$$

$$\Gamma_{sur} = \frac{A v_F}{r} \tag{1.16}$$

where A is a coefficient determined by the theory and always be used as a fitting parameter; and v_F is the Fermi velocity.

As shown in **Figure 1.14**(a), the decay of LSPR will firstly (within 1-100 fs) excite electrons into a non-thermal distribution, i.e. not following the Fermi-Dirac distribution, which contains the higher energy. The following electron-electron and electron-phonon scattering will lower the energy of the hot carriers within 100 fs to 10 ps. The carriers become 'cooler' due to energy

loss in the form of heat, which further dissipates to the surroundings. Before cooling down to the thermal distribution (Fermi-Dirac distribution), the hot carriers have the chances to transfer to the supported semiconductors, adsorbed molecules to drive the reaction. The time scales for the excitation and the following transfer processes are illustrated in **Figure 1.14**(b).

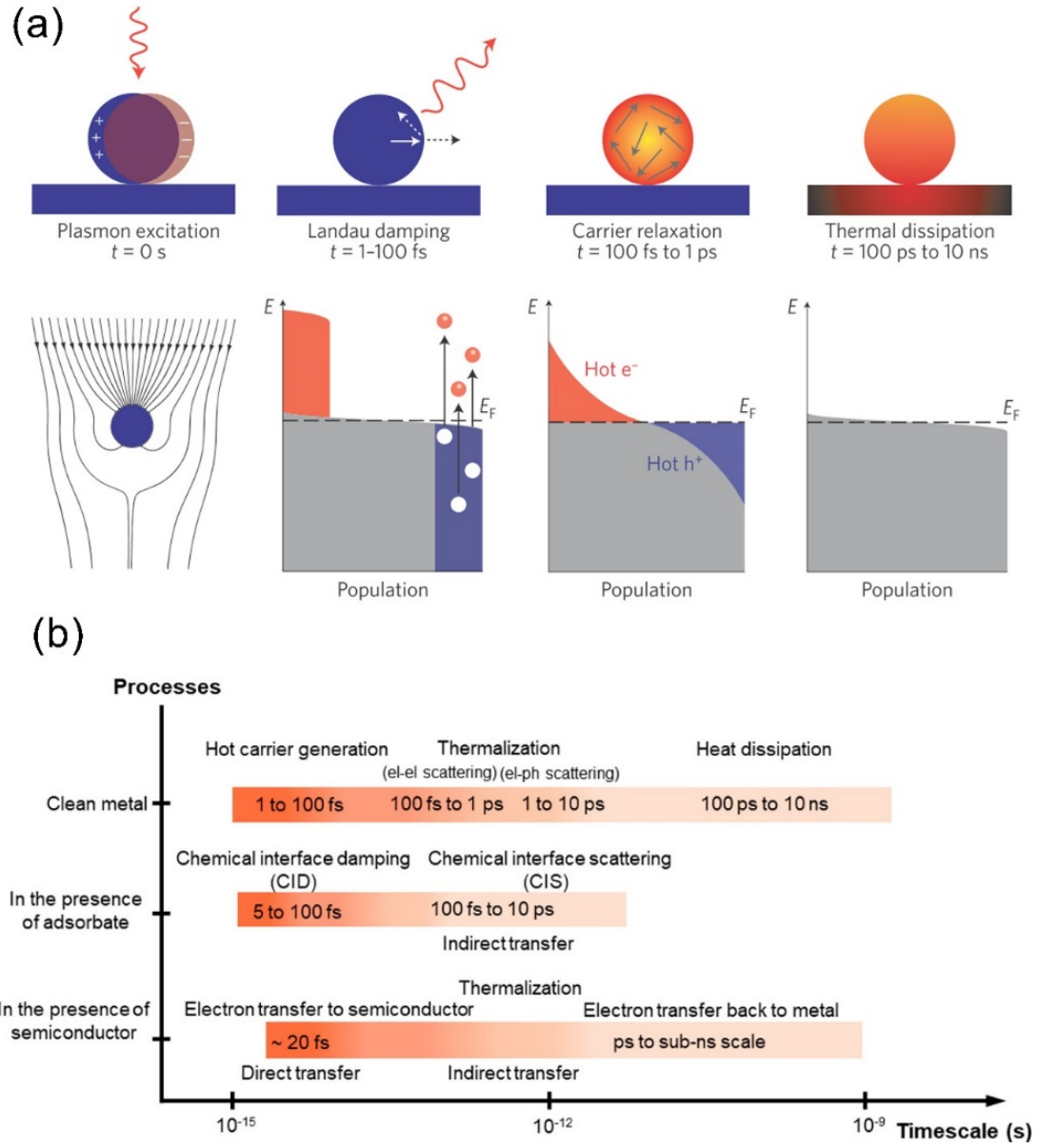

Figure 1.14. The (a) scheme and (b) time scale for hot carriers generation, transfer and thermalization. Reproduced with permissions from references [275, 276].

Besides the time scale, it is also important to know the quantity and the energy distribution of the hot carriers generated due to plasmonic excitation. There are two types of hot electron/hole pairs generations usually observed in the plasmonic materials: the intraband and interband excitations. The intraband excitation is the process for an electron excited from a filled sp

orbital to the unoccupied sp orbital. This process causes the changes in the momentum and requires assistances from phonons or the surface to obey the crystal momentum conservation. Therefore, it is a relatively slow process and only significant in small nanoparticles (< 10 nm [274, 277]). On the contrary, the interband transition from occupied d to unoccupied sp orbital needs no change of the crystal momentum. A more significant d-sp interband excitation contribution is usually observed in the plasmonic metals with relatively large size. The energy distribution of hot carriers in non-thermal distribution is directly related to the different contribution of interband and intraband electronic excitations [277, 278]. As shown in **Figure 1.15**(a), taking Au nanoparticle as an example, the d-band is more localized than the wide-spread sp-band in the electronic band structure. Due to the decay of plasmon with the energy of $\hbar\omega$, the electron in d-band is excited into the unoccupied sp-band with the formation of a hole in the d-band position. The sp-band close to the Fermi level can also be excited to the unoccupied sp-band with the assistance from phonon and surface. As shown in **Figure 1.15**(b), the interband excitation brings excited electrons with lower energy than the intraband excitation. However, the holes excited via interband excitation are more energetic than the intraband excitation, which brings more benefits to the organic pollutants photooxidation process investigated in this thesis. In summary, the interband electronic excitation brings 'hotter' holes and 'cooler' electrons with larger quantity; while the intraband electronic excitation causes 'cooler' holes but 'hotter' electrons in smaller quantity. It is important to emphasize the contributions of interband and intraband are dependent on the electronic structure and geometry of the nanoparticle.

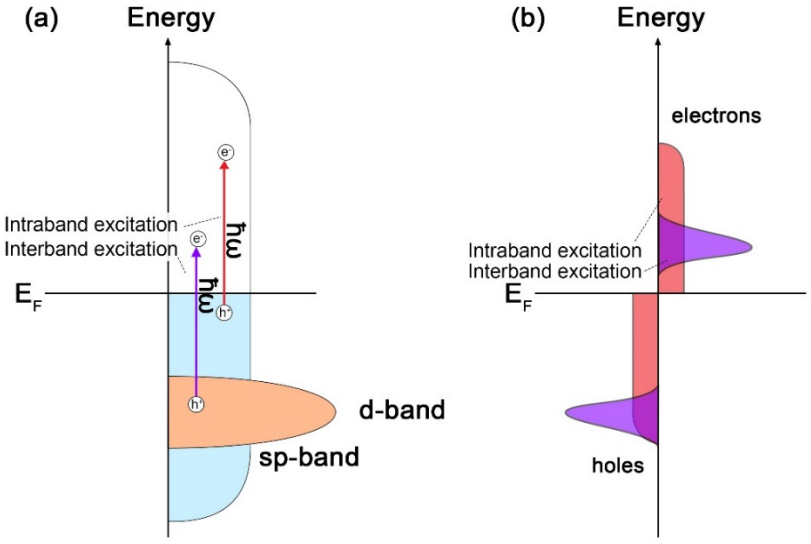

Figure 1.15. Schemes of (a) interband and intraband excitation during the plasmon damping and (b) corresponding non-thermal distribution of hot carriers. The scheme is based on the electronic structure of Au nanoparticle.

1.4.3 Plasmonic excitation in photocatalytic dye degradation.

1.4.3.1 Catalysts design

The plasmonic photocatalysts have shown its promising application in the photocatalytic degradation. The photocatalytic structure design of the plasmonic photocatalysts can be classified into two main categories: modification of plasmonic nanocrystals and heterostructure design. The plasmonic nanoparticle modification includes the chemical composition modification [279-284] and morphology design [285, 286]. In this thesis, with the consideration of the stability, it is focused on the modification of the chemical components on the plasmonic photocatalysts. Kumar et al. [287] compared the plasmonic MO photodegradation performance of Ag, Ni and AgNi alloy. The plasmonic photocatalytic activity of the alloy outperform the single-component counterparts. Verbruggen et al.[288] prepared the Au-Ag nanocrystal alloy with controllable atomic ratio. With the variation of the Au/Ag ratio, the characteristic plasmonic peak can be tuned continuously to achieve a broaden adsorption of solar light. Under simulated solar-light irritation, the Au-Ag plasmonic photocatalyst showed 16% higher activity than the benchmark P25-TiO_2 on stearic acid photodegradation. In addition to direct use the plasmonic nanoparticles, the heterostructure between metal nanoparticles and semiconductor shows its unique efficiency in photoinduced electron/hole separation. The plasmonic metals have been reported to exhibit excellent photocatalytic activity on many supports including TiO_2 [289, 290], SiO_2 [291, 292], ZnO [293, 294], BiOCl [295-297], WO_3 [298, 299] etc. As one of the most well-documented photocatalysts, the Au/TiO_2 has also been proven as high-performance plasmonic photocatalyst for dye degradation. Ding et al. [300] compared the MO photodegradation performance of Au/TiO_2 synthesized via different methods. The good Schottky contact was emphasized by the authors for excellent photocatalytic activity. Different from TiO_2 that only adsorbing light in the UV region, C_3N_4 with a reduced bandgap within the visible light range has also been combined with plasmonic metal to achieve a synergistically enhanced visible-light photocatalytic dye degradation. Bai et al. [301] prepared the Ag@C_3N_4 core-shell structure that achieved a 1.8 times MB photodegradation performance of the pristine g-C_3N_4 sample. Cheng et al. [302] loaded Au on C_3N_4 nanosheets with a photo-deposition method. The improved visible-light MO photodegradation performance was attributed to the enhancement charge separation due to the heterostructure. Zhang et al. [303] synthesized the Au/$NaYF_4$: Yb^{3+}/C_3N_4 heterostructure, which achieved a broad band light adsorption from UV to near infrared (NIR) range for MO photodegradation. The plasmonic Au nanoparticles

provided the stronger photocurrents by a factor of ~ 5.5 times comparing with non-plasmonic control group sample, which was ascribed to the enhancement photocatalytic activity.

1.4.3.2 Plasmonic photodegradation mechanism

The simplest mechanism for plasmonic photodegradation is the direct transfer of plasmon excited hot holes into the adsorbed molecule [304-306]. Boerigter et al. [307, 308] reported the Ag nanoparticles as plasmonic photocatalysts for MO degradation. The experimental results challenged the conventional understanding that the plasmon excited electron-hole pairs underwent the thermalization before being injected into the adsorbed molecule. Instead, the holes in the non-thermal state were direct-injected into the electronic state formed between adsorbed molecule and Ag. Tesema et al.[309] further compared the conversion of MB adsorbed on plasmonic Au nanoparticle surface under different irradiation wavelength. Their results suggested the degradation happened only when both the metal nanoparticle and MB molecule were excited by the incident light.

On the heterostructure between plasmonic nanoparticle and semiconductor, an indirect hot carrier transfer mechanism is often reported [310]. As shown in **Figure 1.14**(b), the hot carriers in the non-thermal state can be injected into the semiconductor at a time scale of ~20 ps. The short separation time ensures the higher energy for the charge carriers before the thermalization, which induces a higher photocatalytic activity. Li et al. [311] synthesized the Ag/AgCl-Bi_2MoO_6 ternary photocatalyst for RhB photodegradation under visible light. The plasmon excited electron was proposed to inject into the CB of both AgCl and Bi_2MoO_6. The plasmon excited holes in Ag and bandgap excited holes in $Bi_2O_4O_6$ contributed together to the photodegradation performance. He et al. [312] proved that the Ni was an efficient plasmonic non-noble catalyst. The Ni nanoparticles were loaded onto TiO_2 and tested with MB photodegradation under visible light irradiation. The mechanism that electron injection from Ni to TiO_2 under plasmonic excitation and the holes staying in Ni for photodegradation was proposed as the mechanism.

In addition to direct or indirect usage of holes generated by plasmonic excitation, the near-field optical enhancement is another mechanism proposed [313]. Hou et al. [314] performed plasmonic photodegradation of MO on Au/TiO_2 under UV-Vis light irradiation. The authors claimed the LSPR induced strong electromagnetic field around the TiO_2 nanoparticles could facilitate the UV light adsorption of TiO_2.

1.5 Conclusions

In the chapter, the principle of photocatalyst design and photocatalytic reaction mechanisms are summarized. The recent progresses are updated and reviewed.

In the case of photocatalyst design, the heterogenous structure design and atom doping strategies are still the two main methods to enhance the photocatalytic activity. Both the two strategies have its advantages and disadvantages, therefore the optimal method for a specific photocatalyst needs to be studied case by case. For heterogeneous structure building, the most outstanding advantage is that it can significantly enhance the charge carrier separation. For more advanced design, such as Z-scheme heterostructure, the high photo-reduction and oxidation can be perfectly reserved. The main advantage of the heterojunction design is its complexity. An extra semiconductor or co-catalyst is needed to be introduced, which will significantly change the chemical composition of the catalysts. Due to the large difference between the two phases across the interface, the reaction selectivity will be altered. For elemental doping strategies, the most outstanding advantage is its ability to modify the electronic structure of the semiconductor. It can just the bandgap, VBM, CBM values to meet the specific requirements of different target reactions. In addition, the doping is very facile to implement, which doesn't require additional steps in photocatalytic preparation. The doping strategy has its drawbacks too. The doping inevitably introduces defects into the crystal, which can cause the decrease of bandgap and compromises on the photo-reduction or oxidation capability.

For photocatalysts aiming for pollutant remediation, the main challenge is still the low photocatalytic activity. Only by increasing its photocatalytic performance, the practical application is economically feasible. From a more fundamental perspective, the mechanisms to enhance the photocatalytic performance are still elusive. A clear understanding of mechanisms can significantly help to optimize the catalysts design. The factors limiting the photocatalytic activity of the photocatalysts include low SSA, high electron-hole recombination rate and unoptimized electronic structure. The goal of this thesis is to further develop the new photocatalyst for high-performance photocatalytic dye degradation. By designing new synthesis methods and using heteroatom doping strategies, it is aimed to achieve a high photocatalytic dye degradation performance for our new photocatalysts. By carefully control the variables in the experiments, the enhancement mechanism of elemental doping is expected to be unravelled.

References

[1] T. Hisatomi, J. Kubota, K. Domen, Recent Advances in Semiconductors for Photocatalytic and Photoelectrochemical Water Splitting, Chemical Society Reviews, 43 (2014) 7520-7535.

[2] S. Zhu, D. Wang, Photocatalysis: Basic Principles, Diverse Forms of Implementations and Emerging Scientific Opportunities, Adv. Energy Mater., 7 (2017) 1700841.

[3] C. Zamfirescu, I. Dincer, Assessment of a New Integrated Solar Energy System for Hydrogen Production, Solar Energy, 107 (2014) 700-713.

[4] A. Criscuoli, J. Zhong, A. Figoli, M.C. Carnevale, R. Huang, E. Drioli, Treatment of Dye Solutions by Vacuum Membrane Distillation, Water Research, 42 (2008) 5031-5037.

[5] C. Galindo, P. Jacques, A. Kalt, Photooxidation of the Phenylazonaphthol AO20 on TiO_2: Kinetic and Mechanistic Investigations, Chemosphere, 45 (2001) 997-1005.

[6] S.S. Patil, V.M. Shinde, Biodegradation Studies of Aniline and Nitrobenzene in Aniline Plant Wastewater by Gas Chromatography, Environmental Science & Technology, 22 (1988) 1160-1165.

[7] Y.M. Slokar, A. Majcen Le Marechal, Methods of Decoloration of Textile Wastewaters, Dyes and Pigments, 37 (1998) 335-356.

[8] D.M. Blake, Bibliography of Work on the Photocatalytic Removal of Hazardous Compounds From Water and Air, United States, 1994.

[9] S. Dong, J. Feng, M. Fan, Y. Pi, L. Hu, X. Han, M. Liu, J. Sun, J. Sun, Recent developments in heterogeneous photocatalytic water treatment using visible light-responsive photocatalysts: a review, RSC Adv., 5 (2015) 14610-14630.

[10] U.G. Akpan, B.H. Hameed, Parameters affecting the photocatalytic degradation of dyes using TiO_2-based photocatalysts: A review, J. Hazard. Mater., 170 (2009) 520-529.

[11] A.W.D. Larkum, Limitations and Prospects of Natural Photosynthesis for Bioenergy Production, Current Opinion in Biotechnology, 21 (2010) 271-276.

[12] M. Fagnoni, D. Dondi, D. Ravelli, A. Albini, Photocatalysis for the Formation of the C-C Bond, Chem. Rev., 107 (2007) 2725-2756.

[13] A. Albini, M. Fagnoni, 1908: Giacomo Ciamician and the Concept of Green Chemistry, ChemSusChem, 1 (2008) 63-66.

[14] L. Bruner, J. Kozak, Zur Kenntnis der Photokatalyse. I. Die Lichtreaktion in Gemischen: Uransalz + Oxalsäure, Zeitschrift für Elektrochemie und angewandte physikalische Chemie, 17 (1911) 354-360.

[15] E. Baur, A. Perret, Über die Einwirkung von Licht auf gelöste Silbersalze in Gegenwart von Zinkoxyd, Helvetica Chimica Acta, 7 (1924) 910-915.

[16] C.F. Goodeve, J.A. Kitchener, Photosensitisation by Titanium Dioxide, Transactions of the Faraday Society, 34 (1938) 570-579.

[17] A. Fujishima, K. Honda, Electrochemical Photolysis of Water at a Semiconductor Electrode, Nature, 238 (1972) 37-38.

[18] J.H. Carey, J. Lawrence, H.M. Tosine, Photodechlorination of PCB's in The Presence of Titanium Dioxide in Aqueous Suspensions, Bulletin of Environmental Contamination and Toxicology, 16 (1976) 697-701.

[19] S.N. Frank, A.J. Bard, Heterogeneous Photocatalytic Oxidation of Cyanide Ion in Aqueous Solutions at Titanium Dioxide Powder, Journal of the American Chemical Society, 99 (1977) 303-304.

[20] S.K. Loeb, P.J.J. Alvarez, J.A. Brame, E.L. Cates, W. Choi, J. Crittenden, D.D. Dionysiou, Q. Li, G. Li-Puma, X. Quan, D.L. Sedlak, T. David Waite, P. Westerhoff, J.H. Kim, The Technology Horizon for Photocatalytic Water Treatment: Sunrise or Sunset?, Environ Sci Technol, 53 (2019) 2937-2947.

[21] C. Byrne, G. Subramanian, S.C. Pillai, Recent Advances in Photocatalysis for Environmental Applications, Journal of Environmental Chemical Engineering, 6 (2018) 3531-3555.

[22] N. Shaham-Waldmann, Y. Paz, Away from TiO_2: A Critical Minireview on the Developing of New Photocatalysts for Degradation of Contaminants in Water, Mater. Sci. Semicond. Process., 42 (2016) 72-80.

[23] M.R. Hoffmann, S.T. Martin, W. Choi, D.W. Bahnemann, Environmental Applications of Semiconductor Photocatalysis, Chem. Rev., 95 (1995) 69-96.

[24] L. Huang, R. Zhang, X. Sun, X. Cheng, Synthesis and Characterization of g-C_3N_4/α-Fe_2O_3 Composites With Enhanced Photocatalytic Activity, Key Eng. Mater., 2014, pp. 225-228.

[25] L. Wang, P. Wang, B. Huang, X. Ma, G. Wang, Y. Dai, X. Zhang, X. Qin, Synthesis of Mn-doped ZnS Microspheres With Enhanced Visible Light Photocatalytic Activity, Appl. Surf. Sci., 391 (2017) 557-564.

[26] C. Tian, Q. Zhang, A. Wu, M. Jiang, Z. Liang, B. Jiang, H. Fu, Cost-Effective Large-Scale Synthesis of ZnO Photocatalyst With Excellent Performance for Dye Photodegradation, Chemical Communications, 48 (2012) 2858-2860.

[27] S. Martha, P. Chandra Sahoo, K.M. Parida, An Overview on Visible Light Responsive Metal Oxide Based Photocatalysts for Hydrogen Energy Production, RSC Adv., 5 (2015) 61535-61553.

[28] A. Fujishima, T.N. Rao, D.A. Tryk, Titanium Dioxide Photocatalysis, Journal of Photochemistry and Photobiology C: Photochemistry Reviews, 1 (2000) 1-21.

[29] M.N. Chong, B. Jin, C.W.K. Chow, C. Saint, Recent Developments in Photocatalytic Water Treatment Technology: A Review, Water Research, 44 (2010) 2997-3027.

[30] T. Inoue, A. Fujishima, S. Konishi, K. Honda, Photoelectrocatalytic Reduction of Carbon Dioxide in Aqueous Suspensions of Semiconductor Powders, Nature, 277 (1979) 637-638.

[31] X. Chang, T. Wang, J. Gong, CO_2 Photo-Reduction: Insights Into CO_2 Activation and Reaction on Surfaces of Photocatalysts, Energy & Environmental Science, 9 (2016) 2177-2196.

[32] S.N. Habisreutinger, L. Schmidt-Mende, J.K. Stolarczyk, Photocatalytic Reduction of CO_2 on TiO_2 and Other Semiconductors, Angew. Chem., Int. Ed., 52 (2013) 7372-7408.

[33] A. Kudo, Y. Miseki, Heterogeneous Photocatalyst Materials for Water Splitting, Chemical Society Reviews, 38 (2009) 253-278.

[34] J. Wang, P. Wang, Y. Cao, J. Chen, W. Li, Y. Shao, Y. Zheng, D. Li, A High Efficient Photocatalyst Ag_3VO_4/TiO_2/Graphene Nanocomposite With Wide Spectral Response, Appl. Catal., B, 136-137 (2013) 94-102.

[35] Section 10 - Solar, in: C.J. Cleveland, C. Morris (Eds.) Handbook of Energy, Elsevier, Amsterdam, 2013, pp. 405-450.

[36] D.R. Lide, CRC Handbook of Chemistry and Physics: A Ready-Reference Book of Chemical and Physical Data, CRC Press, New York, 1996.

[37] J. Kim, C.W. Lee, W. Choi, Platinized WO_3 as an Environmental Photocatalyst that Generates OH Radicals under Visible Light, Environmental Science & Technology, 44 (2010) 6849-6854.

[38] W. Wu, J. Changzhong, V.A.L. Roy, Recent Progress in Magnetic IRON Oxide-Semiconductor Composite Nanomaterials as Promising Photocatalysts, Nanoscale, 7 (2015) 38-58.

[39] M. Xu, Y. Gao, E.M. Moreno, M. Kunst, M. Muhler, Y. Wang, H. Idriss, C. Wöll, Photocatalytic Activity of Bulk TiO_2 Anatase and Rutile Single Crystals Using Infrared Absorption Spectroscopy, Physical Review Letters, 106 (2011) 138302.

[40] A.L. Linsebigler, G. Lu, J.T. Yates, Photocatalysis on TiO_2 Surfaces: Principles, Mechanisms, and Selected Results, Chem. Rev., 95 (1995) 735-758.

[41] D.O. Scanlon, C.W. Dunnill, J. Buckeridge, S.A. Shevlin, A.J. Logsdail, S.M. Woodley, C.R. Catlow, M.J. Powell, R.G. Palgrave, I.P. Parkin, G.W. Watson, T.W. Keal, P. Sherwood, A. Walsh, A.A. Sokol, Band Alignment of Rutile and Anatase TiO_2, Nat. Mater., 12 (2013) 798-801.

[42] Y. Yamada, Y. Kanemitsu, Determination of Electron and Hole Lifetimes of Rutile and Anatase TiO_2 Single Crystals, Applied Physics Letters, 101 (2012).

[43] N. Harada, M. Goto, K. Iijima, H. Sakama, N. Ichikawa, H. Kunugita, K. Ema, Time-Resolved Luminescence of TiO_2 Powders with Different Crystal Structures, Japanese Journal of Applied Physics, 46 (2007) 4170-4171.

[44] B. Mguig, M. Calatayud, C. Minot, CO Oxidation over Anatase TiO_2-(001), Journal of Molecular Structure: THEOCHEM, 709 (2004) 73-78.

[45] L. Liu, H. Zhao, J.M. Andino, Y. Li, Photocatalytic CO_2 Reduction with H_2O on TiO_2 Nanocrystals: Comparison of Anatase, Rutile, and Brookite Polymorphs and Exploration of Surface Chemistry, ACS Catal., 2 (2012) 1817-1828.

[46] S. Bai, L. Wang, Z. Li, Y. Xiong, Facet-Engineered Surface and Interface Design of Photocatalytic Materials, Adv Sci (Weinh), 4 (2017) 1600216.

[47] F.A. Frame, F.E. Osterloh, CdSe-MoS_2: A Quantum Size-Confined Photocatalyst for Hydrogen Evolution from Water under Visible Light, J. Phys. Chem. C, 114 (2010) 10628-10633.

[48] W. Wang, J. Fang, H. Chen, Nano-confined g-C_3N_4 in Mesoporous SiO_2 with Improved Quantum Size Effect and Tunable Structure for Photocatalytic Tetracycline Antibiotic Degradation, J. Alloys Compd., 819 (2020) 153064.

[49] C. Kittel, Introduction to Solid State Physics, 8th ed., John Wiley & Sons2004.

[50] J.B. Baxter, C. Richter, C.A. Schmuttenmaer, Ultrafast Carrier Dynamics in Nanostructures for Solar Fuels, Annual Review of Physical Chemistry, 65 (2014) 423-447.

[51] T. Yasutake, H. Tomohiro, I. Takuya, I. Takashi, K. Shuichi, Selective Reduction of Nitrogen Monoxide with Hydrocarbons over SnO_2 Catalyst, Chemistry Letters, 22 (1993) 773-776.

[52] M.I. Litter, Heterogeneous Photocatalysis: Transition Metal Ions in Photocatalytic Systems, Appl. Catal., B, 23 (1999) 89-114.

[53] H. Xiao, W. Wang, G. Liu, Z. Chen, K. Lv, J. Zhu, Photocatalytic Performances of g-C_3N_4 Based Catalysts for RhB Degradation: Effect of Preparation Conditions, Appl. Surf. Sci., 358 (2015) 313-318.

[54] N.Z. Muradov, A. T-Raissi, D. Muzzey, C.R. Painter, M.R. Kemme, Selective Photocatalytic Destruction of Airborne VOCs, Solar Energy, 56 (1996) 445-453.

[55] C. Kormann, D.W. Bahnemann, M.R. Hoffmann, Photolysis of Chloroform and Other Organic Molecules in Aqueous Titanium Dioxide Suspensions, Environmental Science & Technology, 25 (1991) 494-500.

[56] J. Fernández, J. Kiwi, J. Baeza, J. Freer, C. Lizama, H.D. Mansilla, Orange II Photocatalysis on Immobilised TiO_2: Effect of the pH and H_2O_2, Appl. Catal., B, 48 (2004) 205-211.

[57] Z. Zhao, H. Zhou, L. Zheng, P. Niu, G. Yang, W. Hu, J. Ran, S. Qiao, J. Wang, H. Zheng, Molecules Interface Engineering Derived External Electric Field for Effective Charge Separation in Photoelectrocatalysis, Nano Energy, 42 (2017) 90-97.

[58] J. Li, L. Cai, J. Shang, Y. Yu, L. Zhang, Giant Enhancement of Internal Electric Field Boosting Bulk Charge Separation for Photocatalysis, Adv. Mater., 28 (2016) 4059-4064.

[59] I.K. Konstantinou, T.A. Albanis, TiO_2-Assisted Photocatalytic Degradation of Azo Dyes in Aqueous Solution: Kinetic and Mechanistic Investigations: A Review, Appl. Catal., B, 49 (2004) 1-14.

[60] V. Augugliaro, C. Baiocchi, A. Bianco Prevot, E. García-López, V. Loddo, S. Malato, G. Marcí, L. Palmisano, M. Pazzi, E. Pramauro, Azo-Dyes Photocatalytic Degradation in Aqueous Suspension of TiO_2 Under Solar Irradiation, Chemosphere, 49 (2002) 1223-1230.

[61] O. Carp, C.L. Huisman, A. Reller, Photoinduced Reactivity of Titanium Dioxide, Progress in Solid State Chemistry, 32 (2004) 33-177.

[62] S. Al-Qaradawi, S.R. Salman, Photocatalytic Degradation of Methyl Orange as a Model Compound, J. Photochem. Photobiol., A, 148 (2002) 161-168.

[63] M.R.D. Khaki, M.S. Shafeeyan, A.A.A. Raman, W. Daud, Application of Doped Photocatalysts for Organic Pollutant Degradation - A Review, J Environ Manage, 198 (2017) 78-94.

[64] V. Kumaravel, S. Mathew, J. Bartlett, S.C. Pillai, Photocatalytic Hydrogen Production Using Metal Doped TiO_2: A Review of Recent Advances, Appl. Catal., B, 244 (2019) 1021-1064.

[65] F. Zhang, Y. Lu, D.S. Schulman, T. Zhang, K. Fujisawa, Z. Lin, Y. Lei, A.L. Elias, S. Das, S.B. Sinnott, M. Terrones, Carbon Doping of WS_2 Monolayers: Bandgap Reduction and p-type Doping Transport, Sci Adv, 5 (2019) eaav5003.

[66] S. Na Phattalung, S. Limpijumnong, J. Yu, Passivated Co-Doping Approach to Bandgap Narrowing of Titanium Dioxide With Enhanced Photocatalytic Activity, Appl. Catal., B, 200 (2017) 1-9.

[67] C. Mao, F. Zuo, Y. Hou, X. Bu, P. Feng, In Situ Preparation of a Ti^{3+} Self-Doped TiO_2 Film with Enhanced Activity as Photoanode by N_2H_4 Reduction, Angew. Chem., Int. Ed., 53 (2014) 10485-10489.

[68] R. Long, J. Liu, O.V. Prezhdo, Unravelling the Effects of Grain Boundary and Chemical Doping on Electron-Hole Recombination in $CH_3NH_3PbI_3$ Perovskite by Time-Domain Atomistic Simulation, J. Am. Chem. Soc., 138 (2016) 3884-3890.

[69] B. Ehrler, K.P. Musselman, M.L. Bohm, F.S. Morgenstern, Y. Vaynzof, B.J. Walker, J.L. Macmanus-Driscoll, N.C. Greenham, Preventing Interfacial Recombination in Colloidal Quantum Dot Solar Cells by Doping the Metal Oxide, ACS Nano, 7 (2013) 4210-4220.

[70] S. Fischer, A.W. Munz, K.-D. Schierbaum, W. Göpel, The Geometric Structure of Intrinsic Defects At TiO_2(110) Surfaces: An STM Study, Surface Science, 337 (1995) 17-30.

[71] S.J. Clark, J. Robertson, S. Lany, A. Zunger, Intrinsic Defects in ZnO Calculated by Screened Exchange and Hybrid Density Functionals, Phys. Rev. B, 81 (2010).

[72] X. Chen, L. Liu, P.Y. Yu, S.S. Mao, Increasing Solar Absorption for Photocatalysis With Black Hydrogenated Titanium Dioxide Nanocrystals, Science, 331 (2011) 746-750.

[73] G. Wang, H. Wang, Y. Ling, Y. Tang, X. Yang, R.C. Fitzmorris, C. Wang, J.Z. Zhang, Y. Li, Hydrogen-treated TiO_2 Nanowire Arrays for Photoelectrochemical Water Splitting, Nano Lett, 11 (2011) 3026-3033.

[74] A. Naldoni, M. Allieta, S. Santangelo, M. Marelli, F. Fabbri, S. Cappelli, C.L. Bianchi, R. Psaro, V. Dal Santo, Effect of Nature and Location of Defects on Bandgap Narrowing in Black TiO_2 Nanoparticles, J. Am. Chem. Soc., 134 (2012) 7600-7603.

[75] J. Nowotny, T. Bak, M.K. Nowotny, L.R. Sheppard, TiO_2 Surface Active Sites for Water Splitting, J Phys Chem B, 110 (2006) 18492-18495.

[76] C. Sun, T. Liao, G.Q. Lu, S.C. Smith, The Role of Atomic Vacancy on Water Dissociation over Titanium Dioxide Nanosheet: A Density Functional Theory Study, J. Phys. Chem. C, 116 (2012) 2477-2482.

[77] S. Wang, L. Pan, J.J. Song, W. Mi, J.J. Zou, L. Wang, X. Zhang, Titanium-defected Undoped Anatase TiO_2 with p-type Conductivity, Room-Temperature Ferromagnetism, and Remarkable Photocatalytic Performance, J. Am. Chem. Soc., 137 (2015) 2975-2983.

[78] L. Pan, S. Wang, W. Mi, J. Song, J.-J. Zou, L. Wang, X. Zhang, Undoped ZnO Abundant With Metal Vacancies, Nano Energy, 9 (2014) 71-79.

[79] M. Guan, C. Xiao, J. Zhang, S. Fan, R. An, Q. Cheng, J. Xie, M. Zhou, B. Ye, Y. Xie, Vacancy Associates Promoting Solar-Driven Photocatalytic Activity of Ultrathin Bismuth Oxychloride Nanosheets, J. Am. Chem. Soc., 135 (2013) 10411-10417.

[80] Y. Zhu, Q. Ling, Y. Liu, H. Wang, Y. Zhu, Photocatalytic Performance of $BiPO_4$ Nanorods Adjusted via Defects, Appl. Catal., B, 187 (2016) 204-211.

[81] J. Zhao, C. Chen, W. Ma, Photocatalytic Degradation of Organic Pollutants Under Visible Light Irradiation, Topics in Catalysis, 35 (2005) 269-278.

[82] Z. Li, Y. Fang, X. Zhan, S. Xu, Facile Preparation of Squarylium Dye Sensitized TiO_2 Nanoparticles and Their Enhanced Visible-Light Photocatalytic Activity, J. Alloys Compd., 564 (2013) 138-142.

[83] T. Komeda, K. Katoh, M. Yamashita, Double-Decker Phthalocyanine Complex: Scanning Tunneling Microscopy Study of Film Formation and Spin Properties, Progress in Surface Science, 89 (2014) 127–160.

[84] X. Zhang, T. Peng, L. Yu, R. Li, Q. Li, Z. Li, Visible/Near-Infrared-Light-Induced H_2 Production over g-C_3N_4 Co-sensitized by Organic Dye and Zinc Phthalocyanine Derivative, ACS Catal., 5 (2015) 504-510.

[85] X. Zhang, L. Yu, C. Zhuang, T. Peng, R. Li, X. Li, Highly Asymmetric Phthalocyanine as a Sensitizer of Graphitic Carbon Nitride for Extremely Efficient Photocatalytic H_2 Production under Near-Infrared Light, ACS Catal., 4 (2014) 162-170.

[86] M. Kaur, D.H. Choi, Diketopyrrolopyrrole: Brilliant Red Pigment Dye-Based Fluorescent Probes and Their Applications, Chemical Society Reviews, 44 (2015) 58-77.

[87] J. Qin, J. Huo, P. Zhang, J. Zeng, T. Wang, H. Zeng, Improving the Photocatalytic Hydrogen Production Of Ag/g-C_3N_4 Nanocomposites by Dye-Sensitization Under Visible Light Irradiation, Nanoscale, 8 (2016) 2249-2259.

[88] E. Fogler, J.A. Garg, P. Hu, G. Leitus, L.J.W. Shimon, D. Milstein, System with Potential Dual Modes of Metal-Ligand Cooperation: Highly Catalytically Active Pyridine-Based PNNH-Ru Pincer Complexes, Chem. - Eur. J., 20 (2014) 15727-15731.

[89] J. Shang, F. Zhao, T. Zhu, J. Li, Photocatalytic Degradation of Rhodamine B by Dye-Sensitized TiO_2 Under Visible-Light Irradiation, Science China Chemistry, 54 (2011) 167-172.

[90] J. Zhang, M. Zhang, R.-Q. Sun, X. Wang, A Facile Band Alignment of Polymeric Carbon Nitride Semiconductors to Construct Isotype Heterojunctions, Angew. Chem., Int. Ed., 51 (2012) 10145-10149.

[91] R. Marschall, Semiconductor Composites: Strategies for Enhancing Charge Carrier Separation to Improve Photocatalytic Activity, Adv. Funct. Mater., 24 (2014) 2421-2440.

[92] H. Wang, L. Zhang, Z. Chen, J. Hu, S. Li, Z. Wang, J. Liu, X. Wang, Semiconductor Heterojunction Photocatalysts: Design, Construction, and Photocatalytic Performances, Chem Soc Rev, 43 (2014) 5234-5244.

[93] Z. He, Y. Shi, C. Gao, L. Wen, J. Chen, S. Song, BiOCl/$BiVO_4$ p-n Heterojunction with Enhanced Photocatalytic Activity under Visible-Light Irradiation, J. Phys. Chem. C, 118 (2013) 389-398.

[94] H. Huang, K. Xiao, Y. He, T. Zhang, F. Dong, X. Du, Y. Zhang, In Situ Assembly of BiOI@$Bi_{12}O_{17}Cl_2$ p-n Junction: Charge Induced Unique Front-Lateral Surfaces Coupling Heterostructure With High Exposure of BiOI {001} Active Facets for Robust and Nonselective Photocatalysis, Appl. Catal., B, 199 (2016) 75-86.

[95] X. Yu, J. Zhang, Z. Zhao, W. Guo, J. Qiu, X. Mou, A. Li, J.P. Claverie, H. Liu, NiO-TiO_2 p-n splittingHeterostructured Nanocables Bridged by Zero-Bandgap rGO for Highly Efficient Photocatalytic Water Nano Energy, 16 (2015) 207-217.

[96] J. Low, C. Jiang, B. Cheng, S. Wageh, A.A. Al-Ghamdi, J. Yu, A Review of Direct Z-Scheme Photocatalysts, Small Methods, 1 (2017).

[97] P. Zhou, J. Yu, M. Jaroniec, All-solid-state Z-Scheme Photocatalytic Systems, Adv. Mater., 26 (2014) 4920-4935.

[98] K. Qi, B. Cheng, J. Yu, W. Ho, A Review on TiO_2-based Z-Scheme Photocatalysts, Chin. J. Catal., 38 (2017) 1936-1955.

[99] G. Zhang, Z.A. Lan, X. Wang, Conjugated Polymers: Catalysts for Photocatalytic Hydrogen Evolution, Angew. Chem., Int. Ed., 55 (2016) 15712-15727.

[100] Y. Ni, W. Wang, W. Huang, C. Lu, Z. Xu, Graphene Strongly Wrapped TiO_2 for High-Reactive Photocatalyst: A New Sight for Significant Application of Graphene, J. Colloid Interface Sci., 428 (2014) 162-169.

[101] T. Hasobe, S. Hattori, P.V. Kamat, S. Fukuzumi, Supramolecular nanostructured assemblies of different types of porphyrins with fullerene using TiO_2 nanoparticles for light energy conversion, Tetrahedron, 62 (2006) 1937-1946.

[102] J.X. Sun, Y.P. Yuan, L.G. Qiu, X. Jiang, A.J. Xie, Y.H. Shen, J.F. Zhu, Fabrication of Composite Photocatalyst g-C_3N_4-ZnO and Enhancement of Photocatalytic Activity Under Visible Light, Dalton Transactions, 41 (2012) 6756-6763.

[103] R. Marschall, L. Wang, Photocatalysis on TiO_2 Surfaces: Principles, Mechanisms, and Selected Results, Catal. Today, 225 (2014) 111-135.

[104] M. Humayun, F. Raziq, A. Khan, W. Luo, Modification Strategies of TiO_2 for Potential Applications in Photocatalysis: A Critical Review, Green Chemistry Letters and Reviews, 11 (2018) 86-102.

[105] D. Liu, L. Jing, P. Luan, J. Tang, H. Fu, Enhancement Effects of Cobalt Phosphate Modification on Activity for Photoelectrochemical Water Oxidation of TiO_2 and Mechanism Insights, ACS Appl. Mater. Interfaces, 5 (2013) 4046-4052.

[106] Y. Cao, L. Jing, X. Shi, Y. Luan, J.R. Durrant, J. Tang, H. Fu, Enhanced Photocatalytic Activity of nc-TiO_2 by Promoting Photogenerated Electrons Captured by the Adsorbed Oxygen, Phys. Chem. Chem. Phys., 14 (2012) 8530-8536.

[107] Z. He, J. Tang, J. Shen, J. Chen, S. Song, Enhancement of Photocatalytic Reduction of CO_2 to CH_4 over TiO_2 Nanosheets by Modifying With Sulfuric Acid, Appl. Surf. Sci., 364 (2016) 416-427.

[108] X. Wang, K. Maeda, A. Thomas, K. Takanabe, G. Xin, J.M. Carlsson, K. Domen, M. Antonietti, A Metal-Free Polymeric Photocatalyst for Hydrogen Production From Water Under Visible Light, Nat. Mater., 8 (2009) 76-80.

[109] Uber Einige Stickstoff-Verbindungen, (1834).

[110] E.C. Franklin, The Ammono Carbonic Acids, Journal of the American Chemical Society, 44 (1922) 486-509.

[111] L. Pauling, J.H. Sturdivant, The Structure of Cyameluric Acid, Hydromelonic Acid and Related Substances, Proceedings of the National Academy of Sciences, 23 (1937) 615.

[112] C.E. Redemann, H.J. Lucas, Some Derivatives of Cyameluric Acid and Probable Structures of Melam, Melem and Melon, Journal of the American Chemical Society, 62 (1940) 842-846.

[113] A.Y. Liu, M.L. Cohen, Prediction of New Low Compressibility Solids, Science, 245 (1989) 841.

[114] D.M. Teter, R.J. Hemley, Low-Compressibility Carbon Nitrides, Science, 271 (1996) 53.

[115] F. Goettmann, A. Fischer, M. Antonietti, A. Thomas, Metal-Free Catalysis of Sustainable Friedel-Crafts Reactions: Direct Activation of Benzene by Carbon Nitrides to Avoid the Use of Metal Chlorides and Halogenated Compounds, Chemical Communications, (2006) 4530-4532.

[116] J. Zhang, J. Sun, K. Maeda, K. Domen, P. Liu, M. Antonietti, X. Fu, X. Wang, Sulfur-Mediated Synthesis of Carbon Nitride: Band-Gap Engineering and Improved Functions for Photocatalysis, Energy & Environmental Science, 4 (2011) 675-678.

[117] Y. Cui, Z. Ding, P. Liu, M. Antonietti, X. Fu, X. Wang, Metal-free Activation of H_2O_2 by g-C_3N_4 Under Visible Light Irradiation for the Degradation of Organic Pollutants, Phys. Chem. Chem. Phys., 14 (2012) 1455-1462.

[118] X. Ma, Y. Lv, J. Xu, Y. Liu, R. Zhang, Y. Zhu, A Strategy of Enhancing the Photoactivity of g-C_3N_4 via Doping of Nonmetal Elements: A First-Principles Study, J. Phys. Chem. C, 116 (2012) 23485-23493.

[119] G. Dong, K. Zhao, L. Zhang, Carbon Self-Doping Induced High Electronic Conductivity and Photoreactivity of g-C_3N_4, Chemical Communications, 48 (2012) 6178-6180.

[120] Y. Xu, S. Gao, Band Gap of C_3N_4 in the GW Approximation, International Journal of Hydrogen Energy, 37 (2012) 11072-11080.

[121] W.-J. Ong, L.-L. Tan, Y.H. Ng, S.-T. Yong, S.-P. Chai, Graphitic Carbon Nitride (g-C_3N_4)-Based Photocatalysts for Artificial Photosynthesis and Environmental Remediation: Are We a Step Closer To Achieving Sustainability?, Chem. Rev., 116 (2016) 7159-7329.

[122] E. Kroke, M. Schwarz, E. Horath-Bordon, P. Kroll, B. Noll, A.D. Norman, Tri-s-triazine derivatives. Part I. From Trichloro-tri-s-triazine to Graphitic C_3N_4 Structures, New Journal of Chemistry, 26 (2002) 508-512.

[123] A. Thomas, A. Fischer, F. Goettmann, M. Antonietti, J.-O. Müller, R. Schlögl, J.M. Carlsson, Graphitic Carbon Nitride Materials: Variation of Structure and Morphology and Their Use as Metal-Free Catalysts, J. Mater. Chem., 18 (2008) 4893-4908.

[124] P.M. Schaber, J. Colson, S. Higgins, D. Thielen, B. Anspach, J. Brauer, Thermal Decomposition (Pyrolysis) of Urea in an Open Reaction Vessel, Thermochim. Acta, 424 (2004) 131-142.

[125] G. Zhang, J. Zhang, M. Zhang, X. Wang, Polycondensation of Thiourea Into Carbon Nitride Semiconductors as Visible Light Photocatalysts, J. Mater. Chem., 22 (2012) 8083-8091.

[126] Q. Li, J. Yang, D. Feng, Z. Wu, Q. Wu, S.S. Park, C.-S. Ha, D. Zhao, Facile Synthesis of Porous Carbon Nitride Spheres With Hierarchical Three-Dimensional Mesostructures for CO_2 Capture, Nano Res., 3 (2010) 632-642.

[127] E. Kroke, M. Schwarz, Novel Group 14 Nitrides, Coordination Chemistry Reviews, 248 (2004) 493-532.

[128] S.C. Yan, Z.S. Li, Z.G. Zou, Photodegradation Performance of g-C_3N_4 Fabricated by Directly Heating Melamine, Langmuir, 25 (2009) 10397-10401.

[129] M. Groenewolt, M. Antonietti, Synthesis of g-C_3N_4 Nanoparticles in Mesoporous Silica Host Matrices, Adv. Mater., 17 (2005) 1789-1792.

[130] Y. Zhang, J. Liu, G. Wu, W. Chen, Porous Graphitic Carbon Nitride Synthesized via Direct Polymerization of Urea for Efficient Sunlight-Driven Photocatalytic Hydrogen Production, Nanoscale, 4 (2012) 5300-5303.

[131] Q. Fu, C.-B. Cao, H.-S. Zhu, A Solvothermal Synthetic Route to Prepare Polycrystalline Carbon Nitride, Chemical Physics Letters, 314 (1999) 223-226.

[132] H. Montigaud, B. Tanguy, G. Demazeau, I. Alves, M. Birot, J. Dunogues, Solvothermal Synthesis of the Graphitic Form Of C_3N_4 as Macroscopic Sample, Diamond and Related Materials, 8 (1999) 1707-1710.

[133] Y.-J. Bai, B. Lü, Z.-G. Liu, L. Li, D.-L. Cui, X.-G. Xu, Q.-L. Wang, Solvothermal Preparation of Graphite-Like C_3N_4 Nanocrystals, Journal of Crystal Growth - J CRYST GROWTH, 247 (2003) 505-508.

[134] Q. Guo, Y. Xie, X. Wang, S. Lv, T. Hou, X. Liu, Characterization of Well-Crystallized Graphitic Carbon Nitride Nanocrystallites via a Benzene-Thermal Route at Low Temperatures, Chemical Physics Letters, 380 (2003) 84-87.

[135] Q. Guo, Y. Xie, X. Wang, S. Zhang, T. Hou, S. Lv, Synthesis of Carbon Nitride Nanotubes With the C_3N_4 Stoichiometry via a Benzene-Thermal Process at Low Temperatures, Chemical Communications, (2004) 26-27.

[136] Y. Cui, Z. Ding, X. Fu, X. Wang, Construction of Conjugated Carbon Nitride Nanoarchitectures in Solution at Low Temperatures for Photoredox Catalysis, Angew. Chem., Int. Ed., 51 (2012) 11814-11818.

[137] Q. Gu, Y. Liao, L. Yin, J. Long, X. Wang, C. Xue, Template-Free Synthesis of Porous Graphitic Carbon Nitride Microspheres for Enhanced Photocatalytic Hydrogen Generation With High Stability, Appl. Catal., B, 165 (2015) 503-510.

[138] S.V. Volkov, Chemical Reactions in Molten Salts and Their Classification, Chemical Society Reviews, 19 (1990) 21-28.

[139] D.H. Kerridge, Recent Advances in Molten Salts as Reaction Media, Pure and Applied Chemistry, 41 (1975) 355-371.

[140] J.L. Sudworth, The Sodium/Nickel Chloride (ZEBRA) Battery, J. Power Sources, 100 (2001) 149-163.

[141] G.Z. Chen, D.J. Fray, T.W. Farthing, Direct Electrochemical Reduction of Titanium Dioxide to Titanium in Molten Calcium Chloride, Nature, 407 (2000) 361-364.

[142] T. Nohira, K. Yasuda, Y. Ito, Pinpoint and Bulk Electrochemical Reduction of Insulating Silicon Dioxide to Silicon, Nature Materials, 2 (2003) 397-401.

[143] M.J. Bojdys, J.O. Muller, M. Antonietti, A. Thomas, Ionothermal Synthesis of Crystalline, Condensed, Graphitic Carbon Nitride, Chem. - Eur. J., 14 (2008) 8177-8182.

[144] J. Zhao, L. Ma, H. Wang, Y. Zhao, J. Zhang, S. Hu, Novel band gap-tunable K-Na co-doped graphitic carbon nitride prepared by molten salt method, Appl. Surf. Sci., 332 (2015) 625-630.

[145] M.K. Bhunia, S. Melissen, M.R. Parida, P. Sarawade, J.-M. Basset, D.H. Anjum, O.F. Mohammed, P. Sautet, T. Le Bahers, K. Takanabe, Dendritic Tip-on Polytriazine-Based Carbon Nitride Photocatalyst with High Hydrogen Evolution Activity, Chem. Mater., 27 (2015) 8237-8247.

[146] F. Li, Y. Xue, B. Li, Y. Hao, X. Wang, R. Liu, J. Zhao, Precipitation Synthesis of Mesoporous Photoactive Al_2O_3 for Constructing g-C_3N_4-Based Heterojunctions with Enhanced Photocatalytic Activity, Ind. Eng. Chem. Res., 53 (2014) 19540-19549.

[147] D. Dontsova, S. Pronkin, M. Wehle, Z. Chen, C. Fettkenhauer, G. Clavel, M. Antonietti, Triazoles: A New Class of Precursors for the Synthesis of Negatively Charged Carbon Nitride Derivatives, Chem. Mater., 27 (2015) 5170-5179.

[148] D. Dontsova, C. Fettkenhauer, V. Papaefthimiou, J. Schmidt, M. Antonietti, 1,2,4-Triazole-Based Approach to Noble-Metal-Free Visible-Light Driven Water Splitting over Carbon Nitrides, Chem. Mater., 28 (2016) 772-778.

[149] S. Hu, X. Qu, J. Bai, P. Li, Q. Li, F. Wang, L. Song, Effect of Cu(I)-N Active Sites on the N_2 Photofixation Ability over Flowerlike Copper-Doped g-C_3N_4 Prepared via a Novel Molten Salt-Assisted Microwave Process: The Experimental and Density Functional Theory Simulation Analysis, ACS Sustainable Chemistry & Engineering, 5 (2017) 6863-6872.

[150] N. Li, J. Zhou, Z. Sheng, W. Xiao, Molten Salt-Mediated Formation of g-C_3N_4-MoS_2 for Visible-Light-Driven Photocatalytic Hydrogen Evolution, Appl. Surf. Sci., 430 (2018) 218-224.

[151] G. Zhang, G. Li, Z.-A. Lan, L. Lin, A. Savateev, T. Heil, S. Zafeiratos, X. Wang, M. Antonietti, Optimizing Optical Absorption, Exciton Dissociation, and Charge Transfer of a Polymeric Carbon Nitride with Ultrahigh Solar Hydrogen Production Activity, Angew. Chem., Int. Ed., 56 (2017) 13445-13449.

[152] L. Lin, W. Ren, C. Wang, A.M. Asiri, J. Zhang, X. Wang, Crystalline carbon nitride semiconductors prepared at different temperatures for photocatalytic hydrogen production, Appl. Catal., B, 231 (2018) 234-241.

[153] L.H. Lin, H.H. Ou, Y.F. Zhang, X.C. Wang, Tri-s-triazine-Based Crystalline Graphitic Carbon Nitrides for Highly Efficient Hydrogen Evolution Photocatalysis, ACS Catal., 6 (2016) 3921-3931.

[154] J. Liu, W. Fang, Z. Wei, Z. Qin, Z. Jiang, W. Shangguan, Efficient Photocatalytic Hydrogen Evolution on N-Deficient g-C_3N_4 Achieved by a Molten Salt Post-Treatment Approach, Appl. Catal., B, 238 (2018) 465-470.

[155] F. Dong, Z. Ni, P. Li, Z. Wu, A General Method for Type I and Type II g-C_3N_4/g-C_3N_4 Metal-Free Isotype Heterostructures With Enhanced Visible Light Photocatalysis, New Journal of Chemistry, 39 (2015) 4737-4744.

[156] R. Hao, G. Wang, C. Jiang, H. Tang, Q. Xu, In Situ Hydrothermal Synthesis of g-C_3N_4/TiO_2 Heterojunction Photocatalysts With High Specific Surface Area for Rhodamine B Degradation, Appl. Surf. Sci., 411 (2017) 400-410.

[157] Z. Wei, F. Liang, Y. Liu, W. Luo, J. Wang, W. Yao, Y. Zhu, Photoelectrocatalytic Degradation of Phenol-Containing Wastewater by TiO_2/C_3N_4 Hybrid Heterostructure Thin Film, Appl. Catal., B, 201 (2017) 600-606.

[158] H. Wang, Y. Liang, L. Liu, J. Hu, W. Cui, Highly Ordered TiO_2 Nanotube Arrays Wrapped with g-C_3N_4 Nanoparticles for Efficient Charge Separation and Increased Photoelectrocatalytic Degradation of Phenol, J Hazard Mater, 344 (2018) 369-380.

[159] Y. Wang, W. Yang, X. Chen, J. Wang, Y. Zhu, Photocatalytic Activity Enhancement of Core-Shell Structure g-C_3N_4@TiO_2 via Controlled Ultrathin g-C_3N_4 Layer, Appl. Catal., B, 220 (2018) 337-347.

[160] Y. Wang, R. Shi, J. Lin, Y. Zhu, Enhancement of Photocurrent and Photocatalytic Activity of Zno Hybridized With Graphite-Like C_3N_4, Energy & Environmental Science, 4 (2011).

[161] E. Jang, D.W. Kim, S.H. Hong, Y.M. Park, T.J. Park, Visible Light-driven g-C_3N_4@ZnO Heterojunction Photocatalyst Synthesized via Atomic Layer Deposition With a Specially Designed Rotary Reactor, Appl. Surf. Sci., 487 (2019) 206-210.

[162] J. Wang, Z. Yang, X. Gao, W. Yao, W. Wei, X. Chen, R. Zong, Y. Zhu, Core-shell g-C_3N_4@ZnO Composites as Photoanodes With Double Synergistic Effects for Enhanced Visible-Light Photoelectrocatalytic Activities, Appl. Catal., B, 217 (2017) 169-180.

[163] R. Guan, J. Li, J. Zhang, Z. Zhao, D. Wang, H. Zhai, D. Sun, Photocatalytic Performance and Mechanistic Research of ZnO/g-C_3N_4 on Degradation of Methyl Orange, ACS Omega, 4 (2019) 20742-20747.

[164] H. Jung, T.-T. Pham, E.W. Shin, Effect of g-C_3N_4 Precursors on the Morphological Structures of g-C_3N_4/ZnO Composite Photocatalysts, J. Alloys Compd., 788 (2019) 1084-1092.

[165] J. Wang, Y. Xia, H. Zhao, G. Wang, L. Xiang, J. Xu, S. Komarneni, Oxygen Defects-Mediated Z-Scheme Charge Separation in g-C_3N_4/ZnO Photocatalysts for Enhanced Visible-Light Degradation of 4-Chlorophenol and Hydrogen Evolution, Appl. Catal., B, 206 (2017) 406-416.

[166] J. Wen, J. Xie, X. Chen, X. Li, A Review on g-C_3N_4-based Photocatalysts, Appl. Surf. Sci., 391 (2017) 72-123.

[167] Y. Liu, H. Zhang, J. Ke, J. Zhang, W. Tian, X. Xu, X. Duan, H. Sun, M. O Tade, S. Wang, 0D (MoS_2)/2D (g-C_3N_4) Heterojunctions in Z-Scheme for Enhanced Photocatalytic and Electrochemical Hydrogen Evolution, Appl. Catal., B, 228 (2018) 64-74.

[168] J.-W. Shi, Y. Zou, L. Cheng, D. Ma, D. Sun, S. Mao, L. Sun, C. He, Z. Wang, In-situ Phosphating to Synthesize Ni2P Decorated NiO/g-C_3N_4 p-n Junction for Enhanced Photocatalytic Hydrogen Production, Chem. Eng. J., 378 (2019).

[169] F. Guo, W. Shi, H. Wang, M. Han, H. Li, H. Huang, Y. Liu, Z. Kang, Facile Fabrication of a CoO/g-C_3N_4 p-n Heterojunction With Enhanced Photocatalytic Activity and Stability for Tetracycline Degradation Under Visible Light, Catalysis Science & Technology, 7 (2017) 3325-3331.

[170] L. Yang, J. Liu, L. Yang, M. Zhang, H. Zhu, F. Wang, J. Yin, Co3O4 Imbedded g-C_3N_4 Heterojunction Photocatalysts for Visible-Light-Driven Hydrogen Evolution, Renewable Energy, 145 (2020) 691-698.

[171] S. Liang, D. Zhang, X. Pu, X. Yao, R. Han, J. Yin, X. Ren, A Novel Ag_2O/g-C_3N_4 p-n Heterojunction Photocatalysts With Enhanced Visible and Near-Infrared Light Activity, Sep. Purif. Technol., 210 (2019) 786-797.

[172] P.J. Mafa, A.T. Kuvarega, B.B. Mamba, B. Ntsendwana, Photoelectrocatalytic Degradation of Sulfamethoxazole On g-C_3N_4/BiOI/EG p-n Heterojunction Photoanode Under Visible Light Irradiation, Appl. Surf. Sci., 483 (2019) 506-520.

[173] W. Chang, W. Xue, E. Liu, J. Fan, B. Zhao, Highly Efficient H_2 Production over $NiCo_2O_4$ Decorated g-C_3N_4 by Photocatalytic Water Reduction, Chem. Eng. J., 362 (2019) 392-401.

[174] G. Fan, B. Du, J. Zhou, W. Yu, Z. Chen, S. Yang, Stable Ag_2O/g-C_3N_4 p-n Heterojunction Photocatalysts for Efficient Inactivation of Harmful Algae Under Visible Light, Appl. Catal., B, 265 (2020).

[175] M. Makaremi, S. Grixti, K.T. Butler, G.A. Ozin, C.V. Singh, Band Engineering of Carbon Nitride Monolayers by N-Type, P-Type, and Isoelectronic Doping for Photocatalytic Applications, ACS Appl. Mater. Interfaces, 10 (2018) 11143-11151.

[176] J. Luo, G. Dong, Y. Zhu, Z. Yang, C. Wang, Switching of Semiconducting Behavior From N-Type to P-Type Induced High Photocatalytic No Removal Activity in g-C_3N_4, Appl. Catal., B, 214 (2017) 46-56.

[177] J. Jing, Z. Chen, C. Feng, Dramatically Enhanced Photoelectrochemical Properties and Transformed p/n Type of g-C_3N_4 Caused by K and I Co-doping, Electrochimica Acta, 297 (2019) 488-496.

[178] N. Sagara, S. Kamimura, T. Tsubota, T. Ohno, Photoelectrochemical CO_2 Reduction by a P-Type Boron-Doped G-C_3N_4 Electrode Under Visible Light, Appl. Catal., B, 192 (2016) 193-198.

[179] Z. Ai, Y. Shao, B. Chang, L. Zhang, J. Shen, Y. Wu, B. Huang, X. Hao, Rational Modulation of p-n Homojunction in P-Doped g-C_3N_4 Decorated With Ti3C2 for Photocatalytic Overall Water Splitting, Appl. Catal., B, 259 (2019).

[180] W. Guo, J. Zhang, G. Li, C. Xu, Enhanced Photocatalytic Activity of P-type (K, Fe) Co-doped g-C_3N_4 Synthesized in Self-generated NH_3 Atmosphere, Appl. Surf. Sci., 470 (2019) 99-106.

[181] S. Li, G. Dong, R. Hailili, L. Yang, Y. Li, F. Wang, Y. Zeng, C. Wang, Effective photocatalytic H_2O_2 production under visible light irradiation at g-C_3N_4 modulated by carbon vacancies, Appl. Catal., B, 190 (2016) 26-35.

[182] J. Cao, C. Pan, Y. Ding, W. Li, K. Lv, H. Tang, Constructing Nitrogen Vacancy Introduced g-C_3N_4 p-n Homojunction for Enhanced Photocatalytic Activity, Journal of Environmental Chemical Engineering, 7 (2019).

[183] G. Liu, G. Zhao, W. Zhou, Y. Liu, H. Pang, H. Zhang, D. Hao, X. Meng, P. Li, T. Kako, J. Ye, In Situ Bond Modulation of Graphitic Carbon Nitride to Construct p-n Homojunctions for Enhanced Photocatalytic Hydrogen Production, Adv. Funct. Mater., 26 (2016) 6822-6829.

[184] S. Hua, D. Qu, L. An, W. Jiang, Y. Wen, X. Wang, Z. Sun, Highly Efficient p-type Cu_3P/n-type g-C_3N_4 Photocatalyst Through Z-Scheme Charge Transfer Route, Appl. Catal., B, 240 (2019) 253-261.

[185] H. Katsumata, T. Sakai, T. Suzuki, S. Kaneco, Highly Efficient Photocatalytic Activity of g-C_3N_4/Ag_3PO_4 Hybrid Photocatalysts through Z-Scheme Photocatalytic Mechanism under Visible Light, Ind. Eng. Chem. Res., 53 (2014) 8018-8025.

[186] Y. Wu, H. Wang, W. Tu, Y. Liu, Y.Z. Tan, X. Yuan, J.W. Chew, Quasi-Polymeric Construction of Stable Perovskite-Type $LaFeO_3$/g-C_3N_4 Heterostructured Photocatalyst for Improved Z-Scheme Photocatalytic Activity via Solid P-N Heterojunction Interfacial Effect, J Hazard Mater, 347 (2018) 412-422.

[187] J. Yang, D. Wang, H. Han, C. Li, Roles of Cocatalysts in Photocatalysis and Photoelectrocatalysis, Accounts of Chemical Research, 46 (2013) 1900-1909.

[188] L. Wang, C. Wang, X. Hu, H. Xue, H. Pang, Metal/Graphitic Carbon Nitride Composites: Synthesis, Structures, and Applications, Chemistry – An Asian Journal, 11 (2016) 3305-3328.

[189] Y. Shiraishi, Y. Kofuji, S. Kanazawa, H. Sakamoto, S. Ichikawa, S. Tanaka, T. Hirai, Platinum Nanoparticles Strongly Associated With Graphitic Carbon Nitride as Efficient Co-Catalysts for Photocatalytic Hydrogen Evolution Under Visible Light, Chemical Communications, 50 (2014) 15255-15258.

[190] S. Cao, J. Jiang, B. Zhu, J. Yu, Shape-Dependent Photocatalytic Hydrogen Evolution Activity Over a Pt Nanoparticle Coupled g-C_3N_4 Photocatalyst, Phys. Chem. Chem. Phys., 18 (2016) 19457-19463.

[191] Z. Yin, Y. Tian, P. Gao, L. Feng, Y. Liu, Z. Du, L. Zhang, Photodegradation Mechanism and Genetic Toxicity of Bezafibrate by Pd/g-C_3N_4 Catalysts Under Simulated Solar Light Irradiation: The Role of Active Species, Chem. Eng. J., 379 (2020).

[192] K. Gu, X. Pan, W. Wang, J. Ma, Y. Sun, H. Yang, H. Shen, Z. Huang, H. Liu, In Situ Growth of Pd Nanosheets on g-C_3N_4 Nanosheets with Well-Contacted Interface and Enhanced Catalytic Performance for 4-Nitrophenol Reduction, Small, (2018) e1801812.

[193] R. Kuriki, K. Sekizawa, O. Ishitani, K. Maeda, Visible-Light-Driven CO_2 Reduction With Carbon Nitride: Enhancing the Activity of Ruthenium Catalysts, Angew. Chem., Int. Ed., 54 (2015) 2406-2409.

[194] W. Zhang, Z. Zhang, S. Kwon, Z. Fuchun, S. Boandoh, K. Kim, R. Jung, S. Kwon, K.-B. Chung, W. Yang, Photocatalytic Improvement of Mn-adsorbed g-C_3N_4, Appl. Catal., B, 206 (2017).

[195] L. Bi, D. Xu, L. Zhang, Y. Lin, D. Wang, T. Xie, Metal Ni-loaded g-C_3N_4 for Enhanced Photocatalytic H_2 Evolution Activity: The Change in Surface Band Bending, Phys. Chem. Chem. Phys., 17 (2015) 29899-29905.

[196] L. Kong, Y. Dong, P. Jiang, G. Wang, H. Zhang, N. Zhao, Light-assisted Rapid Preparation of a Ni/g-C_3N_4 Magnetic Composite for Robust Photocatalytic H_2 Evolution From Water, J. Mater. Chem. A, 4 (2016) 9998-10007.

[197] W. Liu, Y. Li, F. Liu, W. Jiang, D. Zhang, J. Liang, Visible-Light-Driven Photocatalytic Degradation of Diclofenac by Carbon Quantum Dots Modified Porous g-C_3N_4: Mechanisms, Degradation Pathway and DFT Calculation, Water Res, 151 (2019) 8-19.

[198] Y. Yang, C. Zhang, D. Huang, G. Zeng, J. Huang, C. Lai, C. Zhou, W. Wang, H. Guo, W. Xue, R. Deng, M. Cheng, W. Xiong, Boron Nitride Quantum Dots Decorated Ultrathin Porous g-C_3N_4: Intensified Exciton Dissociation and Charge Transfer for Promoting Visible-Light-Driven Molecular Oxygen Activation, Appl. Catal., B, 245 (2019) 87-99.

[199] Z. Huang, J. Song, L. Pan, Z. Wang, X. Zhang, J. Zou, W. Mi, X. Zhang, L. Wang, Carbon Nitride With Simultaneous Porous Network and O-Doping for Efficient Solar-Energy-Driven Hydrogen Evolution, Nano Energy, 12 (2015) 646-656.

[200] J. Liu, W. Li, L. Duan, X. Li, L. Ji, Z. Geng, K. Huang, L. Lu, L. Zhou, Z. Liu, W. Chen, L. Liu, S. Feng, Y. Zhang, A Graphene-like Oxygenated Carbon Nitride Material for Improved Cycle-Life Lithium/Sulfur Batteries, Nano Letters, 15 (2015) 5137-5142.

[201] Y. Bu, Z. Chen, Effect of Oxygen-doped C_3N_4 on the Separation Capability of the Photoinduced Electron-Hole Pairs Generated by O-C_3N_4@TiO_2 With Quasi-Shell-Core Nanostructure, Electrochimica Acta, 144 (2014) 42-49.

[202] X. She, L. Liu, H. Ji, Z. Mo, Y. Li, L. Huang, D. Du, H. Xu, H. Li, Template-Free Synthesis of 2D Porous Ultrathin Nonmetal-Doped g-C_3N_4 Nanosheets With Highly Efficient Photocatalytic H_2 Evolution From Water Under Visible Light, Appl. Catal., B, 187 (2016) 144-153.

[203] Z. Zhao, Y. Sun, F. Dong, Y. Zhang, H. Zhao, Template Synthesis of Carbon Self-Doped g-C_3N_4 With Enhanced Visible to Near-Infrared Absorption and Photocatalytic Performance, RSC Adv., 5 (2015) 39549-39556.

[204] P. Zhang, X. Li, C. Shao, Y. Liu, Hydrothermal Synthesis of Carbon-Rich Graphitic Carbon Nitride Nanosheets for Photoredox Catalysis, J. Mater. Chem. A, 3 (2015) 3281-3284.

[205] Y. Zhou, L. Zhang, W. Huang, Q. Kong, X. Fan, M. Wang, J. Shi, N-Doped Graphitic Carbon-Incorporated g-C_3N_4 for Remarkably Enhanced Photocatalytic H_2 Evolution Under Visible Light, Carbon, 99 (2016) 111-117.

[206] G. Liu, P. Niu, C. Sun, S.C. Smith, Z. Chen, G.Q. Lu, H.-M. Cheng, Unique Electronic Structure Induced High Photoreactivity of Sulfur-Doped Graphitic C_3N_4, Journal of the American Chemical Society, 132 (2010) 11642-11648.

[207] J. Hong, X. Xia, Y. Wang, R. Xu, Mesoporous Carbon Nitride With in Situ Sulfur Doping for Enhanced Photocatalytic Hydrogen Evolution From Water Under Visible Light, J. Mater. Chem., 22 (2012) 15006-15012.

[208] K. Wang, Q. Li, B. Liu, B. Cheng, W. Ho, J. Yu, Sulfur-doped g-C_3N_4 with Enhanced Photocatalytic CO_2-reduction Performance, Appl. Catal., B, 176-177 (2015) 44-52.

[209] Y. Zhou, L. Zhang, J. Liu, X. Fan, B. Wang, M. Wang, W. Ren, J. Wang, M. Li, J. Shi, Brand New P-Doped g-C_3N_4: Enhanced Photocatalytic Activity for H_2 Evolution and Rhodamine B Degradation Under Visible Light, J. Mater. Chem. A, 3 (2015) 3862-3867.

[210] S. Hu, L. Ma, J. You, F. Li, Z. Fan, F. Wang, D. Liu, J. Gui, A Simple and Efficient Method to Prepare a Phosphorus Modified g-C_3N_4 Visible Light Photocatalyst, RSC Adv., 4 (2014) 21657-21663.

[211] Y. Zhu, T. Ren, Z. Yuan, Mesoporous Phosphorus-Doped g-C_3N_4 Nanostructured Flowers with Superior Photocatalytic Hydrogen Evolution Performance, ACS Appl. Mater. Interfaces, 7 (2015) 16850-16856.

[212] Z.-A. Lan, G. Zhang, X. Wang, A Facile Synthesis of Br-Modified g-C_3N_4 Semiconductors for Photoredox Water Splitting, Appl. Catal., B, 192 (2016) 116-125.

[213] X. Wang, X. Chen, A. Thomas, X. Fu, M. Antonietti, Metal-Containing Carbon Nitride Compounds: A New Functional Organic-Metal Hybrid Material, Adv. Mater., 21 (2009) 1609-1612.

[214] L. Gao, T. Wen, J. Xu, X. Zhai, M. Zhao, G. Hu, P. Chen, Q. Wang, H. Zhang, Iron-Doped Carbon Nitride-Type Polymers as Homogeneous Organocatalysts for Visible Light-Driven Hydrogen Evolution, ACS Appl. Mater. Interfaces, 8 (2016) 617-624.

[215] B. Yue, Q. Li, H. Iwai, T. Kako, J. Ye, Hydrogen Production Using Zinc-Doped Carbon Nitride Catalyst Irradiated With Visible Light, Sci. Technol. Adv. Mater., 12 (2011) 034401.

[216] Z. Ding, X. Chen, M. Antonietti, X. Wang, Synthesis of Transition Metal-Modified Carbon Nitride Polymers for Selective Hydrocarbon Oxidation, ChemSusChem, 4 (2011) 274-281.

[217] S. Hu, R. Jin, G. Lu, D. Liu, J. Gui, The Properties and Photocatalytic Performance Comparison of Fe^{3+}-doped g-C_3N_4 and Fe_2O_3/g-C_3N_4 Composite Catalysts, RSC Adv., 4 (2014) 24863-24869.

[218] S. Tonda, S. Kumar, S. Kandula, V. Shanker, Fe-Doped and -Mediated Graphitic Carbon Nitride Nanosheets for Enhanced Photocatalytic Performance Under Natural Sunlight, J. Mater. Chem. A, 2 (2014) 6772-6780.

[219] G. Ding, W. Wang, T. Jiang, B. Han, H. Fan, G. Yang, Highly Selective Synthesis of Phenol from Benzene over a Vanadium-Doped Graphitic Carbon Nitride Catalyst, ChemCatChem, 5 (2013) 192-200.

[220] H. Gao, S. Yan, J. Wang, Z. Zou, Ion Coordination Significantly Enhances the Photocatalytic Activity of Graphitic-Phase Carbon Nitride, Dalton Transactions, 43 (2014) 8178-8183.

[221] J. Zhang, S. Hu, Y. Wang, A Convenient Method to Prepare a Novel Alkali Metal Sodium Doped Carbon Nitride Photocatalyst With a Tunable Band Structure, RSC Adv., 4 (2014) 62912-62919.

[222] S. Hu, F. Li, Z. Fan, F. Wang, Y. Zhao, Z. Lv, Band Gap-Tunable Potassium Doped Graphitic Carbon Nitride With Enhanced Mineralization Ability, Dalton Transactions, 44 (2015) 1084-1092.

[223] T. Xiong, W. Cen, Y. Zhang, F. Dong, Bridging the g-C_3N_4 Interlayers for Enhanced Photocatalysis, ACS Catal., 6 (2016) 2462-2472.

[224] S. Hu, L. Ma, J. You, F. Li, Z. Fan, G. Lu, D. Liu, J. Gui, Enhanced Visible Light Photocatalytic Performance of g-C_3N_4 Photocatalysts Co-Doped With IRON and Phosphorus, Appl. Surf. Sci., 311 (2014) 164-171.

[225] S. Zhang, J. Li, M. Zeng, J. Li, J. Xu, X. Wang, Bandgap Engineering and Mechanism Study of Nonmetal and Metal Ion Codoped Carbon Nitride: C+Fe as an Example, Chem. - Eur. J., 20 (2014) 9805-9812.

[226] Y. Guo, T. Chen, Q. Liu, Z. Zhang, X. Fang, Insight into the Enhanced Photocatalytic Activity of Potassium and Iodine Codoped Graphitic Carbon Nitride Photocatalysts, J. Phys. Chem. C, 120 (2016) 25328-25337.

[227] P. Niu, G. Liu, H.-M. Cheng, Nitrogen Vacancy-Promoted Photocatalytic Activity of Graphitic Carbon Nitride, J. Phys. Chem. C, 116 (2012) 11013-11018.

[228] P. Niu, L.C. Yin, Y.Q. Yang, G. Liu, H.M. Cheng, Increasing the Visible Light Absorption of Graphitic Carbon Nitride (Melon) Photocatalysts by Homogeneous Self-Modification With Nitrogen Vacancies, Adv. Mater., 26 (2014) 8046-8052.

[229] Q. Tay, P. Kanhere, C.F. Ng, S. Chen, S. Chakraborty, A.C.H. Huan, T.C. Sum, R. Ahuja, Z. Chen, Defect Engineered g-C_3N_4 for Efficient Visible Light Photocatalytic Hydrogen Production, Chem. Mater., 27 (2015) 4930-4933.

[230] X. Li, J. Zhang, F. Zhou, H. Zhang, J. Bai, Y. Wang, H. Wang, Preparation of N-vacancy-doped g-C_3N_4 With Outstanding Photocatalytic H_2O_2 Production Ability by Dielectric Barrier Discharge Plasma Treatment, Chin. J. Catal., 39 (2018) 1090-1098.

[231] Z. Wang, Y. Huang, M. Chen, X. Shi, Y. Zhang, J. Cao, W. Ho, S.C. Lee, Roles of N-Vacancies over Porous g-C_3N_4 Microtubes during Photocatalytic NO x Removal, ACS Appl. Mater. Interfaces, 11 (2019) 10651-10662.

[232] H. Lan, L. Li, X. An, F. Liu, C. Chen, H. Liu, J. Qu, Microstructure of Carbon Nitride Affecting Synergetic Photocatalytic Activity: Hydrogen Bonds vs. Structural Defects, Appl. Catal., B, 204 (2017) 49-57.

[233] Y. Li, W. Ho, K. Lv, B. Zhu, S.C. Lee, Carbon Vacancy-Induced Enhancement of the Visible Light-Driven Photocatalytic Oxidation of NO over g-C_3N_4 nanosheets, Appl. Surf. Sci., 430 (2018) 380-389.

[234] G. Dong, D.L. Jacobs, L. Zang, C. Wang, Carbon Vacancy Regulated Photoreduction Of NO to N_2 over Ultrathin g-C_3N_4 Nanosheets, Appl. Catal., B, 218 (2017) 515-524.

[235] F. Ling, W. Li, L. Ye, The Synergistic Effect of Non-Metal Doping or Defect Engineering and Interface Coupling on the Photocatalytic Property of g-C_3N_4: First-principle Investigations, Appl. Surf. Sci., 473 (2019) 386-392.

[236] C. Ren, Y. Zhang, Y. Li, Y. Zhang, S. Huang, W. Lin, K. Ding, Whether Corrugated or Planar Vacancy Graphene-like Carbon Nitride (g-C_3N_4) Is More Effective for Nitrogen Reduction Reaction?, J. Phys. Chem. C, 123 (2019) 17296-17305.

[237] M. Groenewolt, M. Antonietti, Synthesis of g-C_3N_4 Nanoparticles in Mesoporous Silica Host Matrices, Adv. Mater., 17 (2005) 1789-1792.

[238] A. Vinu, K. Ariga, T. Mori, Y. Shen, S. Hishita, D. Golberg, Y. Bando, Preparation and Characterization of Well-Ordered Hexagonal Mesoporous Carbon Nitride, Adv. Mater., 17 (2005) 1648-1652.

[239] F. Goettmann, A. Fischer, M. Antonietti, A. Thomas, Chemical Synthesis of Mesoporous Carbon Nitrides Using Hard Templates and Their Use as a Metal-Free Catalyst for Friedel-Crafts Reaction of Benzene, Angew. Chem., Int. Ed., 45 (2006) 4467-4471.

[240] J. Sun, J. Zhang, M. Zhang, M. Antonietti, X. Fu, X. Wang, Bioinspired Hollow Semiconductor Nanospheres as Photosynthetic Nanoparticles, Nature Communications, 3 (2012) 1139.

[241] F. Xiao, J. Miao, H.B. Tao, S. Hung, H. Wang, H.B. Yang, J. Chen, R. Chen, B. Liu, One-Dimensional Hybrid Nanostructures for Heterogeneous Photocatalysis and Photoelectrocatalysis, Small, 11 (2015) 2115-2131.

[242] B. Weng, S. Liu, Z. Tang, Y. Xu, One-Dimensional Nanostructure Based Materials for Versatile Photocatalytic Applications, RSC Adv., 4 (2014) 12685-12700.

[243] J. Tian, Z. Zhao, A. Kumar, R.I. Boughton, H. Liu, Recent Progress in Design, Synthesis, and Applications of One-Dimensional TiO_2 Nanostructured Surface Heterostructures: A Review, Chemical Society Reviews, 43 (2014) 6920-6937.

[244] X. Li, X. Wang, M. Antonietti, Mesoporous g-C_3N_4 Nanorods as Multifunctional Supports of Ultrafine Metal Nanoparticles: Hydrogen Generation From Water and Reduction of Nitrophenol With Tandem Catalysis in One Step, Chemical Science, 3 (2012) 2170-2174.

[245] X.F. Chen, Y.S. Jun, K. Takanabe, K. Maeda, K. Domen, X.Z. Fu, M. Antonietti, X.C. Wang, Ordered Mesoporous SBA-15 Type Graphitic Carbon Nitride: A Semiconductor Host Structure for Photocatalytic Hydrogen Evolution with Visible Light, Chem. Mater., 21 (2009) 4093-4095.

[246] Z. Huang, F. Li, B. Chen, T. Lu, Y. Yuan, G. Yuan, Well-dispersed g-C_3N_4 Nanophases in Mesoporous Silica Channels and Their Catalytic Activity for Carbon Dioxide Activation and Conversion, Appl. Catal., B, 136-137 (2013) 269-277.

[247] A. Fihri, M. Bouhrara, U. Patil, D. Cha, Y. Saih, V. Polshettiwar, Fibrous Nano-Silica Supported Ruthenium (KCC-1/Ru): A Sustainable Catalyst for the Hydrogenolysis of Alkanes with Good Catalytic Activity and Lifetime, ACS Catal., 2 (2012) 1425-1431.

[248] M. Dhiman, B. Chalke, V. Polshettiwar, Efficient Synthesis of Monodisperse Metal (Rh, Ru, Pd) Nanoparticles Supported on Fibrous Nanosilica (KCC-1) for Catalysis, ACS Sustainable Chemistry & Engineering, 3 (2015) 3224-3230.

[249] J. Wang, C. Zhang, Y. Shen, Z. Zhou, J. Yu, Y. Li, W. Wei, S. Liu, Y. Zhang, Environment-Friendly Preparation of Porous Graphite-Phase Polymeric Carbon Nitride Using Calcium Carbonate as Templates, and Enhanced Photoelectrochemical Activity, J. Mater. Chem. A, 3 (2015) 5126-5131.

[250] Y. Wang, X. Wang, M. Antonietti, Y. Zhang, Facile One-Pot Synthesis of Nanoporous Carbon Nitride Solids by Using Soft Templates, ChemSusChem, 3 (2010) 435-439.

[251] H. Yan, Soft-Templating Synthesis of Mesoporous Graphitic Carbon Nitride With Enhanced Photocatalytic H_2 Evolution Under Visible Ligh, Chemical Communications, 48 (2012) 3430-3432.

[252] W. Wang, J.C. Yu, Z. Shen, D.K.L. Chan, T. Gu, g-C_3N_4 Quantum Dots: Direct Synthesis, Upconversion Properties and Photocatalytic Application, Chemical Communications, 50 (2014) 10148-10150.

[253] M. Tahir, C. Cao, N. Mahmood, F.K. Butt, A. Mahmood, F. Idrees, S. Hussain, M. Tanveer, Z. Ali, I. Aslam, Multifunctional g-C_3N_4 Nanofibers: A Template-Free Fabrication and Enhanced Optical, Electrochemical, and Photocatalyst Properties, ACS Appl. Mater. Interfaces, 6 (2014) 1258-1265.

[254] M. Tahir, C. Cao, F.K. Butt, F. Idrees, N. Mahmood, Z. Ali, I. Aslam, M. Tanveer, M. Rizwan, T. Mahmood, Tubular Graphitic-C_3N_4: A Prospective Material for Energy Storage and Green Photocatalysis, J. Mater. Chem. A, 1 (2013) 13949-13955.

[255] M. Tahir, C. Cao, F.K. Butt, S. Butt, F. Idrees, Z. Ali, I. Aslam, M. Tanveer, A. Mahmood, N. Mahmood, Large Scale Production of Novel g-C_3N_4 Micro Strings With High Surface Area and Versatile Photodegradation Ability, CrystEngComm, 16 (2014) 1825-1830.

[256] S. Wang, C. Li, T. Wang, P. Zhang, A. Li, J. Gong, Controllable Synthesis of Nanotube-Type Graphitic C_3N_4 and Their Visible-Light Photocatalytic and Fluorescent Properties, J. Mater. Chem. A, 2 (2014).

[257] J. Xu, L. Zhang, R. Shi, Y. Zhu, Chemical Exfoliation of Graphitic Carbon Nitride for Efficient Heterogeneous Photocatalysis, J. Mater. Chem. A, 1 (2013).

[258] Q. Lin, L. Li, S. Liang, M. Liu, J. Bi, L. Wu, Efficient Synthesis of Monolayer Carbon Nitride 2D Nanosheet With Tunable Concentration and Enhanced Visible-Light Photocatalytic Activities, Appl. Catal., B, 163 (2015) 135-142.

[259] T. Sano, S. Tsutsui, K. Koike, T. Hirakawa, Y. Teramoto, N. Negishi, K. Takeuchi, Activation of Graphitic Carbon Nitride (g-C_3N_4) by Alkaline Hydrothermal Treatment for Photocatalytic NOOxidation in Gas Phase, J. Mater. Chem. A, 1 (2013) 6489-6496.

[260] W. Ong, L. Tan, S. Chai, S. Yong, A.R. Mohamed, Facet-Dependent Photocatalytic Properties of TiO_2-Based Composites for Energy Conversion and Environmental Remediation, ChemSusChem, 7 (2014) 690-719.

[261] H. Zollinger, Color Chemistry: Syntheses, Properties, and Applications of Organic Dyes and Pigments, WILEY-VCH, New York, 2003.

[262] A.S. Özen, V. Aviyente, R.A. Klein, Modeling the Oxidative Degradation of Azo Dyes: A Density Functional Theory Study, The Journal of Physical Chemistry A, 107 (2003) 4898-4907.

[263] A.S. Özen, V. Aviyente, F. De Proft, P. Geerlings, Modeling the Substituent Effect on the Oxidative Degradation of Azo Dyes, The Journal of Physical Chemistry A, 108 (2004) 5990-6000.

[264] A. Neren Ökte, Ö. Yılmaz, Photodecolorization of Methyl Orange by Yttrium Incorporated TiO_2 Supported ZSM-5, Appl. Catal., B, 85 (2008) 92-102.

[265] S. Xu, Y. Zhu, L. Jiang, Y. Dan, Visible Light Induced Photocatalytic Degradation of Methyl Orange by Polythiophene/TiO_2 Composite Particles, Water, Air, & Soil Pollution, 213 (2010) 151-159.

[266] W. Zhong, T. Jiang, Y. Dang, J. He, S.-Y. Chen, C.-H. Kuo, D. Kriz, Y. Meng, A.G. Meguerdichian, S.L. Suib, Mechanism Studies on Methyl Orange Dye Degradation by Perovskite-Type $LaNiO_3$-δ Under Dark Ambient Conditions, Appl. Catal., A, 549 (2018) 302-309.

[267] C. Xiaoyang, X. Zhiyong, Y. Yanlai, W. Weiping, Z. Fengxiang, H. Chunlai, Oxidation Degradation of Rhodamine B in Aqueous by UV/$S_2O_8^{2-}$ Treatment System, International Journal of Photoenergy, (2012) 1-5.

[268] K. Yu, S. Yang, H. He, C. Sun, C. Gu, Y. Ju, Visible Light-Driven Photocatalytic Degradation of Rhodamine B over $NaBiO_3$: Pathways and Mechanism, The Journal of Physical Chemistry A, 113 (2009) 10024-10032.

[269] T. Rasheed, M. Bilal, H.M.N. Iqbal, S.Z.H. Shah, H. Hu, X. Zhang, Y. Zhou, TiO_2/UV-assisted Rhodamine B Degradation: Putative Pathway and Identification of Intermediates by UPLC/MS, Environmental Technology, 39 (2018) 1533-1543.

[270] S.C. Yan, Z.S. Li, Z.G. Zou, Photodegradation of Rhodamine B and Methyl Orange over Boron-Doped g-C_3N_4 under Visible Light Irradiation, Langmuir, 26 (2010) 3894-3901.

[271] F. Chen, Z. Deng, X. Li, J. Zhang, J. Zhao, Visible Light Detoxification by 2,9,16,23-Tetracarboxyl Phthalocyanine Copper Modified Amorphous Titania, Chemical Physics Letters, 415 (2005) 85-88.

[272] U. Kreibig, M. Vollmer, Optical Properties of Metal Clusters, Springer-Verlag Berlin Heidelberg1995.

[273] K.A. Willets, R.P. Van Duyne, Localized Surface Plasmon Resonance Spectroscopy and Sensing, Annu Rev Phys Chem, 58 (2007) 267-297.

[274] G.V. Hartland, L.V. Besteiro, P. Johns, A.O. Govorov, What's so Hot about Electrons in Metal Nanoparticles?, ACS Energy Lett., 2 (2017) 1641-1653.

[275] Y.C. Zhang, S. He, W. Guo, Y. Hu, J. Huang, J.R. Mulcahy, W.D. Wei, Surface-Plasmon-Driven Hot Electron Photochemistry, Chem. Rev., 118 (2018) 2927-2954.

[276] M.L. Brongersma, N.J. Halas, P. Nordlander, Plasmon-Induced Hot Carrier Science and Technology, Nat Nanotechnol, 10 (2015) 25-34.

[277] A.M. Brown, R. Sundararaman, P. Narang, W.A. Goddard, 3rd, H.A. Atwater, Nonradiative Plasmon Decay and Hot Carrier Dynamics: Effects of Phonons, Surfaces, and Geometry, ACS Nano, 10 (2016) 957-966.

[278] M. Bernardi, J. Mustafa, J.B. Neaton, S.G. Louie, Theory and Computation of Hot Carriers Generated by Surface Plasmon Polaritons in Noble Metals, Nat Commun, 6 (2015) 7044.

[279] M.B. Cortie, A.M. McDonagh, Synthesis and Optical Properties of Hybrid and Alloy Plasmonic Nanoparticles, Chem. Rev., 111 (2011) 3713-3735.

[280] C. Gong, M.S. Leite, Noble Metal Alloys for Plasmonics, ACS Photonics, 3 (2016) 507-513.

[281] E. Dilena, D. Dorfs, C. George, K. Miszta, M. Povia, A. Genovese, A. Casu, M. Prato, L. Manna, Colloidal Cu_{2-x}(SySe1−y) Alloy Nanocrystals With Controllable Crystal Phase: Synthesis, Plasmonic Properties, Cation Exchange and Electrochemical Lithiation, J. Mater. Chem., 22 (2012).

[282] Y. Wang, L. Li, C. An, Y. Wang, C. Chen, L. Jiao, H. Yuan, Facile synthesis of TiN decorated graphene and its enhanced catalytic effects on dehydrogenation performance of magnesium hydride, Nanoscale, 6 (2014) 6684-6691.

[283] S. Liu, G. Chen, P.N. Prasad, M.T. Swihart, Synthesis of Monodisperse Au, Ag, and Au-Ag Alloy Nanoparticles with Tunable Size and Surface Plasmon Resonance Frequency, Chem. Mater., 23 (2011) 4098-4101.

[284] M. Kumar, S. Ishii, N. Umezawa, T. Nagao, Band Engineering of Ternary Metal Nitride System $Ti_{1-x}Zr_xN$ for Plasmonic Applications, Optical Materials Express, 6 (2015).

[285] M. Rycenga, C.M. Cobley, J. Zeng, W. Li, C.H. Moran, Q. Zhang, D. Qin, Y. Xia, Controlling the Synthesis and Assembly of Silver Nanostructures for Plasmonic Applications, Chem. Rev., 111 (2011) 3669-3712.

[286] X. Lu, M. Rycenga, S.E. Skrabalak, B. Wiley, Y. Xia, Chemical Synthesis of Novel Plasmonic Nanoparticles, Annu Rev Phys Chem, 60 (2009) 167-192.

[287] M. Kumar, S. Deka, Multiply Twinned AgNi Alloy Nanoparticles as Highly Active Catalyst for Multiple Reduction and Degradation Reactions, ACS Appl. Mater. Interfaces, 6 (2014) 16071-16081.

[288] S.W. Verbruggen, M. Keulemans, B. Goris, N. Blommaerts, S. Bals, J.A. Martens, S. Lenaerts, Plasmonic 'Rainbow' Photocatalyst With Broadband Solar Light Response for Environmental Applications, Appl. Catal., B, 188 (2016) 147-153.

[289] S. Mukherjee, F. Libisch, N. Large, O. Neumann, L.V. Brown, J. Cheng, J.B. Lassiter, E.A. Carter, P. Nordlander, N.J. Halas, Hot Electrons Do the Impossible: Plasmon-Induced Dissociation of H_2 on Au, Nano Lett, 13 (2013) 240-247.

[290] Z. Bian, T. Tachikawa, P. Zhang, M. Fujitsuka, T. Majima, Au/TiO_2 Superstructure-Based Plasmonic Photocatalysts Exhibiting Efficient Charge Separation and Unprecedented Activity, J. Am. Chem. Soc., 136 (2014) 458-465.

[291] S. Bera, J.E. Lee, S.B. Rawal, W.I. Lee, Size-Dependent Plasmonic Effects of Au and Au@SiO_2 Nanoparticles in Photocatalytic CO_2 Conversion Reaction of Pt/TiO_2, Appl. Catal., B, 199 (2016) 55-63.

[292] A.E. Schlather, A. Manjavacas, A. Lauchner, V.S. Marangoni, C.J. DeSantis, P. Nordlander, N.J. Halas, Hot Hole Photoelectrochemistry on Au@SiO_2@Au Nanoparticles, J Phys Chem Lett, 8 (2017) 2060-2067.

[293] D.M. Fragua, R. Abargues, P.J. Rodriguez-Canto, J.F. Sanchez-Royo, S. Agouram, J.P. Martinez-Pastor, Au-ZnO Nanocomposite Films for Plasmonic Photocatalysis, Advanced Materials Interfaces, 2 (2015).

[294] Y.-G. Lin, Y.-K. Hsu, Y.-C. Chen, S.-B. Wang, J.T. Miller, L.-C. Chen, K.-H. Chen, Plasmonic Ag@$Ag_3(PO_4)_{1-x}$ Nanoparticle Photosensitized ZnO Nanorod-Array Photoanodes for Water Oxidation, Energy & Environmental Science, 5 (2012).

[295] F. Dong, T. Xiong, S. Yan, H. Wang, Y. Sun, Y. Zhang, H. Huang, Z. Wu, Facets and Defects Cooperatively Promote Visible Light Plasmonic Photocatalysis With Bi Nanowires@BiOCl Nanosheets, Journal of Catalysis, 344 (2016) 401-410.

[296] H. Wang, W. Zhang, X. Li, J. Li, W. Cen, Q. Li, F. Dong, Highly Enhanced Visible Light Photocatalysis and in Situ FT-IR Studies on Bi Metal@defective BiOCl Hierarchical Microspheres, Appl. Catal., B, 225 (2018) 218-227.

[297] H. Lin, L. Ding, Z. Pei, Y. Zhou, J. Long, W. Deng, X. Wang, Au Deposited BiOCl with Different Facets: On Determination of the Facet-Induced Transfer Preference of Charge Carriers and the Different Plasmonic Activity, Appl. Catal., B, 160-161 (2014) 98-105.

[298] Y. Ren, Q. Xu, X. Zheng, Y. Fu, Z. Wang, H. Chen, Y. Weng, Y. Zhou, Building of Peculiar Heterostructure of Ag/Two-Dimensional Fullerene Shell-WO_3-X for Enhanced Photoelectrochemical Performance, Appl. Catal., B, 231 (2018) 381-390.

[299] A. Tanaka, K. Hashimoto, H. Kominami, Visible-light-induced Hydrogen and Oxygen Formation Over Pt/Au/WO_3 Photocatalyst Utilizing Two Types of Photoabsorption Due to Surface Plasmon Resonance and Band-Gap Excitation, J. Am. Chem. Soc., 136 (2014) 586-589.

[300] D. Ding, K. Liu, S. He, C. Gao, Y. Yin, Ligand-exchange Assisted Formation of Au/TiO_2 Schottky Contact for Visible-Light Photocatalysis, Nano Lett, 14 (2014) 6731-6736.

[301] X. Bai, R. Zong, C. Li, D. Liu, Y. Liu, Y. Zhu, Enhancement of Visible Photocatalytic Activity via Ag@C_3N_4 Core-Shell Plasmonic Composite, Appl. Catal., B, 147 (2014) 82-91.

[302] N. Cheng, J. Tian, Q. Liu, C. Ge, A.H. Qusti, A.M. Asiri, A.O. Al-Youbi, X. Sun, Au-Nanoparticle-Loaded Graphitic Carbon Nitride Nanosheets: Green Photocatalytic Synthesis and Application Toward the Degradation of Organic Pollutants, ACS Appl. Mater. Interfaces, 5 (2013) 6815-6819.

[303] Q. Zhang, J. Deng, Z. Xu, M. Chaker, D. Ma, High-Efficiency Broadband C_3N_4 Photocatalysts: Synergistic Effects from Upconversion and Plasmons, ACS Catal., 7 (2017) 6225-6234.

[304] M.J. Kale, T. Avanesian, H. Xin, J. Yan, P. Christopher, Econtrolling Catalytic Selectivity on Metal Nanoparticles by Direct Photoexcitation of Adsorbate-Metal Bonds, Nano Lett, 14 (2014) 5405-5412.

[305] E. Kazuma, J. Jung, H. Ueba, M. Trenary, Y. Kim, Direct Pathway to Molecular Photodissociation on Metal Surfaces Using Visible Light, J. Am. Chem. Soc., 139 (2017) 3115-3121.

[306] E. Kazuma, J. Jung, H. Ueba, M. Trenary, Y. Kim, Real-Space and Real-Time Observation of a Plasmon-Induced Chemical Reaction of a Single Molecule, Science, 360 (2018) 521-526.

[307] C. Boerigter, U. Aslam, S. Linic, Mechanism of Charge Transfer from Plasmonic Nanostructures to Chemically Attached Materials, ACS Nano, 10 (2016) 6108-6115.

[308] C. Boerigter, R. Campana, M. Morabito, S. Linic, Evidence and Implications of Direct Charge Excitation as the Dominant Mechanism in Plasmon-Mediated Photocatalysis, Nat Commun, 7 (2016) 10545.

[309] T.E. Tesema, B. Kafle, M.G. Tadesse, T.G. Habteyes, Plasmon-Enhanced Resonant Excitation and Demethylation of Methylene Blue, J. Phys. Chem. C, 121 (2017) 7421-7428.

[310] T. Tatsuma, H. Nishi, T. Ishida, Plasmon-induced Charge Separation: Chemistry and Wide Applications, Chem Sci, 8 (2017) 3325-3337.

[311] X. Li, S. Fang, L. Ge, C. Han, P. Qiu, W. Liu, Synthesis of Flower-like Ag/AgCl-Bi_2MoO_6 Plasmonic Photocatalysts With Enhanced Visible-Light Photocatalytic Performance, Appl. Catal., B, 176-177 (2015) 62-69.

[312] S. He, J. Huang, J.L. Goodsell, A. Angerhofer, W.D. Wei, Plasmonic Nickel-TiO_2 Heterostructures for Visible-Light-Driven Photochemical Reactions, Angew. Chem., Int. Ed., 58 (2019) 6038-6041.

[313] H. Wang, L. Cui, S. Chen, M. Guo, S. Lu, Y. Xiang, A New Perspective on Metal Particles Enhanced MoS_2 Photocatalysis in Hydrogen Evolution: Excited Electric Field by Surface Plasmon Resonance, Journal of Applied Physics, 126 (2019).

[314] W. Hou, Z. Liu, P. Pavaskar, W.H. Hung, S.B. Cronin, Plasmonic Enhancement of Photocatalytic Decomposition of Methyl Orange Under Visible Light, Journal of Catalysis, 277 (2011) 149-153.

Chapter 2 Materials and Methodology

2.1 Materials

The chemicals used in the research are summarized in **Table 2.1**.

Table 2.1. The list of chemicals used in the thesis

Chemicals	Grade	Supplier
Potassium Chloride	Extra pure, 99+%	ACROS organics
Zinc Chloride	≥98%	Sigma-Aldrich
Lithium Chloride	≥99%	Sigma-Aldrich
Nitric Acid	≥65% (T)	Sigma-Aldrich
Cyanamide	99%	Sigma-Aldrich
Dicyandiamide	99.5%	ACROS organics
Melamine	99%	ACROS organics
Cyanuric Chloride	≥99.5% (w/w)	Sigma-Aldrich
Titanium Chloride	99.9%	ACROS organics
Urea	99.5%, for analysis	ACROS organics
Acetonitrile	Extra pure	ACROS organics
Barium Sulfate	Precipitated, 99%	Alfa Aesar
Hydrochloric acid	0.1 M	Fisher scientific
Ethanol	Absolute, ≥99.8%	Fisher scientific
Sodium Sulfate	Anhydrous, ≥99%	Sigma-Aldrich
Nafion solution	5 wt.%	Sigma-Aldrich
Methyl Orange	Pure	Honeywell Fluka
Rhodamine B	Pure	ACROS organics

2.2 Experimental procedures and nomenclatures

2.2.1 Synthesis of g-C_3N_4 via the molten salt method

To synthesize g-C_3N_4, 3 g of melamine and 5 g of KCl (1.58 g), $ZnCl_2$ (3.42 g) mixture with a molar ratio of 0.457:0.543 were fully ground in an agate mortar, and the as-obtained powder was then transferred to a ceramic crucible (20 mL) and covered with a ceramic lid. The crucible was then placed into the centre of a tube furnace. The furnace was firstly vacuumed and then back-filled with N_2 for 3 times in order to get rid of O_2. The tube furnace was then heated to 500 °C with a ramping rate of 1 °C min^{-1} and kept at 500 °C for 2 h under N_2 gas flow (100 sccm). The as-obtained solid was washed with HNO_3 (5%) aqueous solution under reflux condition. After further rinsing with DI-water for several times until the pH=7 and the powder was dried at 80 °C under vacuum overnight. The as-prepared sample was marked as C_3N_4-M. The other 2 samples were prepared in a similar way, except the precursors were cyanamide and dicyandiamide, respectively. The samples were denoted as C_3N_4-C and C_3N_4-D accordingly.

A eutectic system is a homogeneous, solid mixture of two or more substances; the mixture either melts or solidifies at a lower temperature than the melting point of any of the individual substances. A eutectic system only forms when there is a specific ratio between the components. At this ratio, the eutectic temperature corresponding to the lowest melting point of a mixture of components. In order to unravel the advantage of the unique C_3N_4 synthesis method using KCl-$ZnCl_2$ eutectic system, the control group C_3N_4 sample was prepared via a conventional KCl-LiCl molten salt method. A typical eutectic mixture of 2.79g KCl and 2.21 g LiCl (0.418:0.582 in molar ratio) was used as the molten salt. 3 g of dicyandiamide was fully mixed by grinding them in a mortar and treated in the same procedure as described above. The as-obtained control group sample was marked as C_3N_4-D-Li.

Another important control group sample is the C_3N_4 prepared by directly calcinating melamine in static air. As the prevailing method used to prepare the C_3N_4 in the literature, this control group sample could act as the benchmark for comparison. Typically, 10 g of melamine powder was put into an alumina crucible with a cover. The crucible was then placed into the centre of a muffle furnace, then heated to 500 ^oC at a ramp rate of 10 ^oC min^{-1}. After soaking at 500 ^oC for 2h, the furnace was cooled down to room temperature naturally, the yellow product was collected and then ground into fine powder in an agate mortar and denoted as C_3N_4-M-Air.

2.2.2 Synthesis of agitation assisted C_3N_4

Cl- doped C_3N_4 was successfully prepared by a one-step template-free solvothermal method under controlled agitation. To prepare Cl doped C_3N_4, 15 mmol of cyanuric chloride, 7.5 mmol of dicyandiamide, and 60 ml acetonitrile were added into a 150 ml Teflon-lined autoclave. The temperature of the reactor was monitored via a K-type thermocouple inserted into a blind hole in the wall of the stainless-steel reactor. The heating tapes tightly surrounding the reactor was controlled by a proportional–integral–derivative (PID) temperature controller. The ceramic wool cover was used for the thermal insulation of the reactor (as shown in **Figure 2.1**). The reaction system was agitated by a Teflon coated magnetic stirring bar (6mm × 30mm) under controlled agitation speed. In the synthesis progress, the reactor was heated to 180˚C with the ramp rate of ~10 ºC min^{-1}. During 48 hours of soaking at 180 ˚C, the agitation was maintained constantly. After cooling down to room temperature naturally, the sample was collected and washed by deionized water and ethanol (~300 mL) under vigorous stirring for three times. Then, the sample was dried in a vacuum oven at 80°C overnight.

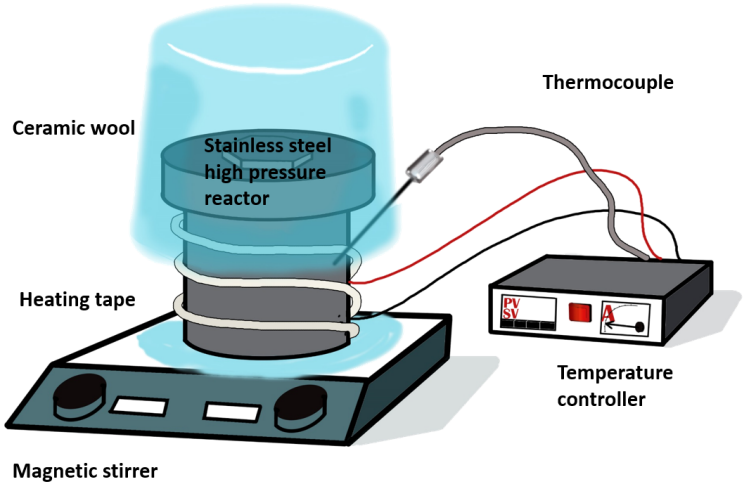

Figure 2.1. Schematic illustration of the synthesis instrument

The C_3N_4 samples synthesized via solvothermal method with agitation rates of 0 rpm, 60 rpm (minimum rate of magnetic stirrer), 100 rpm, 400rpm, 750rpm and 1100rpm (maximum rate of magnetic stirrer) have been denoted as 0-C_3N_4, 60-C_3N_4, 100-C_3N_4, 400-C_3N_4, 750-C_3N_4, and 1100-C_3N_4, respectively, in the rest of this thesis.

2.2.3 Synthesis of C-doped TiN/ultrathin carbon layer

TiN/ultrathin carbon layer heterostructures were synthesized via the calcination of $TiCl_4$/ethanol with urea glass mixture under N_2 flow. Two parameters, calcination temperature and urea/$TiCl_4$ molar ratios, were controlled during the synthesis procedure. To be more specific, 580 μL $TiCl_4$ liquid was added into 3 mL ethanol under vigorous stirring (Safety caution: the reaction is extremely exothermic and generates toxic vapours). Then 0.3, 0.9, 1.5, 3 and 4.5 g urea, which are 1, 3, 5, 10, 15 times of $TiCl_4$ molarity, was added to the solution forming the 'urea glass' gel [1]. After achieving a homogenous paste after 30 min, the 'urea glass' was transferred to a crucible and placed in the middle of a tube furnace. To get rid of air inside the quartz tube, the tubing furnace was purged with N_2 flow (100 sccm) for 1 h at room temperature. Then the furnace was heated to 900 ^oC with 300 min soaking time. The ramping and cooling rates was kept at 3 ^oC min^{-1}. After cooling to room temperature, the prepared powder was withdrawn from the tube furnace and stored inside a desiccator. To keep the names of the samples concise, the samples were denoted as TiN-0.3-900, TiN-0.9-900, TiN-1.5-900, TiN-3.0-900 and TiN-4.5-900, respectively, depending on the amount of urea used. The other groups of samples were prepared in a similar way, except keeping the urea amount at 3 g and calcinated within the temperature range from 500 to 1100 ^oC in a step of 100 ^oC. The prepared samples are named as TiN-3.0-500, TiN-3.0-600, TiN-3.0-700, TiN-3.0-800, TiN-3.0-900, TiN-3.0-1000, and TiN-3.0-1100 to represent the different calcination temperature.

2.3 Characterization techniques

2.3.1 Molecular structure analyses

Powder X-ray diffraction (XRD) patterns of the prepared samples were characterized using an X-ray diffractometer (Phaser-D2, Bruker) with Cu Kα X-ray source (K-Alpha1 [Å]=1.5406) at the voltage of 40 kV and current of 40 mA. The XRD patterns were collected using step scans with a step of 0.05^o and a counting time of 0.2 s per step between 5^o and 80^o. XRD was performed with an X-ray diffractometer (Bruker D2 PHASER diffractometer) equipped. The Debye–Scherrer equation (see Eq.(2.1)) was used to calculate the average crystal sizes:

$$D = \frac{K\lambda}{\beta cos\theta} \tag{2.1}$$

where D is mean size of the crystalline domains; K is the shape factor and usually takes the typical value of 0.89; β is the full width at half maximum of the peak in radians (FWHM); λ is the X-ray wavelength; θ is the diffraction angle, respectively [2].

Both core-level and VB X-ray photoelectron spectroscopy (XPS) were recorded using an X-ray photoelectron spectrometer (ThermoFisher K-Alpha) with the Al Kα X-ray source. The C, H and N chemical compositions of the prepared C_3N_4 samples were determined with an organic elemental analyser (Carlo Erba NA2500).

The infrared (IR) transmission spectrum was collected on a Fourier transform infrared spectrophotometer (FTIR, Shimadzu IRTracer-100) following the KBr pellet method. The sample was first mixed with 100 mg pre-dried KBr powder by carefully grinding in a mortar. Then, the mixture was pressed into a pellet in the diameter of 13 mm using a hydraulic press. The prepared KBr pellet was placed inside the FTIR spectrometer vertically to the incident beam. The spectrum within the range of 600-4000 cm^{-1} was collected in the resolution of 4 cm^{-1} by averaging 64 scans.

The thermal properties of the obtained samples were investigated using thermogravimetric analysis with a simultaneous thermal analyser (Mettler Toledo, TGA/DSC 3+.) About 5 mg of each sample was heated in aluminium crucibles from 25 ºC to 1000 ºC and collect the differential scanning calorimetry (DSC) and thermogravimetric analyses (TGA) data.

2.3.2 Morphology characterization

To obtain the morphological information of the prepared samples, a scanning electron microscope (SEM, Carl Zeiss SIGMA HD VP Field Emission SEM) was used. The sample was directly held on the copper tape (gold coating for non-conducting sample). An additional X-ray energy dispersive spectrometer (EDS, Oxford AZtecEnergy) in the SEM was used to determine the elemental composition of the samples. The partial sizes and structure were further examined by the transmission electron microscopy (TEM, JEOL JEM-2100F), the representative images were collected on a GATAN One View camera. Scanning transmission electron microscope (STEM) of as-prepared samples were conducted in the same instrument.

2.3.3 Measurements of specific surface areas

Nitrogen adsorption–desorption isotherms were determined at 77k with an automatic gas0-sorption analyser (Quantachrome, Autosorb-iQ). The BET (Brunauer–Emmett–Teller) theory

is used to calculate the SSA of the samples based on the N_2 adsorption results. BET adsorption isotherm at the boiling temperature of nitrogen can be seen in Eq. ((2.2). The plot of $\frac{1}{v[(\frac{P_0}{P})-1]}$ as a function of $\frac{P}{P_0}$ could also be called BET graph. When P/P_0 is in the range of 0.05-0.35, the points in BET plot shows better linearity. The adsorption isotherm can be used to calculate the SSA of solid materials by Eq. (2.3), where N_A is Avogadro's number, s the adsorption cross section of the adsorbing species, V representing the molar volume of the adsorbate gas and a is the mass of the adsorbent material [3].

$$\frac{1}{v[(\frac{P_0}{P})-1]} = \frac{c-1}{v_m c}\left(\frac{P}{P_0}\right) + \frac{1}{v_m c} \tag{2.2}$$

$$S_{BET} = \frac{v_m N_A s}{Va} \tag{2.3}$$

Where P, P_0 are the equilibrium and the saturation pressure, v, v_m are the adsorbed gas quantity, monolayer adsorbed gas quantity, and c is BET constant, respectively.

2.3.4 Electronic structure analyses

Light adsorption and bandgap determination were conducted by ultraviolet-visible diffuse reflectance spectroscopy (UV-Vis DRS) on a UV-Vis spectrophotometer (UV-3600 plus, Shimadzu) equipped with a commercial accessory (Praying Mantis, Harrick). Generally, the band gap energy of the powdery sample was determined using the Tauc approach, which is given by the Eq. (2.4)[4].

$$ahv = \mathrm{A}(hv - E_g)^n \tag{2.4}$$

Where hv is the photon energy; E_g is the forbidden band gap; A is a constant; n takes 1/2 or 2 values depending on the direct or indirect bandgap transition of the semiconductor; a is the absorption coefficient. As for powder samples with “infinite thickness”, DRS is more accurate than optical absorption spectroscopy[5]. The Kubelka-Munk (K-M) theory was applied to convert DRS into the equivalent absorption coefficient:

$$F(R) = \frac{(1-R)^2}{2R} = \frac{K}{S} \tag{2.5}$$

Where R is the reflectance of the sample, K is the absorption and S is the spectral scattering factor as a constant in common assumption. The band gap E_g can be estimated by fitting a

tangent line to the linear portion of the plot of $(F(R)hv)^{\frac{1}{n}}$ vs hv and extrapolating its value to hv-axis[6].

In Chapter 5, Density functional theory (DFT) theoretical calculations were used to investigate the electronic structures of the samples. The DFT calculation were conducted using plane-wave basis sets implemented in the Quantum Espresso package [7, 8]. The Perdew-burke-Ernzerh of functional optimised for solids (PBEsol [9]) was used to describe the exchange-correlation energy and potential. Ultrasoft pseudopotentials in GBRV-library [10] were used to represent the nucleus and core electrons and the energy of 45 and 450 Ry was used as the cutoff energy for the wave function and charge density/potential, respectively. A gaussian smearing of 0.01 Ry was used to accelerate the convergence. The 2 × 2 × 2 supercells of TiN were built up with 1 N atom replacing by C atom representing the C doped TiN crystal structure. The Monkhorst-Pack k-points meshes with the size of 20 × 20 × 20 and 10 × 10 × 10 were used for the structure relaxation of the TiC, TiN primitive cells and C-doped TiN supercell, respectively. The denser k-points meshes of 40 × 40 × 40 and 20 × 20 × 20 for more accurate sampling of the Brillouin zone were adopted for the electronic structure calculations for TiC, TiN primitive cells and C-doped TiN structure.

2.3.5 Photoelectrochemical experiments

Photoelectrochemical tests were conducted with a typical 3-electrode configuration using a potentiostat (Metrohm, Autolab PGSTAT204). The reference electrode was Ag/AgCl (0.1 M KCl, CHI Instruments), the counter electrode was a Pt-coil (CHI Instruments) and the electrolyte was the 0.1 M KCl aqueous solution,as shown in **Figure 2.2**(a). The working electrode was prepared via the following procedure. A 15 × 15 mm^2 indium tin oxide coated glass (ITO glass) was used to support the catalysts as working electrode. A geometric area of 0.75 cm^2 was kept as an active area on the ITO glass with the rest of the surface insulated by scotch tape. For the simulated solar light irradiation photoelectrochemical test, 0.1 mol L^{-1} KCl aqueous solution was used as the electrolyte and a graphite rode as the counter electrode. No potential bias was applied during the experiments, as shown in **Figure 2.2**(b). A glassy carbon electrode in 1.5 × 1.5 cm^2 size was used as the substrate for catalysts and an active area of 0.75 cm^2 was defined by covering the rest surface with insulation tape. A crocodile clamp with copper lead was used for the wire of the working electrode. The whole clamp and wire were kept out of the solution to prevent any corrosion. 2 mg of catalysts were dispersed into 0.2 mL ethanol by ultrasonication. 10 μL Nafion 5% solution was then added into the solution forming a homogenous mixture. A total amount of 0.1 mL mixture was then added onto the glass in

portions of 20 μL each time. After dried at room temperature, the working electrode was ready for the photoelectrochemical experiments. During the transient photocurrent response experiments, a Xenon lamp (Thorlabs, SLS 401) was used to provide the simulated solar light; the Xenon lamp equipped with a 420 nm long-pass filter was used to provide the visible light for catalysts excitation. A build-in optical shutter was used to chop the light beam regularly. A bias potential of 0.2 V (vs Ag/AgCl, 0.1M KCl) was applied to the working electrode during the tests and the data acquisition interval was set at 0.1 s.

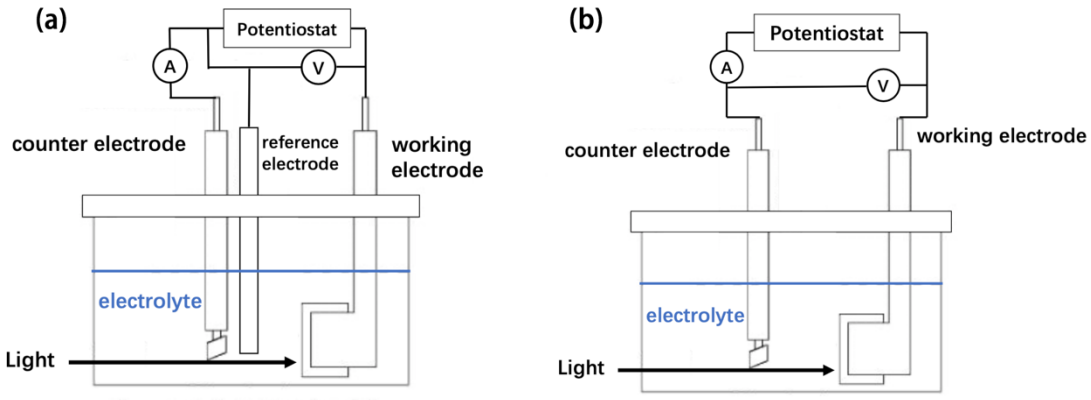

Figure 2.2. Schematic illustration of the (a) three-electrode system and (b) two-electrode system

2.3.6 Carriers dynamics analyses

Photoluminescence (PL) spectra were measured on a fluorescence spectrometer (RF6000, Shimadzu) with the excitation wavelength of 325 nm, and the emission wavelength range is 350-620 nm. The time-resolved fluorescence spectroscopy was conducted on the fluorescence spectrometer (FLS920, Edinburgh Instrument) with a pulsed excitation source of 325 nm and monitoring the fluorescence intensity decay at the corresponding PL peak wavelength.

2.4 Photocatalytic evaluations

The photocatalytic activity of the prepared samples was evaluated by the probe reaction, i.e. photocatalytic RhB or MO degradation under visible light irradiation. A 300 W Xenon lamp (PLS-SXE300, Beijing Perfectlight technology co.) with/without a 420 nm long-pass filter was used to provide the visible light/UV-Vis light to drive the reaction. The power density of the light reaching the catalysts was measured to be 508 ± 10 mW cm^{-2} using a thermopile light power meter (Thorlabs, PM16-401). A jacketed glass beaker was used as the reactor with water circulation to keep the solution temperature constant during the photocatalytic experiments, a

schematic diagram is shown in **Figure 2.3**. For each degradation experiment, 12 mg of catalyst was dispersed into a 60 mL RhB aqueous solution in the concentration of 10 ppm. Before the photocatalytic reaction, the solution was ultrasonicated for 10 min and kept under mechanical stirring for another 25 min in dark to achieve a homogeneous catalyst dispersion and enable the estimation of the adsorption capability of the catalysts towards RhB. Then, visible light driven photocatalytic RhB degradation experiments were conducted for 125 min under constant stirring. 3 mL aliquots were collected every 25 min for RhB concentration measurements. The aliquots were firstly centrifuged at 9000 rpm for 7 min to separate the catalysts. Then, the catalyst-free solutions were transferred into a cuvette and tested by a UV-Vis spectrometer (Analytik Jena, SPECORD PC 250). The test parameter details for each sample are listed in the table below (**Table 2.2**).

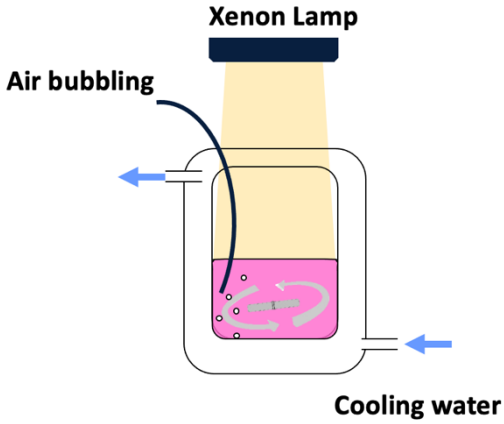

Figure 2.3. Schematic illustration of degradation reactor

Table 2.2. The parameters of photodegradation experiments in each chapter

Sample	Filter	The power density of the light (±10 mW cm^{-2})	Dye	Photocatalysts usage (mg ml^{-1})
Chapter 3	no filter	720	MO and RhB	0.2
Chapter 3	420 nm long-pass	508	MO and RhB	0.2
Chapter 4	420 nm long-pass	508	RhB	0.2
Chapter 5	420 nm long-pass	508	RhB	0.2

2.5 Models and calculations

2.5.1 Evaluation methods for photocatalytic degradation of dye

UV-Vis absorption spectroscopy was used to determine the concentration of the dye solution after different photocatalytic reaction time. When the solution is dilute enough, the absorbance of monochromatic light by the dilute solutions with different concentrations follows the Beer-Lambert law:

$$A = \lg\frac{I_0}{I_T} = \alpha \cdot l \cdot c \tag{2.6}$$

In Eq. (2.6), A is the light absorbance; I_0 and I_T are the incident and transmitted light intensities, respectively; α ($L \cdot g^{-1} \cdot cm^{-1}$) is absorptivity; l is the optical path length in solution, and c is the concentration of the dye solution.

The concentration of organic pollutants we choose is generally a dilute solution at the ppm level. There is a linear relationship between absorbance and concentration according to Beer-Lambert law. The calibration curves of MO and RhB concentration and absorbance are presented in **Figure 2.4**. Therefore, the concentrations of dye after different light-irradiation time can be indirectly calculated by measuring the absorbance of the dye solution. The apparent degradation rate of pollutants can be calculated according to Eq. (2.7):

$$\text{Degradation}\% = \frac{A_0 - A_t}{A_0} \times 100\% = \frac{C_0 - C_t}{C_0} \times 100\% \tag{2.7}$$

In the Eq. (2.7), A_0, C_0 and A_t, C_t represent the absorbance and concentration of the pollutant before the photocatalytic reaction and after t minutes of photocatalytic reaction, respectively.

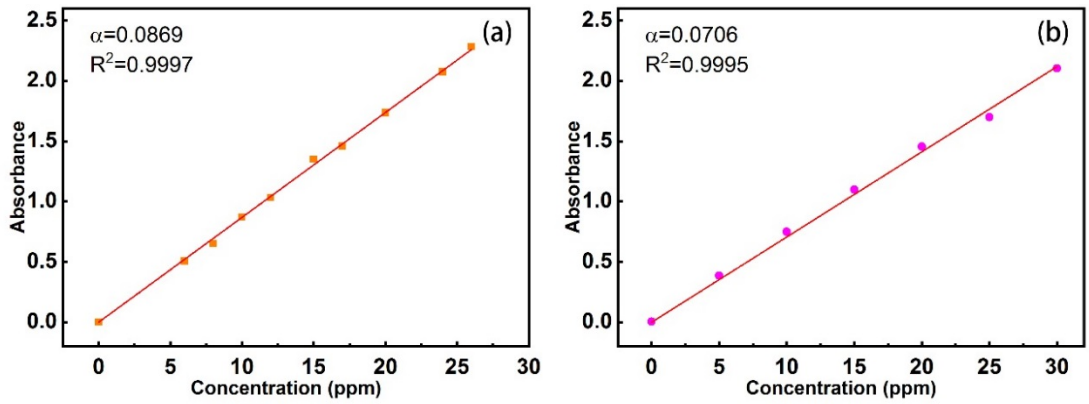

Figure 2.4. Calibration curves of (a) MO and (b) RhB absorbance plotted in the function of concentration

2.5.2 Kinetic model of degradation

Several experimental results demonstrated that the photocatalytic degradation model follows the Langmuir-Hinshelwood (L-H) kinetic model in the experimental concentration range presented in this thesis. The L-H kinetic model assumes that the reaction occurs on the surface of the catalyst particles. This model has recently been used to describe the kinetics of mineralization in solid-liquid reactions accordance to the kinetic analysis [11]. As described in Eq.(2.8), k_r is the true reaction rate constant; the reaction rate (r) is proportional to θ

$$r = -\frac{\mathrm{dC}}{\mathrm{dt}} = k_r\theta \tag{2.8}$$

Where θ in Langmuir's equation：

$$\theta = \frac{KC}{1+KC} \tag{2.9}$$

The reaction rate:

$$\mathrm{r} = -\frac{\mathrm{dC}}{\mathrm{dt}} = k_r \cdot \frac{KC}{1+KC} \tag{2.10}$$

In the kinetics studies of photocatalysis, starting from Langmuir's isotherm, the value of K is the constant of adsorption equilibrium which obtained through a kinetic study under light. The equation will be integrated to:

$$\ln\frac{C_0}{C} + K(C_0 - C) = k_r K t \tag{2.11}$$

Where C_0 is the initial concentration, C is the concentration at any time t. In the first-order reaction kinetics, the solution is highly diluted, and the value of C is extremely small that KC can be neglected[12]:

$$\mathrm{r} = -\frac{\mathrm{dC}}{\mathrm{dt}} = k_r \cdot KC = k_{app}C \tag{2.12}$$

The apparent rate constant (k_{app}) of a pseudo-first-order reaction can be determined from the slope of the fitted curve when plotting ln ($\frac{C_0}{C}$) versus reaction time t from following simplified equation (Eq.(2.13)):

$$\ln\left(\frac{C_0}{C}\right) = k_{app} \cdot t \tag{2.13}$$

References

[1] D.H. Youn, G. Bae, S. Han, J.Y. Kim, J.-W. Jang, H. Park, S.H. Choi, J.S. Lee, A Highly Efficient Transition Metal Nitride-Based Electrocatalyst for Oxygen Reduction Reaction: TiN on a CNT-graphene Hybrid Support, J. Mater. Chem. A, 1 (2013).

[2] B. Ingham, M.F. Toney, X-ray Diffraction for Characterizing Metallic Films, in: K. Barmak, K. Coffey (Eds.) Metallic Films for Electronic, Optical and Magnetic Applications, Woodhead Publishing2014, pp. 3-38.

[3] S. Brunauer, P.H. Emmett, E. Teller, Adsorption of Gases in Multimolecular Layers, Journal of the American Chemical Society, 60 (1938) 309-319.

[4] J. Tauc, R. Grigorovici, A. Vancu, Optical Properties and Electronic Structure of Amorphous Germanium, physica status solidi (b), 15 (1966) 627-637.

[5] A. Escobedo Morales, E. Sánchez Mora, U. Pal, Use of Diffuse Reflectance Spectroscopy for Optical Characterization of Un-Supported Nanostructures, Revista Mexicana de Física, 53 (2007) 18-22.

[6] A. Escobedo-Morales, I.I. Ruiz-López, M.d. Ruiz-Peralta, L. Tepech-Carrillo, M. Sánchez-Cantú, J.E. Moreno-Orea, Automated Method for the Determination of the Band Gap Energy of Pure and Mixed Powder Samples Using Diffuse Reflectance Spectroscopy, Heliyon, 5 (2019) e01505.

[7] P. Giannozzi, O. Andreussi, T. Brumme, O. Bunau, M. Buongiorno Nardelli, M. Calandra, R. Car, C. Cavazzoni, D. Ceresoli, M. Cococcioni, N. Colonna, I. Carnimeo, A. Dal Corso, S. de Gironcoli, P. Delugas, R.A. DiStasio, A. Ferretti, A. Floris, G. Fratesi, G. Fugallo, R. Gebauer, U. Gerstmann, F. Giustino, T. Gorni, J. Jia, M. Kawamura, H.Y. Ko, A. Kokalj, E. Küçükbenli, M. Lazzeri, M. Marsili, N. Marzari, F. Mauri, N.L. Nguyen, H.V. Nguyen, A. Otero-de-la-Roza, L. Paulatto, S. Poncé, D. Rocca, R. Sabatini, B. Santra, M. Schlipf, A.P. Seitsonen, A. Smogunov, I. Timrov, T. Thonhauser, P. Umari, N. Vast, X. Wu, S. Baroni, Advanced Capabilities for Materials Modelling With Quantum ESPRESSO, Journal of Physics: Condensed Matter, 29 (2017) 465901.

[8] P. Giannozzi, S. Baroni, N. Bonini, M. Calandra, R. Car, C. Cavazzoni, D. Ceresoli, G.L. Chiarotti, M. Cococcioni, I. Dabo, A. Dal Corso, S. de Gironcoli, S. Fabris, G. Fratesi, R. Gebauer, U. Gerstmann, C. Gougoussis, A. Kokalj, M. Lazzeri, L. Martin-Samos, N. Marzari, F. Mauri, R. Mazzarello, S. Paolini, A. Pasquarello, L. Paulatto, C. Sbraccia, S. Scandolo, G. Sclauzero, A.P. Seitsonen, A. Smogunov, P. Umari, R.M. Wentzcovitch, QUANTUM ESPRESSO: Pseudopotentials for High-Throa Modular and Open-Source Software Project for Quantum Simulations of Materialsughput DFT Calculations, J Phys Condens Matter, 21 (2009) 395502.

[9] J.P. Perdew, A. Ruzsinszky, G.I. Csonka, O.A. Vydrov, G.E. Scuseria, L.A. Constantin, X. Zhou, K. Burke, Restoring the Density-Gradient Expansion for Exchange in Solids and Surfaces, Physical Review Letters, 100 (2008) 136406.

[10] K.F. Garrity, J.W. Bennett, K.M. Rabe, D. Vanderbilt, Pseudopotentials for High-Throughput DFT Calculations, Computational Materials Science, 81 (2014) 446-452.

[11] I.K. Konstantinou, T.A. Albanis, TiO_2-Assisted Photocatalytic Degradation of Azo Dyes in Aqueous Solution: Kinetic and Mechanistic Investigations: A Review, Appl. Catal., B, 49 (2004) 1-14.

[12] N.A. Laoufi, D. Tassalit, F. Bentahar, The Degradation of Phenol in Water Solution by TiO_2 Photocatalysis in a Helical Reactor, Global Nest Journal, 10 (2008) 404-418.

Chapter 3 Synthesis of Zn Doped C_3N_4 in KCl-$ZnCl_2$ Molten Salts: The Importance of Low Eutectic Temperature on Promoting the Photocatalytic Activity

This work has been published by the Applied Surface Science. It is written by the first author, who is also the author of the present thesis. The introduction and the conclusion part are reproduced from original paper with some modifications. Full published version is in the appendix.

3.1 Introduction

Carbon nitride (C_3N_4) is regarded as a promising organic semiconductor for photocatalytic CO_2 reduction [1, 2], water splitting [3, 4], pollutants degradation [5, 6], etc. It shows some unique advantages including free of transition metal elements, low toxicity and relatively high photocatalytic performance, and has attracted significant interests from researchers. However, the photocatalytic performance of pristine C_3N_4 still cannot meet the requirement for the practical applications, due to its low specific surface area (SSA), unoptimized electronic structure and high electron/hole recombination rate.

The strategies to improve the photocatalytic activity of C_3N_4 can be classified into two categories: (i) modifying the molecular and electronic structures of C_3N_4 by heteroatom doping, and (ii) building up a heterostructure on C_3N_4. The heteroatom doping strategy includes the atomic doping of alkaline metal (Li, Na, K) [2, 7-11], halogen (F, Cl, Br, I) [12-16], non-noble transition metals (Zn, Cu, Fe, Co) [5, 16-22], noble transition metals (Ag, Pt, Pd, Ir, Au) [23-27], and other main group elements (O, S, B, C, N, P) [9, 28-34], etc. Among them, Zn has been investigated and introduced into C_3N_4 interstitial sites via different methods [5, 17, 19, 35, 36]. However, one of the major drawbacks of the pristine C_3N_4, the low SSA, has not been much improved after the Zn doping, and the effects of Zn doping on the photocatalytic dye degradation have not been investigated. The typical SSA of C_3N_4 synthesized via the most popular thermal polycondensation method is only ~ 10 $m^2 g^{-1}$, and several attempts have been

reported in the literature to increase the SSA of modified C_3N_4 [9, 17, 28] One of the most successful methods is to use the hard templates to increase the SSA of C_3N_4. The hard template method is indeed effective, but its application is limited by the high cost of the templates and highly toxic compounds indispensable for template removal. Using the soft template is another approach to improve C_3N_4 SSA. The soft template method is low-cost and multi-functionality, but less effective than the hard template approach [4, 19, 37, 38]. Therefore, it is still a challenge to increase the SSA of C_3N_4 in a facile and effective way.

Synthesis of C_3N_4 in molten salt (ionothermal synthesis) has been reported to produce C_3N_4 with optimized morphology and electronic structure [3]. The melted salts as the media for the polycondensation of organic precursors can enhance the homogeneity and crystallinity of the prepared C_3N_4. C_3N_4 synthesis via polycondensation of melamine in eutectic KCl-LiCl was reported for the first time by Bojdys et al. [39] Because of the enhanced dispersion of precursors inside the molten salts; the C_3N_4 was synthesized with larger SSA and higher crystallinity. Gao et al. [40] reported that the C_3N_4 with nanotube morphology was synthesized in molten NaCl-KCl-LiCl ternary system. Zhang et al. [41] reported that the condensation of urea inside LiCl-KCl resulted in the C_3N_4 with reduced interlayer distance and the enhanced π-π interaction, which strongly improved its photocatalytic activity. In addition, the molten salts have also been used to achieve the triazine based C_3N_4 and as a post-treatment method to increase the crystallinity [3, 42-44]. Although the synthesis of C_3N_4 in molten salts has been extensively investigated, most of the researches only focus on the LiCl-KCl system, and the essential topic of what is the optimal eutectic temperature of salt mixture for C_3N_4 synthesis has not been investigated. Moreover, because the polycondensation synthesis of C_3N_4 is a multiple-step process taking places at discrete temperatures, the specific role of melted salts at different polycondensation stages are still lack of understanding.

To address the challenges and knowledge gaps mentioned above, herein, the C_3N_4 was prepared in low-temperature KCl-$ZnCl_2$ eutectic salts with cyanamide, dicyandiamide and melamine as precursors, respectively. During the C_3N_4 synthesis, the organic precursors, cyanamide, dicyandiamide and melamine with increasing polycondensation degrees are the three major intermediates representing the three main stages. By comparing the molecular and electronic structures of the prepared C_3N_4 from different precursors, the specific roles of melted salts at the different stages of C_3N_4 synthesis were unravelled. It was found that the sample synthesized from dicyandiamide (C_3N_4-D) in molten KCl-$ZnCl_2$ gave the high SSA of 138.6 $m^2 g^{-1}$, and the valence band edge (VBM) position of C_3N_4 was shifted to the positive direction, therefore enhancing the oxidation capability. Additionally, a moderate amount of

Zn was introduced as the interstitial dopant during the synthesis in KCl-$ZnCl_2$ molten salts and a longer photo-excited carrier lifetime was observed due to the suppressed electron-hole recombination. The photocatalytic dye degradation performance has been significantly promoted on C_3N_4-D comparing with the C_3N_4 synthesized via the thermal polycondensation method or in conventionally used LiCl-KCl system.

3.2 Results and discussion

3.2.1 The matching between the polycondensation temperature and melting temperature of KCl-$ZnCl_2$

To understand the working mechanism of melted KCl-$ZnCl_2$ at different stages of the C_3N_4 polycondensation, it is necessary to identify the temperature for each polycondensation step taking place. According to the literature, the preparation of C_3N_4 via thermal polycondensation is a step-wise polymerisation of monomers and oligomers, as illustrated in **Figure 3.1** [45-48]. The cyanamide firstly dimerizes to dicyandiamide and then condenses to melamine. The melamine monomers can further polymerize to the melem with the release of NH_3. The polymerization of melem unit further produces the di-melem, melon monomer and melon sheets. The stacking of melon sheets with interlayer van de Waals force generates the commonly believed g-C_3N_4 structure. To determine the temperature for each polycondensation steps during the C_3N_4 synthesis, the TGA experiments were conducted on the three most commonly used precursors under a N_2 flow of 100 sccm: cyanamide, dicyandiamide and melamine. As illustrated by the weight percentage curves in **Figure 3.2**(a-c), all three precursors show 2 main weight losses at ~400 and ~700 ºC respectively, which are attributable to the thermal condensation forming C_3N_4 and following C_3N_4 decomposition respectively. In addition, the heat flow curves offer more detailed molecular structure evolution information during the polymerization process. As illustrated in **Figure 3.2**(a), there are 8 heat flow peaks in the TGA-DSC profile. The first 7 peaks are related to C_3N_4 formation and the last is attributed to C_3N_4 decomposition. The endothermal peak i refers to the melting of cyanamide at ~ 44 ºC. The peak ii at 170-174 ºC can be assigned to the reaction that converting cyanamide to dicyandiamide. The peak iii at 207 ºC matches the melting temperature of dicyandiamide. Within the range of 248-262 ºC, the peak iv represents the formation of melamine from dicyandiamide. After the melting and sublimation of melamine at 328-343 ºC (peak v), the melamine further converts to melem at ~394 ºC (peak vi). The final C_3N_4 formation from melem condensation step happens at ~524 ºC (peak vii). Similar to cyanamide

polycondensation process, the dicyandiamide (**Figure 3.2** (b)) and melamine (**Figure 3.2** (c)) show the similar polycondensation steps except that the steps related to the formation of dicyandiamide or melamine are not included. All these steps and corresponding peak assignments of the thermal analyses results and the references are summarized in **Table 3.1**. For conventional KCl-LiCl eutectic system (KCl:LiCl at 0.418:0.582 in molar ratio), the melting temperature is 352 ºC [49]. In this work, the KCl:$ZnCl_2$ with the molar ratio of 0.457:0.543 exhibits a much lower eutectic temperature of 230 ºC [50]. The corresponding phase diagrams are shown in **Figure 3.3**(a, b). Comparing the temperature between each polycondensation step and eutectic temperature of two different salt mixtures, two conclusions can be reached: (i) for conventional KCl-LiCl mixture, the eutectic temperature locates between the steps of melamine melting and formation of melem; (ii) for KCl-$ZnCl_2$ mixture, the eutectic temperature is between the steps of dicyandiamide melting and formation of melamine. Therefore, when using the KCl-$ZnCl_2$ eutectic salts mixture, the dicyanamide and melamine oligomers show a significantly improved dispersion in the melting salts during their polycondensation process.

Table 3.1. The stages during the C_3N_4 synthesis from precursors and corresponding peak assignments.

Temperature (ºC)	Endo/exothermal (END/EXO)	Physical/chemical process	Peak assignment cyanamide	dicyandiamide	melamine	Ref
45	END	melting of cyanamide	i			[51]
170-174	EXO	reaction of cyanamide to dicyandiamide	ii			[48]
207	END	melting of dicyandiamide	iii	i		[51]
248-273	EXO	reaction of dicyandiamide to melamine	iv	ii, iii		[48]
330-343	END	melting/fast sublimation of melamine	v	iv	i	[51-53]
367	END	fast deamination of melamine			ii	[54]
381-394	END	reaction of melamine to melem	vi	v	iii	[48, 54]
516-553	END	reaction of melem to C_3N_4	vii	vi	iv	[46, 48, 55]
718-730	END	decomposition of C_3N_4	viii	vii	v	[52, 53, 56]

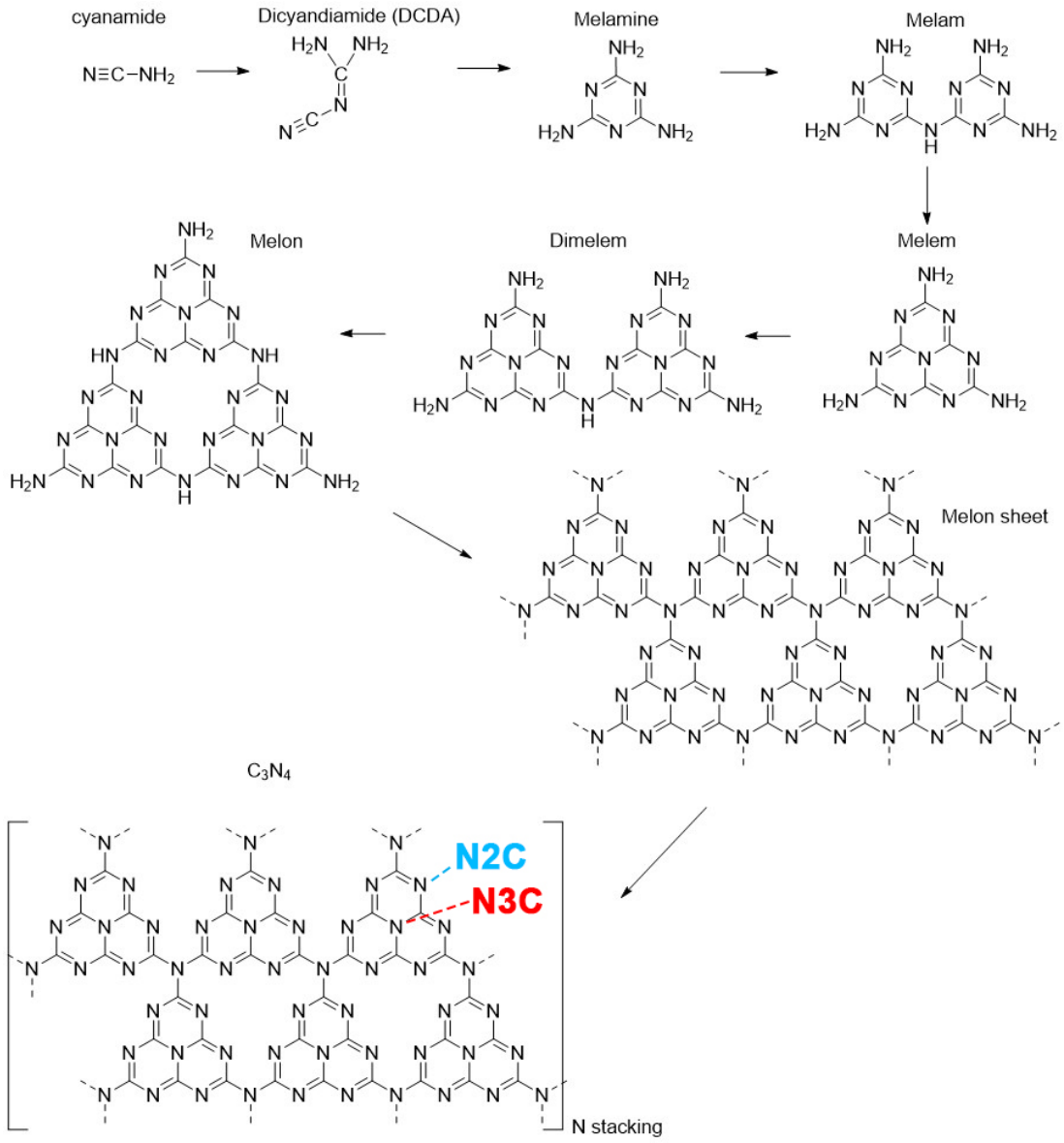

Figure 3.1. Scheme of C_3N_4 formation process via thermal polycondensation process from cyanamide

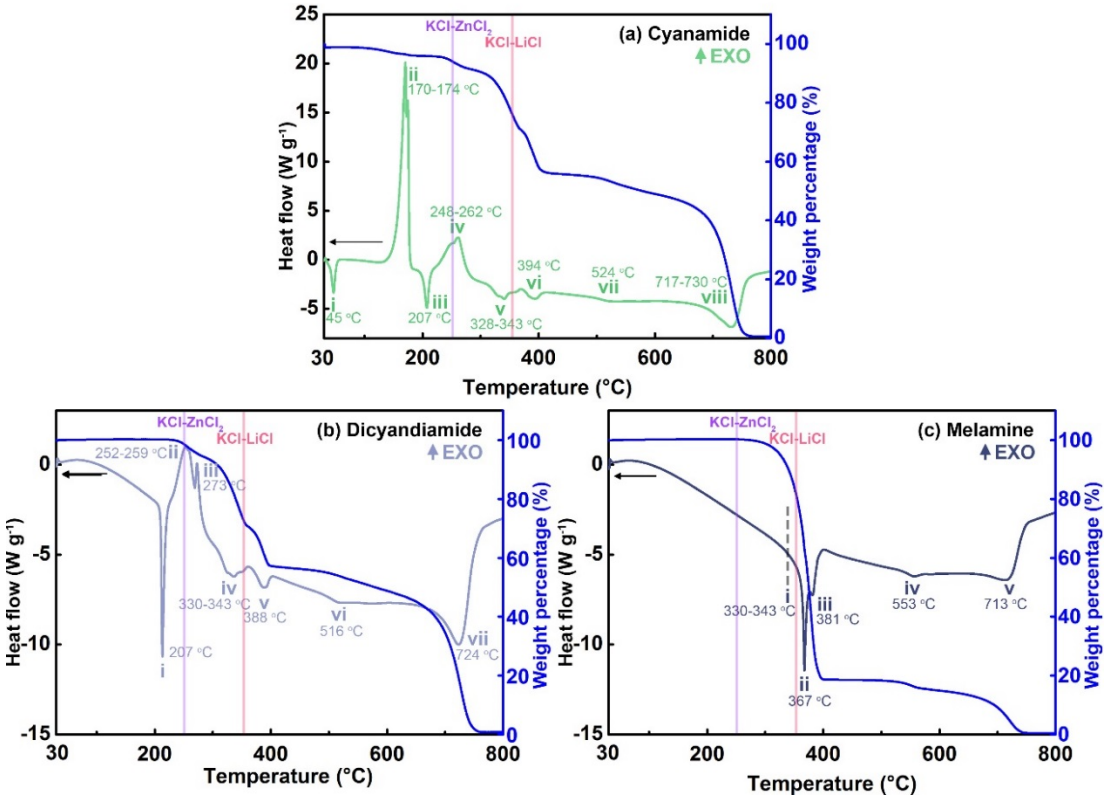

Figure 3.2. The TGA and heat flow curves of (a) cyanamide (b) dicyandiamide and (c) melamine under protection of flowing N_2 (100 sccm). The peak pointing up representing the exothermal process. The eutectic temperatures of LiCl-KCl mixture (352 ºC) and KCl-$ZnCl_2$ (250 ºC) were marked using pink and purple solid lines respectively.

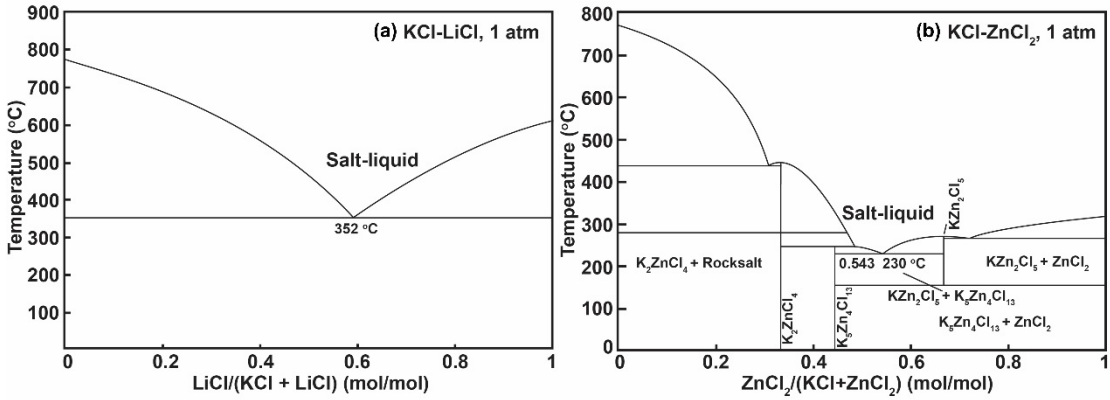

Figure 3.3. Phase diagrams of (a) KCl-LiCl and (b) KCl-$ZnCl_2$ salt mixture systems [49, 50]

3.2.2 Characterization of molecular structure

The crystal structure of prepared C_3N_4 has been characterized via the XRD experiments. **Figure 3.4**(a) indicates that all the samples prepared in KCl-$ZnCl_2$ molten salts exhibit the typical diffraction pattern of C_3N_4 with only one prominent peak located at 27°. This peak is attributed to the (002) facets derived from the stacking of C_3N_4 layers[28]. Comparing with the control group samples of C_3N_4-M-Air and C_3N_4-D-Li, the samples prepared in KCl-$ZnCl_2$ molten salts show lower crystallinity. The peak corresponding to the (100) facets is only observable in the control group samples C_3N_4-M-Air and C_3N_4-D-Li, whereas this peak is not observed in the XRD patterns of the C_3N_4 synthesized in molten KCl-$ZnCl_2$. The absence of (1 0 0) peak indicates the less ordered on-plane heptazine unit repetition ascribed to the doping and structure distortion. The FTIR spectroscopy is used to characterize the molecular structures of the prepared C_3N_4 samples and the collected spectra are presented in **Figure 3.4**(b). It can be seen that all the 3 samples prepared in molten KCl-$ZnCl_2$ system show similar patterns with C_3N_4-M-Air. The peak at 807 cm^{-1} is assigned to the breathing mode of the triazine unit is weak, which indicates the high condensation degree for all three samples. The peak at 807 cm^{-1} can be assigned to the breathing mode of the triazine unit. The peaks from 1621 to 1240 cm^{-1} can be attributed to the C-N-C or C-NH-C vibration in the heptazine heterocyclic structure [28, 45, 57]. And the peak at 2177 is derived from the vibration of -C≡N group [7, 57]. Comparing the FTIR spectra of samples synthesized in eutectic KCl-$ZnCl_2$ salts with C_3N_4-D-Air, the C_3N_4-C, C_3N_4-D, C_3N_4-M samples shows weaker absorption for the C-N-C heterocycle range (1240-1621 cm^{-1}). It suggests the samples synthesized in eutectic KCl-$ZnCl_2$ salts exhibit a more disordered structure than the C_3N_4-D-Air, which is consistent with XRD results (**Figure 3.4**(a)).

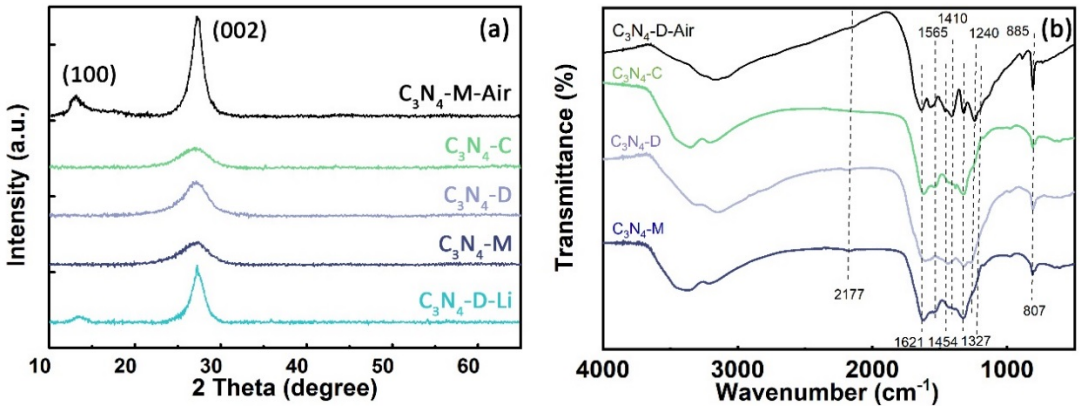

Figure 3.4.The (a) XRD patterns and (b) FTIR spectra of C_3N_4-C, C_3N_4-D, C_3N_4-M and control groups of C_3N_4-M-Air and C_3N_4-D-Li.

XPS is an effective tool to analyse the molecular structure of the prepared C_3N_4. The samples synthesized in eutectic KCl-$ZnCl_2$ with different precursors exhibit similar XPS spectra with the control group samples. As presented in **Figure 3.5**(a), the C 1s spectra can be further deconvoluted into 3 peaks for all 5 samples. Peaks located at 284.6 eV, 286.4 eV and 288.2 eV are ascribed to the adventitious carbon and C-NH_2, N-C=N bonds in the heptazine unit, respectively [58, 59]. There is an extra C 1s peak at 287.3 eV in the spectrum of C_3N_4-C, which is attributed to the C=N or C=O [60-62]. Similarly, the N 1s spectra, shown in **Figure 3.5**(b), are further deconvoluted into 3 peaks too. The peak at a binding energy of 398.7 eV is assigned to the sp^2-hybridized aromatic triazine rings (N2C, C-N=C); peak at 399.9 eV is assigned to the tertiary nitrogen (N3C) bonding; peak at 400.8 eV is attributed to the -NH_x functional groups [2, 59]. The similar assignments of C 1s and N 1s peaks suggest that the samples synthesized in eutectic KCl-$ZnCl_2$ salts are constituted by on-plane repeating heptazine units. The slightly different C 1s spectrum of C_3N_4-C indicates its highly disordered structure and low crystallinity, which is in consistency with XRD and FTIR analyses (**Figure 3.4** (a, b)). These experimental results suggest that the precursor with a smaller initial condensation degree results in a more disordered final C_3N_4 structure during the molten salts synthesis. The reason can be attribute to the initial molecule polymer condensation degree of precursor is low, it can be greatly affected by molten salt during the synthesis process. Therefore, the degree of disorder of C_3N_4 is high.

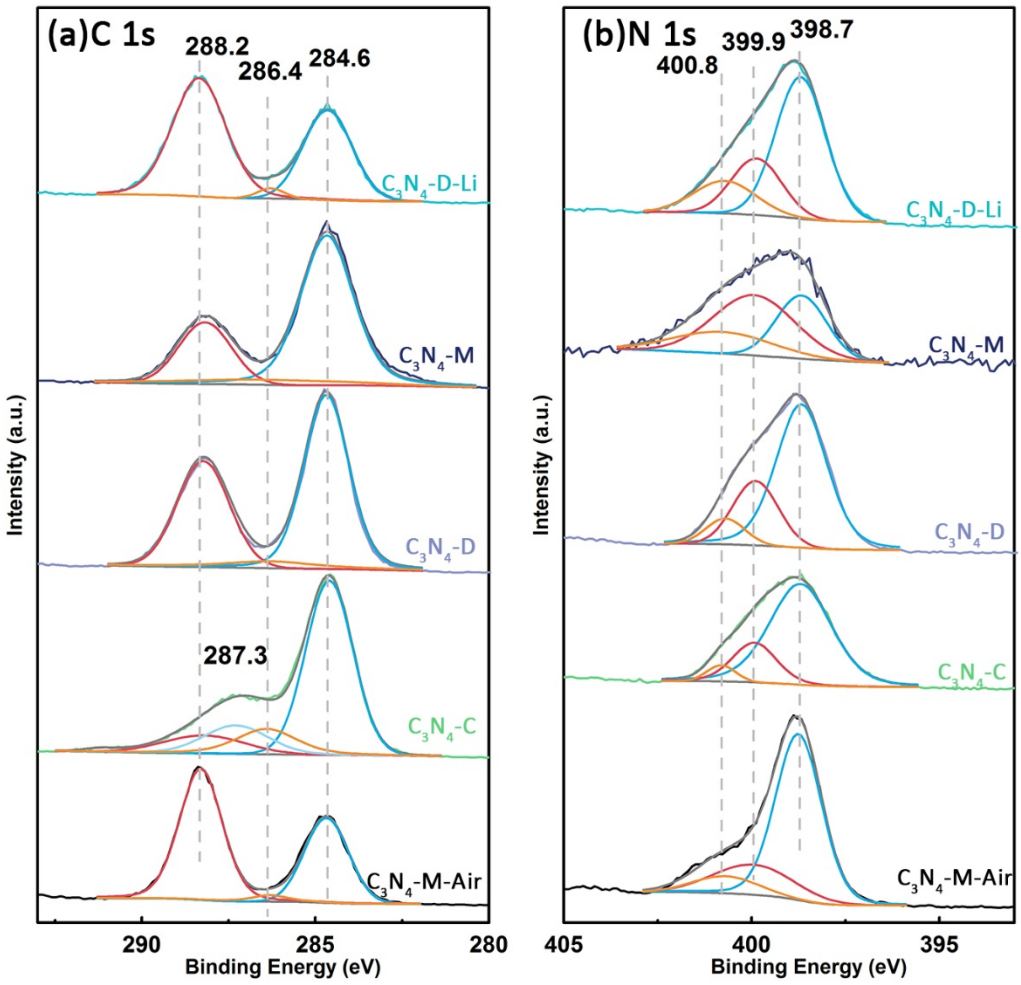

Figure 3.5. XPS (a) C 1s and (b) N 1s spectra of C_3N_4-C, C_3N_4-D, C_3N_4-M and control groups of C_3N_4-M-Air and C_3N_4-D-Li.

To further examine the possible doping during the synthesis in the molten salts, the Zn 2p, K 2p and Cl 2p spectra are collected and plotted in **Figure 3.6**(a-c). It can be seen that the Zn dopants are only found in C_3N_4-D, C_3N_4-C samples with significant concentration. In C_3N_4-M, the Zn dopant is of trace quantities. The Zn 2p3/2 and 2p1/2 peaks are located at 1021.6 and 1044.6 eV, respectively, which are assigned to Zn^{2+} coordinated into the electron-rich heptazine unit [5, 17]. Although K and Cl are common dopants for C_3N_4 in the literature, the XPS spectra of K 2p and Cl 2p suggest the non-existence of K and Cl dopants in all the 5 C_3N_4 samples. Therefore, it can be concluded that Zn is the only dopant in the C_3N_4 synthesized in KCl-$ZnCl_2$ molten salts. The Zn doping to C_3N_4 is likely to happen before the formation of melamine oligomers because no dopant is found when using melamine as the precursor (C_3N_4-M). It also needs to be noted no dopant was observed in C_3N_4-D-Li, which suggests that the

presence of melted phase of salts is also essential for the success of atomic doping. As shown in **Figure 3.2** and **Table 3.1**, the melting point of KCl-$ZnCl_2$ (230 °C) is lower than the formation temperature of melamine. On the contrary, the conventional KCl-LiCl system has a melting point (352 °C) remarkably higher than the melamine formation temperature (248-273°C). In summary, the successful preparation of doped C_3N_4 via molten salt synthesis method needs to meet two conditions: (i) the condensation degree of the precursor is lower than melamine; (ii) the melting temperature of the salt mixture is lower than the formation temperature of melamine.

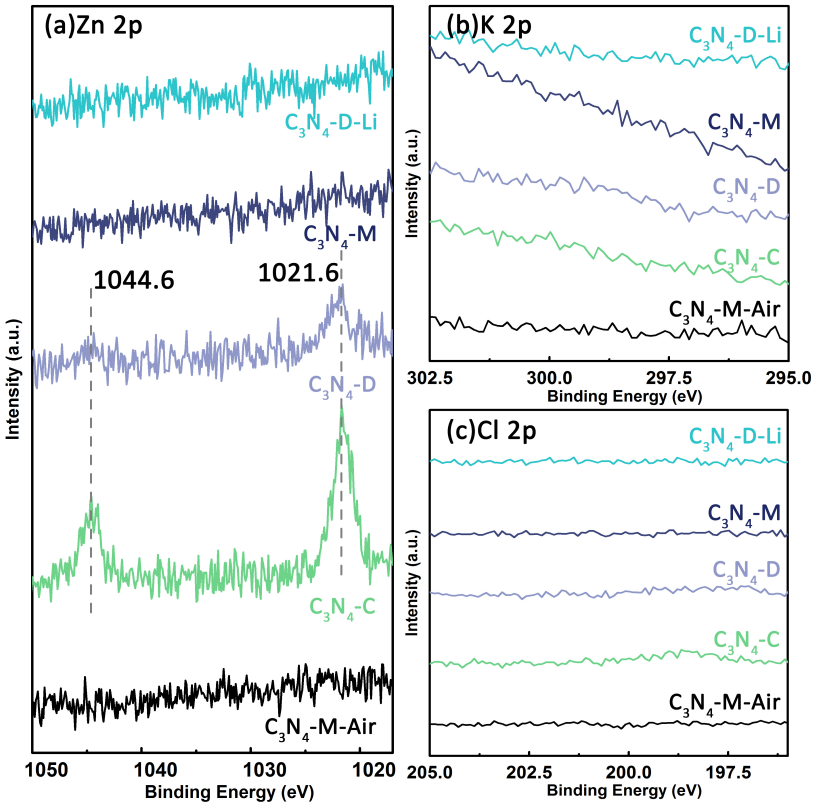

Figure 3.6. (a) Zn 2p (b) K 2p and (c) Cl 2p spectra of C_3N_4-C, C_3N_4-D, C_3N_4-M and control groups of C_3N_4-M-Air and C_3N_4-D-Li.

Organic elemental analysis (C, N, H) is an important method to help understand the effects of different organic precursors on the molecular structures of C_3N_4 synthesized in KCl-$ZnCl_2$ molten salts. As summarized in **Table 3.2**, the C_3N_4-M-Air shows the C/N atomic ratio of ~0.69, which is close to the theoretical C/N atom ratio in the melon and also in consistence with former reports [2, 46, 63]. The C/N atomic ratio of C_3N_4-M-Air also provides a good reference for other samples. It can be seen that the C/N atomic ratios of C_3N_4-D, C_3N_4-M and C_3N_4-D-Li samples are very similar to the C_3N_4-M-Air reference. This result suggests that the

molten salts environment for C_3N_4 synthesis doesn't affect the C/N ratios, and the Zn atoms embedded are present as interstitial rather than the substitutional dopants. The only exception is the C_3N_4-C with significantly reduced C/N atomic ratio, which is estimated at ~0.678. Additionally, the C_3N_4 synthesized in molten salts also show higher contents of H atoms. The C_3N_4-C, C_3N_4-D and C_3N_4-M contain the H atoms in the weight percentages of 2.85%, 3.11% and 3.06%, which are remarkably higher than C_3N_4-M-Air of 1.65%. These results are ascribed to the higher structure distortion and doping concentration, as also suggested by the XRD, FTIR, XPS and TGA analyses (**Figure 3.5** and **Figure 3.12**).

Table 3.2. Organic elemental results of C_3N_4-C, C_3N_4-D, C_3N_4-M and control groups of C_3N_4-M-Air and C_3N_4-D-Li.

Photocatalyst	N (wt%)	C (wt%)	H (wt%)	C/N (weight ratio)	C/N (atomic ratio)
C_3N_4-M-Air	57.61	34.10	1.65	0.5919	0.6906
C_3N_4-C	48.80	28.34	2.85	0.5807	0.6775
C_3N_4-D	51.27	30.36	3.11	0.5922	0.6908
C_3N_4-M	52.06	30.93	3.06	0.5941	0.6932
C_3N_4-D-Li	50.56	30.06	2.75	0.5945	0.6936

3.2.3 Electronic structure of C_3N_4 synthesized in eutectic KCl-$ZnCl_2$ salts

Comparing with molecular structures, the electronic structures of C_3N_4 samples is more important because the VBM and CBM determine the photooxidation and photoreduction potentials of the catalysts, respectively. The VBM positions are measured via the XPS VB spectroscopy analyses and the binding energy for VBM is determined by finding the intersects on the axis of binding energy. As shown in **Figure 3.7**, all samples exhibit the typical semiconductor VB spectra features. For C_3N_4 synthesized in eutectic KCl-$ZnCl_2$, the C_3N_4-C, C_3N_4-D, C_3N_4-M show the binding energy of VBM at 1.28, 2.33, 2.47 eV respectively. While the VBM binding energy of the control group sample C_3N_4-M-Air and C_3N_4-D-Li are 2.25 and 2.11 eV respectively. In order to further align the band edge positions between different samples, the VBM versus standard hydrogen electrode (SHE) is calculated using following equation with the X-ray photoelectron spectrometer work function (Φ) of 3.83 eV and the binding energy of VBM (E_{BE}) [2, 64]:

$$VBM(vs.SHE) = \Phi + E_{BE} - 4.44 \quad (3.1)$$

where -4.44 (eV) is the energy of vacuum referring to SHE. Therefore, the VBM (vs. SHE) of C_3N_4-C, C_3N_4-D, C_3N_4-M are calculated to be 0.67, 1.72, 1.86 eV, the VBM (vs. SHE) of C_3N_4-M-Air and C_3N_4-D-Li are calculated to be 1.64, 1.50 eV, respectively.

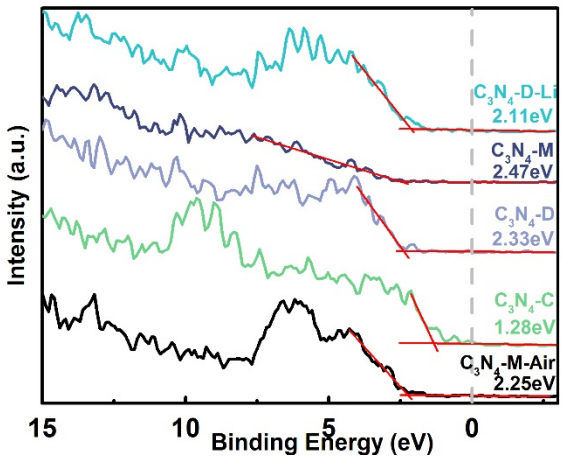

Figure 3.7. XPS VB spectra of C_3N_4-C, C_3N_4-D, C_3N_4-M and control groups of C_3N_4-M-Air and C_3N_4-D-Li.

The optical bandgaps of the prepared samples are derived from the UV-Vis DR spectroscopy. The optical responses of the samples to the incident light are plotted in Kubelka-Monk, as shown in **Figure 3.8**(a). It can be seen that the samples exhibit typical semiconductor behaviour. The optical bandgaps are determined by converting **Figure 3.8**(a) to the corresponding Tauc plot, as shown in **Figure 3.8**(b). Based on extrapolating the linear range of the curves to the incident light energy axis, the optical bandgaps are determined to be 3.07, 3.17 and 3.15 eV for C_3N_4-C, C_3N_4-D and C_3N_4-M, respectively. Using the same method, the bandgaps of C_3N_4-M-Air and C_3N_4-D-Li are calculated to be 2.65 eV and 2.90 eV, respectively, which are in consistence with previous investigations [2, 28, 65]. It is also noted that all samples synthesized in the molten salts show broadened bandgap than the C_3N_4-M-Air. The bandgap increase positively correlates with the SSA increase (**Figure 3.10** (a)), which is possibly due to the effects that reduced the g-C_3N_4 particle size can narrow the bandgap [1, 4, 66].

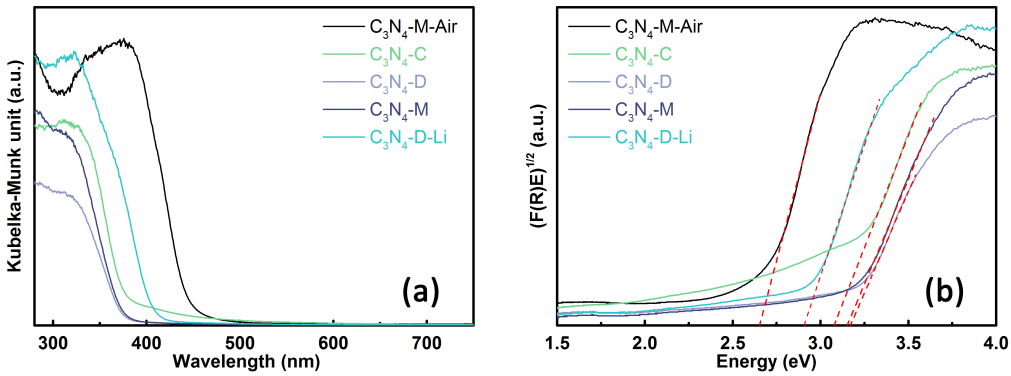

Figure 3.8. (a) UV-Vis DRS and (b) corresponding Tauc plot of C_3N_4-C, C_3N_4-D, C_3N_4-M and control groups of C_3N_4-M-Air and C_3N_4-D-Li.

The CBM (*vs* SHE) can be determined from the sum of VBM (*vs* SHE) and optical bandgap (E_g):

$$\mathrm{CBM}(vs\ \mathrm{SHE}) = \mathrm{VBM}(vs\ \mathrm{SHE}) - \mathrm{E_g} \tag{3.2}$$

The energy positions of CBM (vs SHE) are calculated to be -2.40, -1.45, -1.29 eV for C_3N_4-C, C_3N_4-D, C_3N_4-M, and -1.01, -1.40 eV for control groups C_3N_4-M-Air, C_3N_4-D-Li, respectively. The band position alignments are summarized and plotted in **Figure 3.9**. It can be seen from the band position alignment plot that the C_3N_4-D and C_3N_4-M show the more positive VBM comparing with control group sample C_3N_4-M-Air and C_3N_4-D-Li, which ensures the higher photooxidation capability. However, it is worth emphasizing that the moderate Zn doping concentration is critical because Zn dopant with smaller Mulliken electronegativity than C/N intends to shift the CBM/VBM to the negative direction.

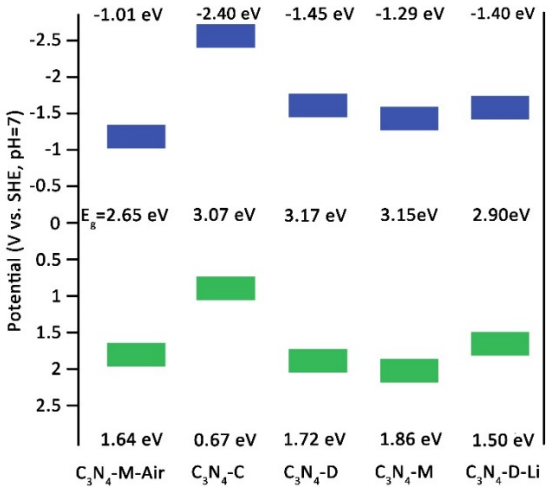

Figure 3.9. Band position alignment plot for samples prepared in KCl-$ZnCl_2$: C_3N_4-C, C_3N_4-D, C_3N_4-M and the control group samples C_3N_4-M-Air, C_3N_4-D-Li.

3.2.4 Morphology and specific surface area

SSA is a critical parameter for the high-performance photocatalysts since a larger SSA ensures more active sites for reaction. However, low SSA is one of the main drawbacks of C_3N_4. For conventional thermal polymerization of melamine or dicyandiamide in the air at 500 °C, the SSA for prepared C_3N_4 is usually ~10 m^2 g^{-1} [28]. Even for urea or thiourea as the precursor, the reported SSA for the derived two-dimensional or porous C_3N_4 is typically only ~50-70 m^2 g^{-1} [54, 67-69]. The SSA of the samples prepared in this work is calculated based on the N_2 sorption isotherms obtained at 77 K, using the Brunauer-Emmett-Teller (BET) method (**Figure 3.10** (a)). The derived SSA for C_3N_4-M-Air as the control group is 14.9 m^2 g^{-1}, which is consistent with the result in the literature [28]. For C_3N_4-D-Li, the C_3N_4 synthesized in the conventional KCl-LiCl eutectic system shows an improved SSA of 57.5 m^2 g^{-1}. Comparatively, this new molten salt synthesis method using KCl-$ZnCl_2$ eutectic salt mixture shows extraordinary enhancement on the SSA of C_3N_4. The SSAs for C_3N_4-C, C_3N_4-D and C_3N_4-M are measured to be 110, 138.6 and 171.6 m^2 g^{-1}, respectively. They are significantly higher than either of the control group samples. It is worth comparing the pore size distribution curves to unravel the structural differences. As shown in **Figure 3.10**(b), the C_3N_4-M-Air synthesized via thermal condensation of melamine in air shows no obvious peaks, which is ascribed to its non-porous bulk structure. On the contrary, the C_3N_4-C, C_3N_4-D and C_3N_4-M show the peaks corresponding to the pore size of 3-4 nm. These mesopores are likely derived from the stacking of C_3N_4 nanoparticles with reduced sizes. In summary, it is proven that the C_3N_4 synthesized in KCl-$ZnCl_2$ molten salts show larger SSA than the C_3N_4 synthesized via the conventional thermal polycondensation in static air or in KCl-LiCl salt mixture with higher melting temperature.

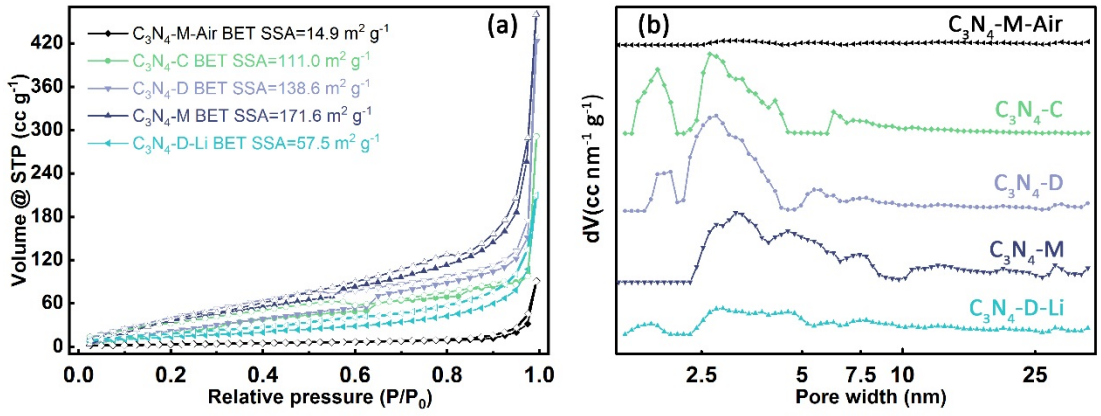

Figure 3.10. (a) N_2 sorption isotherms at 77 K and (b) pore size distribution curve of C_3N_4-C, C_3N_4-D, C_3N_4-M and control groups of C_3N_4-M-Air and C_3N_4-D-Li

The morphologies of the prepared samples are examined with SEM images and the corresponding EDS analyses, as shown in **Figure 3.11**(a-o). **Figure 3.11** (a, b) indicates that the control group sample C_3N_4-M-Air exhibit the relatively large particles with the diameter of several microns. The large size of the particles limits the SSA to 14.9 $m^2 g^{-1}$. For the sample synthesized in eutectic LiCl-KCl, the C_3N_4-D-Li (**Figure 3.11** (m, n)) exhibits a smaller particle in submicron size. The reduced particle size induces an enlarged SSA of 57.5 $m^2 g^{-1}$. For the samples synthesized in eutectic KCl-$ZnCl_2$, the C_3N_4-C (**Figure 3.11** (d, e)), C_3N_4-D (**Figure 3.11** (g, h)) and C_3N_4-M(**Figure 3.11** (j, k)) exhibit the nanoparticles with a diameter smaller than 200 nm and the size decreases in the sequence of C_3N_4-C, C_3N_4-D, C_3N_4-M, which is in consistence with the BET-SSA results (**Figure 3.11** (a)). The EDS is used to identify the possible doping elements in the prepared C_3N_4 samples. From **Figure 3.11** (c, f, i, l, o), it can be summarized that all the samples are mainly constituted by the C, N, O elements. For the control group sample C_3N_4-M-Air and C_3N_4-D-Li, the EDS spectra suggest that no dopant exists in the C_3N_4 crystals. For the samples synthesized in the eutectic KCl-$ZnCl_2$, the EDS results indicate that the Zn is doped in the C_3N_4-C, C_3N_4-D and Cl is only in negligible amount. Different from C_3N_4-C and C_3N_4-D, Zn EDS signal is very weak in the C_3N_4-M. The EDS results suggest the C_3N_4 synthesized using the cyanamide with lowest condensation degree exhibits the highest possibility of doping, while the melamine with the highest condensation degree shows the lowest doping possibility.

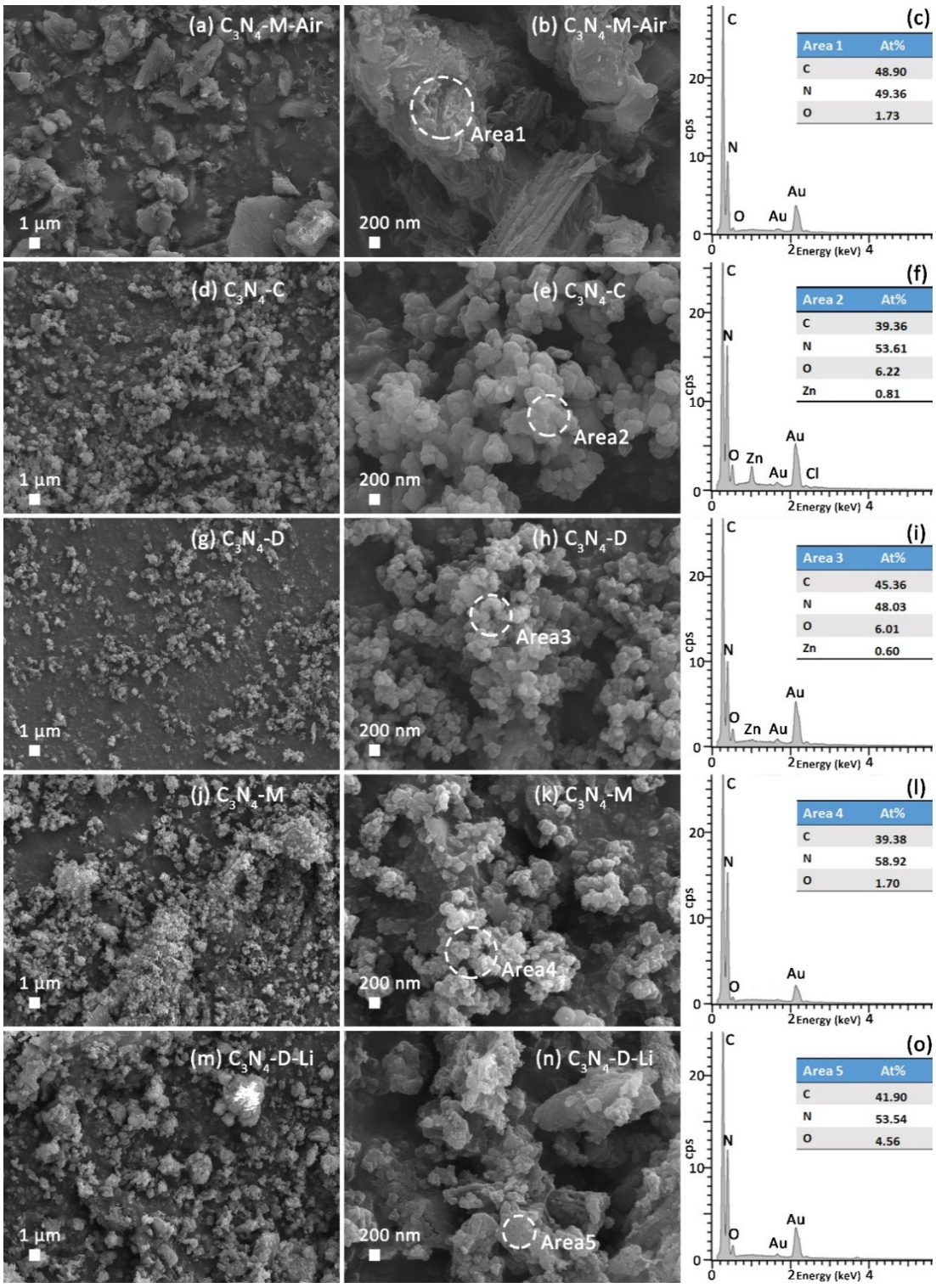

Figure 3.11. SEM images and corresponding EDS analyses of (a, b, c) C_3N_4-M-Air, (c, d, e) C_3N_4-C, (g, h, i) C_3N_4-D, (j, k, l) C_3N_4-M and (m, n, o) C_3N_4-D-Li.

3.2.5 Thermogravimetric results

In order to quantitively determine the concentration of Zn dopants, TGA analyses were conducted on the C_3N_4-C, C_3N_4-D, C_3N_4-M and control group samples C_3N_4-D-Li and C_3N_4-M-Air from room temperature to 1000 ºC under flowing Air (100 sccm). The remained weights in the air at 1000 ºC are 6.71%, 5.40%, 0.24% for C_3N_4-C, C_3N_4-D, C_3N_4-M, respectively (as shown in **Figure 3.12**). The control group samples C_3N_4-M-Air and C_3N_4-D-Li shows negligible residual weights. These remained materials should be the doping elements in their most stable oxide form. Since Zn has been proven as the only dopant as detected by XPS (**Figure 3.6**), EDS (**Figure 3.11**) analyses, the remained weights are believed to be ZnO. Therefore, the calculated Zn dopants concentrations are 5.39wt%, 4.34wt% and 0.19wt% for C_3N_4-C, C_3N_4-D, C_3N_4-M, respectively (summarized in **Table 3.3**). Note that the content of the dopant increases in the sequence of C_3N_4-M< C_3N_4-D < C_3N_4-C, which is opposite to the sequence of organic precursor polycondensation degree. The result indicates the use of the precursor with a lower condensation degree will result in a more heavily doped C_3N_4.

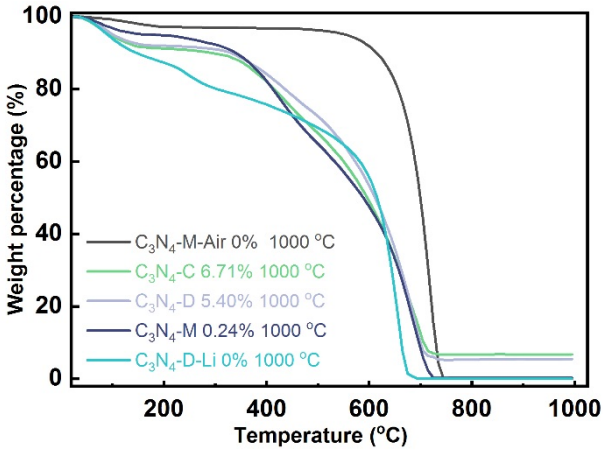

Figure 3.12. TGA analyses in flowing air (50 sccm) of C_3N_4-C, C_3N_4-D, C_3N_4-M and control group sample C_3N_4-D-Li.

Table 3.3. Zn doping concentrations calculated by TGA

	Zn dopant (wt%, TGA)
C_3N_4-C	5.39
C_3N_4-D	4.34
C_3N_4-M	0.19
C_3N_4-M-Air	0
C_3N_4-D-Li	0

3.2.6 Photoelectrochemical analyses

Photocurrent response is an important evidence reflecting the ability of photocatalysts in generating electron-hole pairs under light irradiation. As shown in **Figure 3.13**, the C_3N_4-D shows the highest photocurrent density under irradiation. The photocurrent density generated by C_3N_4-D reaches 370.3 nA cm^{-2} on average, which is ~9.8 times as much as the C_3N_4-M-Air (37.9 nA cm^{-2}). The C_3N_4-M shows the second-largest photocurrents of 92.9 nA cm^{-2}. The remarkably enhanced photocurrent density of C_3N_4-D proves that the moderate Zn doping introduced during the $ZnCl_2$-KCl molten salts synthesis can facilitate the electron/hole separation and increase the carrier lifetime. The slightly inferior current density of C_3N_4-M and C_3N_4-C can be explained by the enlarged band gap (**Figure 3.9**), lower crystallinity and nonoptimal Zn doping concentration. (**Table 3.3**).

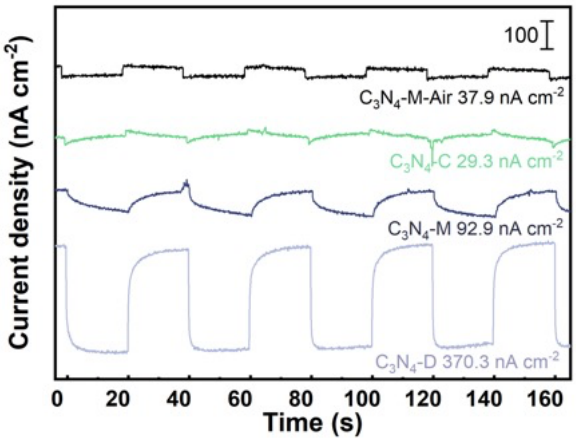

Figure 3.13. Transient photocurrent responses for C_3N_4-C, C_3N_4-D, C_3N_4-M and control group C_3N_4-M-Air.

3.2.7 Charge separation efficiency

To rationalize the enhanced photocatalytic performance of C_3N_4-D in comparison with other counterparts, the charge carrier separation efficiencies of the prepared samples are characterized by the photoluminence (PL) spectroscopy method. As shown in **Figure 3.14** (a), the steady-state PL spectra of C_3N_4 synthesized in KCl-$ZnCl_2$ eutectic salts shows the emission peaks at ~ 400 nm, which indicates the broader bandgaps of these samples. It is important to emphasize that the reduced steady-state PL intensity can be attributed to the larger probability of non-radioactive recombination. Therefore, the charge carrier separation efficiency is further characterized by the time-resolved PL spectroscopy. By monitoring the peak emission

wavelength, the time-resolved PL decays are measured for C_3N_4-D, C_3N_4-M and two control group samples C_3N_4-M-Air and C_3N_4-D-Li. As presented in **Figure 3.14** (b), the average carrier lifetime of C_3N_4-D is 1.34 ns, which is significantly longer than the 0.61 ns of C_3N_4-M, 0.86 ns of C_3N_4-M-Air and 0.79 ns of C_3N_4-D-Li. The longer carrier lifetime of the C_3N_4-D is attributed to the fact that the Zn dopant energy level can trap the charge carriers temporally before the recombination.

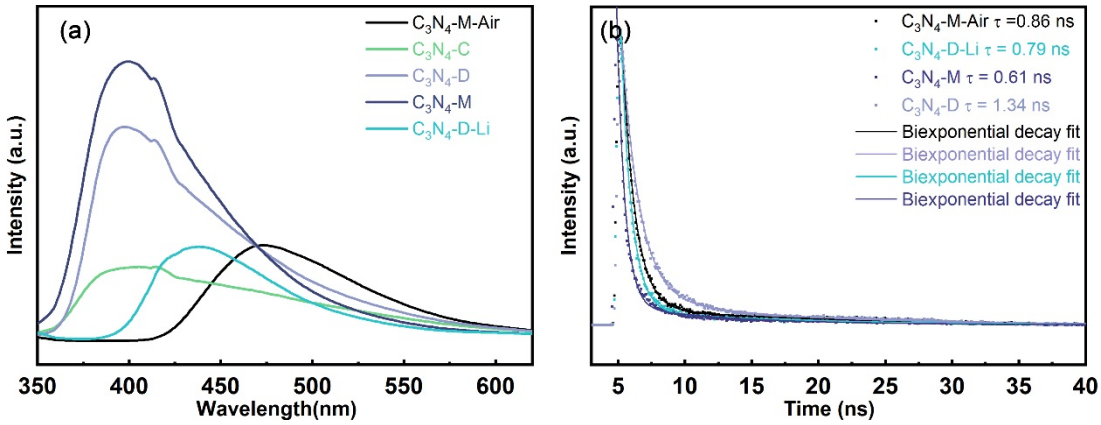

Figure 3.14. (a) Steady-state and (b) time-resolved photoluminence spectra of C_3N_4-D, C_3N_4-M and control group sample C_3N_4-M-Air and C_3N_4-D-Li.

3.3 Photocatalytic dye-degradation performance

3.3.1 Comparison between UV-vis and visible light photodegradation

Before doing a systematic photocatalytic degradation experiment, it is very important to determine the appropriate reaction conditions. To find the suitable irradiation condition of photocatalytic degradation for prepared samples, different types of light illumination were tested on C_3N_4-C. The precursor of the sample C_3N_4-C is cyanamide, and the specific synthesis process can be found in **section 2.2.1**. At the first 25 min, the solution with catalysts was kept in the dark under the stirring condition to demonstrate the adsorption capabilities of the samples. The photocatalytic reaction was conducted for 125 min, and the aliquots concentrations were measured every 25 min. The incident light sources are visible light (420 nm cut-off filter) and simulated solar light range (no filter). The RhB decomposition reached 14.99% after 125-min visible light irradiation. When the illumination changes to the simulated solar light range, the photocatalytic RhB degradation increased to 47.37% under the same reaction conditions (as shown in **Figure 3.15**). This phenomenon agreed well with the wide

bandgap of the prepared samples. The bang gap calculated from DRS for C_3N_4-C, C_3N_4-D and C_3N_4-M are 3.07 eV, 3.17 eV and 3.15 eV, respectively (**Figure 3.8**). According to the Eq.(1.12), to generate the photoinduced electron-hole pairs in C_3N_4-C, the wavelength of incident light λ_g should be smaller than 403.8 nm. Therefore, the UV-Vis light is needed to drive the dye photodegradation over g- C_3N_4 synthesized in molten salts. The incident light range of simulated sunlight is 190-1100 nm, which can make the sample have obvious photocatalytic degradation efficiency. To compare the photocatalytic activities of the prepared sample, simulated solar light spectrum provided by a Xenon lamp was used throughout the experiments.

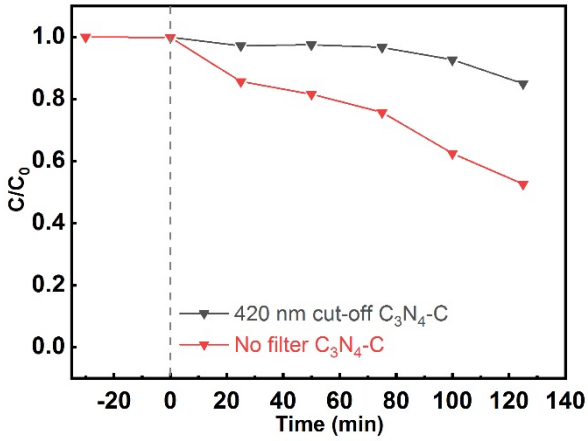

Figure 3.15. Photocatalytic RhB degradation performance of C_3N_4-C under visible light and UV-Vis light irradiation

3.3.2 Comparison between MO and RhB photodegradation

To unravel the surface charge of g-C_3N_4 synthesized in molten salts, the photodegradation performances are compared between MO and RhB over C_3N_4-C. Since MO is an anionic dye and RhB is a non-ionic dye, the surface charge of g-C_3N_4 will largely affect their photodegradation rate. As shown in **Figure 3.16** in dark the g-C_3N_4 shows a stronger MO adsorption, whereas the RhB shows negligible adsorption. It proves that the g-C_3N_4 synthesized in molten-salts shows positive charge on the surface. The positive charge might derive from the preparation process. After polymerization of g-C_3N_4 in molten salts, the HNO_3 (5%) aqueous solution was used to wash the powders and remove the residual salts from the g-C_3N_4 surface. Although the samples were then well-rinsed by DI water, H^+ still inevitably remains on the surface, resulting in extra positive surface charges. The faster photo-

degradation of MO to RhB can be partially attributed to the enhanced MO adsorption on the surface.

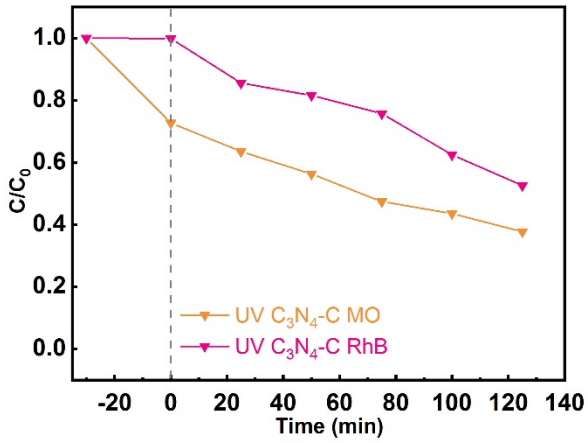

Figure 3.16. Photocatalytic RhB and MO degradation performance of C_3N_4-C under UV-Vis light irradiation

3.3.3 Photocatalytic dye-degradation performance

The photocatalytic activities of the C_3N_4 prepared under different conditions are evaluated via the probe reaction MO photocatalytic degradation. After the first 25 min under dark (at time 0), two control group samples (C_3N_4-M-Air and C_3N_4-D-Li) show negligible adsorption ability, which can be attributed to their poor SSA (14.9 and 57.5 m^2 g^{-1} respectively). In the case of the samples synthesized in KCl-$ZnCl_2$ molten salts, all the samples exhibit the improved adsorption ability to MO comparing with C_3N_4-D-Li and C_3N_4-M-Air due to the larger SSAs. Among them, the C3N4-D exhibits the highest adsorption ability that the MO concentration (C) drops to 72.8% of the initial concentration (C_0). Although the SSA of the g- C_3N_4 synthesized in KCl-$ZnCl_2$ shows the sequence of C_3N_4-M > C_3N_4- D > C_3N_4-C, the sequence of MO adsorption capability is C_3N_4-D > C_3N_4-M ≈ C_3N_4-D. Therefore, the optimal adsorption performance of C_3N_4-D is likely to be explained by the balance achieved between SSA, polycondensation degree and Zn doping: low poly- condensation degree and higher Zn doping concentration increase the MO adsorption ability [28, 70, 71] whereas decrease the SSA (as shown in **Figure 3.10**(a)).

In the photocatalytic MO degradation under simulated solar light, the C_3N_4-D also exhibits the highest photocatalytic activity. After 125 min of photocatalytic reaction, the C_3N_4-D degrades the MO concentration to the 2.5% of the initial concentration. While C_3N_4-C, C_3N_4-M only

reduce the MO concentration to 37.7% and 27.7% of the initial concentration, respectively. In addition, all the samples synthesized via the KCl-$ZnCl_2$ molten salts method outperform the control group samples C_3N_4-M-Air and C_3N_4-D-Li, which only reduce the MO concentrations to 43.5% and 64.3%, respectively. To further compare the photocatalytic activity of the photocatalysts, the kinetic reaction rate constants are calculated based on the pseudo-first kinetic model. As shown in **Figure 3.17**(b), the pseudo-first-order reaction kinetic model can be well fitted with the experimental data with the R^2. The calculated rate constant *k* is summarized in **Table 3.4**. It is noted that the reaction rate constant *k* for the optimal sample C_3N_4-D is 415% and 659% of the control group samples C_3N_4-M-Air and C_3N_4-D-Li. The significantly enhanced photocatalytic activity of C_3N_4-D strongly demonstrates the superiority of the new C_3N_4 synthesis method in KCl-$ZnCl_2$ molten salts towards the conventional thermal polymerization method in static air or LiCl-KCl molten salts.

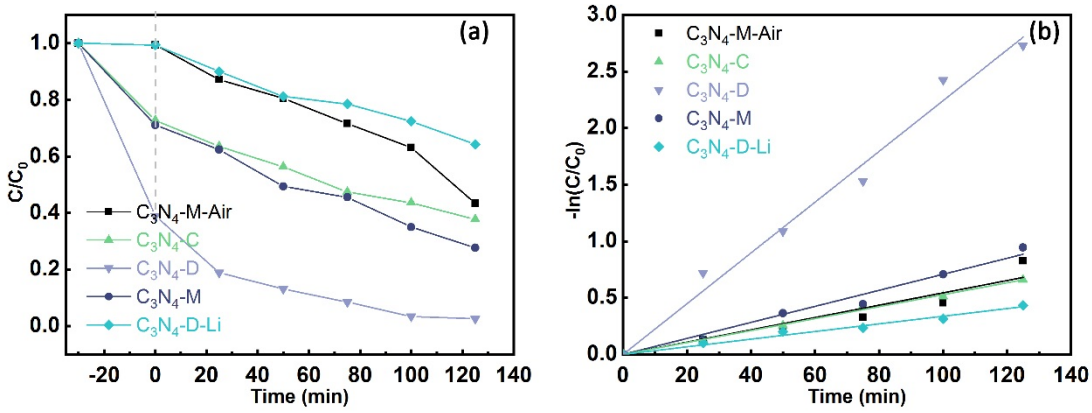

Figure 3.17. (a) Photocatalytic MO degradation performance and (b) pseudo-first-order kinetic plot of C_3N_4-C, C_3N_4-D, C_3N_4-M and control group sample C_3N_4-D-Li under UV-Vis light irradiation.

Table 3.4. Fitting results of the reaction rate constants based on the pseudo-first-order kinetic model

Photocatalyst	Rate constant *k* (min^{-1}) (10^{-3})	R^2
C_3N_4-M-Air	5.4	0.9621
C_3N_4-C	5.2	0.9986
C_3N_4-D	22.4	0.9824
C_3N_4-M	7.1	0.9923
C_3N_4-D-Li	3.4	0.9941

3.3.4 Cyclic performance tests

The stability of the prepared catalysts is an important criterion for performance evaluation. The optimal C_3N_4-D catalyst was chosen to perform the recycling experiments. The fresh C_3N_4-D was firstly conducted a photocatalytic MO degradation and recycled from the solution via centrifuging. After rinsing with DI-water for several times and drying under vacuum, the recycled C_3N_4-D was used to conduct another photocatalytic MO degradation experimental following the same procedure. The photocatalytic MO degradation performances of the 3 recycling experiments are presented in **Figure 3.18**. It can be seen that the C_3N_4-D shows no apparent deactivation after 3 successive photocatalytic degradations. The results indicate that the C_3N_4-D synthesized via the molten salt method exhibit good stability in working conditions.

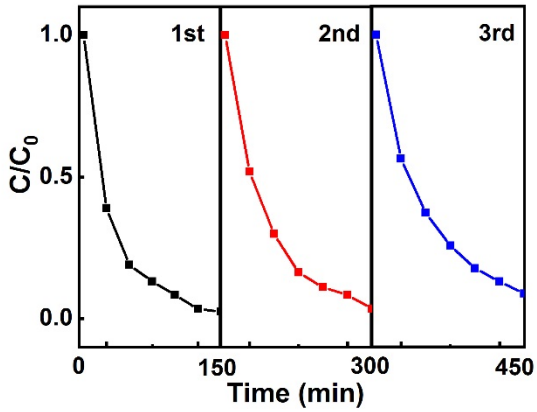

Figure 3.18. Photocatalytic degradation of MO performances for recycled C_3N_4-D under UV-Vis light irradiation

3.3.5 Mechanism underpins the enhanced photocatalytic activity

The enhanced photocatalytic activities of the samples synthesized in KCl-$ZnCl_2$ eutectic salts are reasonably ascribed to the following four reasons: (i) enlarged SSA, (ii) enhanced MO adsorption, (iii) optimized VBM position and (vi) reduced electron-hole recombination due to Zn doping. Firstly, as shown in **Figure 3.10**(a), the SSA is remarkably increased under the assistance of KCl-$ZnCl_2$ molten salts. The SSA of C_3N_4-D is 9.3 times of the C_3N_4-M-Air synthesized via the conventional thermal polymerization method and 2.4 times of C_3N_4-D-Li synthesized in conventional KCl-LiCl molten salts. It can be explained by the better dispersion of reaction intermediates in KCl-$ZnCl_2$ molten salts due to its lower melting temperature. The larger SSA provides more active sites for the photocatalytic degradation reaction and the

smaller particle size ensures a short transportation length for photo-excited charge carriers. Secondly, the Zn dopants and lower polycondensation degree induce the enhanced MO adsorption. As shown in **Figure 3.17**(a), the C_3N_4-D shows the highest adsorption to MO, whereas its SSA is not the largest. The Zn doping and moderate polycondensation degree are believed as the reasons for the promoted MO adsorption capability. Thirdly, C_3N_4-D shows the enhanced photooxidation capability due to the positively shifted VBM (**Figure 3.9**). Since the photocatalytic degradation is the MO oxidization driven by the photo-excited holes, a more positive VBM is preferred. Lastly, the appropriate amount of Zn dopant can help to suppress the photo-induced charge carrier recombination. It has been reported that a proper amount of dopant can suppress the recombination of photo-excited carriers by trapping them inside dopant energy states, while over-doped C_3N_4 exhibits deteriorated recombination due to the dopant acting as the recombination centre [72-75]. As characterized by XPS and TGA (**Figure 3.6**, **Figure 3.12**, **Table 3.3**), the Zn doping is achieved in a moderate concentration in C_3N_4-D comparing with C_3N_4-C and C_3N_4-M. The appropriate amount of Zn dopant ensures the facilitated electron-hole separation in the semiconductor, which is supported by the photocurrent response experiments (**Figure 3.13**) and time-resolved PL experiments (**Figure 3.14** (b)). It also rationalizes the result that C_3N_4-D shows superior photocatalytic activity to the C_3N_4-M, though the SSA and oxidation potential of C_3N_4-D is inferior to C_3N_4-M.

It is important to emphasize that the four advantages need to be balanced to achieve an optimal photocatalytic MO degradation performance. The low polycondensation degree of g-C_3N_4 benefits the MO adsorption capability and Zn doping suppresses electron-hole recombination. However, the over-doped Zn decreases the SSA, photooxidation capability and enhances recombination; the too low polycondensation degree is detrimental for charge carrier transportation and light absorption. Therefore, it rationalizes the existence of a temperature window in the g-C_3N_4 polycondensation process for the successful optimization of g-C_3N_4 via molten salts method.

3.4 Conclusion

In this chapter, C_3N_4 has been prepared via a novel method by conducting the thermal polycondensation of organic precursors in KCl-$ZnCl_2$ molten salts with low eutectic temperature. The effects of matching the condensation degrees of different precursors and KCl-$ZnCl_2$ eutectic temperature on the structure and photocatalytic activities of prepared C_3N_4

samples have been investigated with the carefully designed control groups. The experimental results suggest that locating the melting temperature of salt mixture within the temperature window between dicyandiamide and melamine formation steps in the polycondensation process is critical to the photocatalytic activity enhancement. Attributed to the low eutectic temperature of KCl-$ZnCl_2$ (230 ºC), the precursors can be better dispersed in the molten salts before converting to the larger melem molecules during the polycondensation process. The high SSA of 111.0, 138.6 and 171.6 m^2 g^{-1} have been achieved for the prepared C_3N_4 using cyanamide, dicyandiamide and melamine precursors, which are at least ~7.4 times as large as that of the C_3N_4 synthesized via the conventional procedure.

The samples synthesized in eutectic KCl-$ZnCl_2$ using dicyandiamide and melamine precursors (C_3N_4-D and C_3N_4-M) exhibit the optimized electronic structure for photocatalytic dye degradation. The VBM positions of those two samples shift to a positive direction, which ensures them an enhanced oxidation capability. In addition, the lower eutectic temperature of KCl-$ZnCl_2$ ensures the polycondensation step of converting the dicyandiamide oligomers to melamine species occurring in the liquid phase. It directly results in the Zn interstitial doping inside the C_3N_4 crystals. The C_3N_4-D shows a moderate Zn doping concentration, which helps to suppress the electron-hole recombination and contributes to the facilitated photocatalytic activity. This new C_3N_4 synthesis method of KCl-$ZnCl_2$ molten-salt and the effects of matching between eutectic temperature and polycondensation process on the photocatalytic activity of C_3N_4 catalysts could inspire future researches on the development of C_3N_4 as high-performance photocatalytic activity in many research fields.

References

[1] P. Xia, B. Zhu, J. Yu, S. Cao, M. Jaroniec, Ultra-Thin Nanosheet Assemblies of Graphitic Carbon Nitride for Enhanced Photocatalytic CO_2 Reduction, J. Mater. Chem. A, 5 (2017) 3230-3238.

[2] K. Wang, J.L. Fu, Y. Zheng, Insights into Photocatalytic CO_2 Reduction on C_3N_4: Strategy of Simultaneous B, K Co-doping and Enhancement by N Vacancies, Appl. Catal., B, 254 (2019) 270-282.

[3] L.H. Lin, H.H. Ou, Y.F. Zhang, X.C. Wang, Tri-s-triazine-Based Crystalline Graphitic Carbon Nitrides for Highly Efficient Hydrogen Evolution Photocatalysis, ACS Catal., 6 (2016) 3921-3931.

[4] Y. Li, R. Jin, Y. Xing, J. Li, S. Song, X. Liu, M. Li, R. Jin, Macroscopic Foam-Like Holey Ultrathin g-C3N4Nanosheets for Drastic Improvement of Visible-Light Photocatalytic Activity, Adv. Energy Mater., 6 (2016).

[5] X. Yuan, S. Duan, G. Wu, L. Sun, G. Cao, D. Li, H. Xu, Q. Li, D. Xia, Enhanced Catalytic Ozonation Performance of Highly Stabilized Mesoporous ZnO Doped g-C_3N_4 Composite for Efficient Water Decontamination, Appl. Catal., A, 551 (2018) 129-138.

[6] Z. Lu, L. Zeng, W. Song, Z. Qin, D. Zeng, C. Xie, In Situ Synthesis of C-TiO_2/g-C_3N_4 Heterojunction Nanocomposite as Highly Visible Light Active Photocatalyst Originated From Effective Interfacial Charge Transfer, Appl. Catal., B, 202 (2017) 489-499.

[7] H. Yu, R. Shi, Y. Zhao, T. Bian, Y. Zhao, C. Zhou, G.I.N. Waterhouse, L.Z. Wu, C.H. Tung, T. Zhang, Alkali-Assisted Synthesis of Nitrogen Deficient Graphitic Carbon Nitride with Tunable Band Structures for Efficient Visible-Light-Driven Hydrogen Evolution, Adv. Mater., 29 (2017).

[8] L. Ruan, G. Xu, L. Gu, C. Li, Y. Zhu, Y. Lu, The Physical Properties of Li-Doped g-C_3N_4 Monolayer Sheet Investigated by the First-Principles, Mater. Res. Bull., 66 (2015) 156-162.

[9] T. Xiong, W. Cen, Y. Zhang, F. Dong, Bridging the g-C_3N_4 Interlayers for Enhanced Photocatalysis, ACS Catal., 6 (2016) 2462-2472.

[10] J. Jiang, S. Cao, C. Hu, C. Chen, A Comparison Study of Alkali Metal-Doped g-C_3N_4 for Visible-Light Photocatalytic Hydrogen Evolution, Chin. J. Catal., 38 (2017) 1981-1989.

[11] Y. Pan, D. Li, H.L. Jiang, Sodium-Doped C_3N_4/MOF Heterojunction Composites with Tunable Band Structures for Photocatalysis: Interplay between Light Harvesting and Electron Transfer, Chem. - Eur. J., 24 (2018) 18403-18407.

[12] B. Zhu, J. Zhang, C. Jiang, B. Cheng, J. Yu, First Principle Investigation of Halogen-Doped Monolayer g-C_3N_4 Photocatalyst, Appl. Catal., B, 207 (2017) 27-34.

[13] Y. Huang, Q. Yan, H. Yan, Y. Tang, S. Chen, Z. Yu, C. Tian, B. Jiang, Layer Stacked Iodine and Phosphorus Co-doped C_3N_4 for Enhanced Visible-Light Photocatalytic Hydrogen Evolution, ChemCatChem, 9 (2017) 4083-4089.

[14] Z.-A. Lan, G. Zhang, X. Wang, A Facile Synthesis of Br-Modified g-C_3N_4 Semiconductors for Photoredox Water Splitting, Appl. Catal., B, 192 (2016) 116-125.

[15] K. Ding, L. Wen, M. Huang, Y. Zhang, Y. Lu, Z. Chen, How Does the B,F-Monodoping and B/F-Codoping Affect the Photocatalytic Water-Splitting Performance of g-C_3N_4?, Phys. Chem. Chem. Phys., 18 (2016) 19217-19226.

[16] L. Zeng, X. Ding, Z. Sun, W. Hua, W. Song, S. Liu, L. Huang, Enhancement of Photocatalytic Hydrogen Evolution Activity of g-C_3N_4 Induced by Structural Distortion via Post-Fluorination Treatment, Appl. Catal., B, 227 (2018) 276-284.

[17] B. Yue, Q. Li, H. Iwai, T. Kako, J. Ye, Hydrogen Production Using Zinc-Doped Carbon Nitride Catalyst Irradiated With Visible Light, Sci. Technol. Adv. Mater., 12 (2011) 034401.

[18] Z. Xing, Y. Chen, C. Liu, J. Yang, J. Xu, Y. Situ, H. Huang, Synthesis of Core-Shell ZnO/Oxygen Doped g-C_3N_4 Visible Light Driven Photocatalyst via Hydrothermal Method, J. Alloys Compd., 708 (2017) 853-861.

[19] X.D. Sun, Y.Y. Li, J. Zhou, C. Hai Ma, Y. Wang, J.H. Zhu, Facile Synthesis of High Photocatalytic Active Porous g-C_3N_4 with $ZnCl_2$ Template, J. Colloid. Interface Sci., 451 (2015) 108-116.

[20] W.-D. Oh, V.W.C. Chang, Z.-T. Hu, R. Goei, T.-T. Lim, Enhancing the Catalytic Activity of g-C_3N_4 Through Me Doping (Me = Cu, Co and Fe) for Selective Sulfathiazole Degradation via Redox-Based Advanced Oxidation Process, Chem. Eng. J., 323 (2017) 260-269.

[21] X. Zou, R. Silva, A. Goswami, T. Asefa, Cu-Doped Carbon Nitride: Bio-Inspired Synthesis of H_2-Evolving Electrocatalysts Using Graphitic Carbon Nitride (g-C_3N_4) as a Host Material, Appl. Surf. Sci., 357 (2015) 221-228.

[22] J. Gao, Y. Wang, S. Zhou, W. Lin, Y. Kong, A Facile One-Step Synthesis of Fe-doped g-C_3N_4 Nanosheets and Their Improved Visible-Light Photocatalytic Performance, ChemCatChem, 9 (2017) 1708-1715.

[23] X. Li, W. Bi, L. Zhang, S. Tao, W. Chu, Q. Zhang, Y. Luo, C. Wu, Y. Xie, Single-Atom Pt as Co-Catalyst for Enhanced Photocatalytic H_2 Evolution, Adv. Mater., 28 (2016) 2427-2431.

[24] Z. Chen, S. Mitchell, E. Vorobyeva, R.K. Leary, R. Hauert, T. Furnival, Q.M. Ramasse, J.M. Thomas, P.A. Midgley, D. Dontsova, M. Antonietti, S. Pogodin, N. López, J. Pérez-Ramírez, Stabilization of Single Metal Atoms on Graphitic Carbon Nitride, Adv. Funct. Mater., 27 (2017).

[25] Y. Wang, X. Zhao, D. Cao, Y. Wang, Y. Zhu, Peroxymonosulfate Enhanced Visible Light Photocatalytic Degradation Bisphenol a by Single-Atom Dispersed Ag Mesoporous g-C_3N_4 Hybrid, Appl. Catal., B, 211 (2017) 79-88.

[26] G. Gao, Y. Jiao, E.R. Waclawik, A. Du, Single Atom (Pd/Pt) Supported on Graphitic Carbon Nitride as an Efficient Photocatalyst for Visible-Light Reduction of Carbon Dioxide, J. Am. Chem. Soc., 138 (2016) 6292-6297.

[27] X. Huang, Y. Xia, Y. Cao, X. Zheng, H. Pan, J. Zhu, C. Ma, H. Wang, J. Li, R. You, S. Wei, W. Huang, J. Lu, Enhancing Both Selectivity and Coking-Resistance of a Single-Atom Pd1/C_3N_4 Catalyst for Acetylene Hydrogenation, Nano Res., 10 (2017) 1302-1312.

[28] S.C. Yan, Z.S. Li, Z.G. Zou, Photodegradation Performance of g-C_3N_4 Fabricated by Directly Heating Melamine, Langmuir, 25 (2009) 10397-10401.

[29] G. Liu, P. Niu, C. Sun, S.C. Smith, Z. Chen, G.Q. Lu, H.M. Cheng, Unique Electronic Structure Induced High Photoreactivity of Sulfur-Doped Graphitic C_3N_4, J. Am. Chem. Soc., 132 (2010) 11642-11648.

[30] K. Wang, Q. Li, B. Liu, B. Cheng, W. Ho, J. Yu, Sulfur-doped g-C_3N_4 with Enhanced Photocatalytic CO_2-reduction Performance, Appl. Catal., B, 176-177 (2015) 44-52.

[31] N. Tian, Y. Zhang, X. Li, K. Xiao, X. Du, F. Dong, G.I.N. Waterhouse, T. Zhang, H. Huang, Precursor-Reforming Protocol to 3D Mesoporous g-C_3N_4 Established by Ultrathin Self-Doped Nanosheets for Superior Hydrogen Evolution, Nano Energy, 38 (2017) 72-81.

[32] S. Cao, Q. Huang, B. Zhu, J. Yu, Trace-Level Phosphorus and Sodium Co-Doping of g-C_3N_4 for Enhanced Photocatalytic H_2 Production, J. Power Sources, 351 (2017) 151-159.

[33] J. Fu, B. Zhu, C. Jiang, B. Cheng, W. You, J. Yu, Hierarchical Porous O-Doped g-C_3N_4 with Enhanced Photocatalytic CO_2 Reduction Activity, Small, 13 (2017).

[34] F.-Y. Su, C.-Q. Xu, Y.-X. Yu, W.-D. Zhang, Carbon Self-Doping Induced Activation of n-π* Electronic Transitions of g-C_3N_4 Nanosheets for Efficient Photocatalytic H_2 Evolution, ChemCatChem, 8 (2016) 3527-3535.

[35] Y. Li, X. Liu, L. Tan, Z. Cui, X. Yang, Y. Zheng, K.W.K. Yeung, P.K. Chu, S. Wu, Rapid Sterilization and Accelerated Wound Healing Using Zn^{2+} and Graphene Oxide Modified g-C_3N_4 under Dual Light Irradiation, Adv. Funct. Mater., 28 (2018).

[36] Z. Qin, W. Fang, J. Liu, Z. Wei, Z. Jiang, W. Shangguan, Zinc-doped g-C_3N_4/$BiVO_4$ as a Z-Scheme Photocatalyst System for Water Splitting Under Visible Light, Chin. J. Catal., 39 (2018) 472-478.

[37] W. Zhang, Z. Zhao, F. Dong, Y. Zhang, Solvent-Assisted Synthesis of Porous g-C_3N_4 With Efficient Visible-Light Photocatalytic Performance for NO Removal, Chin. J. Catal., 38 (2017) 372-378.

[38] Y. Wang, X. Wang, M. Antonietti, Y. Zhang, Facile One-Pot Synthesis of Nanoporous Carbon Nitride Solids by Using Soft Templates, ChemSusChem, 3 (2010) 435-439.

[39] M.J. Bojdys, J.-O. Müller, M. Antonietti, A. Thomas, Ionothermal Synthesis of Crystalline, Condensed, Graphitic Carbon Nitride, Chem. - Eur. J., 14 (2008) 8177-8182.

[40] H. Gao, S. Yan, J. Wang, Y.A. Huang, P. Wang, Z. Li, Z. Zou, Towards Efficient Solar Hydrogen Production by Intercalated Carbon Nitride Photocatalyst, Phys. Chem. Chem. Phys., 15 (2013) 18077-18084.

[41] G. Zhang, G. Li, Z.A. Lan, L. Lin, A. Savateev, T. Heil, S. Zafeiratos, X. Wang, M. Antonietti, Optimizing Optical Absorption, Exciton Dissociation, and Charge Transfer of a Polymeric Carbon Nitride with Ultrahigh Solar Hydrogen Production Activity, Angew. Chem., Int. Ed., 56 (2017) 13445-13449.

[42] M.K. Bhunia, K. Yamauchi, K. Takanabe, Harvesting Solar Light With Crystalline Carbon Nitrides for Efficient Photocatalytic Hydrogen Evolution, Angew. Chem., Int. Ed., 53 (2014) 11001-11005.

[43] G. Algara-Siller, N. Severin, S.Y. Chong, T. Bjorkman, R.G. Palgrave, A. Laybourn, M. Antonietti, Y.Z. Khimyak, A.V. Krasheninnikov, J.P. Rabe, U. Kaiser, A.I. Cooper, A. Thomas, M.J. Bojdys, Triazine-Based Graphitic Carbon Nitride: A Two-Dimensional Semiconductor, Angew. Chem., Int. Ed., 53 (2014) 7450-7455.

[44] Z. Zeng, H. Yu, X. Quan, S. Chen, S. Zhang, Structuring Phase Junction Between Tri-s-triazine and Triazine Crystalline C_3N_4 for Efficient Photocatalytic Hydrogen Evolution, Appl. Catal., B, 227 (2018) 153-160.

[45] E. Wirnhier, M.B. Mesch, J. Senker, W. Schnick, Formation and Characterization of Melam, Melam Hydrate, and a Melam-Melem Adduct, Chem. - Eur. J., 19 (2013) 2041-2049.

[46] I. Papailias, T. Giannakopoulou, N. Todorova, D. Demotikali, T. Vaimakis, C. Trapalis, Effect of Processing Temperature on Structure and Photocatalytic Properties of g-C_3N_4, Appl. Surf. Sci., 358 (2015) 278-286.

[47] B. Jurgens, E. Irran, J. Senker, P. Kroll, H. Muller, W. Schnick, Melem (2,5,8-triamino-tri-s-triazine), An Important Intermediate During Condensation of Melamine Rings to Graphitic Carbon Nitride: Synthesis, Structure Determination by X-Ray Powder Diffractometry, Solid-State NMR, and Theoretical Studies, J. Am. Chem. Soc., 125 (2003) 10288-10300.

[48] X. Wang, K. Maeda, A. Thomas, K. Takanabe, G. Xin, J.M. Carlsson, K. Domen, M. Antonietti, A Metal-Free Polymeric Photocatalyst for Hydrogen Production From Water Under Visible Light, Nat. Mater., 8 (2009) 76-80.

[49] A.S. Basin, A.B. Kaplun, A.B. Meshalkin, N.F. Uvarov, The LiCl-KCl Binary System, Russ. J. Inorg. Chem., 53 (2008) 1509-1511.

[50] A. Romero-Serrano, A. Hernandez-Ramirez, A. Cruz-Ramirez, M. Hallen-Lopez, B. Zeifert, Optimization and Calculation of The MCl-$ZnCl_2$ (M=Li, Na, K) Phase Diagrams, Thermochim. Acta, 510 (2010) 88-92.

[51] J. Rumble, CRC Handbook of Chemistry and Physics, 100th Edition, Taylor & Francis2019.

[52] B. Bann, S.A. Miller, Melamine and Derivatives of Melamine, Chem. Rev., 58 (1958) 131-172.

[53] H. May, Pyrolysis of Melamine, J. Appl. Chem., 9 (2007) 340-344.

[54] F. Dong, M. Ou, Y. Jiang, S. Guo, Z. Wu, Efficient and Durable Visible Light Photocatalytic Performance of Porous Carbon Nitride Nanosheets for Air Purification, Ind. Eng. Chem. Res., 53 (2014) 2318-2330.

[55] S. Dyjak, W. Kiciński, A. Huczko, Thermite-Driven Melamine Condensation to $C_xN_yH_z$ Graphitic Ternary Polymers: Towards an Instant, Large-Scale Synthesis of g-C_3N_4, J. Mater. Chem. A, 3 (2015) 9621-9631.

[56] Y. Wang, X. Wang, M. Antonietti, Polymeric Graphitic Carbon Nitride as a Heterogeneous Organocatalyst: From Photochemistry to Multipurpose Catalysis to Sustainable Chemistry, Angew. Chem., Int. Ed., 51 (2012) 68-89.

[57] Q. Liu, Y. Guo, Z. Chen, Z. Zhang, X. Fang, Constructing a Novel Ternary Fe(III)/Graphene/g-C_3N_4 Composite Photocatalyst With Enhanced Visible-Light Driven Photocatalytic Activity via Interfacial Charge Transfer Effect, Appl. Catal., B, 183 (2016) 231-241.

[58] J. Wang, J. Chen, P. Wang, J. Hou, C. Wang, Y. Ao, Robust Photocatalytic Hydrogen Evolution Over Amorphous Ruthenium Phosphide Quantum Dots Modified g-C_3N_4 Nanosheet, Appl. Catal., B, 239 (2018) 578-585.

[59] J. Wu, N. Li, X.-H. Zhang, H.-B. Fang, Y.-Z. Zheng, X. Tao, Heteroatoms Binary-Doped Hierarchical Porous g-C_3N_4 Nanobelts for Remarkably Enhanced Visible-Light-Driven Hydrogen Evolution, Appl. Catal., B, 226 (2018) 61-70.

[60] F. Raziq, M. Humayun, A. Ali, T. Wang, A. Khan, Q. Fu, W. Luo, H. Zeng, Z. Zheng, B. Khan, H. Shen, X. Zu, S. Li, L. Qiao, Synthesis of S-Doped Porous g-C_3N_4 by Using Ionic Liquids and Subsequently Coupled With Au-TiO_2 For Exceptional Cocatalyst-Free Visible-Light Catalytic Activities, Appl. Catal., B, 237 (2018) 1082-1090.

[61] X.T. Tian, X.B. Yin, Carbon Dots, Unconventional Preparation Strategies, and Applications Beyond Photoluminescence, Small, 15 (2019) e1901803.

[62] R. Wang, H. Wu, R. Chen, Y. Chi, Strong Electrochemiluminescence Emission from Oxidized Multiwalled Carbon Nanotubes, Small, 15 (2019) e1901550.

[63] J. Xu, Z. Wang, Y. Zhu, Enhanced Visible-Light-Driven Photocatalytic Disinfection Performance and Organic Pollutant Degradation Activity of Porous g-C_3N_4 Nanosheets, ACS Appl. Mater. Interfaces, 9 (2017) 27727-27735.

[64] J. Liu, W. Fang, Z. Wei, Z. Qin, Z. Jiang, W. Shangguan, Efficient Photocatalytic Hydrogen Evolution on N-Deficient g-C_3N_4 Achieved by a Molten Salt Post-Treatment Approach, Appl. Catal., B, 238 (2018) 465-470.

[65] Z. Hong, B. Shen, Y. Chen, B. Lin, B. Gao, Enhancement of photocatalytic H_2 evolution over nitrogen-deficient graphitic carbon nitride, J. Mater. Chem. A, 1 (2013).

[66] J. Xu, L. Zhang, R. Shi, Y. Zhu, Chemical Exfoliation of Graphitic Carbon Nitride for Efficient Heterogeneous Photocatalysis, J. Mater. Chem. A, 1 (2013).

[67] M. Zhang, J. Xu, R. Zong, Y. Zhu, Enhancement of Visible Light Photocatalytic Activities via Porous Structure of g-C_3N_4, Appl. Catal., B, 147 (2014) 229-235.

[68] Y. Yang, J. Chen, Z. Mao, N. An, D. Wang, B.D. Fahlman, Ultrathin g-C_3N_4 Nanosheets With an Extended Visible-Light-Responsive Range for Significant Enhancement of Photocatalysis, RSC Adv., 7 (2017) 2333-2341.

[69] Y. Yang, L. Geng, Y. Guo, J. Meng, Y. Guo, Easy Dispersion and Excellent Visible-Light Photocatalytic Activity of the Ultrathin Urea-Derived g-C_3N_4 Nanosheets, Appl. Surf. Sci., 425 (2017) 535-546.

[70] X. Wang, W. Cai, Y. Lin, G. Wang, C. Liang, Mass Production of Micro/Nanostructured Porous ZnO Plates and Their Strong Structurally Enhanced and Selective Adsorption Performance for Environmental Remediation, J. Mater. Chem., 20 (2010).

[71] B. Zhu, P. Xia, W. Ho, J. Yu, Isoelectric Point and Adsorption Activity of Porous g-C_3N_4, Appl. Surf. Sci., 344 (2015) 188-195.

[72] J. Lim, D. Monllor-Satoca, J.S. Jang, S. Lee, W. Choi, Visible Light Photocatalysis of Fullerol-Complexed TiO_2 Enhanced by Nb Doping, Appl. Catal., B, 152-153 (2014) 233-240.

[73] C. Ye, J. Li, Z. Li, X. Li, X. Fan, L. Zhang, B. Chen, C. Tung, L. Wu, Enhanced Driving Force and Charge Separation Efficiency of Protonated g-C_3N_4 for Photocatalytic O_2 Evolution, ACS Catal., 5 (2015) 6973-6979.

[74] W.J. Ong, L.L. Tan, Y.H. Ng, S.T. Yong, S.P. Chai, Graphitic Carbon Nitride (g-C_3N_4)-Based Photocatalysts for Artificial Photosynthesis and Environmental Remediation: Are We a Step Closer To Achieving Sustainability?, Chem. Rev., 116 (2016) 7159-7329.

[75] X. Ma, Y. Lv, J. Xu, Y. Liu, R. Zhang, Y. Zhu, A Strategy of Enhancing the Photoactivity of g-C_3N_4 via Doping of Nonmetal Elements: A First-Principles Study, J. Phys. Chem. C, 116 (2012) 23485-23493.

Chapter 4 Improve Photocatalytic Performance of g-C_3N_4 Through Balancing the Interstitial and Substitutional Chlorine Doping

This work has been published in the Applied Surface Science. It is written by the first author, who is also the author of the present thesis. The introduction and the conclusion part are reproduced from original paper with some modifications. Full published version is in the appendix.

4.1 Introduction

As an organic semiconductor, graphitic C_3N_4 is deemed as a promising candidate for photocatalysis. Constituted mainly by carbon and nitrogen elements, it is low-cost, non-toxic, free of transition metal elements and exhibits reasonably good photocatalytic activity. After proven capable of driving water splitting reaction to produce H_2 [1, 2], there has been a surge of interest in modifying C_3N_4 to further improve its photocatalytic performance [3-5]. The main shortcomings of C_3N_4 are its limited specific surface area (SSA), non-optimized electronic structure and high photon-excited electron-hole recombination rate [3, 6, 7]. The development of new strategies to address the shortcomings of C_3N_4 to further improve its photocatalytic activity remains a challenging task.

The strategies to optimize the property of C_3N_4 itself can be classified into two main categories: doping with heteroatoms and vacancy introduction [8-10]. Whereas vacancy introduction is limited to C or N only, heteroatoms doping is more versatile due to the wide variety of dopants. Heteroatom doping has been reported to improve the photocatalytic performance of C_3N_4 through different mechanisms: (i) trapping photo-excited electrons or holes and retarding the

recombination [10, 11]; (ii) optimising the electronic structure by shifting the edge of valence band or conduction band [9, 12]; (iii) facilitating the interlayer electron/hole transfer [13]; and (iv) enhancing target reactant adsorption [9, 14]. Among all the potential dopants, the Cl atom is one of the most promising candidates due to its unique features. Cl not only enhances the photocatalytic performance of C_3N_4 on its own [15, 16], and as a common anion, Cl can also be introduced into C_3N_4 along with doping other ions [17-20]. Another important feature of Cl as a dopant is that Cl can potentially act as both interstitial and substitutional dopants. However, there is no definite synthesis method that would enable the control of doping sites for Cl. In addition, the roles of Cl at different doping sites in modifying the electronic structure of C_3N_4 and the corresponding influences on the photocatalytic performance remain unknown.

To optimize the property of pristine C_3N_4 for a better photocatalytic activity, one of the most fundamental aspects is to develop a new preparation method. Moreover, the clear understanding of the relationship between preparation parameters and property of the synthesized material is critical. As the most conventional preparation method for C_3N_4, thermal polymerization in a static atmosphere has been intensively investigated. Compared with thermal polymerization, the solvothermal method presents unique advantages such as low temperature, controllable morphology, high homogeneity etc. Although the solvothermal synthesis of C_3N_4 is still not fully understood as it has not been thoroughly studied yet, synthesis methods using dicyandiamide/melamine and cyanuric chloride in acetonitrile have been reported in the literature [21-24]. However, these solvothermal methods to synthesize C_3N_4 were all performed in static conditions. The static solvothermal synthesis usually results in C_3N_4 with low SSA, which significantly hinders its photocatalytic performance. For instance, Hu et al.[25] reported the solvothermal synthesis of C_3N_4 using cyanuric chloride and sodium azide. Their reported SSA value of 4.4 $m^2 g^{-1}$ highlights no obvious advantage compared with C_3N_4 synthesized via conventional thermal polycondensation method. A SSA value of 34 $m^2 g^{-1}$ was reported by Wang et al. [26] using melamine and cyanuric chloride,

while Cui et al. [27] synthesized C_3N_4 hollow microspheres with a SSA value of 20 m^2 g^{-1} via the solvothermal method with cyanuric chloride and dicyandiamide. Moreover, in all these studies though, the role of Cl dopants in C_3N_4 introduced via cyanuric chloride is either neglected [24-26, 28] or largely unexplored [27, 29]. This also implies that the correlation between Cl doping and the solvothermal synthesis condition remains unknown, illustrating the need to understand how Cl dopants may influence the photocatalytic activity of C_3N_4.

Herein, the photocatalytic performance of Cl doped C_3N_4 is successfully improved through controlling Cl dopant sites and the atomic ratio of interstitial over substitutional Cl dopants via the combined effect of dopant dose and agitation during solvothermal synthesis. The effects of agitation rate on the morphology, SSA, Cl doping concentration and their relations with the photocatalytic activity are investigated in detail. The results indicate that both the molecular and electronic structure of the prepared C_3N_4 are determined by Cl dopant sites, and the doping sites of Cl dopants are strongly controlled by the agitation rate. The effect of agitation on the electronic structure takes a U-type correlation. The effects of different Cl doping sites on the morphology, electronic structure, photocatalytic activity are also discussed in detail. Under moderate agitation, the SSA of prepared Cl doped C_3N_4 reaches 82.7 m^2 g^{-1}, which is ~6.67 times of the C_3N_4 prepared via the conventional thermal polymerization method.

4.2 Results and discussion

4.2.1 Molecular structure analysis

As indicated by the potential C_3N_4 synthesis mechanisms via the solvothermal method displayed in **Figure 4.1**, two precursors, cyanuric chloride and dicyandiamide, can be used for the synthesis of C_3N_4. Similar to the conventional C_3N_4 preparation method (i.e. thermal polycondensation), the solvothermal method follows a similar polycondensation process from smaller oligomers to larger ones. The possible reaction intermediates include melamine, melem, melon and their corresponding oligomers with Cl dopants. The resulting C_3N_4 crystal

is based on the stacking of melon layers with infinite size in theory (in practice, melon layers have a certain size due to a limited crystallization degree).

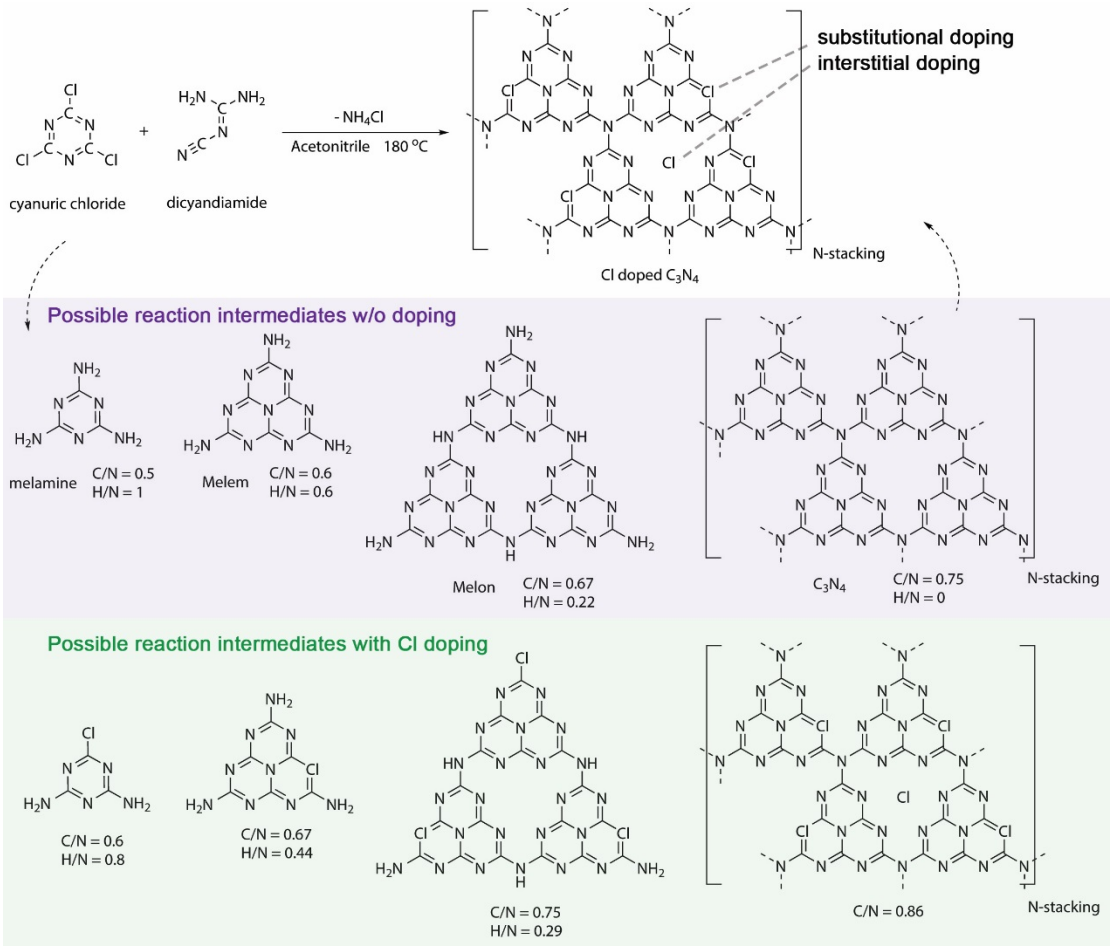

Figure 4.1. Scheme of C_3N_4 synthesis via solvothermal reaction with the feedstocks of cyanuric chloride and dicyandiamide.

The crystal phases of different C_3N_4 samples were first characterized by XRD (**Figure 4.2**(a)). The results indicate that the crystallization degree of C_3N_4 is remarkably affected by the agitation during the solvothermal preparation. The 0-C_3N_4 synthesized under static solution without agitation exhibits the typical XRD pattern of g-C_3N_4. The main peak at 27.3 ° refers to the (002) facts of the crystal [30]. It represents the stacking of the layers of repeating melem units via the van der Waals force. The broad peak at ~ 23 ° can be attributed to the less crystallized C_3N_4 structure. The crystallization degree first drops when agitation is implemented during the synthesis, then increasing with the agitation rate. An increased crystallization was achieved for the 1100-C_3N_4 synthesized under the agitation rate of 1100 rpm. The molecular structure of C_3N_4 prepared via the solvothermal method was further characterized by FTIR spectroscopy. As shown in **Figure 4.2**(b), all the samples prepared via

the solvothermal method exhibited the typical FTIR spectra of graphitic C_3N_4. All spectra include the peaks at 812 cm^{-1}, which is characteristic of the existence of NH/NH_2 groups [31, 32]. The strong adsorption band from 1269 to 1622 cm^{-1} are the typical vibration modes of C-N heterocycles of heptazine units [21, 32, 33] . Moreover, the absence of -CH bands at ~3000 cm^{-1} and -CN bands at ~2200 cm^{-1} appears to rule out the possibility of direct involvement of acetonitrile in the C_3N_4 synthesis [22].

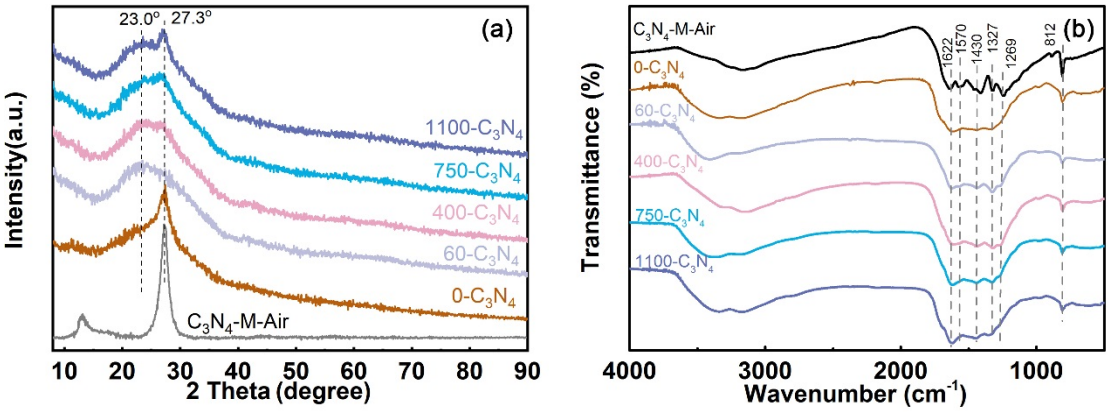

Figure 4.2. The XRD patterns (a) and FTIR spectra (b) of the C_3N_4 prepared under different agitation conditions.

Organic elemental analysis is a more accurate way to quantitatively determine the chemical composition of the samples prepared under different agitation rates. The results are summarized in **Table 4.1**. As illustrated in **Figure 4.1**, the synthesis of C_3N_4 can be described as the polycondensation process. Theoretically, the fully crystallized or polycondensed C_3N_4 possess the atomic C/N, H/N ratios of 0.75 and 0, respectively. Before reaching the full polycondensation, the key intermediates or oligomers are the melamine ($C_3H_6N_6$), melem ($C_6H_6N_{10}$) and melon ($C_{18}N_{27}H_6$). The corresponding atomic C/N ratios are 0.5, 0.6, 0.67 and H/N are 1, 0.6, 0.22, respectively. This result indicates that the higher C/N and lower H/N ratios correspond to a higher condensation degree. More importantly, the substitution of N atoms by Cl dopants can significantly increase the C/N atomic ratio, even surpassing the theoretical 0.75 in C_3N_4. As summarized in **Table 4.1**, the control group sample C_3N_4-M-Air, synthesized via the conventional polycondensation of melamine at 500 °C, comprises N, C, H with weight ratios of 57.61wt%, 34.10wt% and 1.65wt%, respectively. The C/N atomic ratio is 0.691, which is between the melon and fully polycondensed C_3N_4, close to the reported values in the literature [34, 35]. Additionally, the low H weight percentage (1.65wt%) and H/N atomic ratio (0.401) indicate a relatively high crystallization degree of the C_3N_4 prepared via this method. Significantly different from the C_3N_4-M-Air, the C_3N_4 synthesized via the solvothermal method shows the remarkably different chemical compositions and

polycondensation degree. Moreover, the chemical composition and polycondensation are agitation rate-dependent. Different from C_3N_4-M-Air, all the samples synthesized at agitation condition exhibit the H/N atomic ratios higher than 1.0, which suggests the low polycondensation degree. The low crystallization degrees are also proven by the XRD characterization (**Figure 4.2** (a)). In the case of C/N atomic ratio, for the C_3N_4 synthesized under agitation condition with stirring rate of 0, 60, 400, 750 and 1000 rpm, the C/N atomic ratios reached 0.772, 0.845, 0.832, 0.818 and 0.760, respectively. The C/N atomic ratio firstly rises with the agitation rate when the agitation rate is relatively low. Then C/N atomic ratio falls back when the agitation rate further increases to 1100 rpm due to the enhanced crystallisation degree. It is important to point out that the C/N atomic ratios are even higher than the theoretical 0.75 of the fully condensed C_3N_4. This strongly suggests the Cl dopants substitute the N atoms in the molecular structure of C_3N_4, which is further confirmed via the XPS analyses (**Figure 4.4**). The much higher crystallization/polycondensation degree of C3N4-M-Air than the solvothermally synthesized C_3N_4 can be explained by their different preparation temperature. The C_3N_4-M-Air was prepared at 500 °C; by contrast, the Cl doped g-C3N4 was prepared at 180 °C.

Table 4.1. Chemical compositions of C_3N_4 prepared at different agitation conditions determined by organic elemental analyses.

sample	N (wt%)	C (wt%)	H (wt%)	C/N (atomic ratio)	H/N (atomic ratio)
0-C_3N_4	47.74	31.60	2.95	0.772	1.120
60-C_3N_4	45.59	33.02	2.88	0.845	1.048
400-C_3N_4	45.64	32.53	2.79	0.832	1.029
750-C_3N_4	46.42	32.53	2.81	0.818	1.037
1100-C_3N_4	47.65	31.05	3.04	0.760	1.174
C_3N_4-M-Air	57.61	34.10	1.65	0.691	0.401

The molecular structures of Cl doped C_3N_4 prepared via solvothermal method can be determined via XPS analyses. As shown in **Figure 4.3**(a), the C 1s XPS spectra of Cl doped C_3N_4 synthesized via the solvothermal method are deconvoluted into 3 peaks, which is in agreement with the control group sample C_3N_4-M-Air. The peak positioned at the binding energy of 284.6 eV is assigned to the adventitious carbon. It is used to calibrate all the XPS spectra for surface charge compensation. The other two peaks with the binding energy of 286.4 and 288.2 eV can be attributed to the C-NH_x and dicoordinated C (N-C=N) in the melem unit, respectively [13, 22]. The N 1s spectra of all the samples are presented in **Figure 4.3**(b). The peaks centred at 398.7, 399.9 and 400.8 eV are assigned to the sp^2-hybridized N (C=N-C), sp^3-hybrideized N (N-$(C)_3$) and NH_x functional group, respectively [30, 36, 37]. The C 1s and N

1s spectra of the samples prepared via solvothermal method shows consistency with C_3N_4-M-Air. It proves that the C_3N_4 synthesized via solvothermal method still follow the graphitic C_3N_4 molecular structure.

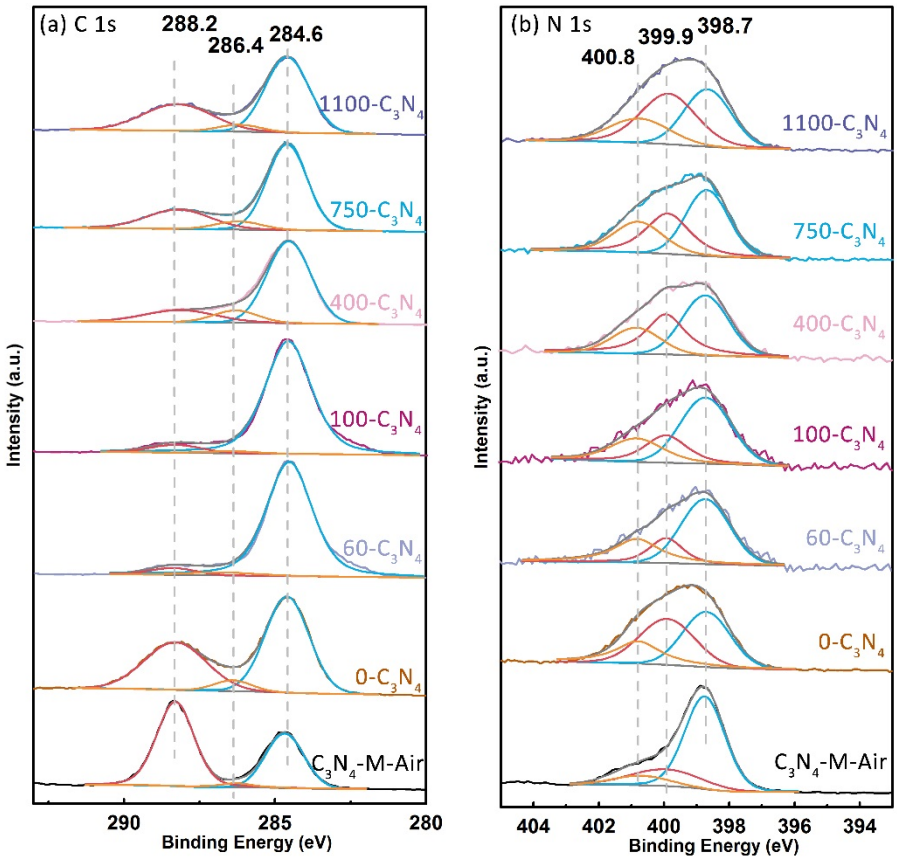

Figure 4.3. The XPS (a) C 1s and (b) N 1s spectra of C_3N_4 prepared via solvothermal method with agitation rates of 0, 60, 100, 400, 750 and 1100 rpm respectively. The corresponding spectra of control group sample C_3N_4-M-Air are also presented.

In Cl doped C_3N_4, there are two possible sites for Cl doping in C_3N_4: substitutional and interstitial sites (Cl_{sub} and Cl_{int}), as schemed in **Figure 4.1**. Since the Cl possesses the moderate electronegativity and atom radius, the possibilities of doping at these two sites are very similar. As being pointed out via the DFT calculation, the formation energy for substitutional (dicoordinated N) and interstitial doping are calculated to be 3.60 and 3.52 eV, respectively [38]. To distinguish the Cl_{int} and Cl_{sub}, the Cl 2p spectra are deconvoluted and presented in **Figure 4.4**.

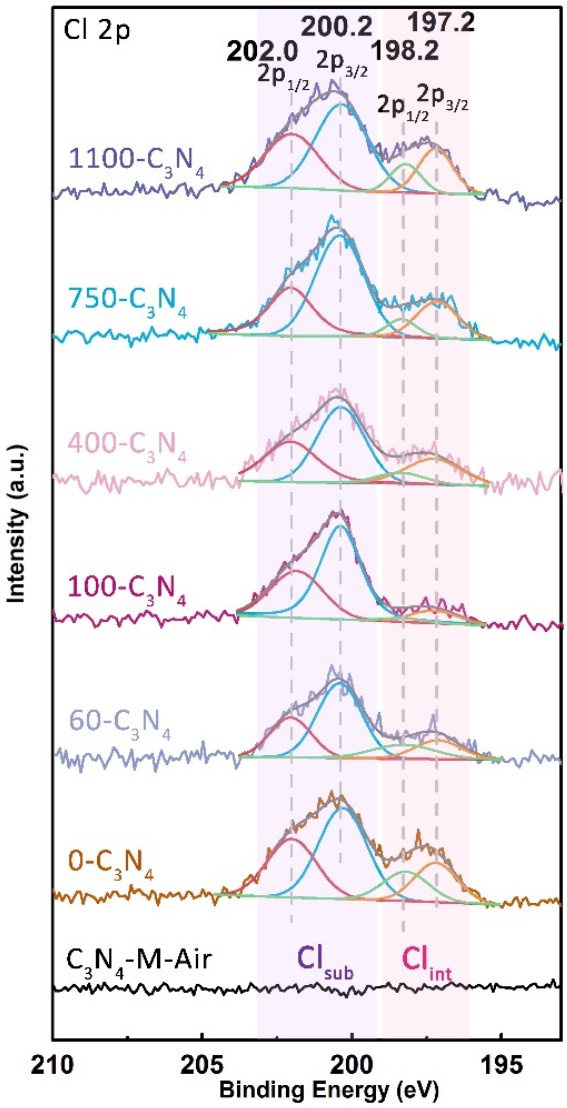

Figure 4.4. The XPS Cl 2p spectra of Cl doped C_3N_4 prepared via solvothermal methods with agitation rates of 0, 60, 100, 400, 750 and 1100 rpm respectively. The corresponding spectra of control group sample C_3N_4-M-Air are also presented.

The peak centred at 202.0 and 200.2 eV can be attributed to the $2p_{1/2}$ and $2p_{3/2}$ peaks of Cl_{sub} dopants, which are consistent with the reported binding energy of C-Cl bond in the literature [16, 39, 40]. And the peaks with the binding energy of 198.2 and 197.2 eV can be assigned to the Cl_{int} dopants derived from the Cl^- ions in the solution. The binding energy matches the typical values of NH_4Cl [41] and previous work [42] of Cl-doped C_3N_4. The assignments of Cl_{sub} and Cl_{int} are rationalized by their different origins. The Cl_{sub} dopants are brought by the cyanuric chloride (schemed in **Figure 4.1**). While the Cl_{int} dopants come from the negatively charged Cl^- ions due to the formation of NH_4Cl during the polycondensation for C_3N_4 synthesis. Therefore, the Cl_{sub} should exhibit more positive oxidation state than the Cl_{int}, which causes the larger binding energy of Cl_{sub} than Cl_{int}.

The effects of agitation on Cl dopants concentration and distribution can be investigated via XPS semi-quantitative analyses of **Figure 4.4**. The atomic and weight percentages of element *i* (A_i% and W_i%) in Cl doped C_3N_4 can be determined based on the peak area of S_i, molecular weight m_i, relative sensitivity factor RSF_i and energy compensation factor ECF_i:

$$A_i\% = \frac{S_i/(RSF_i \times ECF_i)}{\sum[S_i/(RSF_i \times ECF_i)]} \times 100\% \quad (4.1)$$

$$W_i\% = \frac{A_i \times m_i}{\sum(A_i \times m_i)} \times 100\% \quad (4.2)$$

The Cl doping concentrations (W_{Cl}%) at different agitation conditions are calculated to be 1.93%, 3.68%, 3.94%, 3.97%, 5.51%, 6.23% for the Cl doped C_3N_4 synthesized with agitation rates of 0, 60, 100, 400, 750, 1100 rpm respectively, as summarized in **Figure 4.5**. It is noted that the total Cl doping concentration increases when the agitation rate rises. It can be attributed to the facilitated Cl diffusion derived from agitation during the crystallization of C_3N_4. XPS analyses also provide a semi-quantitative understanding of the atomic ratios of substitutional and interstitial Cl dopants. Due to the same *RSF* and *ECF* for the Cl dopants at different sites, the atomic ratio of substitutional and interstitial Cl dopants (Cl_{int}/Cl_{sub}) can be directly determined by the comparison of corresponding $2p_{3/2}$ peak areas. As shown in **Figure 4.5**, the calculated atomic Cl_{int}/Cl_{sub} are 0.48, 0.28, 0.22, 0.35, 0.36 and 0.49 for the C_3N_4 synthesized with the agitation rates of 0, 60, 100, 400, 750, 1100 rpm respectively. When no agitation is applied, the Cl_{int} and Cl_{sub} concentration are determined by thermodynamics. It is important to emphasize that the Cl_{int}/Cl_{sub} atomic ratio shows a reducing trend when the agitation rate increases from 0 to 100 rpm at first. However, the Cl_{int}/Cl_{sub} atomic ratio increases when the agitation rate further increases from 100 to 1100 rpm. This U-shape curve describing the correlation between Cl_{int}/Cl_{sub} atomic ratio and agitation rate can be explained by the different dependence of Cl_{int} and Cl_{sub} doping concentration on agitation rates. In the case of Cl_{int}, the intensified agitation facilitates the Cl_{int} doping due to the enhanced mass transfer. In addition, the shearing force brought by agitation can help the Cl^- diffuse into the interlayer site of C_3N_4. The similar phenomenon has been observed in other van der Waals crystals such as graphite [43, 44], BN [45], MoS_2 [46], etc. Different from Cl_{int}, the correlation between agitation rate and Cl_{sub} is more complicated. Comparing with a static condition, the moderate agitation could increase the condensation degree of C_3N_4 (as suggested by XRD patterns **Figure 4.2(a)**), which means the larger size of the melon unit, the more layers stacking and bigger particle size (also confirmed by BET-SSA (**Figure 4.6**) and SEM analyses (**Figure 4.7**)). Since the cyanuric chloride is used as the C, N sources during the polycondensation, it

is likely to form Cl_{sub} dopant at the beginning of oligomer formation. In low agitation rate condition, the Cl_{sub} doped oligomers are added to the edge of the melon unit, which causes the increase of Cl_{sub} concentration. However, at higher agitation rate, the significantly increased crystallization degree of C_3N_4 (**Figure 4.2** (a)) reduces the number of on-plane defects such as the Cl_{sub}. It is consistent with the negative correlation between C/N atomic ratio and agitation rate (**Table 4.1**). In summary, the different agitation dependence of Cl_{int} and Cl_{sub} is responsible for the unique U shape correlation between the atomic ratio of Cl_{int}/Cl_{sub} dopants and agitation rate.

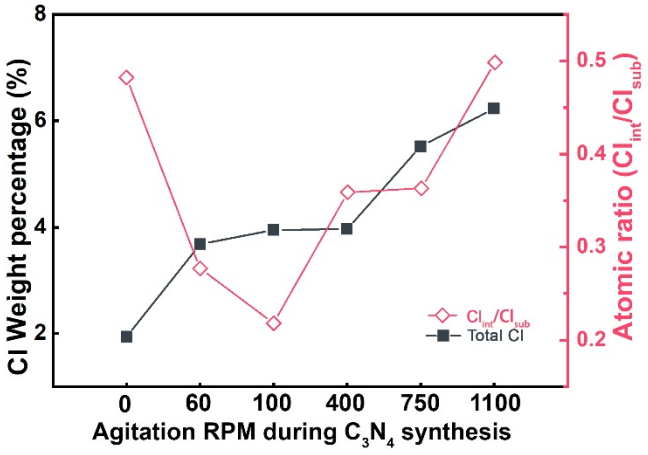

Figure 4.5. Concentration of Cl dopants in the samples synthesized via solvothermal method. And the effects of agitation on the atomic ratio of interstitial and substitutional Cl dopants.

4.2.2 The surface morphology and specific surface area

The SSA of the C_3N_4 synthesized via the solvothermal method was characterized via the N_2 sorption experiments at 77 K. The corresponding isotherms are presented in **Figure 4.6**. The SSAs calculated based on the Brunauer-Emmett-Teller (BET) theory are listed in the legend. All the N_2 sorption isotherms exhibit the characteristic hysteresis of non-porous structure. It is noted that the BET-SSA shows no correlation with the concentration of Cl_{int} or total Cl dopants, which can rule out the possibility that Cl^- is mainly adsorbed on the surface. The sample synthesized at a static solution without agitation, 0-C_3N_4, has the SSA of 12.4 $m^2 g^{-1}$, which is similar to the reported data in the literature [21-23] and control group C_3N_4-M-Air (14.9 $m^2 g^{-1}$). It is noted that the BET-SSA shows the agitation rate dependence too. When the agitation rate firstly increases to 60 rpm, the SSA of 60-C_3N_4 is enlarged to 82.7 $m^2 g^{-1}$. However, when the agitation rate further increases, the corresponding SSA reduces accordingly.

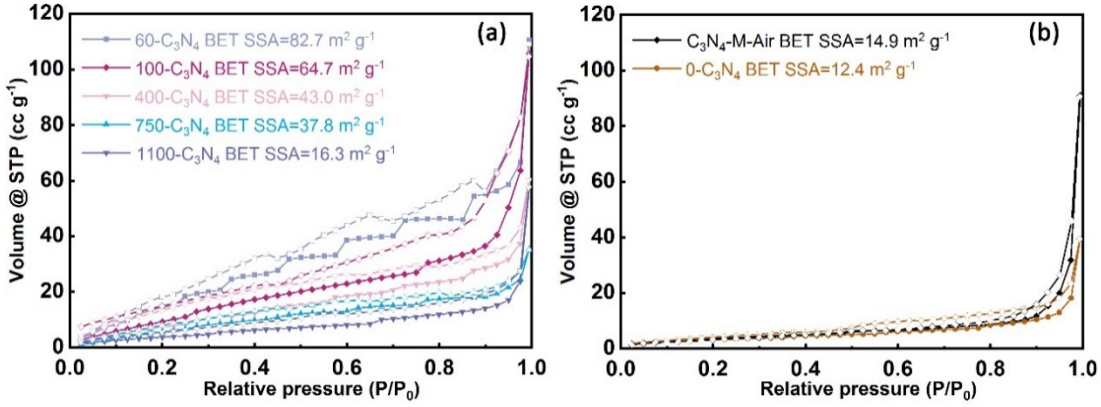

Figure 4.6. The isotherms of the N_2 sorption at 77 K for (a) the C_3N_4 synthesized in the solvothermal method under different agitation rates and (b) 0-C_3N_4 and control group samples C_3N_4-M-Air.

The morphologies of the C_3N_4 prepared via solvothermal method were examined using SEM, and the corresponding images are shown in **Figure 4.7**. The C_3N_4-M-Air shows the morphology of particles as large as several microns (**Figure 4.7**(a, b)). Though the surface of the particle is relatively rough, the large particle size limits the SSA to ~14.9 m^2 g^{-1}. As shown in **Figure 4.7**(d, e), the 0-C_3N_4 synthesized in the static solvothermal condition shows the morphology of aggregated spheres in the size of several microns. The micron-scale large particle is the reason for the relatively small BET-SSA of 12.4 m^2 g^{-1}. When the agitation rate increases to 60 rpm, the primary size of 60-C_3N_4 particles reduce to ~200 nm, which further aggregates into sub-micron particles (**Figure 4.7**(g, h)). The smaller primary particle size of 60-C_3N_4 comparing with 0-C_3N_4 induces a significantly enlarged SSA of 82.7 m^2 g^{-1}. Further increase of the agitation rate to 400 rpm, the primary particle size starts to increase again, as shown by 400-C_3N_4, 750-C_3N_4 and 1100-C_3N_4 (**Figure 4.7**(j-q)). From the SEM morphology analyses, it can be concluded that the changes in the C_3N_4 particle size are responsible for the evolution of SSA at different agitation rates. The EDS spectra were used to unravel the elemental information on all the samples. It can be seen that all the samples are mainly constituted by the C, N, with O as the minor component. Comparing with the C_3N_4-M-Air, the C_3N_4 synthesized via the solvothermal method all show the existence of Cl dopants. While it is also needed to emphasize that the EDS results here are only qualitative since C, N, O elements could not be quantitatively determined by EDS spectra.

It is noted that the correlation between SSA and agitation rate in this work is different from the conventional understanding that a more vigorous agitation leads to smaller particle size and larger SSA [47-50]. However, during the solvothermal synthesis of Cl doped C_3N_4 under agitation, the correlation between agitation rate and particle size is controlled by a combined effect of crystallization and Cl_{int} induced C_3N_4 interlayer bonding. When no agitation is applied,

the nucleation rate is slow, which results in large primary particle size (0-C_3N_4). In the case of 60-C_3N_4, the agitation in a relatively slow rate can significantly increase the nucleation rate [50], which results in the smaller primary particle size. At a more intensive agitation rate, the mass transfer is no longer the control factor. Therefore, the larger particle size can be explained by the enhanced crystal growth due to the intensified interparticle interaction [51] or suppressed homogeneous nucleation [52, 53]. The rise of interstitial Cl doping inducing C_3N_4 interlayer bonding is another reason for the enlarged primary C_3N_4 particle size. When higher agitation speed applied, the doping of Cl tends to occur at the interstitial sites, as indicated by the XPS analyses (**Figure 4.5**). The higher concentration of Cl_{int} dopants will decrease the BET-SSA, because the interstitial dopants can form the chemical bonds between the melon layers, which promotes the formation of larger crystal sizes. This mechanism has been proven by many previous investigations focusing on the interstitially doped C_3N_4 [9, 13, 33, 54-56].

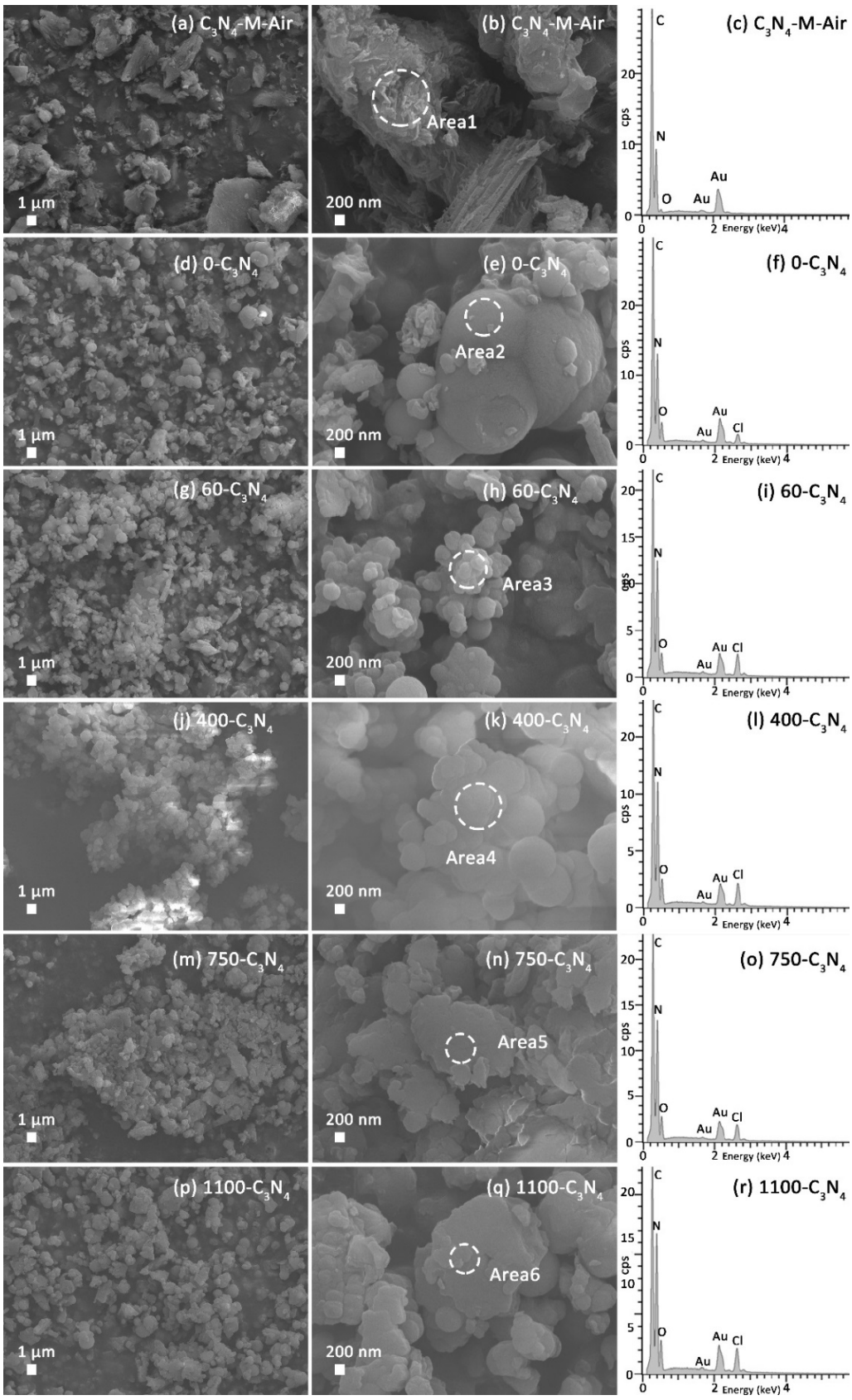

Figure 4.7. The SEM images and corresponding EDS spectra of (a-c) C_3N_4-M-Air, (d-f) 0-C_3N_4, (g-i) 60-C_3N_4, (j-l) 400-C_3N_4, (m-o)750-C_3N_4, (p-r) 1100-C_3N_4,

4.2.3 The electronic structure analyses

The bandgap of the samples prepared via solvothermal method was determined via the UV-Vis DRS spectroscopy method. As shown in **Figure 4.8**(a), the optical absorbance of all C_3N_4 show the typical spectra of the semiconductor. The Tauc plots derived from the UV-Vis DRS spectra to determine the bandgap are presented in **Figure 4.8**(b). It can be seen that the C_3N_4-M-Air shows much wider bandgap energy than the samples synthesized via the solvothermal method. Additionally, the samples synthesized in solvothermal method with different agitation rates exhibit reduced bandgap with similar values. To be specific, the 0-C_3N_4, 60-C_3N_4, 100-C_3N_4, 400-C_3N_4, 750-C_3N_4, 1100-C_3N_4 samples exhibited bandgap energy values of 1.82, 1.78, 1.78, 1.77, 1.82 and 1.87 eV, respectively. In addition, the control group sample C_3N_4-M-Air presented a bandgap of 2.65 eV, which is in agreement with previous studies in the literature [57, 58]. The correlation between bandgap and agitation rate presented a U-shape curve, as displayed in **Figure 4.9**.

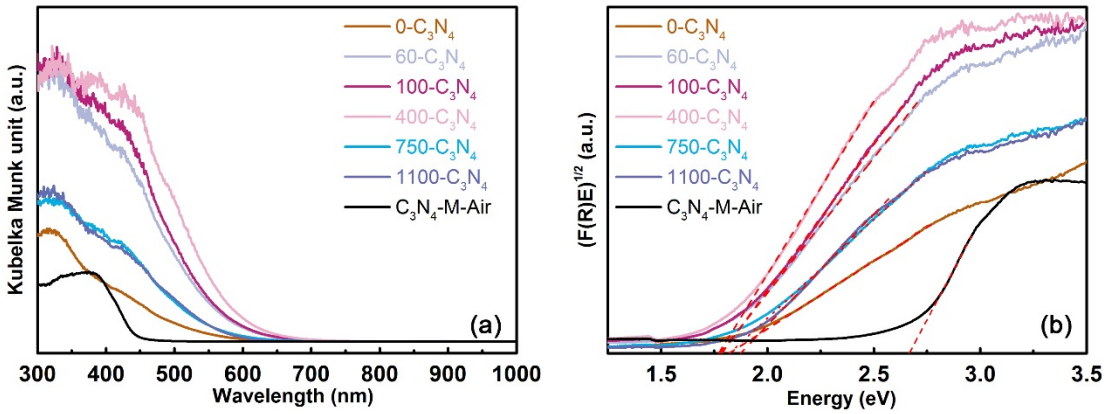

Figure 4.8. (a) UV-Vis DRS spectroscopy and (b) Tauc plots of samples prepared via solvothermal method with different agitation rates: 0-C_3N_4, 60-C_3N_4, 100-C_3N_4, 400-C_3N_4, 750-C_3N_4, 1100-C_3N_4 and control group sample C_3N_4-M-Air

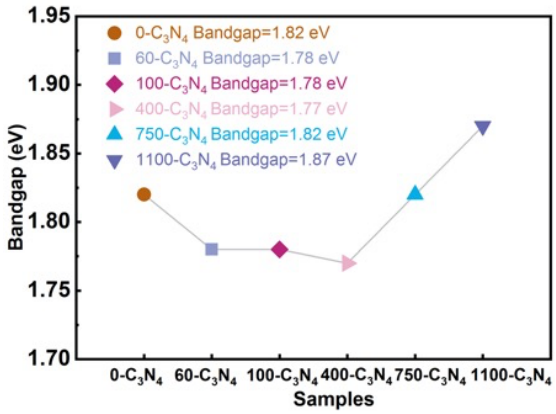

Figure 4.9. The calculated bandgap energy of samples prepared via solvothermal method with different agitation rates: 0-C_3N_4, 60-C_3N_4, 100-C_3N_4, 400-C_3N_4, 750-C_3N_4, 1100-C_3N_4.

The valence band maximum (VBM) is another important parameter affecting the photocatalytic dye degradation performance because the VBM determines the oxidation capability of photon-excited holes. To calculate the VBM, the XPS VB characterization was conducted, and results are presented in **Figure 4.10**. VBM binding energy calculated based on the XPS VB spectra are 2.43, 2.91, 3.01, 3.0, 2.82, 2.66 eV for 0-C_3N_4, 60-C_3N_4, 100-C_3N_4, 400-C_3N_4, 750-C_3N_4, 1100-C_3N_4 respectively. The VBM binding energy needs to be further converted to the chemical potential versus standard hydrogen electrode (SHE) potential using the following equation [9, 34]:

$$\mathrm{VBM(vs.\,SHE)} = \Phi + \mathrm{E_{binding}} - 4.44 \tag{4.3}$$

where the $E_{binding}$ represents the VBM binding energy achieved from the XPS VB spectra and Φ the work function of the XPS spectrometer (3.83 eV). The 4.44 eV is the potential difference between the SHE and vacuum. The converted VBM (vs. SHE) are calculated to be 1.82, 2.30, 2.40, 2.39, 2.21, 2.05 eV for 0-C_3N_4, 60-C_3N_4, 100-C_3N_4, 400-C_3N_4, 750-C_3N_4, 1100-C_3N_4 respectively. For comparison, the VBM of C_3N_4-M-Air is determined to be 1.64 eV. Combining the optical bandgap determined from the UV-Vis DRS spectra (**Figure 4.8**), the conduction band minimum (CBM) of the samples can be calculated by adding CBM and bandgap together. To illustrate the effects of Cl dopants distribution on the electronic structure of C_3N_4, the band alignment based on the calculated CBM and VBM is plotted as in **Figure 4.11**. By comparing the electronic structures of samples presented in **Figure 4.11**, it can be seen that all the samples synthesized via the solvothermal method show the lower VBM than the control group C_3N_4-M-Air. It suggests that the higher oxidation capability of the Cl doped C_3N_4 synthesized via the solvothermal method than the C_3N_4-M-Air synthesized via conventional thermal polycondensation method. More importantly, the agitation rate during the solvothermal synthesis shows the significant impacts on the VBM positions.

The agitation rate dependent VBM, CBM positions and bandgap can be explained by the different influences of Cl_{int} and Cl_{sub} on the electronic structure of Cl-doped C_3N_4. It is derived from the different coordination environment of the Cl_{int} and Cl_{sub} in the molecule. The Cl_{int} interacts with all the surrounding N atoms in the melem unit (theoretically 6 N atoms) and the Cl_{sub} replacing one N atom forms the strong covalent bonds with 2 adjacent C atoms. On one hand, the negatively charged Cl_{int} as the interstitial dopant will bring extra electrons to the C_3N_4 molecules, which can significantly shift the Fermi energy level (E_F) to the negative direction in the band diagram (**Figure 4.11**) [38, 59]. On the other hand, the atomic Mulliken electronegativity (χ) of C, N and Cl is 8.58, 9.77 and 14.06 eV respectively [60]. The higher

electronegativity suggests the Cl_{sub} dopants can shift the VBM to positive direction as described via the approximation from the electronegativity [61-64]:

$$\mathrm{VBM} = -\left(\chi_A{}^a \chi_B{}^b\right)^{1/(a+b)} + \frac{1}{2}E_g + E_0 \tag{4.4}$$

where E_0 is the energy of free electrons on the hydrogen scale (~4.4 eV), E_g the bandgap energy of the semiconductor, χ is the atomic Mulliken electronegativity in the compound A_aB_b. In summary, the Cl_{int} and Cl_{sub} shift the CBM/VBM to the opposite direction, and the experimentally determined electronic structures are derived from the balance between Cl_{int} and Cl_{sub} influences. As a consequence, the VBM, CBM positions also show the U-shape correlation with the agitation rate (shown in **Figure 4.11**). It is in consistence with the U-shape correlation between Cl_{int}/Cl_{sub} ratio and agitation rate (**Figure 4.5**).

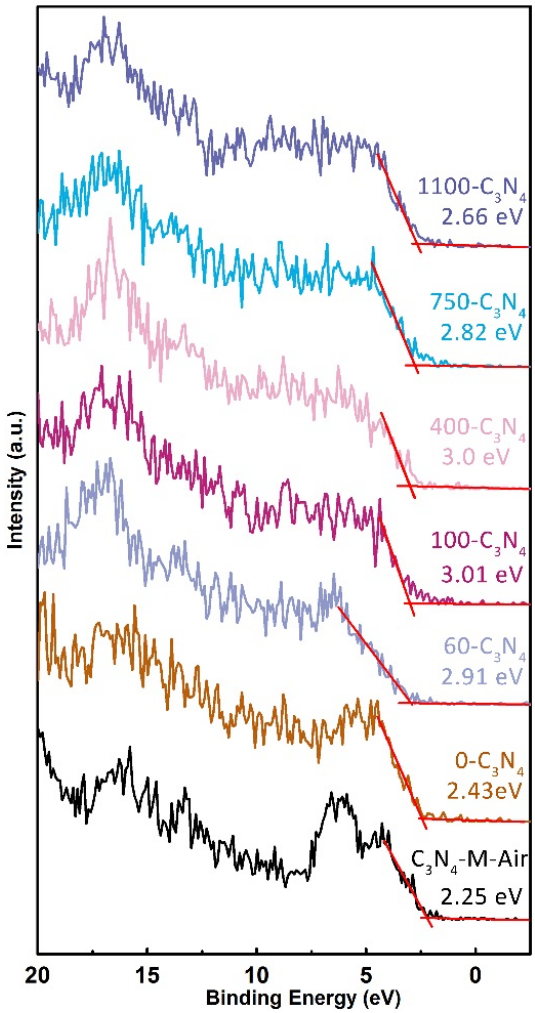

Figure 4.10. The XPS valence band (VB) spectra of samples prepared via solvothermal method with different agitation rates: 0-C_3N_4, 60-C_3N_4, 100-C_3N_4, 400-C_3N_4, 750-C_3N_4, 1100-C_3N_4. The C_3N_4-M-Air as control group is also presented.

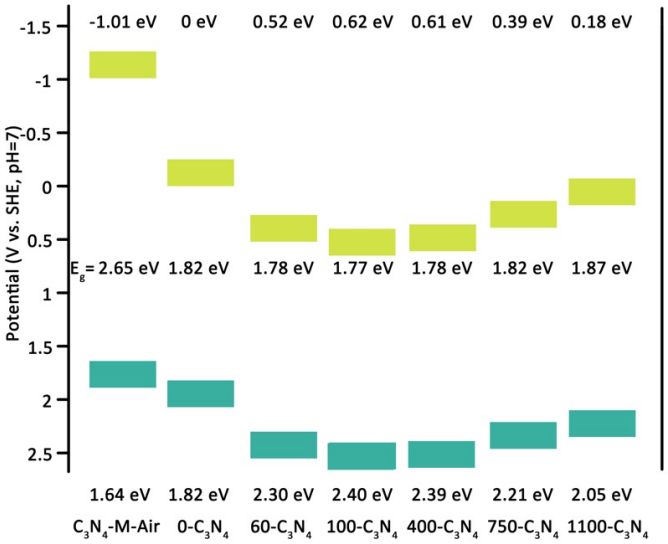

Figure 4.11. Band alignment diagram of Cl-doped C_3N_4 prepared via solvothermal method with different agitation rates: 0-C_3N_4, 60-C_3N_4, 100-C_3N_4, 400-C_3N_4, 750-C_3N_4, 1100-C_3N_4. The C_3N_4-M-Air synthesized via the conventional thermal polycondensation in static air is presented for comparison.

4.2.4 Photoluminescence (PL) analyses

Static PL analyses are a method to investigate the efficiency of photo-excited electron/hole separation and recombination. As shown in **Figure 4.12**, the C_3N_4-M-Air synthesized via conventional thermal condensation method shows the significantly strong PL emission spectra, which is at least two orders of magnitude larger than the C_3N_4 synthesized via the solvothermal method. It suggests the remarkable photo-excited electron/hole recombination in conventional C_3N_4, as already pointed out in the literature [9, 20, 65, 66]. Different from the C_3N_4-M-Air, the C_3N_4 synthesized via the solvothermal method exhibits greatly reduced PL intensity due to Cl doping. The PL emission intensity decreases in the sequence of 0-C_3N_4 > 1100-C_3N_4 > 750-C_3N_4 > 60-C_3N_4, 100-C_3N_4 > 400-C_3N_4. From the PL intensity sequence, it could be seen that the reduction of PL intensity not only relates to the total amount of Cl dopants but also Cl doping sites dependent. As illustrated in **Figure 4.5**, the total Cl doping concentration increases monotonically along with the agitation rate rise, while the highest total Cl doping doesn't guarantee the lowest PL intensity. To unravel more explicitly the roles of Cl at different doping sites in the photo-excited electron/hole separation, time-resolved PL spectroscopy experiments were conducted on the 4 most important samples: 0-C_3N_4, 60-C_3N_4, 1100-C_3N_4 and benchmark C_3N_4-M-Air. As shown in **Figure 4.12**(b), the average carriers lifetime of 0-C_3N_4, 60-C_3N_4, 1100-C_3N_4 and C_3N_4-M-Air are 0.62, 0.98, 1.08 and 0.92 ns, respectively. It is noted that the 1100-C_3N_4 with the highest concentration of Cl_{int} shows the longest average lifetime of photo-excited carriers. On the contrary, the 0-C_3N_4 with lowest Cl_{int} doping concentration exhibits the shortest average lifetime of photo-excited carriers.

These results suggest the Cl_{int} dopants mainly contribute to the enhanced charge carrier separation by acting as the bridge for inter-layer charge transfer. The reduced steady-state PL intensities of solvothermally synthesized samples are attributed to the facilitated non-radiative recombination. It is also worth mentioning that the 60-C_3N_4 still shows long carrier lifetime than C_3N_4-M-Air, which indicates the more efficient suppression of radiative recombination of charge carriers.

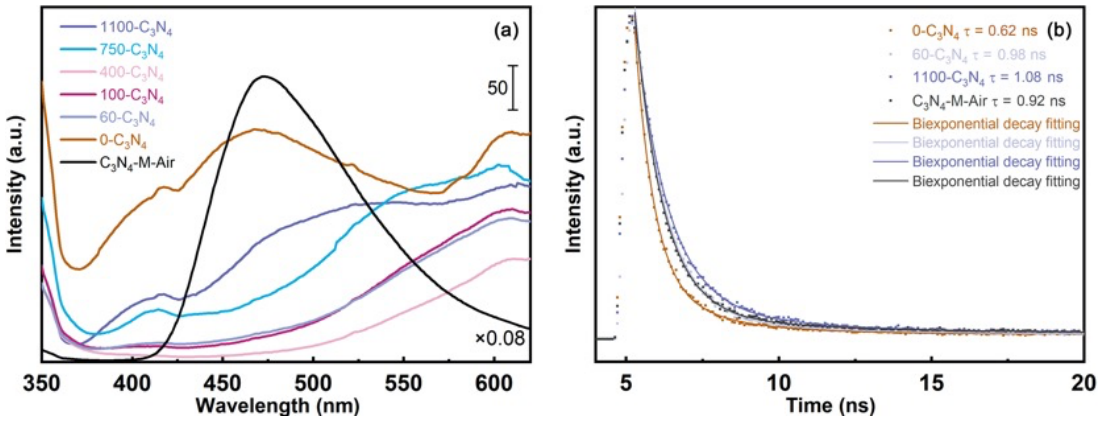

Figure 4.12. (a) Steady-state photoluminescence (PL) spectra of 0-C_3N_4, 60-C_3N_4, 100-C_3N_4, 400-C_3N_4, 750-C_3N_4, 1100-C_3N_4 and C_3N_4-M-Air as control group under 325 nm UV light excitation. The intensity of C_3N_4-M-Air PL spectrum is multiplied by 0.08 to improve legibility. (b) Time-resolved PL spectra of 0-C_3N_4, 60-C_3N_4, 1100-C_3N_4 and C_3N_4-M-Air.

4.2.5 Photocurrent measurement

Transient photocurrent experiments can elucidate the efficiency of electron/hole generation for catalysts under light irradiation. As shown in **Figure 4.13**, all the C_3N_4 synthesized via the solvothermal method shows significantly larger transient photocurrent density of the control group sample C_3N_4-M-Air, which shows only 34.2 nA cm^{-2} photocurrent response. The significant enhancement of the transient photocurrent density for the C_3N_4 synthesized via the solvothermal method can be mainly explained by the reduced bandgap. The solvothermal synthesis can introduce the Cl dopants into the C_3N_4, which results in the reduction of bandgap (**Figure 4.8**). The smaller bandgap could induce broader adsorption of incident light and produce larger photocurrent density. For Cl doped C_3N_4 synthesized via solvothermal method, the transient photocurrent densities under visible light ($\lambda > 420$ nm) irradiation for 0-C_3N_4, 60-C_3N_4, 100-C_3N_4, 400-C_3N_4, 750 C_3N_4 and 1100-C_3N_4 are 72.1, 113.9, 100.2, 96.7 and 94.5 nA cm^{-2} respectively. The 60-C_3N_4 exhibits the highest transient photocurrent density suggesting its more robust photocatalytic activity. It is noticed that the reduced bandgap is not sufficient to explain the dependence of transient photocurrent density on agitation rate since the

bandgaps are very similar for all these 6 samples (**Figure 4.11**). The higher photocurrent density can only be attributed to the suppressed electron/hole recombination by the Cl dopants and enlarged SSA (**Figure 4.6** and **Figure 4.12**). Specifically, the recombination suppression is due to the trapping effects of Cl dopant energy level in the electronic structure. The photogenerated charge carriers can be temporarily trapped by these dopant energy levels before recombination.

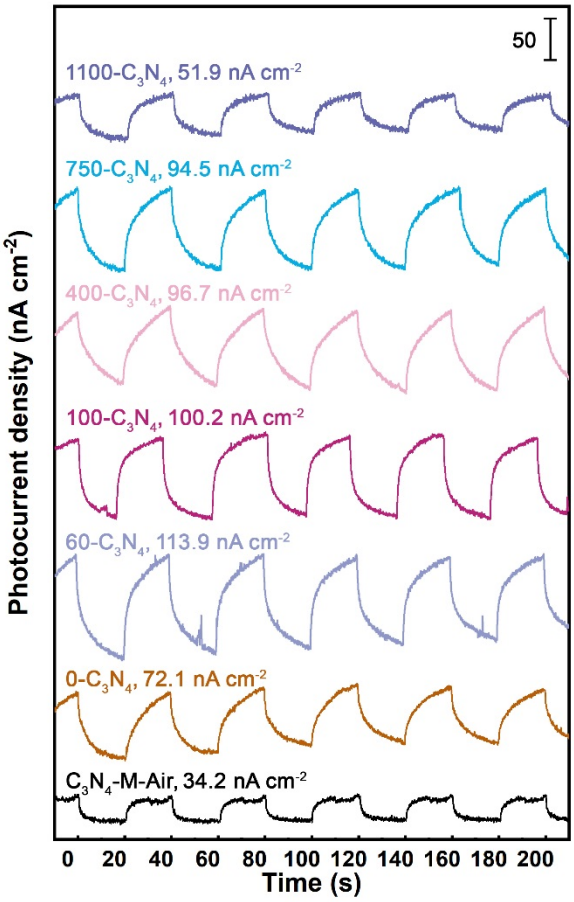

Figure 4.13. Transient photocurrent responses of 0-C_3N_4, 60-C_3N_4, 100-C_3N_4, 400-C_3N_4, 750-C_3N_4, 1100-C_3N_4 and C_3N_4-M-Air as control group under visible light ($\lambda > 420$ nm) on-off irradiation condition.

4.3 The photocatalytic activity

4.3.1 Photocatalytic dye-degradation performance

The photocatalytic activities of the Cl-doped C_3N_4 samples were characterized via the probe reaction, visible-light-driven photocatalytic RhB degradation, to unravel the effects of

agitation on photocatalytic activity. The control group sample of C_3N_4-M-Air prepared via conventional thermal polycondensation in static air is also tested in identical condition for comparison. **Figure 4.14**(a) presents the RhB concentration evolution during the photocatalytic reaction. At the first 25 min, the solution with catalysts was kept in the dark under the stirring condition to demonstrate the adsorption capabilities of the samples. The 60-C_3N_4 and 100-C_3N_4 show good RhB adsorption ability that reduces the RhB concentration (C) to 83.9% and 90.5% of the original concentration (C_0). The rest samples only reduce less than 5% of C_0. This result is in consistence with the BET-SSA results characterized via the N_2 sorption experiments (**Figure 4.6**). After 25 min of RhB adsorption in the dark, the catalysts were further exposed to the visible light provided by a Xenon lamp with 420 nm cut-off filter. After 125 min of photocatalytic reaction, the 0-C_3N_4 can degrade 82.23% of C_0. The best photocatalytic activity was obtained by 60-C_3N_4, with 99.40% of RhB degradation after 125 min. 100-C_3N_4, 400-C_3N_4, 750-C_3N_4 and 1100-C_3N_4 degraded the RhB concentration to 98.45%, 98.98%, 97.36%, 94.38% of the initial concentration, respectively. By comparison, the C_3N_4-M-Air only decompose 16.75% of the RhB after the same 125 min photocatalytic degradation. It can be seen that all the samples prepared via the solvothermal method show the superior photocatalytic RhB degradation performance than the C_3N_4-M-Air. It demonstrates the advantages of the solvothermal C_3N_4 preparation method. In addition, the photocatalytic activities of Cl-doped C_3N_4 synthesized via solvothermal method are largely affected by the agitation condition. To further compare the photocatalytic RhB degradation performances of the Cl doped C_3N_4 synthesized via solvothermal method, the corresponding kinetic curves are plotted in **Figure 4.14**(b). All the data can appropriately fit with the pseudo-first-order kinetic model, which is described by the following equation:

$$\ln\left(\frac{C_0}{C}\right) = kt \tag{4.5}$$

where the C and C_0 are the initial and current concentration of RhB solution after adsorption in the dark, respectively; the k represents the apparent reaction rate constant; the t is the reaction time. Based on the linear fitting of the data in **Figure 4.14**(b), the k is determined to be 12.2, 44.4, 35.8, 32.9, 30.6, 22.5 for 0-C_3N_4, 60-C_3N_4, 100-C_3N_4, 400-C_3N_4, 750-C_3N_4, and 1100-C_3N_4, respectively. By comparison, the C_3N_4-M-Air shows a much smaller k value of 1.24. The kinetic parameters derived from fitting are summarized in **Table 4.2**. The 60-C_3N_4 exhibits the highest photocatalytic RhB degradation performance. The enhanced photocatalytic activity can be attributed to 3 reasons: (i) enlarged SSA (**Figure 4.6**), (ii) higher

oxidation capability brought by the downshifted VBM (**Figure 4.11**) and (iii) suppressed photo-excited electron/hole recombination (**Figure 4.12**) as discussed in previous sections.

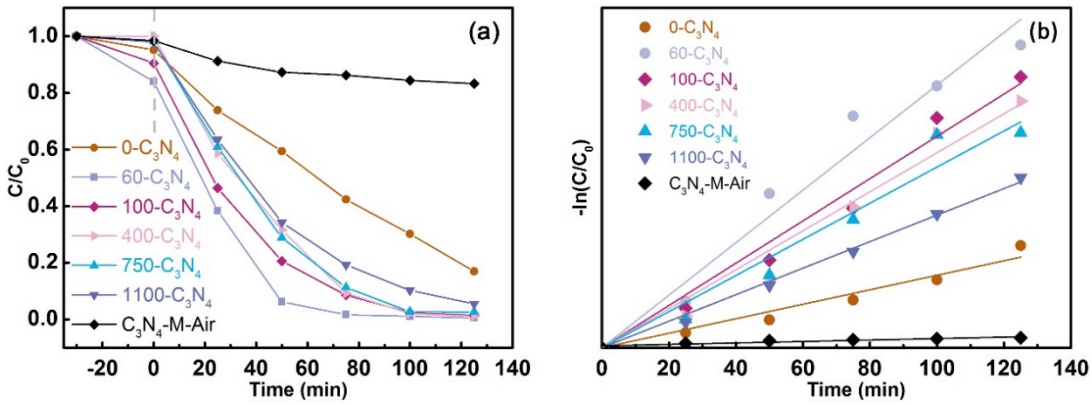

Figure 4.14. (a) The photocatalytic RhB degradation performance under visible light irradiation ($\lambda \geq 420$ nm) and (b) the corresponding pseudo-first-order kinetics plot of 0-C_3N_4, 60-C_3N_4, 100-C_3N_4, 400-C_3N_4, 750-C_3N_4, 1100-C_3N_4 and control group sample C_3N_4-M-Air.

Table 4.2. The summary of photocatalytic RhB degradation performance under visible light ($\lambda \geq 420$ nm)

Photocatalyst	Rate constant k (min^{-1}) (10^{-3})	R^2	SSA ($m^2\ g^{-1}$)
C_3N_4-M-Air	1.24	0.9381	14.9
0-C_3N_4	12.2	0.9847	12.3
60-C_3N_4	44.4	0.9885	82.7
100-C_3N_4	35.8	0.9919	64.7
400-C_3N_4	32.9	0.9878	43.0
750-C_3N_4	30.6	0.9841	37.8
1100-C_3N_4	22.5	0.9983	16.3

4.3.2 Cyclic performance tests

The stability of the prepared catalysts is an important criterion for performance evaluation. The optimal 60-C_3N_4 catalyst was chosen to perform the recycling experiments. The fresh 60-C_3N_4 was firstly conducted a photocatalytic RhB degradation and recycled from the solution via centrifuging. After rinsing with DI-water for several times and drying under vacuum, the recycled 60-C_3N_4 was used to conduct another photocatalytic RhB degradation experiment following the same procedure. The photocatalytic RhB degradation performances of the 3 recycling experiments are presented in **Figure 4.15**. It can be seen that the 60-C_3N_4 shows no

apparent deactivation after 3 successive photocatalytic degradations. The RhB can be completely photocatalytically degraded within 125 min. The results indicate that the Cl doped C_3N_4 synthesized via the solvothermal method exhibit high stability under working condition examined.

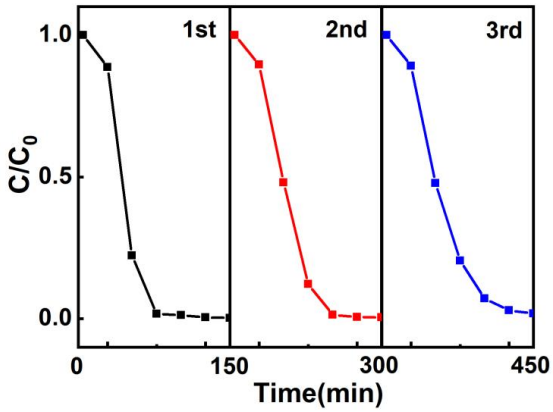

Figure 4.15. Photocatalytic degradation of RhB performances for recycled 60-C_3N_4 under visible light irradiation ($\lambda > 420$ nm).

4.4 Conclusion

In this work, Cl doped C_3N_4 is synthesised for the first time via an agitation-assisted solvothermal method and the atomic ratio of Cl_{int}/Cl_{sub} dopants is controlled by the agitation rate. The significantly improved RhB photodegradation performance of Cl doped C_3N_4 is attributed to the larger SSA, stronger photo-oxidation capability and suppressed electron/hole recombination. The specific surface area of 60-C_3N_4 is ~5.55 times larger than the bulk g-C_3N_4. A U-shape relation is found between agitation rate and molecular/electronic structure of prepared C_3N_4. The mechanism underpins this phenomenon is that the Cl_{sub} and Cl_{int} function differently and even oppositely on influencing the molecular/electronic structure of C_3N_4, which determines the photocatalytic activity. To be specific, the Cl_{int} dopants between the C_3N_4 layers can prolong the lifetime of the charge carriers but result in the smaller SSA and lower photo-oxidation capability. By contrast, the in-plane Cl_{sub} dopants can enhance the photo-oxidation capability, while only exhibit insignificant influence on charge separation efficiency. The optimal photocatalytic dye-degradation performance can only be achieved by balancing the Cl_{int}/Cl_{sub} ratios and synthesising under a moderate agitation rate. The best photocatalytic

performance sample 60-C_3N_4 shows ~35.8 times higher pseudo-first reaction rate constant in RhB photodegradation than the bulk g-C_3N_4.

References

[1] X. Wang, K. Maeda, A. Thomas, K. Takanabe, G. Xin, J.M. Carlsson, K. Domen, M. Antonietti, A Metal-Free Polymeric Photocatalyst for Hydrogen Production From Water Under Visible Light, Nat. Mater., 8 (2009) 76-80.

[2] L. Lin, Z. Yu, X. Wang, Crystalline Carbon Nitride Semiconductors for Photocatalytic Water Splitting, Angew. Chem., Int. Ed., 58 (2019) 6164-6175.

[3] Y. Wang, X. Wang, M. Antonietti, Polymeric Graphitic Carbon Nitride as a Heterogeneous Organocatalyst: From Photochemistry to Multipurpose Catalysis to Sustainable Chemistry, Angew. Chem., Int. Ed., 51 (2012) 68-89.

[4] W.J. Ong, L.L. Tan, Y.H. Ng, S.T. Yong, S.P. Chai, Graphitic Carbon Nitride (g-C_3N_4)-Based Photocatalysts for Artificial Photosynthesis and Environmental Remediation: Are We a Step Closer To Achieving Sustainability?, Chem. Rev., 116 (2016) 7159-7329.

[5] J. Fu, J. Yu, C. Jiang, B. Cheng, g-C_3N_4-Based Heterostructured Photocatalysts, Adv. Energy Mater., 8 (2018).

[6] G. Algara-Siller, N. Severin, S.Y. Chong, T. Bjorkman, R.G. Palgrave, A. Laybourn, M. Antonietti, Y.Z. Khimyak, A.V. Krasheninnikov, J.P. Rabe, U. Kaiser, A.I. Cooper, A. Thomas, M.J. Bojdys, Triazine-Based Graphitic Carbon Nitride: A Two-Dimensional Semiconductor, Angew. Chem., Int. Ed., 53 (2014) 7450-7455.

[7] R. Zhang, T. Ran, Y. Cao, L. Ye, F. Dong, Q. Zhang, L. Yuan, Y. Zhou, Oxygen activation of noble-metal-free g-C_3N_4/α-$Ni(OH)_2$ to control the toxic byproduct of photocatalytic nitric oxide removal, Chem. Eng. J., 382 (2020).

[8] P. Yang, H. Zhuzhang, R. Wang, W. Lin, X. Wang, Carbon Vacancies in a Melon Polymeric Matrix Promote Photocatalytic Carbon Dioxide Conversion, Angew. Chem., Int. Ed., 58 (2019) 1134-1137.

[9] K. Wang, J.L. Fu, Y. Zheng, Insights into Photocatalytic CO_2 Reduction on C_3N_4: Strategy of Simultaneous B, K Co-doping and Enhancement by N Vacancies, Appl. Catal., B, 254 (2019) 270-282.

[10] K. Wang, Q. Li, B. Liu, B. Cheng, W. Ho, J. Yu, Sulfur-doped g-C_3N_4 with Enhanced Photocatalytic CO_2-reduction Performance, Appl. Catal., B, 176-177 (2015) 44-52.

[11] Y. Wang, S. Zhao, Y. Zhang, J. Fang, Y. Zhou, S. Yuan, C. Zhang, W. Chen, One-pot Synthesis of K-doped g-C_3N_4 Nanosheets With Enhanced Photocatalytic Hydrogen Production Under Visible-Light Irradiation, Appl. Surf. Sci., 440 (2018) 258-265.

[12] D. Masih, Y. Ma, S. Rohani, Graphitic C_3N_4 Based Noble-Metal-Free Photocatalyst Systems: A Review, Appl. Catal., B, 206 (2017) 556-588.

[13] T. Xiong, W. Cen, Y. Zhang, F. Dong, Bridging the g-C_3N_4 Interlayers for Enhanced Photocatalysis, ACS Catal., 6 (2016) 2462-2472.

[14] J.-y. Tang, W.-g. Zhou, R.-t. Guo, C.-y. Huang, W.-g. Pan, Enhancement of Photocatalytic Performance In CO_2 Reduction over Mg/g-C_3N_4 Catalysts Under Visible Light Irradiation, Catal. Commun., 107 (2018) 92-95.

[15] C. Liu, Y. Zhang, F. Dong, A.H. Reshak, L. Ye, N. Pinna, C. Zeng, T. Zhang, H. Huang, Chlorine Intercalation in Graphitic Carbon Nitride for Efficient Photocatalysis, Appl. Catal., B, 203 (2017) 465-474.

[16] F. Yi, H. Gan, H. Jin, W. Zhao, K. Zhang, H. Jin, H. Zhang, Y. Qian, J. Ma, Sulfur- and chlorine-co-doped g-C_3N_4 Nanosheets With Enhanced Active Species Generation for Boosting Visible-Light Photodegradation Activity, Sep. Purif. Technol., 233 (2020).

[17] X.D. Sun, Y.Y. Li, J. Zhou, C. Hai Ma, Y. Wang, J.H. Zhu, Facile Synthesis of High Photocatalytic Active Porous g-C_3N_4 with $ZnCl_2$ Template, J. Colloid. Interface Sci., 451 (2015) 108-116.

[18] J. Liu, W. Fang, Z. Wei, Z. Qin, Z. Jiang, W. Shangguan, Efficient Photocatalytic Hydrogen Evolution on N-Deficient g-C_3N_4 Achieved by a Molten Salt Post-Treatment Approach, Appl. Catal., B, 238 (2018) 465-470.

[19] J. Gao, Y. Wang, S. Zhou, W. Lin, Y. Kong, A Facile One-Step Synthesis of Fe-doped g-C_3N_4 Nanosheets and Their Improved Visible-Light Photocatalytic Performance, ChemCatChem, 9 (2017) 1708-1715.

[20] X. Wu, D. Gao, P. Wang, H. Yu, J. Yu, NH4Cl-induced Low-temperature Formation of Nitrogen-rich g-C_3N_4 Nanosheets With Improved Photocatalytic Hydrogen Evolution, Carbon, 153 (2019) 757-766.

[21] Q. Gu, Y. Liao, L. Yin, J. Long, X. Wang, C. Xue, Template-Free Synthesis of Porous Graphitic Carbon Nitride Microspheres for Enhanced Photocatalytic Hydrogen Generation With High Stability, Appl. Catal., B, 165 (2015) 503-510.

[22] Y. Cui, Z. Ding, X. Fu, X. Wang, Construction of Conjugated Carbon Nitride Nanoarchitectures in Solution at Low Temperatures for Photoredox Catalysis, Angew. Chem., Int. Ed., 51 (2012) 11814-11818.

[23] Y. Cui, Y. Tang, X. Wang, Template-Free Synthesis of Graphitic Carbon Nitride Hollow Spheres for Photocatalytic Degradation of Organic Pollutants, Mater. Lett., 161 (2015) 197-200.

[24] H. Montigaud, B. Tanguy, G. Demazeau, I. Alves, S. Courjault, C_3N_4: Dream or Reality? Solvothermal Synthesis as Macroscopic Samples of the C_3N_4 Graphitic Form, J. Mater. Sci., 35 (2000) 2547-2552.

[25] C. Hu, Y. Chu, M. Wang, X. Wu, Rapid Synthesis of g-C_3N_4 Spheres Using Microwave-Assisted Solvothermal Method for Enhanced Photocatalytic Activity, J. Photochem. Photobiol., A, 348 (2017) 8-17.

[26] L. Wang, M. Yu, C. Wu, N. Deng, C. Wang, X. Yao, Synthesis of Ag/g-C_3N_4 Composite as Highly Efficient Visible-Light Photocatalyst for Oxidative Amidation of Aromatic Aldehydes, Adv. Synth. Catal., 358 (2016) 2631-2641.

[27] Y. Wang, H. Wang, F. Chen, F. Cao, X. Zhao, S. Meng, Y. Cui, Facile Synthesis of Oxygen Doped Carbon Nitride Hollow Microsphere for Photocatalysis, Appl. Catal., B, 206 (2017) 417-425.

[28] X. Li, Y. Yuan, X. Pan, L. Zhang, J. Gong, Boosted Photoelectrochemical Immunosensing of Metronidazole in Tablet Using Coral-Like g-C_3N_4 Nanoarchitectures, Biosens. Bioelectron., 123 (2019) 7-13.

[29] Q. Gu, Z. Gao, C. Xue, Self-Sensitized Carbon Nitride Microspheres for Long-Lasting Visible-Light-Driven Hydrogen Generation, Small, 12 (2016) 3543-3549.

[30] L.H. Lin, H.H. Ou, Y.F. Zhang, X.C. Wang, Tri-s-triazine-Based Crystalline Graphitic Carbon Nitrides for Highly Efficient Hydrogen Evolution Photocatalysis, ACS Catal., 6 (2016) 3921-3931.

[31] I. Papailias, T. Giannakopoulou, N. Todorova, D. Demotikali, T. Vaimakis, C. Trapalis, Effect of Processing Temperature on Structure and Photocatalytic Properties of g-C_3N_4, Appl. Surf. Sci., 358 (2015) 278-286.

[32] Z. Hong, B. Shen, Y. Chen, B. Lin, B. Gao, Enhancement of photocatalytic H_2 evolution over nitrogen-deficient graphitic carbon nitride, J. Mater. Chem. A, 1 (2013).

[33] Z.-A. Lan, G. Zhang, X. Wang, A Facile Synthesis of Br-Modified g-C_3N_4 Semiconductors for Photoredox Water Splitting, Appl. Catal., B, 192 (2016) 116-125.

[34] H. Yu, R. Shi, Y. Zhao, T. Bian, Y. Zhao, C. Zhou, G.I.N. Waterhouse, L.Z. Wu, C.H. Tung, T. Zhang, Alkali-Assisted Synthesis of Nitrogen Deficient Graphitic Carbon Nitride with Tunable Band Structures for Efficient Visible-Light-Driven Hydrogen Evolution, Adv. Mater., 29 (2017).

[35] Q. Tay, P. Kanhere, C.F. Ng, S. Chen, S. Chakraborty, A.C.H. Huan, T.C. Sum, R. Ahuja, Z. Chen, Defect Engineered g-C_3N_4 for Efficient Visible Light Photocatalytic Hydrogen Production, Chem. Mater., 27 (2015) 4930-4933.

[36] C. Ye, J. Li, Z. Li, X. Li, X. Fan, L. Zhang, B. Chen, C. Tung, L. Wu, Enhanced Driving Force and Charge Separation Efficiency of Protonated g-C_3N_4 for Photocatalytic O_2 Evolution, ACS Catal., 5 (2015) 6973-6979.

[37] J. Duan, S. Chen, M. Jaroniec, S.Z. Qiao, Porous C_3N_4 Nanolayers@N-graphene Films as Catalyst Electrodes for Highly Efficient Hydrogen Evolution, ACS Nano, 9 (2015) 931-940.

[38] B. Zhu, J. Zhang, C. Jiang, B. Cheng, J. Yu, First Principle Investigation of Halogen-Doped Monolayer g-C_3N_4 Photocatalyst, Appl. Catal., B, 207 (2017) 27-34.

[39] X. Zhang, A. Hsu, H. Wang, Y. Song, J. Kong, M.S. Dresselhaus, T. Palacios, Impact of Chlorine Functionalization on High-Mobility Chemical Vapor Deposition Grown Graphene, ACS Nano, 7 (2013) 7262-7270.

[40] L. Fan, H. Zhang, P. Zhang, X. Sun, One-Step Synthesis of Chlorinated Graphene by Plasma Enhanced Chemical Vapor Deposition, Appl. Surf. Sci., 347 (2015) 632-635.

[41] E.W. Kauffman, XPS and Carbon-13 NMR Spectroscopic Analysis of Composite Rocket Propellants, Virginia Polytechnic Institute and State University, 1983.

[42] L. Liang, Y. Cong, L. Yao, F. Wang, L. Shi, One Step to Prepare Cl Doped Porous Defect Modified g-C_3N_4 With Improved Visible-Light Photocatalytic Performance for H_2 Production and Rhodamine B Degradation, Mater. Res. Express, 5 (2018).

[43] Q. Xu, W. Zhao, J. Zhi, J. Yin, Exfoliation of Graphite in CO_2 Expanded Organic Solvents Combined With Low Speed Shear Mixing, Carbon, 135 (2018) 180-186.

[44] T.-R. Lee, Quantitative Correlation Between Interlayer Distance and Shear Rate in Liquid-Based Exfoliation of Graphene Layers, Carbon, 129 (2018) 661-666.

[45] R. Rizvi, E.P. Nguyen, M.D. Kowal, W.H. Mak, S. Rasel, M.A. Islam, A. Abdelaal, A.S. Joshi, S. Zekriardehani, M.R. Coleman, R.B. Kaner, High-Throughput Continuous Production of Shear-Exfoliated 2D Layered Materials using Compressible Flows, Adv. Mater., 30 (2018) 1800200.

[46] Y. Li, X. Yin, W. Wu, Preparation of Few-Layer MoS_2 Nanosheets via an Efficient Shearing Exfoliation Method, Ind. Eng. Chem. Res., 57 (2018) 2838-2846.

[47] F. Di Renzo, Zeolites as Tailor-Made Catalysts: Control of the Crystal Size, Catal. Today, 41 (1998) 37-40.

[48] W.R. Wilcox, Transport Phenomena in Crystal Growth From Solution, Prog. Cryst. Growth Charact. Mater., 26 (1993) 153-194.

[49] Z.Q. Yu, R.B.H. Tan, P.S. Chow, Effects of Operating Conditions on Agglomeration and Habit of Paracetamol Crystals in Anti-Solvent Crystallization, J. Cryst. Growth, 279 (2005) 477-488.

[50] J. Liu, Å.C. Rasmuson, Influence of Agitation and Fluid Shear on Primary Nucleation in Solution, Cryst. Growth Des., 13 (2013) 4385-4394.

[51] N. Nakamura, K. Inayama, T. Okuno, H. Ogi, M. Hirao, Accelerated crystallization of colloidal glass by mechanical oscillation, Sci. Rep., 7 (2017) 1369.

[52] J.W. Mullin, K.D. Raven, Nucleation in Agitated Solutions, Nature, 190 (1961) 251-251.

[53] D. Richard, T. Speck, The role of shear in crystallization kinetics: From suppression to enhancement, Sci. Rep., 5 (2015) 14610.

[54] S. Zhao, Y. Zhang, Y. Wang, Y. Zhou, K. Qiu, C. Zhang, J. Fang, X. Sheng, Ionic Liquid-Assisted Synthesis of Br-Modified g-C_3N_4 Semiconductors With High Surface Area and Highly Porous Structure for Photoredox Water Splitting, J. Power Sources, 370 (2017) 106-113.

[55] M. Bellardita, E.I. García-López, G. Marcì, I. Krivtsov, J.R. García, L. Palmisano, Selective Photocatalytic Oxidation of Aromatic Alcohols in Water by Using P-doped g-C_3N_4, Appl. Catal., B, 220 (2018) 222-233.

[56] J.C. Wang, C.X. Cui, Y. Li, L. Liu, Y.P. Zhang, W. Shi, Porous Mn Doped g-C_3N_4 Photocatalysts for Enhanced Synergetic Degradation Under Visible-Light Illumination, J Hazard Mater, 339 (2017) 43-53.

[57] P. Niu, L.C. Yin, Y.Q. Yang, G. Liu, H.M. Cheng, Increasing the Visible Light Absorption of Graphitic Carbon Nitride (Melon) Photocatalysts by Homogeneous Self-Modification With Nitrogen Vacancies, Adv. Mater., 26 (2014) 8046-8052.

[58] G. Zhang, G. Li, Z.A. Lan, L. Lin, A. Savateev, T. Heil, S. Zafeiratos, X. Wang, M. Antonietti, Optimizing Optical Absorption, Exciton Dissociation, and Charge Transfer of a Polymeric Carbon Nitride with Ultrahigh Solar Hydrogen Production Activity, Angew. Chem., Int. Ed., 56 (2017) 13445-13449.

[59] S. Lu, C. Li, H.H. Li, Y.F. Zhao, Y.Y. Gong, L.Y. Niu, X.J. Liu, T. Wang, The Effects of Nonmetal Dopants on the Electronic, Optical and Chemical Performances of Monolayer g-C_3N_4 by First-principles Study, Appl. Surf. Sci., 392 (2017) 966-974.

[60] M.V. Putz, N. Russo, E. Sicilia, About the Mulliken Electronegativity in DFT, Theor. Chem. Acc., 114 (2005) 38-45.

[61] M.A. Butler, Prediction of Flatband Potentials at Semiconductor-Electrolyte Interfaces from Atomic Electronegativities, Journal of The Electrochemical Society, 125 (1978).

[62] Y. Xu, M.A.A. Schoonen, The Absolute Energy Positions of Conduction and Valence Bands of Selected Semiconducting Minerals, Am. Mineral., 85 (2000) 543-556.

[63] K. Ding, L. Wen, M. Huang, Y. Zhang, Y. Lu, Z. Chen, How Does the B,F-Monodoping and B/F-Codoping Affect the Photocatalytic Water-Splitting Performance of g-C_3N_4?, Phys. Chem. Chem. Phys., 18 (2016) 19217-19226.

[64] Y.I. Kim, S.J. Atherton, E.S. Brigham, T.E. Mallouk, Sensitized layered metal oxide semiconductor particles for photochemical hydrogen evolution from nonsacrificial electron donors, The Journal of Physical Chemistry, 97 (1993) 11802-11810.

[65] X. Wu, D. Gao, H. Yu, J. Yu, High-Yield Lactic Acid-Mediated Route for a g-C_3N_4 Nanosheet Photocatalyst With Enhanced H_2-Evolution Performance, Nanoscale, 11 (2019) 9608-9616.

[66] H. Tang, R. Wang, C. Zhao, Z. Chen, X. Yang, D. Bukhvalov, Z. Lin, Q. Liu, Oxamide-modified g-C_3N_4 Nanostructures: Tailoring Surface Topography for High-Performance Visible Light Photocatalysis, Chem. Eng. J., 374 (2019) 1064-1075.

Chapter 5 C doped TiN nanocrystals supported by ultrathin carbon layers with high surface area for photocatalytic dye degradation

5.1 Introduction

Localized surface plasmon resonance (LSPR) phenomenon has recently emerged as an attractive approach to take advantage of light energy [1, 2]. The photon energy absorbed by the plasmonic materials and further transfer to hot carriers has been proven a promising energy conversion route in the areas including enhanced spectroscopy [3], solar cell [4] and photocatalysis [5-7]. To date, most of the researches have focused on the application of LSPR based on the "coin metals", especially Ag and Au [8], which largely hinders the large-scale practical implementation due to the scarcity and high costs. The development of low-cost plasmonic photocatalysts maintaining high activity in promoting energy conversion is the main challenge today [9-13].

Among all the non-noble plasmonic material candidates, TiN shows its unique, attractive properties including metallic electronic structure, high thermal stability, low cost, sustainability and prominent plasmon quality [13-17]. TiN has been used as the plasmonic light absorber in many applications including steam generation [18, 19], alcohol oxidation [20, 21], water splitting [22-24], H_2O_2 decomposition [25], CO_2 conversion [2] and dye degradation [26]. Although showing the potentials as the plasmonic photocatalysts, the TiN also exhibits the intrinsic limitation of non-ideal electronic structure and limited surface area, which hinders TiN from achieving satisfactory photocatalytic performance. To further promote the photocatalytic efficiency of the TiN based photocatalysts, catalysts design is the most effective way and can be generally classified into 2 categories [27]: electronic structure modification and heterostructure design. The heterojunction design for facilitating carrier separation has been intensively investigated with building the heterostructures with TiO_2 [23, 24, 28], noble metal clusters [20, 22, 29], C_3N_4 [25], graphene [30] and $SrTiO_3$ [26] etc. Although proven as an effective way to enhance the activity of photocatalysts, the optimization of the electronic structure of plasmonic photocatalysts especially TiN to improve the hot carrier generation and light absorption are rarely investigated in the literature. A few examples are presented as

follows. Maeda et al. [31] investigated the O/F doped TiN and proved the enhancement of visible-light photocatalytic water splitting performance. Kumar et al. [32] performed theoretical calculations on the plasmon quality factor and found the improvement was attributed to the optimized electronic structure of TiN with Zr doping. The doping to the plasmonic photocatalysts can ensure the tunability of the optical response and hot carrier generation property, which is intriguing in plasmonic catalysis [33]. Therefore, further detailed investigations on the modification of the electronic structure of plasmonic photocatalysts and the effects on photocatalytic activity are of great importance.

Herein, the C doped TiN/ultrathin carbon layer catalysts have been prepared via a facile one-pot calcination and proven to be an efficient noble-metal-free plasmonic photocatalyst. By revisiting the effects of urea-glass preparation parameters [34] on chemical composition and plasmonic photocatalytic performances, the correlation between electronic structure modification and plasmonic photocatalytic dye degradation performance has been built up. A high specific surface area (SSA) of ~294 m^2 g^{-1} has been achieved at the synthesis temperature of 900 ºC. The SSA only shows a slight decrease to ~243 m^2 g^{-1} for the sample synthesized at 1100 ºC. The prepared C doped TiN/ultrathin carbon layer catalyst shows improved photocatalytic performance in dye degradation. It not only exhibits higher visible-light-driven photocatalytic dye degradation performance than the benchmark TiO_2 (rutile). Moreover, the C doped TiN/ultrathin carbon layer also outperforms the classical heterostructure of C_3N_4/TiO_2. The C doping into TiN induced plasmonic photocatalytic activity enhancement has been proven from both experimental and theoretical results. The enhanced interband transition and corresponding facilitated hot holes generation in the C dope TiN are ascribed to the main reasons for the improved plasmonic photocatalytic dye degradation performance.

5.2 Results and discussion

5.2.1 Crystal structure analyses

5.2.1.1 Powder X-ray diffraction analyses

The crystal structures of the prepared samples under different conditions are firstly analysed by XRD. The influences of Ti/urea molar ratios and calcination temperature on crystal phases of samples are presented in **Figure 5.1** (a) and (b) respectively. In **Figure 5.1**(a), it can be seen that the TiN-0.9-900 and samples with lower urea usage failed to exhibit the pure TiN phase. TiN-0.9-900 showed the diffraction patterns mainly attributed to rutile TiO_2 phase, which was

in a relatively high crystallization degree. The minor phases include TiN, anatase TiO_2 and Ti_7O_{13}, which is the Magnéli phase [35] derived from the reduced rutile. When the urea usage increases to 0.9 g, the intensity of the TiN peaks grows significantly in TiN-0.9-900. It indicates more TiN is formed during the calcination. Consistently, the rutile peaks nearly vanish in this sample. All the rest 3 samples, TiN-1.5-900, TiN-3.0-900 and TiN-4.5-900 contain diffraction patterns exclusively attributed to TiN (PDF#038-1426). Moreover, the TiN peaks show the increase in intensity and decrease in FWHM (full-width-half-maximum), when the urea usage grows from 1.5 to 4.5 g. This result suggests a better crystallization degree and a larger nanoparticle size are achieved with higher urea usage. As shown in **Figure 5.1**(b), the synthesis temperature plays an important role in TiN phase formation. When calcination temperature is lower than 700 °C, the products are mainly constituted by the rutile phase. The TiN phase emerges when the calcination temperature reaches 700 °C, while the peaks attributed to rutile phases still dominate at this temperature. With the temperature further increasing to 900 °C, only TiN diffraction pattern can be observed at this temperature. At higher synthesis temperature of 1000 and 1100 °C, the diffraction peaks become narrower and show higher intensity. It suggests the higher crystallization degree and larger TiN particles are formed. In summary, the XRD patterns of samples prepared at different conditions suggest that Ti/urea molar ratios and calcination temperature are two critical parameters determining the crystal phases of prepared samples. When either less than 1.5 g urea is used (5:1 urea/Ti molar ratio) or synthesis temperature is lower than 900 °C, the products achieved are the mixtures of TiN and TiO_2 (rutile). Both the higher urea/Ti ratios and calcination temperature will improve the formation and the crystallization degree of TiN.

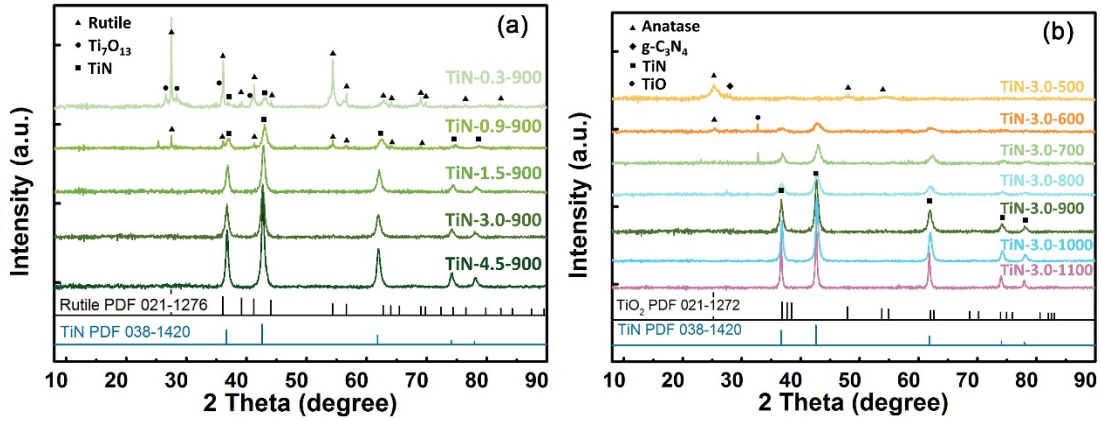

Figure 5.1. The X-ray diffraction patterns of (a) samples prepared at 900 °C with different urea usages (0.3, 0.9, 1.5, 3, 4.5 g urea) and (b) samples prepared with fixed urea usage of 3 g at varying calcination temperatures from 500 to 1100 °C.

5.2.1.2 X-ray photoelectron spectroscopy analyses

XPS is a powerful tool to investigate the chemical compositions of the prepared samples and the chemical environments of each element in the prepared catalysts. As a semi-quantitative analysis, the XPS can provide additional information on the quantity of C doping. **Figure 5.2** and **Figure 5.3** present the high-resolution N 1s and Ti 2p XPS profiles of TiN-0.3-900, TiN-0.9-900, TiN-1.5-900, TiN-3.0-900, TiN-4.5-900, TiN-3.0-500, TiN-3.0-600, TiN-3.0-700, TiN-3.0-800, TiN-3.0-900, TiN-3.0-1000, TiN-3.0-1100, respectively. All the spectra have been corrected by aligning to the adventitious carbon C 1s peak at 284.6 eV [27].

The XPS Ti 2p spectra of samples TiN-0.3-900, TiN-0.9-900, TiN-1.5-900, TiN-3.0-900 and TiN-4.5-900 synthesized at 900 ºC with different urea usages are presented in **Figure 5.2**(a). All the Ti 2p spectra can be deconvoluted into 4 peaks corresponding to TiO_2 (Ia, Ib), TiN (IIa, IIb), TiO_xN_y (IIIa, IIIb), and TiC (IVa, IVb), respectively. The peaks at 458.3 and 464.4 eV can be assigned to TiO_2 due to surface oxidation [36]. It is in high consistency with the control group sample, the commercial rutile powder. The peaks with the binding energy of 456.6 and 462.8 eV are consistent with the reported values of TiO_xN_y [37, 38]. The peaks at 455.4 and 461.2 eV are attributed to the formation of TiN during the synthesis [39-41]. The peaks at 455.0 and 461.0 eV corresponding to Ti-C bonds are derived from C doping to TiN [42-44]. The peak assignments are summarized in **Table 5.1**. Comparing the Ti 2p spectra of the samples synthesized with different urea usages, it can be concluded that the higher urea usage promotes the formation of TiN. In addition, when excessive carbon exists, the C can be doped into the lattice of TiN. As shown in **Figure 5.2**(b), the samples synthesized at 900 ºC with different urea amounts show the N 1s spectra derived from the TiN and N-doped ultrathin carbon layer. The major peak at the binding energy of 397.2 eV can be assigned to the Ti-N bond [45, 46] and the small peak on the shoulder (396.0 eV) is attributed to the surface oxidation N-O-Ti [47, 48]. The rest peaks with relatively small intensity can be assigned to the N-doped ultrathin carbon layer layers: pyridinic N (398.4 eV), pyrrolic N (399.8 eV) and graphitic N (401.0 and 401.7 eV) [49-53]. Overall, the N1s spectra demonstrate that the Ti-N becomes predominant with higher urea usage.

Figure 5.3(a) presents the XPS Ti 2p spectra of the samples synthesized with fixed 3.0 g urea usage at a varying temperature from 500 to 1100 ºC. They can be deconvoluted into 4 peaks attributing to TiO_2, TiO_xN_y, TiN and Ti-C, respectively. The corresponding binding energies are summarized in **Table 5.1**. The spectra indicate that the sample synthesized at 500 ºC contains TiO_2 only. When calcination temperature is higher than 600 ºC, the TiN and TiN_xO_y peaks emerge, and the intensity becomes higher when calcination temperature increases. This

result suggests that the higher synthesis temperature facilitates the TiN formation. It is also worth mentioning that the peaks ascribed to Ti-C bond emerge when calcination temperature is or higher than 900 ºC. This result proves that C is doped into the TiN lattice. The N 1s spectra shown in **Figure 5.3**(b) further elucidate the phase evolution of the samples prepared at different temperature. In the case of TiN-3.0-500, the N 1s spectra are derived from the C_3N_4. The peaks at 398.7, 399.8 and 400.8 eV are assigned to C=N-C, N-$(C)_3$ and NH_x in the repeated heptazine units of C_3N_4 [54, 55]. For the samples synthesized at the temperature higher than 600 ºC, the corresponding spectra can be deconvoluted into 6 peaks. The Ti-N, Ti-O-N are derived from TiN and its surface oxidation. While the graphitic N, pyrrolic N, pyridinic N are attributed to the N doped ultrathin carbon layer. The TiN-3.0-600 sample shows the spectrum corresponding to the mixture of TiN, N doped ultrathin carbon layer and C_3N_4.

Based on the XPS Ti 2p 3/2 peak deconvolution (**Figure 5.2**(a) and **Figure 5.3**(a)), the concentration of C dopants can be determined. It is proven that only TiN-3.0-900, TiN-3.0-1000, TiN-3.0-1100 and TiN-4.5-900 contain C dopants and the corresponding doping concentrations are calculated to be 2.44at%, 2.72at%, 3.03at% and 5.49at%, respectively.

Table 5.1. The XPS Ti 2p spectra assignment and corresponding binding energy

Peak	Component	Binding energy(eV)	Assignment
Ti 2p 3/2	Ia	458.3	TiO_2
	IIa	456.6	TiO_xN_y
	IIIa	455.4	TiN
	IVa	455.0	TiC
Ti 2p 1/2	Ib	464.0	TiO2
	IIb	462.8	TiO_xN_y
	IIIb	461.2	TiN
	IVb	461.0	TiC

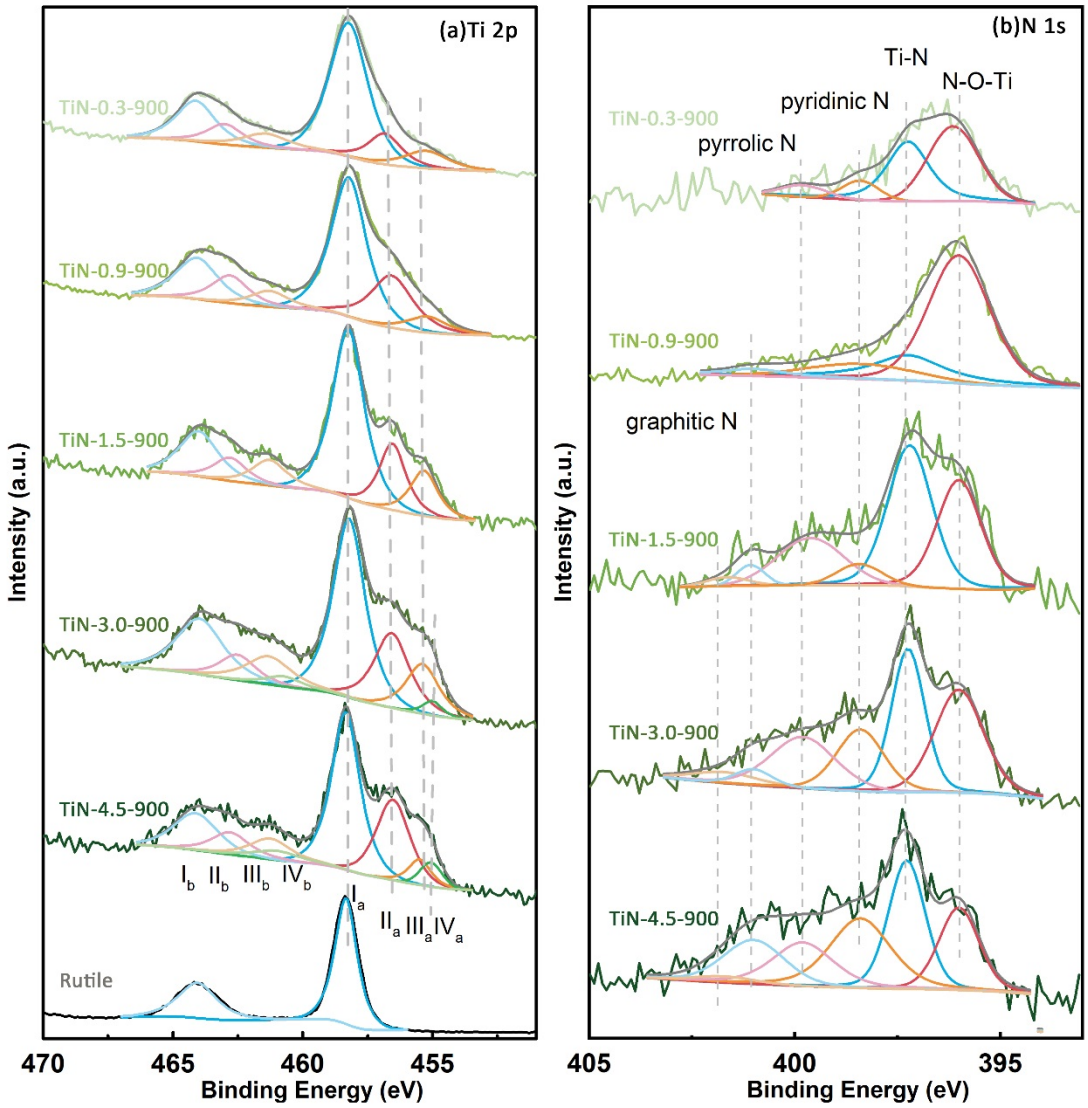

Figure 5.2. The XPS (a) Ti 2p and (b) N 1s spectra of samples prepared with varying urea usage form 0.5 g to 4.5 g at the fixed calcination temperature of 900 ºC. The Ti 2p spectra of rutile TiO_2 is also included for comparison.

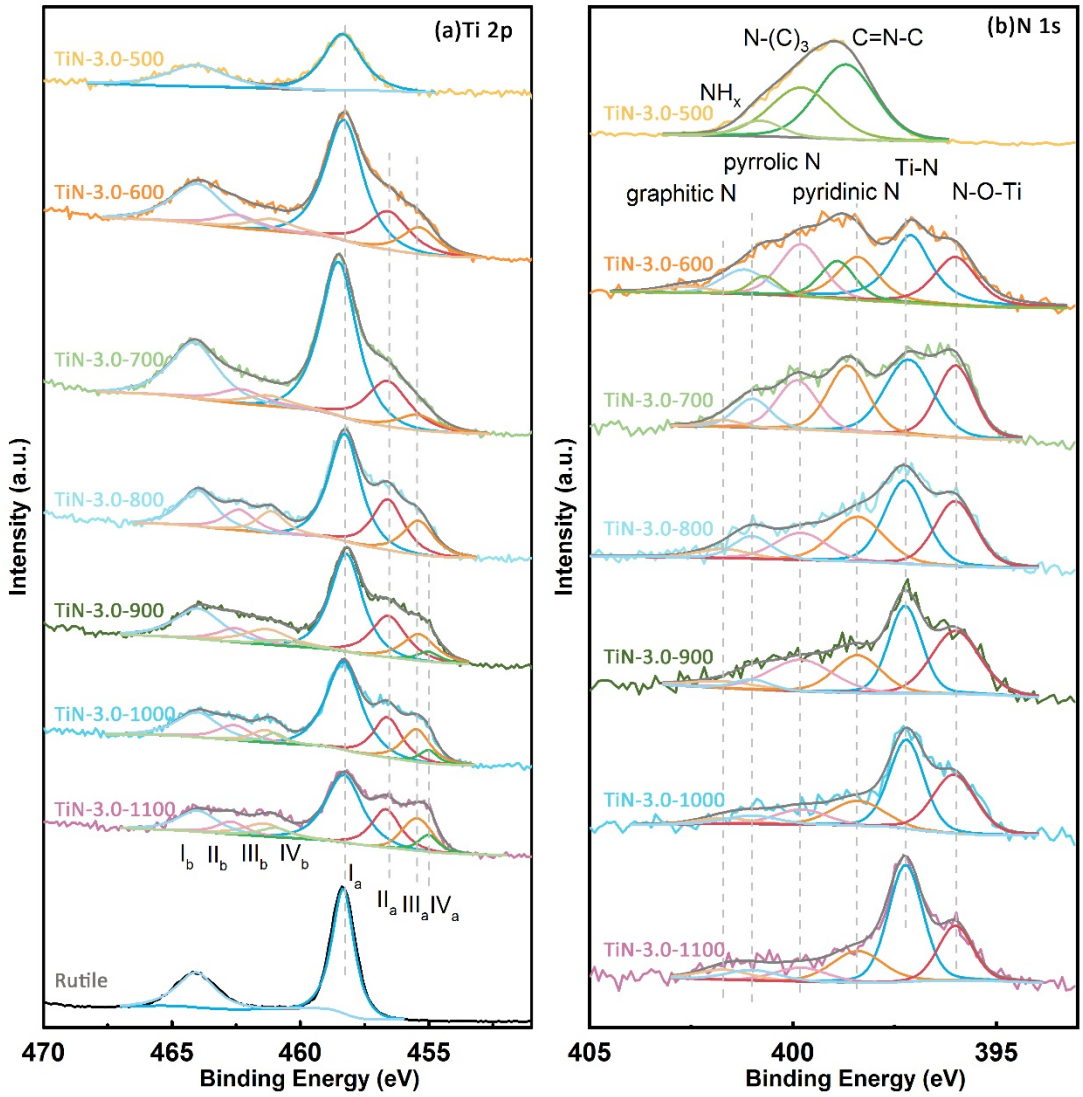

Figure 5.3. The XPS (a) Ti 2p and (b) N 1s spectra of samples prepared with fixed urea usage of 3 g at varying calcination temperature from 500 to 1100 ºC.

5.2.1.3 Thermal analyses

Thermal analyses combining gravimetric and calorimetric information are supplementary tools to unravel the compositions of the prepared samples. Thermal analyse were carried out under flowing Air in 100 sccm within the temperature range from 25 to 1000 ºC (10 K min^{-1} ramping rate) to fully convert samples to rutile TiO_2. The TGA/DSC curves of samples prepared with different Ti/Urea molar ratios at 900 ºC are presented in **Figure 5.4**(a-e). Similarly, the TGA-DSC curves of samples prepared at fixed urea usage of 3.0 g at a temperature range from 500 to 1100 ºC are presented in **Figure 5.4**(f-k). The TGA-DSC curves

share 2 features in common: (1) TiN oxidation (indicated by an amber dash line) and (2) C oxidation (indicated by black dot line). The weight increase starting from ~350 ºC and ending at ~ 500 ºC can be attributed to the TiN oxidation [56]. The weight loss starting from ~480 ºC can be attributed to the oxidation of residual carbon [57] with an exothermal heat flow peak at ~ 510 ºC. The chemical reaction taking places during the thermal analyses can be written as:

$$x\mathrm{TiN} + y\mathrm{TiC} + z\mathrm{C} + (x + z + 2y)\mathrm{O_2} \rightarrow (x + y)\mathrm{TiO_2} + \frac{x}{2}\mathrm{N_2} + (y + z)\mathrm{CO_2} \qquad (5.1)$$

The third DSC peak at ~600 ºC can be attributed to the oxidation of TiC components (C doped TiN) in the structure. It has been reported that TiC_xN_{1-x} composite with higher C concentration exhibits higher oxidation resistance [58]. In addition, another special case is also observed: in TiN-3.0-500 (**Figure 5.4**(f)), the TGA-DSC curves show the typical feature of C_3N_4 oxidation [27].

Based on the TGA-DSC analyses results, the chemical compositions of samples prepared at different conditions can be summarized as follows. The samples synthesized with inadequate urea usage are constituted by the mixtures of TiO_{2-x} and TiN. With excessive urea, the C doped TiN is formed along with N-doped ultrathin carbon layer. With calcination temperature is and higher than 900 ºC, the C doped TiN and N doped ultrathin carbon layer are the main products. When synthesis temperature is 500 ºC, a mixture of TiO_2/C_3N_4 is formed. Moreover, it is also confirmed that the C doping can be enhanced with higher preparation temperature and more urea usage, which is in consistency with XPS characterization results (**Figure 5.2**(a)). Similar phenomena have been reported in the literature [59-61].

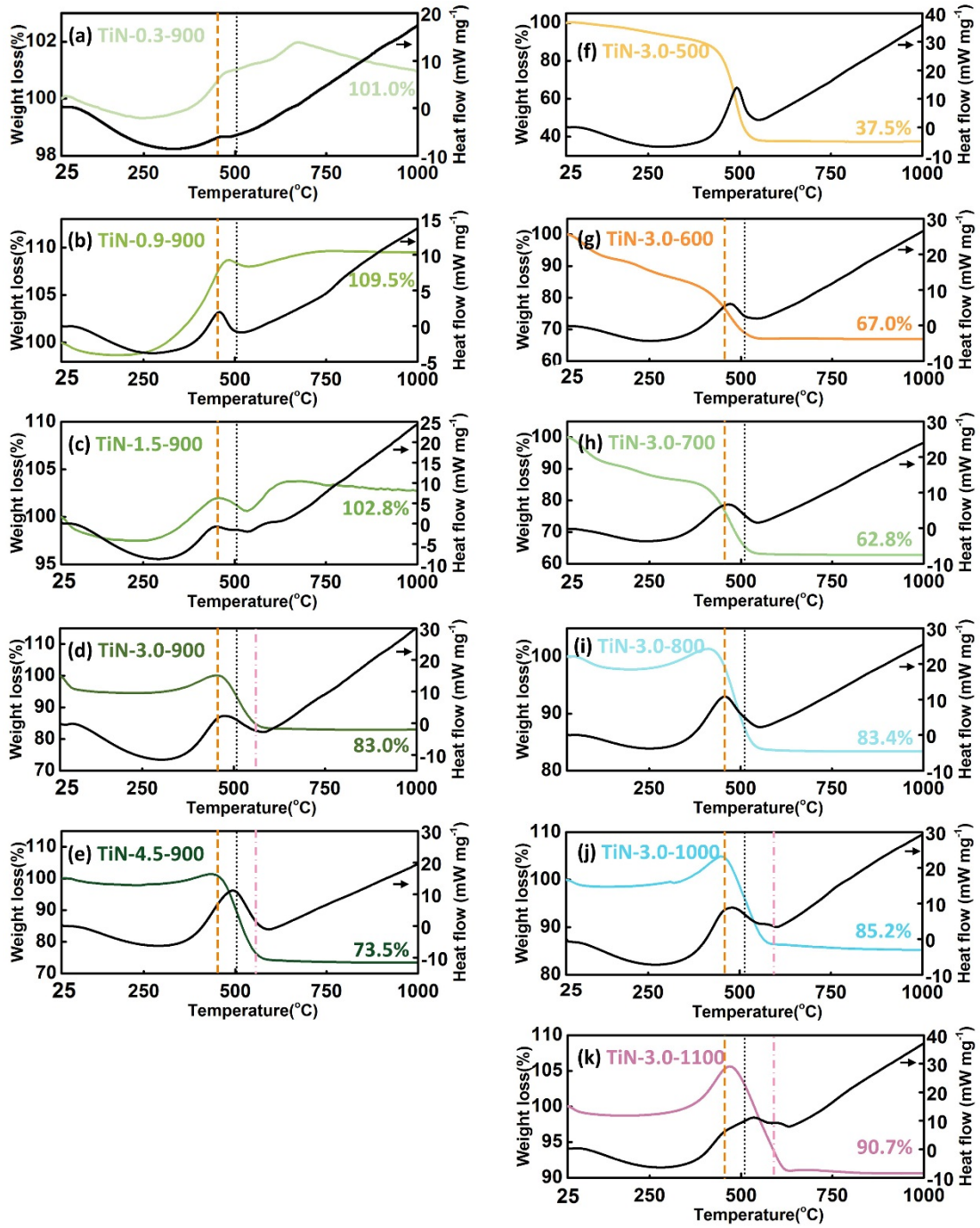

Figure 5.4. TGA-DSC curves of samples prepared at 900 ºC with different urea/Ti molar ratio (a-e): (a) TiN-0.3-900, (b) TiN-0.9-900, (c) TiN-1.5-900, (d) TiN-3.0-900, (e) TiN-4.5-900. And TGA-DSC curves of samples prepared with urea/Ti molar ratio 10 (3.0 g urea) at different temperatures: (f) 500 ºC, (g) 600 ºC, (h) 700 ºC, (i) 800 ºC, (d) 900 ºC, (j) 1000 ºC, (k) 1100 ºC. The positive DSC peak responds to exothermal process. The amber dash, black dot and pink dash-dot lines indicate the TiN, C and TiC oxidation process respectively.

5.2.2 Morphology characterization

SEM is used to investigate the effects of Ti/urea ratio and calcination temperature on the morphology and chemical compositions of prepared samples. The SEM images of samples synthesized with different Ti/urea ratios are presented in **Figure 5.5**. As shown in **Figure 5.5**(a, b) and (c, d), the samples synthesized with 0.3 and 0.9 g urea are the mixture of TiO_2 in size of several microns and TiN nanoparticles smaller than 20 nm. When more urea is used, the TiO_2 crystals disappear, and size of TiN nanocrystals grows (**Figure 5.5**(e-k)). TEM provides more detailed morphology information on the TiN nanocrystals and the carbon support. As shown in **Figure 5.6**, with increasing urea usage, more TiN can be observed. In addition, the TiN nanocrystal size increases accordingly from ~ 10 nm to ~ 40 nm. The C doped TiN/ultrathin carbon layer, which is free of TiO_2, can be clearly observed in TiN-3.0-900 and TiN-4.5-900. For the samples synthesized at a different temperature, the TiN-3.0-500 shows a typical bulk C_3N_4 structure with ultrasmall TiO_2 particles attached. Moreover, it can be seen from the images of TiN-3.0-1000 and TiN-3.0-1100 that the higher calcination temperature results in the rise of TiN nanoparticle size comparing with TiN-3.0-900. Based on the TEM analyses, the particle size distribution curves are plotted in **Figure 5.7**(a-e). To be specific, the TiN-0.9-900, TiN-1.5-900, TiN-3.0-900, TiN-4.5-900 and TiN-3.0-1100 show the mean TiN nanoparticle size of 10.5, 10.5, 16.2, 39.0 and 37.5 nm respectively. This sequence is in consistence with the trend suggested by the XRD analyses with Scherrer's equation (**Figure 5.7**(f)). To further confirm the elemental distribution of the C doped TiN/ultrathin carbon layer, the HRTEM and STEM-EDS were used to characterize the TiN-3.0-1100. As shown in **Figure 5.8**(b), the TiN nanocrystal exhibits the clear lattice fringes with an interplanar distance of 0.21 nm, which can be assigned to the (200) facet of TiN. The C, N, O, Ti EDS mapping based on the STEM image (**Figure 5.8**(c-h)) prove the homogeneous distribution of C, N, Ti in the nanocrystals. The EDS results (**Figure 5.8**(f)) show the Ti/N atomic ratio is 1.05, which is very close to the stoichiometry of TiN. The STEM-EDS analysis results are in consistence with the XRD and XPS results.

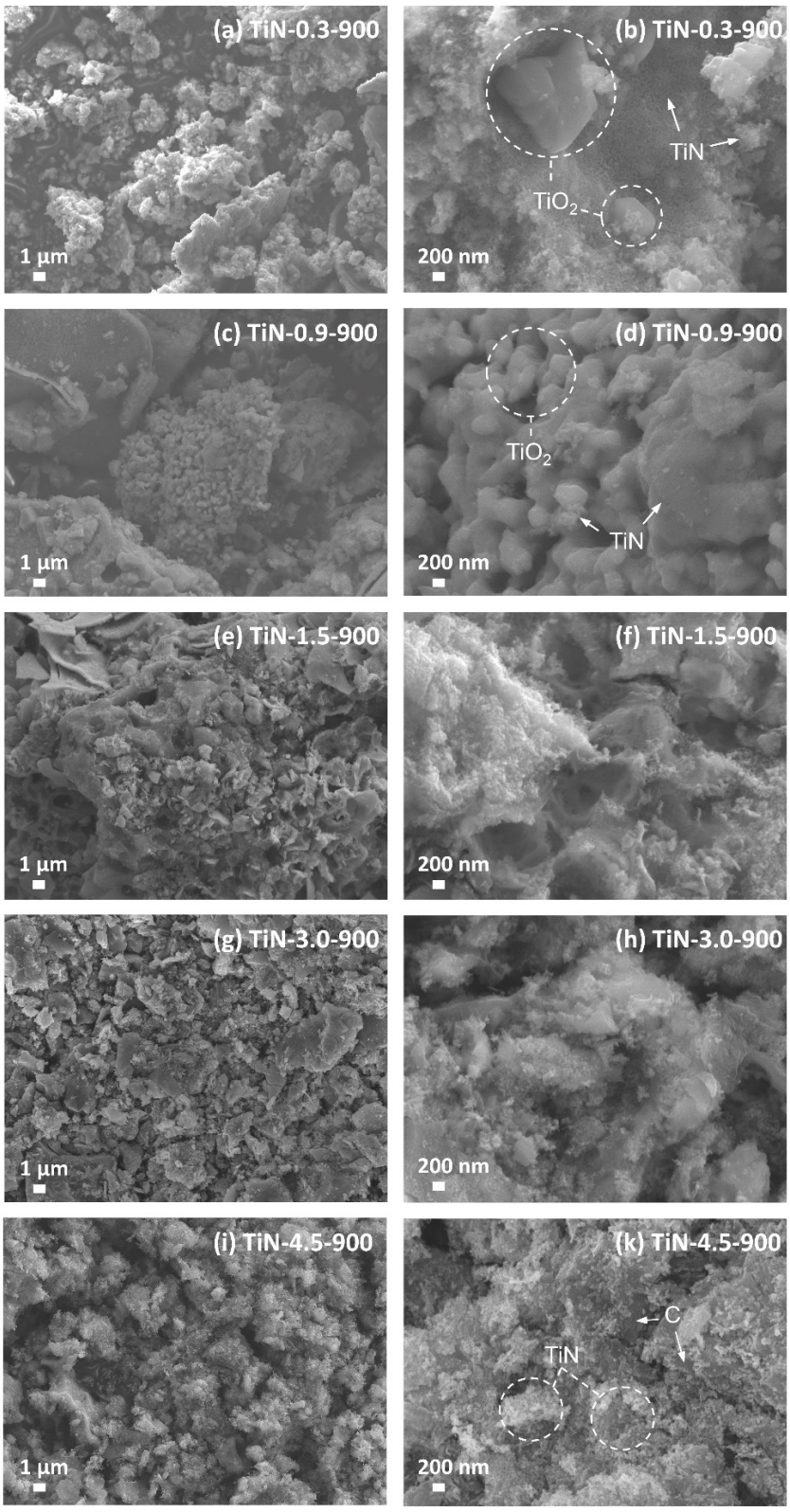

Figure 5.5. SEM images of (a, b) TiN-0.3-900, (c, d) TiN-0.9-900, (e, f) TiN-1.5-900, (g, h) TiN-3.0-900 and (i, j) TiN-4.5-900 at low and high magnification.

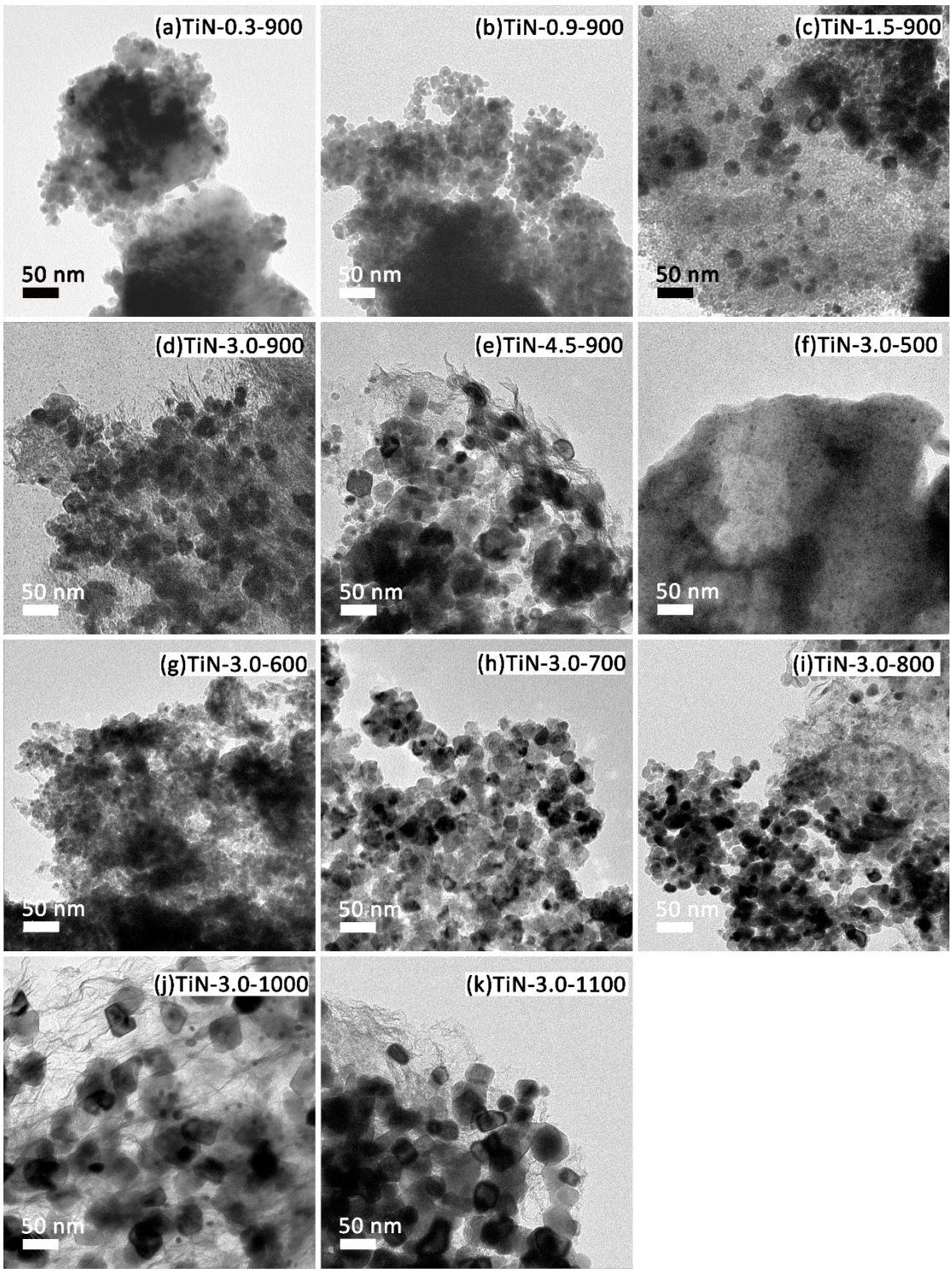

Figure 5.6. TEM images of TiN samples synthesized with different urea usages: (a) TiN-0.3-900, (b) TiN-0.9-900, (c) TiN-1.5-900, (d) TiN-3.0-900, (e) TiN-4.5-900. And TEM images of TiN samples synthesized with fixed urea usage of 3 g at different temperatures: (f) TiN-3.0-500, (g) TiN-3.0-600, (h) TiN-3.0-700, (i) TiN-3.0-800, (j) TiN-3.0-1000, (d) TiN-3.0-1100.

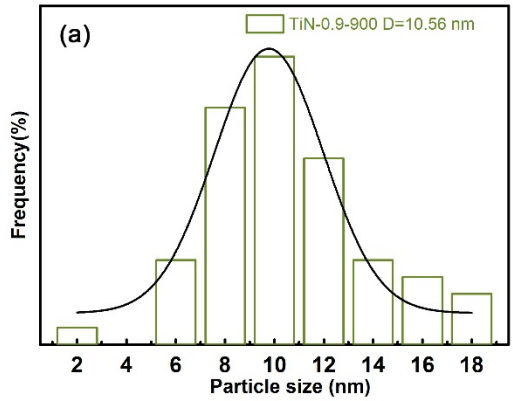

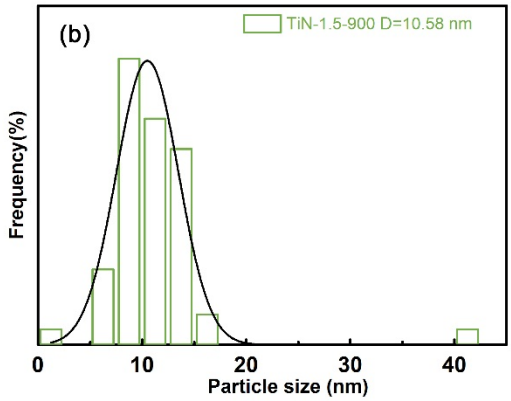

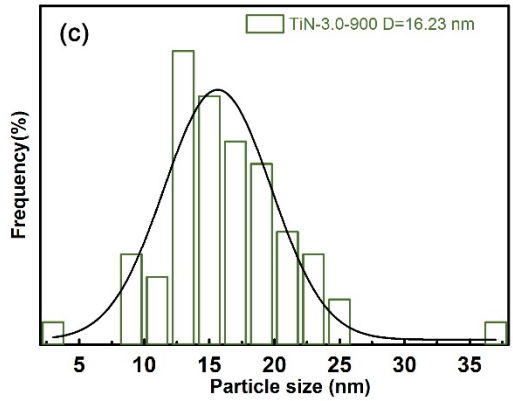

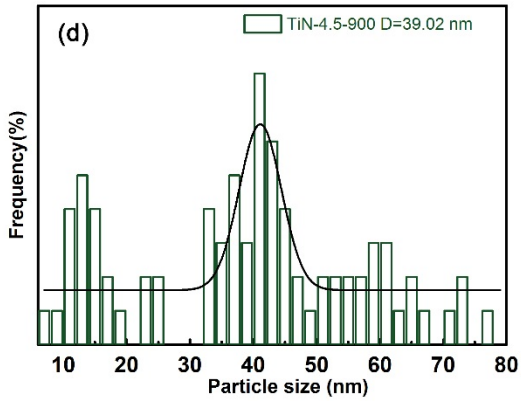

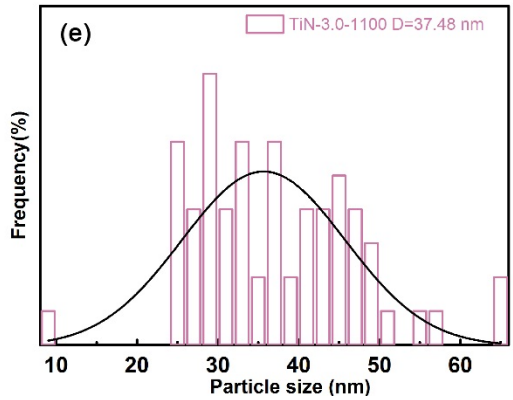

(f)

Photocatalyst	NP Size (nm) (Scherrer's)	NP Size (nm) (TEM)
TiN-0.9-900	10.5	10.560
TiN-1.5-900	14.1	10.588
TiN-3.0-900	18.5	16.231
TiN-4.5-900	26.1	39.028
TiN-3.0-1100	28.6	37.485

Figure 5.7. The TiN nanoparticle size distribution curves of (a) TiN-0.9-900, (b) TiN-1.5-900, (c) TiN-3.0-900, (d) TiN-4.5-900 and (e) TiN-3.0-1100. The summary (f) of the mean nanoparticle (NP) sizes based on the TEM and Scherrer's equation calculation.

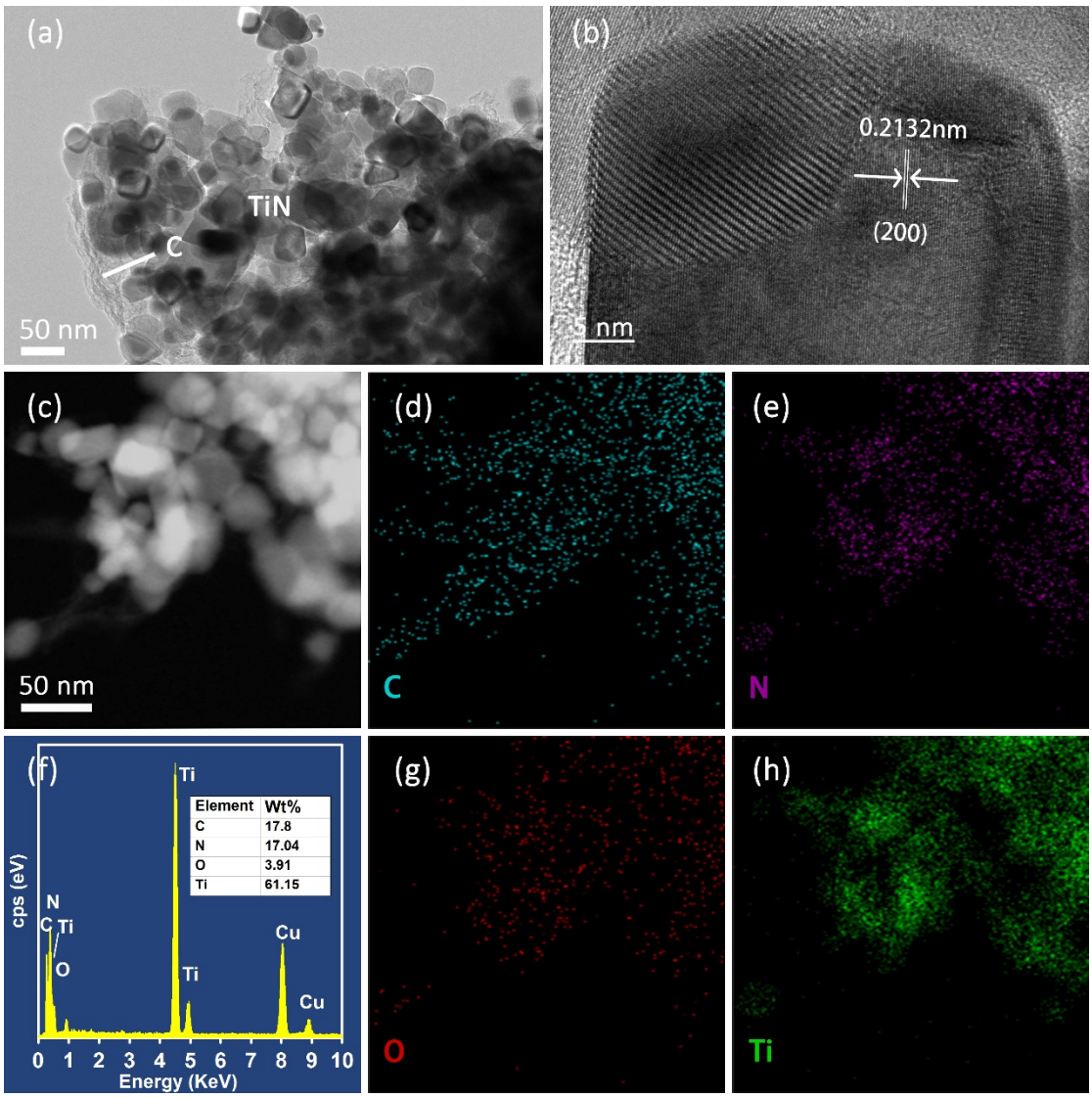

Figure 5.8. (a, b) TEM, (c) STEM images and (d, e, g, h) the corresponding EDS C, N, O, Ti elemental mappings of TiN-3.0-1100. The EDS spectrum and results are presented in (f).

5.2.3 N_2 adsorption/desorption measurements

The SSA is critical for catalysts since larger SSA ensures more actives sites for reaction. To investigate the influences of preparation conditions (Ti/urea ratio and temperature) on the SSA and pore structure, N_2 adsorption/desorption measurements were conducted at 77 K. The achieved isotherms and corresponding pore size distribution curves are presented in **Figure 5.9**. As shown in **Figure 5.9**(a), all the samples synthesized at 900 °C with different urea usages except TiN-0.3-900 exhibit the N_2 sorption isotherms of type IV(a) [62], which

indicates the mesoporous structure. The isotherm of TiN-0.3-900 belongs to type II, which indicates the nonporous structure. The SSAs calculated using Brunauer-Emmett-Teller (BET) theory are 29.6, 107.5, 172.5, 294.2 and 242.6 $m^2 g^{-1}$ for TiN-0.3-900, TiN-0.9-900, TiN-1.5-900, TiN-3.0-900 and TiN-4.5-900, respectively. It is noted that the SSA and urea usage shows a volcano-shape correlation. The SSA firstly increases monotonically with the rise of urea usage and TiN-3.0-900 shows the highest SSA. Then the SSA falls in the case of TiN-4.5-900 sample. The very small SSA of TiN-0.3-900 (29.6 $m^2 g^{-1}$) is due to large TiO_2 crystals with the size of several microns (as shown in **Figure 5.5**). More urea usage reduces the TiO_2 proportion in the catalysts and promotes the formation of TiN, which results in a larger SSA. In TiN-4.5-900, the excessive urea facilitates the growth of TiN nanocrystals and the larger TiN nanocrystal is responsible for the SSA decrease (as shown in TEM images in **Figure 5.6** and **Figure 5.7**). It is worth emphasizing that the residual carbon (ultrathin carbon layers) does not determine the SSA. TiN-4.5-900 using 4.5 g urea exhibits the SSA of 242.6 $m^2 g^{-1}$ while TiN-3.0-900 using 3.0 g urea shows the SSA of 294.2 $m^2 g^{-1}$. This significant SSA difference strongly supports the irrelevance between residual carbon and SSA, which is rationalized by its relatively low amount. The pore-size distribution curves in **Figure 5.9**(b) further confirms the mesoporous structure of the synthesized catalysts with different urea usages. TiN-0.3-900 shows nearly no peak within the diameter range from 2 to 30 nm, which is in consistence with the hysteresis shape of its N_2 sorption isotherm. With higher contents of TiN, the samples exhibit a more prominent preferred pore size of ~ 4 nm. The mesopores are derived from the stacking of TiN nanocrystals.

The N_2 sorption isotherm of samples prepared at different temperature with fixed urea usage and the corresponding pore size distribution curves are presented in **Figure 5.9**(c, d). The TiN-3.0-500 shows the smallest BET-SSA of 59.3 $m^2 g^{-1}$, which is similar to the typical value of TiO_2/C_3N_4 in the literature [63-65]. With the synthesis temperature rising, the BET-SSA shows the increasing trend from 166.5 $m^2 g^{-1}$ (TiN-3.0-600) to 294.2 $m^2 g^{-1}$ (TiN-3.0-900). Further increasing the synthesis temperature causes the decrease of the BET-SSA to 243.4 $m^{-2} g^{-1}$ for TiN-3.0-1100. It is attributed to the growth of the TiN nanoparticle size, as shown in **Figure 5.7**(f). The pore size distribution curves (**Figure 5.9**(d)) provide additional information for the microstructure. The TiN-3.0-500 shows no preferred pore size due to its non-porous structure in agreement with the N_2 sorption isotherm hysteresis shape. With the formation of TiN in higher synthesis temperature, the pore size distribution curves show the dominated peaks at ~4 nm. It is due to the stack of the TiN nanoparticles, which is also found in **Figure 5.9**(b).

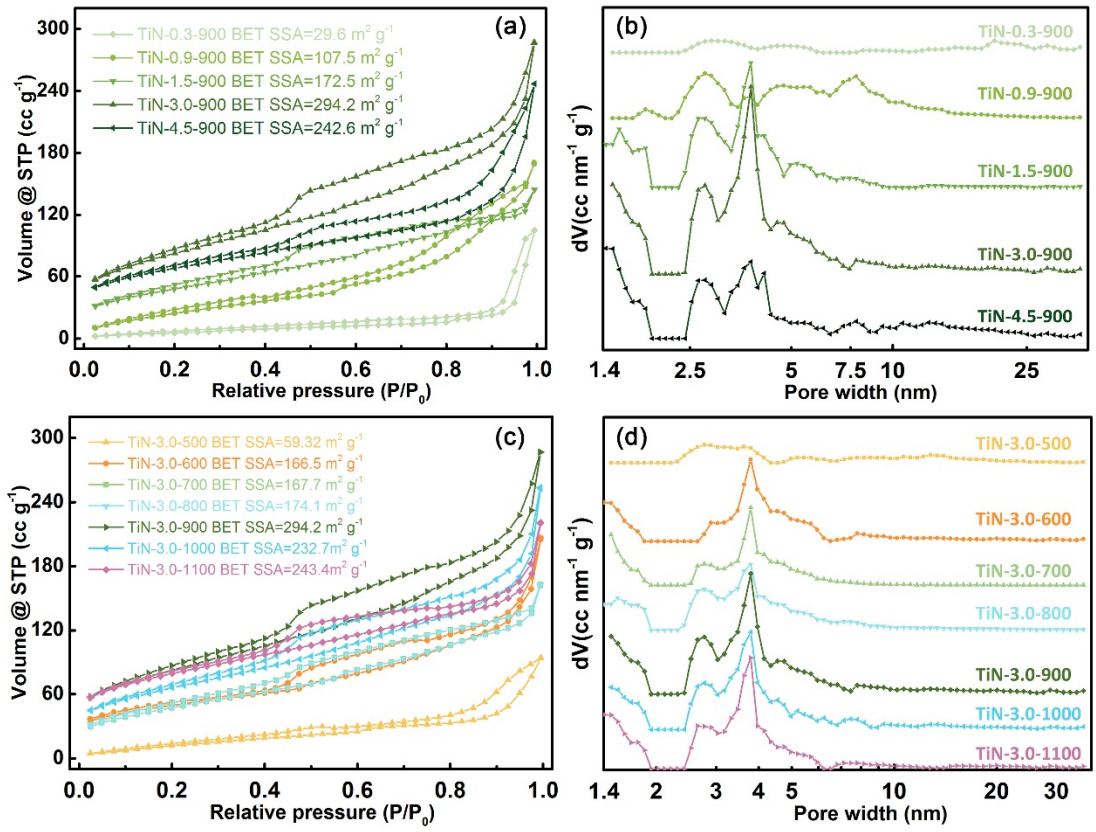

Figure 5.9. (a) N_2 sorption isotherms at 77 K and (b) pore size distribution curves of samples prepared with different urea amounts at 900 °C. (c) N_2 sorption isotherms at 77 K and (d) pore size distribution curves of samples (3 g urea) calcinated at different temperature.

5.2.4 Electronic structure analyses

5.2.4.1 UV-Vis-NIR diffuse reflectance spectroscopy (DRS) analyses

The UV-Vis DRS present the optical responses of prepared catalysts to incident light. As shown in **Figure 5.10**(a), the samples prepared with different urea amounts show two different kinds of spectra. All the samples except the TiN-0.3-900 show the broad absorption from 220-1000 nm, proving them as good light absorber for full UV-Vis-NIR spectrum. The exception, TiN-0.3-900, shows a typical reflectance spectrum of semiconductor: a strong absorption of UV light and low visible light absorption. It is because the TiN-0.3-900 is mainly constituted by reduced TiO_2 with TiN and residual carbon in small portions. The UV-Vis-NIR DR spectra are in agreement with the chemical composition analyses discussed in the earlier sections (**Figure 5.1** and **Figure 5.2**). A similar phenomenon has been observed in **Figure 5.10**(b). The

TiN-3.0-500 exhibits the semiconductor-like response to light. The TiN-3.0-500 shows the strong UV absorption band tailing to the visible range, which is in consistence with the reported C_3N_4/TiO_2 light absorption behaviour [27, 66]. The rest of the samples in **Figure 5.10**(b) exhibit similar broad-band absorption for full UV-Vis-NIR spectra.

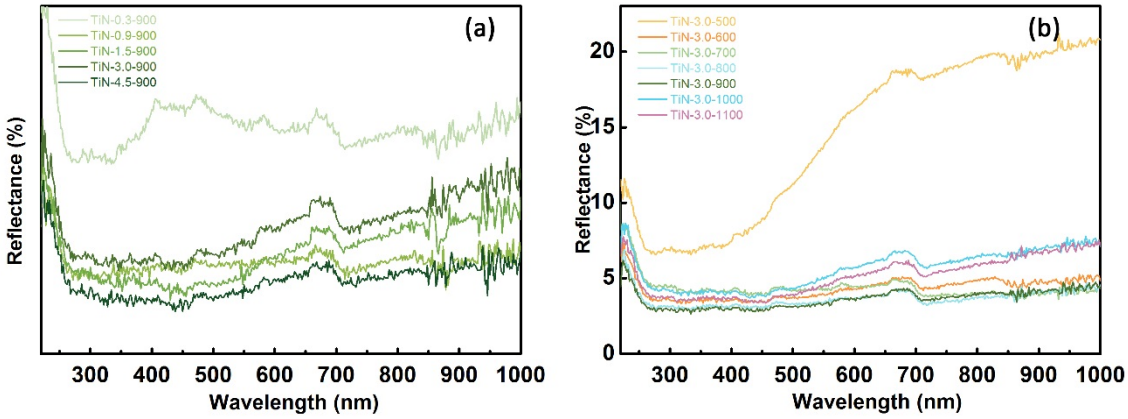

Figure 5.10. The UV-Vis-NIR DRS presented in reflectance of (a) samples prepared at 900 °C with different urea usages (0.3, 0.9, 1.5, 3, 4.5 g urea) and (b) samples prepared with fixed urea usage of 3 g at varying calcination temperature from 500 to 1100 °C.

5.2.4.2 Electronic structure calculation

It is important to know how exactly the C doping changes the electronic structure of TiN. Because the energy distribution of plasmon excited hot carriers is mainly determined by the electronic structure [67]. First-principle calculation using DFT method has been generally adopted to describe the electronic structures of both the intrinsic and doped materials. The primitive cell of most stable TiC and TiN crystals used in the theoretical calculations are schemed in **Figure 5.11**. To represent the C doped TiN crystal structure, a 2 × 2 × 2 supercell of TiN was built up with one N atom being replaced by C. The calculated lattice parameters for TiC and TiN are 3.036 and 2.973 Å, which are very close to the experimental values of 3.051 and 2.995 Å respectively. The difference is smaller than 0.7%. The C doped TiN remains the same cubic crystal structure (no distortion) with an increased lattice parameter of 5.962 Å (2 × 2 × 2 supercells). The slight increase in lattice parameter induced by C doping is in consistence with the peak shift to lower angle in XRD analyses (**Figure 5.1**). The calculated electronic structure of TiC, TiN and C doped TiN are shown in **Figure 5.12**(a-c). It can be clearly seen that the half-filled Ti d band dominates the upper band near the Fermi energy (E_F), which indicates the metallic property of all 3 structures. The non-metal elements contribute to

the bands lower than E_F dominates from a different energy level. By comparing the electronic structures of TiC with TiN (**Figure 5.12**(a, b)), it can be seen that the C sp bands show the similar contribution with Ti d band in the lower energy bands close to the E_F in TiC. Different from the TiC, the N sp bands in TiN don't show significant contribution to the bands lower than E_F until ~ -3 eV vs E_F. Therefore, the TiN exhibits a much lower probability of interband transition for hot carrier generation [17]. Similarly, the C doping introduces extra C sp bands in the occupied bands of TiN at - 2.5 eV to -3.5 eV below E_F (**Figure 5.12**(c)). The extra C sp band in C doped TiN can effectively increase the probability of interband excitation. Moreover, the interband excitation can generate hotter holes (possessing higher oxidation capability) than the intraband excitation due to the lower position of N/C sp bands [68, 69]. The excited holes are the radicals responsible for dye degradation. Additionally, due to the relatively large TiN nanocrystal in the prepared catalysts (~16 nm for TiN-3.0-900 and ~37 nm for TiN-3.0-1100, in **Figure 5.6** and **Figure 5.7**), the Landau damping effects are less significant than in the smaller nanoparticles (< 10 nm) [70], which is believed as the main contributor for the carriers' momentum conservation in small nanoparticles. Therefore, the interband excitation (C/N sp bands → Ti d band) that requires no momentum change becomes more important than the intraband transition requiring the momentum change [33, 71]. In summary, the extra C sp band in C doped TiN can both facilitate the generation of hot holes and increase the energy of the excited holes under visible light irradiation. It is believed as the main reason attributed to the enhanced photocatalytic dye degradation performance under visible light irradiation. Whereas the photocatalytic activity can be retarded by the over-doping of C too. It is attributed to the weak plasmon quality factors of TiC or the rise of defects concentration [13, 17, 32].

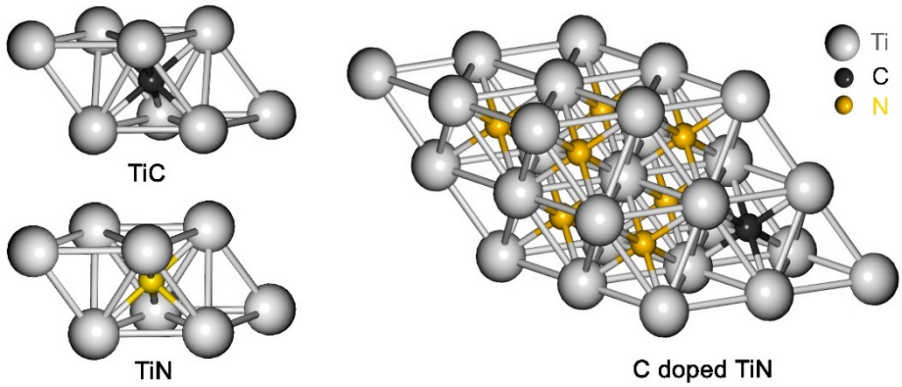

Figure 5.11. The scheme of the crystal structure of TiC, TiN and C doped TiN.

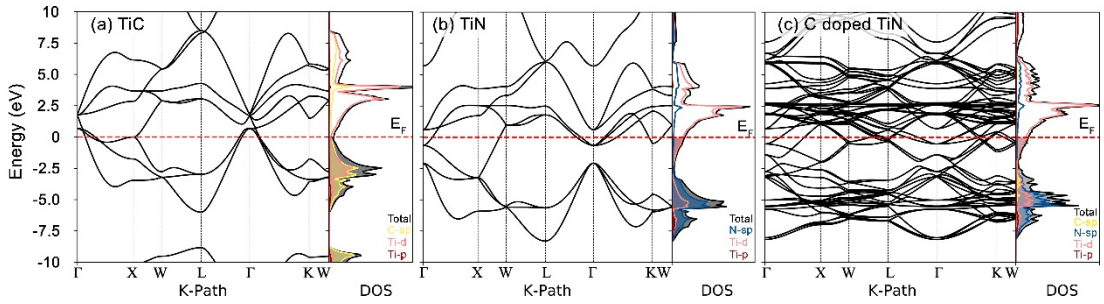

Figure 5.12. Calculated band structure and projected density of states (PDOS) of (a) TiC, (b) TiN and (c) C doped TiN.

5.2.4.3 Photoelectrochemical experiments

Photocurrent response experiments are conducted to provide direct support for the higher electron/hole pair generation efficiency of C doped TiN. As shown in **Figure 5.13**, all the samples exhibit the fast responses to the visible light irradiation during the 5 cycles of light on and off. The TiN-3.0-1100, TiN-3.0-900, TiN-4.5-900 and TiN-1.5-900 exhibit the average photocurrent densities of 558, 313, 183 and 110 nA cm^{-2}, respectively. Comparing the samples synthesized at 900 ºC, the TiN-3.0-900 shows the photocurrent density higher than the TiN-4.5-900 or TiN-1.5-900, which indicates the TiN-3.0-900 can generate more electron-hole pairs under visible light irradiation. It proves the concept that the moderate C doping to TiN can enhance the hot carrier generation under light irradiation. It is also noted that the TiN-3.0-1100 shows the highest photocurrent density among all the samples. This phenomenon can be explained by the larger TiN nanoparticle in TiN-3.0-1100 than TiN-3.0-900.

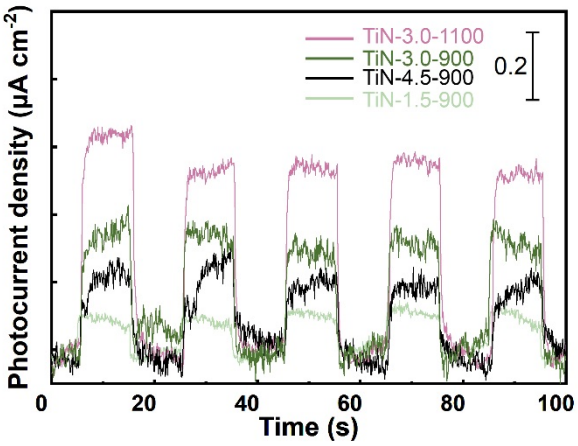

Figure 5.13. The transient photocurrent responses of TiN-3.0-1100, TiN-3.0-900, TiN-4.5-900 and TiN-1.5-900.

5.3 Catalytic performance evaluation

5.3.1 Photocatalytic dye-degradation performance

As a model reaction to evaluate the photocatalytic activity, the photodegradations of RhB were conducted on all the samples to compare their photocatalytic activities under visible light irradiation (λ > 420 nm). The commercial rutile nanocrystals are used as the control group for comparison. **Figure 5.14**(a, b) exhibits the RhB concentration evolution as a function of reaction time. The light irradiation starts from 0 min after 25 min adsorption under dark in advance. First of all, it can be seen from **Figure 5.14**(a) that TiN-3.0-900 shows the highest adsorption and photocatalytic RhB degradation performance comparing with other samples synthesized at 900 ºC. All the prepared catalysts except the TiN-0.3-900 exhibit superior performance to the commercial rutile powders. The control group of rutile itself shows very weak adsorption and photocatalytic activity under visible light irradiation. The slight degradation is attributed to the RhB self-sensitization effects [72, 73]. The TiN-3.0-900 presents the best RhB degradation performance among the samples synthesized at 900 ºC. To achieve a more quantitative understanding of photocatalytic degradation rate, the pseudo-first-order kinetic reaction rate constant *k* is calculated for comparison. As shown in **Figure 5.14**(b), the degradation performances of all samples show high consistency with the pseudo-first-order kinetic model, which can be represented by the following equation:

$$-\ln\left(\frac{C}{C_0}\right) = kt \tag{5.2}$$

where the C and C_0 are the remaining and initial concentration of RhB in the aqueous solution; *t* is the time of reaction; *k* is the apparent first-order rate constant. The calculated reaction rate constants are summarized in **Table 5.2**. The *k* values are 0.4, 1.1, 1.4, 3.2, 6.2 and 3.0 for rutile, TiN-0.3-900, TiN-0.9-900, TiN-1.5-900, TiN-3.0-900, TiN-4.5-900, respectively. It can be seen that the reaction rate constant of TiN-3.0-900 is ~15.5 times of rutile sample, which demonstrates the C doped TiN/N-doped ultrathin carbon layer structure possesses a superior photocatalytic activity to the benchmark commercial rutile powder. In addition, the poor performances of TiN-0.3-900 and TiN-0.9-900 constituted by rutile/TiN suggest neither the heterostructure of TiN/TiO_2 nor the single-phase TiO_2 possesses the satisfied photocatalytic performance under visible light irradiation. These results further indicate that the TiN is the main contributor to the hot carrier generation and photocatalytic activity. Most importantly, the TiN-3.0-900 shows better performance than either TiN-1.5-900 or TiN-4.5-900, which are

all constituted by C doped TiN and N doped ultrathin carbon layer. This phenomenon indicates a proper amount of C doping to TiN is the key to achieve an optimal photocatalytic activity.

The performances of samples prepared with fixed 3.0 g urea usage calcinated at varying temperatures are shown in **Figure 5.14**(b, d). It can be seen that all the samples exhibit remarkably better adsorption and catalytic performances than the rutile benchmark. The calculated rate constants for TiN-3.0-500, TiN-3.0-600, TiN-3.0-700, TiN-3.0-800, TiN-3.0-900, TiN-3.0-1000, TiN-3.0-1100 are 2.1, 1.5, 2.2, 3.1, 11.5, 13.7 respectively (**Table 5.2**).

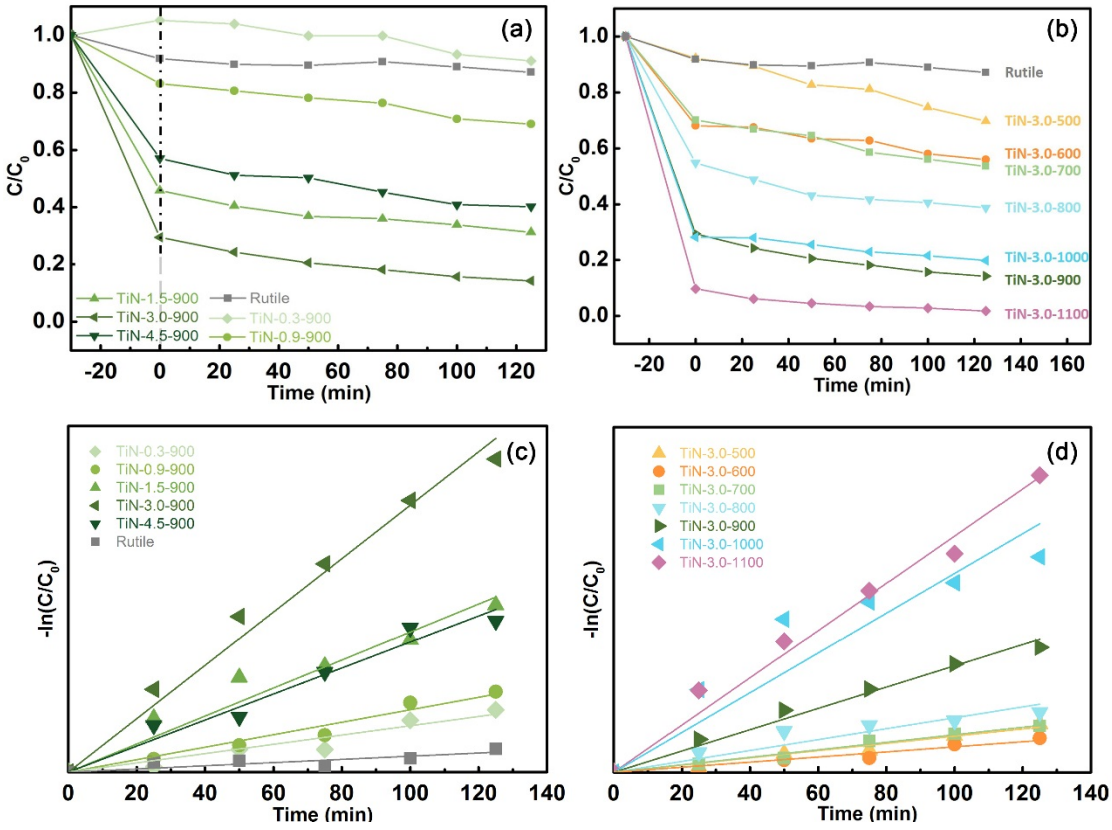

Figure 5.14. Photocatalytic RhB degradation performance under visible light (λ > 420 nm). (a) Time-resolved RhB concentration and (c) corresponding first-order kinetic plot of samples prepared at 900 °C with different urea amounts (0.3, 0.9, 1.5, 3, 4.5 g urea). (b) Time-resolved RhB concentration and (d) corresponding first-order kinetic plot of samples prepared with fixed urea usage of 3g at calcination temperature from 500 to 1100 °C. The performance of commercially available rutile nanoparticles is also presented as the control group.

Noting that the TiN-3.0-500 exhibits superior catalytic activity to TiN-3.0-600, it is attributed to the C_3N_4/TiO_2 heterostructure in TiN-3.0-500 is profitable to the photocatalytic activity. However, the advantage of the C_3N_4/TiO_2 heterostructure is soon surpassed by the formation of TiN plasmonic nanocrystals. It is demonstrated by the fact that all the samples synthesized at the temperature higher than 800 °C (constituted by TiN/N doped ultrathin carbon layer)

show larger reaction rate constants than TiN-3.0-500. The TiN-3.0-1100 presents the highest activity among all the samples, which is due to the larger particle size formed during the synthesis (**Figure 5.7**(f)) and appropriate amount of C doping in TiN.

It is also noted that the TiN-3.0-1100 possesses a significantly high SSA, which results in a strong RhB adsorption capacity. In order to distinguish the adsorption ability and the photo-degradability, a control experiment was conducted under dark. As shown in **Figure 5.15**, the TiN-3.0-1100 was agitated in the RhB solution under darkness for 150 min and the rest conditions were totally the same to the dye-degradation reaction experiments. The results indicate that in the first 25 minutes of dark environment, 90% of the dye has been removed. This is because the dye molecules are adsorbed on the catalyst surface. In the following 125 minutes, the RhB concentration of the control experiment in the dark maintains ~10%; on the contrary, the group under visible light irradiation exhibits the continuous decrease of RhB concentration. This result strongly suggests the RhB reaches saturated adsorption in the dark within 25 minutes, and the subsequent concentration decrease is attributed to the photocatalytic degradation.

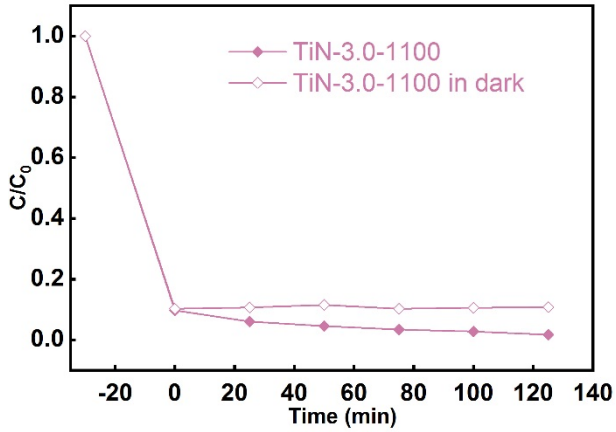

Figure 5.15. Comparison of RhB concentration evolution with TiN-3.0-1100 under darkness and visible light ($\lambda > 420$ nm) irradiation.

5.3.2 Reaction rate normalized by Ti quantity (TOF_{Ti})

Since the Ti quantity of the samples used in the performance evaluation experiments are different from each other, Ti mole normalized performances [74] are calculated to elucidate the intrinsic photocatalytic activities of catalysts in addition to the apparent gravimetric

performances (as illustrated in **Figure 5.14**). Based on the Ti quantity normalized performance, it can further demonstrate the origin of the higher photocatalytic performance. The Turnover frequency normalized by Ti mole (TOF_{Ti} & TON_{Ti}) can be calculated using the following equations [75]:

$$TOF(Ti) = \frac{Degardated\ RhB}{Ti_{mole}} = \frac{\frac{C_t - C_i}{C_i}}{Ti_{mole}} = \frac{C_t - C_i}{C_i \times Ti_{mole}} \quad (5.3)$$

$$TON(Ti) = [\frac{C_t - C_i}{C_i \times Ti_{mole}}]^{-1} \quad (5.4)$$

where C_i and C_t represent the initial and remaining RhB concentration after t min of reaction; Ti_{mole} is the mole of Ti inside the added photocatalyst. The results of calculated TOF_{Ti} are summarised in **Table 5.2** Firstly, it can be seen that the TOF_{Ti} of all prepared samples are much higher than the rutile control group. The TiN-3.0-900 exhibits the highest TOF_{Ti} among the samples prepared at 900 °C with different urea usages. And TiN-3.0-1100 exhibits the highest TOF_{Ti} among samples with the fixed 3 g urea usage at varying temperature. The TOF_{Ti} of TiN-3.0-900 and TiN-3.0-1100 of ~11.9 and 17.4 times of the rutile. It is also worth emphasizing the superior performance of TiN-3.0-1100 to TiN-3.0-500. The TiN-3.0-1100 shows the TOF_{Ti} of 48.21%, which is ~139% of the TiN-3.0-500. As elucidated in the XRD and XPS characterization (**Figure 5.1**(b) and **Figure 5.3**(b)), the TiN-3.0-500 is mainly constituted by TiO_2/C_3N_4. And this classical heterostructure of C_3N_4/TiO_2 has been reported in many researches [63-65, 76-78] showing the excellent photocatalytic activity under visible light irradiation. The higher performance of TiN-3.0-1100 than TiN-3.0-500 can be attributed to the superior photocatalytic activity of C doped TiN to C_3N_4/TiO_2 heterostructure and the signiciantly larger SSA. Moreover, two phenomena cannot be sufficiently explained by the SSA effects: (i) the better performance of TiN-3.0-1100 with smaller SSA than TiN-3.0-900 exhibiting higher SSA; (ii) TiN-3.0-900 shows higher activity than TiN-4.5-900 even the TOF_{Ti} is further normalized by their SSAs. In these two cases, the C doping effects become the dominant factors determining the plasmonic photocatalytic activity [17].

Table 5.2. The summary of photocatalytic performances

Photocatalyst	Rate constant k (min^{-1}) (10^{-3})	R^2	TON_{Ti} (%)	TOF_{Ti} (%)	SSA ($m^2\ g^{-1}$)
Rutile	0.4	0.8964	346.35	2.77	54.78
TiN-0.3-900	1.1	0.9690	882.86	7.06	29.65
TiN-0.9-900	1.4	0.9870	1031.37	8.25	107.55
TiN-1.5-900	3.2	0.9842	2075.90	16.61	172.54
TiN-3.0-900	6.2	0.9949	4130.18	33.04	294.23
TiN-4.5-900	3.0	0.9891	2670.93	21.37	242.65
TiN-3.0-500	2.1	0.9894	4334.11	34.67	59.32
TiN-3.0-600	1.5	0.9743	1782.08	14.26	166.50
TiN-3.0-700	2.2	0.9937	2491.43	19.93	167.70
TiN-3.0-800	3.1	0.9678	2345.38	18.76	174.08
TiN-3.0-1000	11.5	0.9605	5571.74	44.57	232.70
TiN-3.0-1100	13.7	0.9947	6026.54	48.21	243.37

5.3.3 Cyclic performance tests

The stability of the prepared catalysts is an important criterion for performance evaluation. The optimal TiN-3.0-1100 photocatalyst was chosen to perform the recycling experiments. The fresh TiN-3.0-1100 has firstly conducted a photocatalytic RhB degradation and recycled from the solution via centrifuging. After rinsing with DI-water for five times and drying in a vacuum oven at 80 ºC, the recycled TiN-3.0-1100 was used to conduct another photocatalytic RhB degradation experimental following the same procedure. The photocatalytic RhB degradation performances of four recycling experiments are presented in **Figure 5.16**. It can be seen that the TiN-3.0-1100 shows only slight deactivation after four successive photocatalytic degradations. The RhB can be photocatalytically degraded to 6.0% within 125 min after the third recycling. The results indicate that the TiN-3.0-1100 exhibit high stability in the working condition.

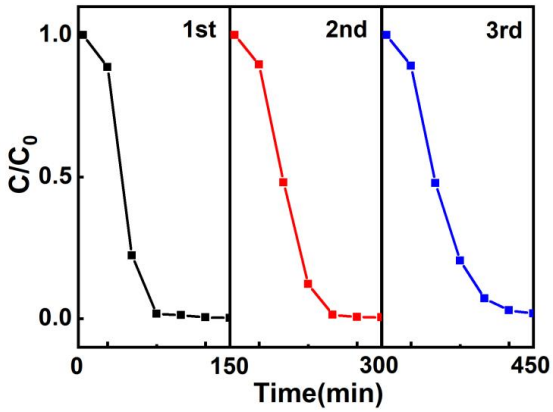

Figure 5.16. Photocatalytic degradation of RhB performances for recycled TiN-3.0-1100 under visible light irradiation ($\lambda > 420$ nm).

5.4 Conclusion

In this work, the preparation of C-doped TiN/ultrathin carbon layer catalysts are systemically investigated, and the preparation condition is optimised. The prepared C-doped TiN/ultrathin carbon layer has been proven as a highly efficient plasmonic photocatalyst outperforming the benchmark rutile TiO_2 and C_3N_4/TiO_2 heterostructure catalysts under visible light irradiation. The high SSA of ~294 $m^2 g^{-1}$ is reached for the C doped TiN/ultrathin carbon layer synthesized at 900 ^oC. In addition, the ultrathin carbon layer support works perfectly to disperse the TiN nanoparticles and the TiN nanoparticle sizes are kept smaller than ~ 40 nm. More importantly, this work demonstrates the validity of elemental doping as an effective method to improve the performance of plasmonic photocatalysts. The optimised electronic structure via doping C to TiN significantly promotes the plasmonic photocatalytic RhB degradation performance. The mechanism of activity enhancement is proven that the extra C-sp bands can enhance the interband transition and promote the generation of holes with higher energy in C doped TiN nanocrystals.

Chapter 5

References

[1] S.V. Boriskina, H. Ghasemi, G. Chen, Plasmonic Materials for Energy: From Physics to Applications, Materials Today, 16 (2013) 375-386.

[2] A. Beierle, P. Gieri, H. Pan, M.D. Heagy, A. Manjavacas, S. Chowdhury, Titanium Nitride Nanoparticles for the Efficient Photocatalysis of Bicarbonate Into Formate, Solar Energy Materials and Solar Cells, 200 (2019).

[3] K.A. Willets, R.P. Van Duyne, Localized Surface Plasmon Resonance Spectroscopy and Sensing, Annu Rev Phys Chem, 58 (2007) 267-297.

[4] Y.H. Jang, Y.J. Jang, S. Kim, L.N. Quan, K. Chung, D.H. Kim, Plasmonic Solar Cells: From Rational Design to Mechanism Overview, Chem. Rev., 116 (2016) 14982-15034.

[5] X.C. Ma, Y. Dai, L. Yu, B.B. Huang, Energy Transfer in Plasmonic Photocatalytic Composites, Light Sci Appl, 5 (2016) e16017.

[6] Z. Zhang, J. Huang, Y. Fang, M. Zhang, K. Liu, B. Dong, A Nonmetal Plasmonic Z-Scheme Photocatalyst with UV- to NIR-Driven Photocatalytic Protons Reduction, Adv. Mater., 29 (2017).

[7] C. Wang, X.G. Nie, Y. Shi, Y. Zhou, J.J. Xu, X.H. Xia, H.Y. Chen, Direct Plasmon-Accelerated Electrochemical Reaction on Gold Nanoparticles, ACS Nano, 11 (2017) 5897-5905.

[8] G.V. Naik, V.M. Shalaev, A. Boltasseva, Alternative Plasmonic Materials: Beyond Gold and Silver, Adv. Mater., 25 (2013) 3264-3294.

[9] A. Agrawal, S.H. Cho, O. Zandi, S. Ghosh, R.W. Johns, D.J. Milliron, Localized Surface Plasmon Resonance in Semiconductor Nanocrystals, Chem. Rev., 118 (2018) 3121-3207.

[10] M.W. Knight, N.S. King, L. Liu, H.O. Everitt, P. Nordlander, N.J. Halas, Aluminum for Plasmonics, ACS Nano, 8 (2014) 834-840.

[11] A. Comin, L. Manna, New Materials for Tunable Plasmonic Colloidal Nanocrystals, Chem Soc Rev, 43 (2014) 3957-3975.

[12] H. Robatjazi, H. Zhao, D.F. Swearer, N.J. Hogan, L. Zhou, A. Alabastri, M.J. McClain, P. Nordlander, N.J. Halas, Plasmon-Induced Selective Carbon Dioxide Conversion on Earth-Abundant Aluminum-Cuprous Oxide Antenna-Reactor Nanoparticles, Nat Commun, 8 (2017) 27.

[13] S. Ishii, S.L. Shinde, T. Nagao, Nonmetallic Materials for Plasmonic Hot Carrier Excitation, Advanced Optical Materials, 7 (2019).

[14] U. Guler, S. Suslov, A.V. Kildishev, A. Boltasseva, V.M. Shalaev, Colloidal Plasmonic Titanium Nitride Nanoparticles: Properties and Applications, Nanophotonics, 4 (2015).

[15] J.A. Briggs, G.V. Naik, Y. Zhao, T.A. Petach, K. Sahasrabuddhe, D. Goldhaber-Gordon, N.A. Melosh, J.A. Dionne, Temperature-Dependent Optical Properties of Titanium Nitride, Applied Physics Letters, 110 (2017).

[16] U. Guler, V.M. Shalaev, A. Boltasseva, Nanoparticle Plasmonics: Going Practical With Transition Metal Nitrides, Materials Today, 18 (2015) 227-237.

[17] M. Kumar, N. Umezawa, S. Ishii, T. Nagao, Examining the Performance of Refractory Conductive Ceramics as Plasmonic Materials: A Theoretical Approach, ACS Photonics, 3 (2015) 43-50.

[18] M. Kaur, S. Ishii, S.L. Shinde, T. Nagao, All-Ceramic Microfibrous Solar Steam Generator: TiN Plasmonic Nanoparticle-Loaded Transparent Microfibers, ACS Sustainable Chemistry & Engineering, 5 (2017) 8523-8528.

[19] S. Ishii, R.P. Sugavaneshwar, T. Nagao, Titanium Nitride Nanoparticles as Plasmonic Solar Heat Transducers, J. Phys. Chem. C, 120 (2016) 2343-2348.

[20] A.A. Barragan, S. Hanukovich, K. Bozhilov, S.S.R.K.C. Yamijala, B.M. Wong, P. Christopher, L. Mangolini, Photochemistry of Plasmonic Titanium Nitride Nanocrystals, J. Phys. Chem. C, 123 (2019) 21796-21804.

[21] B.S. Simpkins, A. Purdy, A. Epshteyn, O. Baturina, Photoelectrochemical Oxidation Enhanced by Nitride Plasmonics, J. Phys. Chem. C, 123 (2019) 13863-13868.

[22] A. Naldoni, U. Guler, Z. Wang, M. Marelli, F. Malara, X. Meng, L.V. Besteiro, A.O. Govorov, A.V. Kildishev, A. Boltasseva, V.M. Shalaev, Broadband Hot-Electron Collection for Solar Water Splitting with Plasmonic Titanium Nitride, Advanced Optical Materials, 5 (2017).

[23] Y. Li, J. Wang, Y. Fan, H. Sun, W. Hua, H. Liu, B. Wei, Plasmonic TiN Boosting Nitrogen-doped TiO_2 for Ultrahigh Efficient Photoelectrochemical Oxygen Evolution, Appl. Catal., B, 246 (2019) 21-29.

[24] E.B. Clatworthy, S. Yick, A.T. Murdock, M.C. Allison, A. Bendavid, A.F. Masters, T. Maschmeyer, Enhanced Photocatalytic Hydrogen Evolution with TiO_2-TiN Nanoparticle Composites, J. Phys. Chem. C, 123 (2019) 3740-3749.

[25] S.L. Shinde, S. Ishii, T.D. Dao, R.P. Sugavaneshwar, T. Takei, K.K. Nanda, T. Nagao, Enhanced Solar Light Absorption and Photoelectrochemical Conversion Using TiN Nanoparticle-Incorporated C_3N_4-C Dot Sheets, ACS Appl. Mater. Interfaces, 10 (2018) 2460-2468.

[26] C. Kang, K. Xiao, Y. Wang, D. Huang, L. Zhu, F. Liu, T. Tian, Synthesis of $SrTiO_3$-TiN Nanocomposites with Enhanced Photocatalytic Activity under Simulated Solar Irradiation, Ind. Eng. Chem. Res., 57 (2018) 11526-11534.

[27] K. Wang, J.L. Fu, Y. Zheng, Insights into Photocatalytic CO_2 Reduction on C_3N_4: Strategy of Simultaneous B, K Co-doping and Enhancement by N Vacancies, Appl. Catal., B, 254 (2019) 270-282.

[28] C. Li, W. Yang, L. Liu, W. Sun, Q. Li, In Situ Growth of TiO_2 on TiN Nanoparticles for Non-Noble-Metal Plasmonic Photocatalysis, RSC Adv., 6 (2016) 72659-72669.

[29] X. Wang, J. Jian, S. Diaz-Amaya, C.E. Kumah, P. Lu, J. Huang, D.G. Lim, V.G. Pol, J.P. Youngblood, A. Boltasseva, L.A. Stanciu, D.M. O'Carroll, X. Zhang, H. Wang, Hybrid Plasmonic Au-TiN Vertically Aligned Nanocomposites: A Nanoscale Platform Towards Tunable Optical Sensing, Nanoscale Advances, 1 (2019) 1045-1054.

[30] G.S. Shanker, G.B. Markad, M. Jagadeeswararao, U. Bansode, A. Nag, Colloidal Nanocomposite of TiN and N-Doped Few-Layer Graphene for Plasmonics and Electrocatalysis, ACS Energy Lett., 2 (2017) 2251-2256.

[31] K. Maeda, Y. Shimodaira, B. Lee, K. Teramura, D. Lu, H. Kobayashi, K. Domen, Studies on $TiN_xO_yF_z$ as a Visible-Light-Responsive Photocatalyst, J. Phys. Chem. C, 111 (2007) 18264-18270.

[32] M. Kumar, S. Ishii, N. Umezawa, T. Nagao, Band Engineering of Ternary Metal Nitride System $Ti_{1-x}Zr_xN$ for Plasmonic Applications, Optical Materials Express, 6 (2015).

[33] U. Aslam, V.G. Rao, S. Chavez, S. Linic, Catalytic Conversion of Solar to Chemical Energy on Plasmonic Metal Manostructures, Nature Catalysis, 1 (2018) 656-665.

[34] C. Giordano, C. Erpen, W. Yao, B. Milke, M. Antonietti, Metal Nitride and Metal Carbide Nanoparticles by a Soft Urea Pathway, Chem. Mater., 21 (2009) 5136-5144.

[35] M. Niu, H. Tan, D. Cheng, Z. Sun, D. Cao, Bandgap Engineering of Magneli Phase Ti_nO_{2n-1}: Electron-hole Self-compensation, J Chem Phys, 143 (2015) 054701.

[36] J. Yan, G. Wu, N. Guan, L. Li, Z. Li, X. Cao, Understanding the Effect of Surface/Bulk Defects on the Photocatalytic Activity of TiO_2: Anatase Versus Rutile, Phys. Chem. Chem. Phys., 15 (2013) 10978-10988.

[37] F. Peng, L. Cai, L. Huang, H. Yu, H. Wang, Preparation of Nitrogen-Doped Titanium Dioxide With Visible-Light Photocatalytic Activity Using a Facile Hydrothermal Method, Journal of Physics and Chemistry of Solids, 69 (2008) 1657-1664.

[38] A. Trenczek-Zajac, M. Radecka, K. Zakrzewska, A. Brudnik, E. Kusior, S. Bourgeois, M.C.M. de Lucas, L. Imhoff, Structural and Electrical Properties of Magnetron Sputtered Ti(ON) Thin Films: The Case of TiN Doped in Situ With Oxygen, J. Power Sources, 194 (2009) 93-103.

[39] R. Ali, E. Alkhateeb, F. Kellner, S. Virtanen, N. Popovska-Leipertz, Chemical vapor deposition of titanium based ceramic coatings on low carbon steel: Characterization and electrochemical evaluation, Surface and Coatings Technology, 205 (2011) 5454-5463.

[40] P.Y. Jouan, M.C. Peignon, C. Cardinaud, G. Lempérière, Characterisation of TiN Coatings and of The TiN/Si Interface by X-Ray Photoelectron Spectroscopy and Auger Electron Spectroscopy, Appl. Surf. Sci., 68 (1993) 595-603.

[41] M. Tacikowski, J. Grzonka, T. Płociński, R. Jakieła, M. Pisarek, T. Wierzchoń, Composite Titanium Nitride Layers Produced on the AZ91D Magnesium Alloy by a Hybrid Method Including Hydrothermal Modification of the Layer, Appl. Surf. Sci., 346 (2015) 394-405.

[42] L. Zhang, R.V. Koka, A Study on the Oxidation and Carbon Diffusion of TiC in Alumina-Titanium Carbide Ceramics Using XPS and Raman Spectroscopy, Materials Chemistry and Physics, 57 (1998) 23-32.

[43] F. Santerre, M.A. El Khakani, M. Chaker, J.P. Dodelet, Properties of TiC Thin Films Grown by Pulsed Laser Deposition, Appl. Surf. Sci., 148 (1999) 24-33.

[44] T.Y. Ma, J.L. Cao, M. Jaroniec, S.Z. Qiao, Interacting Carbon Nitride and Titanium Carbide Nanosheets for High-Performance Oxygen Evolution, Angew. Chem., Int. Ed., 55 (2016) 1138-1142.

[45] I. Bertóti, M. Mohai, J.L. Sullivan, S.O. Saied, Surface Characterisation of Plasma-Nitrided Titanium: An XPS Study, Appl. Surf. Sci., 84 (1995) 357-371.

[46] D. Jaeger, J. Patscheider, A Complete and Self-Consistent Evaluation of XPS Spectra of TiN, Journal of Electron Spectroscopy and Related Phenomena, 185 (2012) 523-534.

[47] A. Glaser, S. Surnev, F.P. Netzer, N. Fateh, G.A. Fontalvo, C. Mitterer, Oxidation of Vanadium Nitride and Titanium Nitride Coatings, Surface Science, 601 (2007) 1153-1159.

[48] I. Milošev, H.H. Strehblow, B. Navinšek, Comparison of TiN, ZrN and CrN Hard Nitride Coatings: Electrochemical and Thermal Oxidation, Thin Solid Films, 303 (1997) 246-254.

[49] D. Wei, Y. Liu, Y. Wang, H. Zhang, L. Huang, G. Yu, Synthesis of N-doped Graphene by Chemical Vapor Deposition and Its Electrical Properties, Nano Lett, 9 (2009) 1752-1758.

[50] B. Zheng, J. Wang, F.-B. Wang, X.-H. Xia, Synthesis of Nitrogen Doped Graphene With High Electrocatalytic Activity Toward Oxygen Reduction Reaction, Electrochemistry Communications, 28 (2013) 24-26.

[51] U. Sim, T.-Y. Yang, J. Moon, J. An, J. Hwang, J.-H. Seo, J. Lee, K.Y. Kim, J. Lee, S. Han, B.H. Hong, K.T. Nam, N-Doped Monolayer Graphene Catalyst on Silicon Photocathode for Hydrogen Production, Energy & Environmental Science, 6 (2013).

[52] X. Li, H. Wang, J.T. Robinson, H. Sanchez, G. Diankov, H. Dai, Simultaneous Nitrogen Doping and Reduction of Graphene Oxide, J. Am. Chem. Soc., 131 (2009) 15939-15944.

[53] Z. Mou, X. Chen, Y. Du, X. Wang, P. Yang, S. Wang, Forming Mechanism of Nitrogen Doped Graphene Prepared by Thermal Solid-State Reaction of Graphite Oxide and Urea, Appl. Surf. Sci., 258 (2011) 1704-1710.

[54] G. Zhang, G. Li, Z.A. Lan, L. Lin, A. Savateev, T. Heil, S. Zafeiratos, X. Wang, M. Antonietti, Optimizing Optical Absorption, Exciton Dissociation, and Charge Transfer of a Polymeric Carbon Nitride with Ultrahigh Solar Hydrogen Production Activity, Angew. Chem., Int. Ed., 56 (2017) 13445-13449.

[55] M. Bellardita, E.I. García-López, G. Marcì, I. Krivtsov, J.R. García, L. Palmisano, Selective Photocatalytic Oxidation of Aromatic Alcohols in Water by Using P-doped g-C_3N_4, Appl. Catal., B, 220 (2018) 222-233.

[56] D.C. Higgins, J.-Y. Choi, J. Wu, A. Lopez, Z. Chen, Titanium Nitride-Carbon Nanotube Core-Shell Composites as Effective Electrocatalyst Supports for Low Temperature Fuel Cells, J. Mater. Chem., 22 (2012).

[57] L.S.K. Pang, J.D. Saxby, S.P. Chatfield, Thermogravimetric Analysis of Carbon Nanotubes and Nanoparticles, The Journal of Physical Chemistry, 97 (1993) 6941-6942.

[58] P.K. Ajikumar, M. Kamruddin, T.R. Ravindran, S. Kalavathi, A.K. Tyagi, Oxidation Behavior of TiCxN1−x Coatings as a Function of C/N Ratio, Ceramics International, 40 (2014) 10523-10529.

[59] Z. Jiang, W.E. Rhine, Preparation of Titanium Nitride (TiN) and Titanium Carbide (TiC) From a Polymeric Precursor, Chem. Mater., 3 (1991) 1132-1137.

[60] K. Kuroda, Y. Tanaka, Y. Sugahara, C. Kato, Preparation of Titanium Nitride (TiN1-x-yCxOy) from Ti(OPri)4-Triethanolamine Condensation Product by Pyrolysis, MRS Proceedings, 121 (1988) 575.

[61] H. Zheng, K. Oka, J.D. Mackenzie, Preparation of Titanium Carbonitride Coatings by the Sol-Gel Process, MRS Proceedings, 271 (1992) 893.

[62] M. Thommes, K. Kaneko, A.V. Neimark, J.P. Olivier, F. Rodriguez-Reinoso, J. Rouquerol, K.S.W. Sing, Physisorption of Gases, With Special Reference to the Evaluation of Surface Area and Pore Size Distribution (IUPAC Technical Report), Pure and Applied Chemistry, 87 (2015) 1051-1069.

[63] U. Caudillo-Flores, M.J. Muñoz-Batista, R. Luque, M. Fernández-García, A. Kubacka, g-C_3N_4/TiO_2 Composite Catalysts for the Photo-Oxidation of Toluene: Chemical and Charge Handling Effects, Chem. Eng. J., 378 (2019).

[64] Y. Sheng, Z. Wei, H. Miao, W. Yao, H. Li, Y. Zhu, Enhanced Organic Pollutant Photodegradation via Adsorption/Photocatalysis Synergy Using a 3D g-C_3N_4/TiO_2 Free-separation Photocatalyst, Chem. Eng. J., 370 (2019) 287-294.

[65] Y. Tan, Z. Shu, J. Zhou, T. Li, W. Wang, Z. Zhao, One-Step Synthesis of Nanostructured g-C_3N_4/TiO_2 Composite for Highly Enhanced Visible-Light Photocatalytic H_2 Evolution, Appl. Catal., B, 230 (2018) 260-268.

[66] J. Yan, H. Wu, H. Chen, Y. Zhang, F. Zhang, S.F. Liu, Fabrication of TiO_2/C_3N_4 Heterostructure for Enhanced Photocatalytic Z-Scheme Overall Water Splitting, Appl. Catal., B, 191 (2016) 130-137.

[67] Y.C. Zhang, S. He, W. Guo, Y. Hu, J. Huang, J.R. Mulcahy, W.D. Wei, Surface-Plasmon-Driven Hot Electron Photochemistry, Chem. Rev., 118 (2018) 2927-2954.

[68] J. Zhao, S.C. Nguyen, R. Ye, B. Ye, H. Weller, G.A. Somorjai, A.P. Alivisatos, F.D. Toste, A Comparison of Photocatalytic Activities of Gold Nanoparticles Following Plasmonic and Interband Excitation and a Strategy for Harnessing Interband Hot Carriers for Solution Phase Photocatalysis, ACS Cent. Sci., 3 (2017) 482-488.

[69] S. Yu, A.J. Wilson, J. Heo, P.K. Jain, Plasmonic Control of Multi-Electron Transfer and C-C Coupling in Visible-Light-Driven CO_2 Reduction on Au Nanoparticles, Nano Letters, 18 (2018) 2189-2194.

[70] J.B. Khurgin, How to Deal With the Loss in Plasmonics and Metamaterials, Nat. Nanotechnol., 10 (2015) 2-6.

[71] A.M. Brown, R. Sundararaman, P. Narang, W.A. Goddard, 3rd, H.A. Atwater, Nonradiative Plasmon Decay and Hot Carrier Dynamics: Effects of Phonons, Surfaces, and Geometry, ACS Nano, 10 (2016) 957-966.

[72] M.A.I. Molla, I. Tateishi, M. Furukawa, H. Katsumata, T. Suzuki, S. Kaneco, Photocatalytic Decolorization of Dye with Self-Dye-Sensitization under Fluorescent Light Irradiation, ChemEngineering, 1 (2017).

[73] T.T. Le, M.S. Akhtar, D.M. Park, J.C. Lee, O.B. Yang, Water Splitting on Rhodamine-B Dye Sensitized Co-Doped TiO_2 Catalyst Under Visible Light, Appl. Catal., B, 111-112 (2012) 397-401.

[74] I.E. Wachs, S.P. Phivilay, C.A. Roberts, Reporting of Reactivity for Heterogeneous Photocatalysis, ACS Catal., 3 (2013) 2606-2611.

[75] M. Alvaro, C. Aprile, M. Benitez, E. Carbonell, H. Garcia, Photocatalytic Activity of Structured Mesoporous TiO_2 Materials, J Phys Chem B, 110 (2006) 6661-6665.

[76] Z.a. Huang, Q. Sun, K. Lv, Z. Zhang, M. Li, B. Li, Effect of Contact Interface Between TiO_2 and g-C_3N_4 on the Photoreactivity of g-C_3N_4/TiO_2 Photocatalyst: (0 0 1) vs (1 0 1) Facets of TiO_2, Appl. Catal., B, 164 (2015) 420-427.

[77] K. Dai, L. Lu, C. Liang, Q. Liu, G. Zhu, Heterojunction of Facet Coupled g-C_3N_4/Surface-fluorinated TiO_2 Nanosheets for Organic Pollutants Degradation Under Visible LED Light Irradiation, Appl. Catal., B, 156-157 (2014) 331-340.

[78] Z. Lu, L. Zeng, W. Song, Z. Qin, D. Zeng, C. Xie, In Situ Synthesis of C-TiO_2/g-C_3N_4 Heterojunction Nanocomposite as Highly Visible Light Active Photocatalyst Originated From Effective Interfacial Charge Transfer, Appl. Catal., B, 202 (2017) 489-499.

Chapter 6 Conclusion

6.1 Conclusion

Photocatalysts design and optimization have become one of the hottest topics in the field of environmental pollutants degradation. Traditional semiconductor photocatalysts such like TiO_2 exhibits the disadvantages including the limited utilization of solar light, small specific surface area, high photo-excited electron/hole recombination rate and low photocatalytic activity. The drawbacks severely hinder the practical implementation of photocatalysis technology in industry. To address the challenges mentioned above, this thesis focuses on the development of high-performance photocatalysts for dye photodegradation. Taking advantages of heteroatom doping strategy, the photocatalytic activities of C_3N_4 and TiN have been significantly improved. Moreover, the detailed mechanisms underpin the performance enhancement induced by heteroatom dopants are unravelled. The main conclusions of this thesis are summarized as follows.

(1) C_3N_4 has been prepared for the first time by conducting the thermal polycondensation of organic precursors in KCl-$ZnCl_2$ molten salts with low eutectic temperature. The results suggest that the location of the melting temperature of salt mixture within the temperature window between dicyandiamide and melamine formation steps in the polycondensation process is critical to the successful enhancement of photocatalytic activity. The advantages of using KCl-$ZnCl_2$ molten salts can be summarized into three aspects. Firstly, due to the low eutectic temperature of KCl-$ZnCl_2$ (230 ^oC), the precursors are dispersed better in the molten salts during the polycondensation process. As a result, the large SSAs of 111.0, 138.6 and 171.6 $m^2 g^{-1}$ have been achieved for the prepared C_3N_4 using cyanamide, dicyandiamide and melamine precursors, which are at least ~7.4 times as large as the bulk C_3N_4 synthesized via the conventional procedure. Secondly, C_3N_4 synthesized in KCl-$ZnCl_2$ molten salts shows the optimized electronic structure for photocatalytic dye degradation. The VBM is shifted to the positive direction, therefore enhancing oxidation capability. Lastly, Zn doping at an appropriate concentration suppresses electron-hole recombination, which significantly contributes to the higher photocatalytic activity.

(2) The controllable Cl-doping concentration and Cl doping sites are used for the first time to improve the photocatalytic performance of C_3N_4 synthesized via agitation-assisted solvothermal method. The results indicate that the balance between Cl_{sub} and Cl_{int} dopants is the key to successfully enhance the photocatalytic RhB degradation performance of C_3N_4 due to the significantly improved SSA, stronger photooxidation capability and suppressed electron/hole recombination. Additionally, a U-shape relation has been found between agitation rate and molecular/electronic structure of prepared C_3N_4. The mechanism underpins this phenomenon is that the agitation rate determines the atomic ratio of Cl_{sub}/Cl_{int} dopants. More importantly, the effects of Cl_{sub} and Cl_{int} dopants on the photocatalytic activity are rationally distinguished based on the experimental results. The Cl_{int} dopants between the C_3N_4 layers can prolong the lifetime of the charge carriers but cause a decrease of SSA. Comparatively, the in-plane Cl_{sub} dopants are responsible for the positive shift of VBM and the enhancement of oxidation capability. The optimal photocatalytic dye-degradation performance can only be achieved by balancing the Cl_{int}/Cl_{sub} ratios and synthesizing under a moderate agitation rate.

(3) C-doped TiN/graphene has been synthesized via the calcination of $TiCl_4$/urea mixture and shows superior photodegradation performance to C_3N_4/TiO_2 heterostructure and commercial rutile TiO_2 under visible light irradiation. In optimised synthesis condition, the TiN nanoparticles, with the size of ~ 40 nm, are well-dispersed on N doped graphene layers. In addition, the C has been found doped into TiN nanoparticles when excessive urea is used. The rate constant *k* of photocatalytic degradation of TiN-3.0-900 and TiN-3.0-1100 under visible light is 2.95 and 6.52 times of C_3N_4/TiO_2, and 15.5 and 34.25 times of rutile TiO_2, respectively. The enhanced plasmonic photocatalytic performance can be attributed to the C doping. Based on the DFT calculation, the additional C-sp bands in TiN can enhance the interband transition of electrons in TiN nanocrystals, which boosts the formation of holes with higher energy.

Overall, this thesis focuses on the development of the synthesis method to improve the photocatalytic performance of the photocatalysts. Using the synthesis methods developed in this thesis, photocatalysts with enlarged SSA and higher photocatalytic dye degradation performance has been prepared. In addition, heteroatom doping has been used as the main strategy to further improve the photocatalytic activity of C_3N_4. Heteroatom doping with appropriate concentration has been successfully introduced during the synthesis and can significantly enhance the photocatalytic activity of C_3N_4. The positive effects of doping are summarized as follows: (i) optimising the electronic structure (ii) the dopants can suppress the photo-induced charge carrier recombination.

6.2 Future Works

(1) Although the doping has been proven effective in enhancing the photocatalytic dye degradation of photocatalysts, the works in the thesis have not conducted molecular-level investigations on the doping effects on the electronic structure. In future work, the DFT calculation can be used to achieve a more comprehensive understanding of the doping effects on the spatial distribution of LUMO and HOMO. Moreover, the detailed mechanism of how the dopants help to suppress the photon-induced electron/hole separation can be analysed.

(2) This thesis focuses on the design and optimisation of the photocatalysts, therefore the dye photodegradation is used as the probe reaction to elucidate the photocatalytic activities of prepared photocatalysts. The mechanism of degradation including the key active spices in each system and the degradation pathway is worth further investigation. In future works, the scavengers of holes, $\cdot O_2^-$ and $\cdot OH^-$ can be used as trapping agents to identify the key radicals in dye photodegradation. HPLC-MS and TOC analyses can be used to reveal the degradation intermediates and final product during the mineralization processes. Notably, the degradation target can be extended beyond organic dyes. Other organic pollutants in the liquid phase, such like bisphenol A, phenol and toluene are worth being investigated too.

(3) Due to the high SSA of the prepared catalysts in this thesis, strong dye adsorption can be observed before degradation. Both adsorption and degradation have been reported to efficiently remove dyes from effluents. Therefore, the dye adsorption process is also worth investigations. More adsorption studies can be conducted in future works, including the establishment of adsorption models and investigation of adsorption kinetics.

Appendix

Applied Surface Science 533 (2020) 147429

Contents lists available at ScienceDirect

Applied Surface Science

journal homepage: www.elsevier.com/locate/apsusc

Synthesis of Zn doped g-C_3N_4 in KCl-$ZnCl_2$ molten salts: The temperature window for promoting the photocatalytic activity

Mengyu Cao, Ke Wang*, Ignacio Tudela, Xianfeng Fan*

Institute for Materials and Processes, School of Engineering, the University of Edinburgh, Edinburgh EH9 3FB, Scotland, UK

ARTICLE INFO

Keywords:
Molten salts
Zn doped g-C_3N_4
Photocatalysis
Dye degradation
KCl-$ZnCl_2$
Temperature window for modification

ABSTRACT

The Zn doped g-C_3N_4 is successfully synthesized in eutectic KCl-$ZnCl_2$ salt mixture with low melting temperature for the first time. More importantly, the significant improvement in the photocatalytic activity can only be achieved by locating the melting point of the salt mixture within the temperature window between dicyandiamide and melamine oligomer formation steps in the polycondensation process. The prepared g-C_3N_4 using dicyandiamide as the precursor (C_3N_4-D) shows ~9.3 times larger specific surface area (SSA), ~9.8 times larger photocurrent density and ~1.56 times longer photo-excited carrier lifetime than the bulk g-C_3N_4 synthesized via the conventional thermal polymerization method in air (C_3N_4-M-Air). In photocatalytic methyl orange (MO) degradation, the pseudo-first reaction rate constant of C_3N_4-D is ~4.15 times higher than the C_3N_4-M-Air control group. The significantly promoted MO photodegradation performance is attributed to the remarkably enlarged SSA, enhanced MO adsorption, the positively shifted valence band maximum (VBM) and suppressed electron-hole recombination due to Zn dopants.

1. Introduction

Graphitic carbon nitride (g-C_3N_4) as an organic semiconductor shows potential applications in photocatalytic CO_2 reduction [1,2], water splitting [3,4], pollutants degradation [5,6], etc. It exhibits some unique advantages including free of transition metal elements, low toxicity and relatively good photocatalytic performance. Organic dye such as methyl orange (MO) is an important kind of pollutants in water resources due to the large-amount usage in dye industry. Therefore, it is promising to take advantage of g-C_3N_4 as photocatalysts to remove MO with the help of solar energy. However, the photocatalytic performance of pristine g-C_3N_4 still fails to meet the requirements for practical implementation, due to its low specific surface area (SSA), unoptimized electronic structure and high electron/hole recombination rate.

The heteroatom doping has been proven as an effective strategy to improve the photocatalytic activity of g-C_3N_4. The successful cases include the atomic doping of alkaline metal (Li, Na, K) [7–11], halogen (F, Cl, Br, I) [12–16], non-noble transition metal (Zn, Cu, Fe, Co) [5,16–22], noble transition metal (Ag, Pt, Pd, Ir, Au) [23–27], and other main group elements (O, S, B, C, N, P) [9,28–34], etc. Among them, Zn has been investigated and introduced into g-C_3N_4 interstitial sites via different methods too [5,17,19,35,36]. However, one of the major drawbacks of the pristine g-C_3N_4, the low SSA, has not been improved after the Zn doping. The typical SSA of g-C_3N_4 synthesized via the most popular thermal polycondensation method is only ~10 m^2 g^{-1} [9,17,28]. Although hard [37,38] or soft templates [4,19,39,40] can be used to increase the SSA of g-C_3N_4, the application is limited by the high cost of the templates and highly toxic compounds indispensable for template removal. Therefore, it is still a challenge to increase the SSA of g-C_3N_4 in a facile and effective way. Additionally, no research in the literature has ever investigated the effects of Zn doping on the photocatalytic dye degradation.

Synthesis of g-C_3N_4 in molten salt (ionothermal synthesis) has been reported as a unique method to produce g-C_3N_4 with optimized morphology and electronic structure [3]. The melted salts as the media for the polycondensation of organic precursors can enhance the homogeneity and crystallinity of the prepared g-C_3N_4. g-C_3N_4 synthesis via polycondensation of melamine in eutectic KCl-LiCl was reported for the first time by Bojdys et al. [41]. Because of the enhanced dispersion of precursors inside the molten salts, the synthesized g-C_3N_4 exhibited larger SSA and higher crystallinity. A few more examples are presented as follows. Gao et al. [42] reported that the g-C_3N_4 with nanotube morphology was synthesized in molten NaCl-KCl-LiCl ternary system. Zhang et al. [43] reported that the condensation of urea inside LiCl-KCl resulted in the g-C_3N_4 with reduced interlayer distance and the enhanced π-π interaction, which strongly improved the photocatalytic

* Corresponding authors.
E-mail addresses: k.wang@ed.ac.uk (K. Wang), x.fan@ed.ac.uk (X. Fan).

https://doi.org/10.1016/j.apsusc.2020.147429
Received 26 May 2020; Received in revised form 14 July 2020; Accepted 30 July 2020
Available online 15 August 2020

activity. In addition, the molten salts have also been used to achieve the triazine based g-C_3N_4 and as a post-treatment method to increase the crystallinity [3,44–46]. Although the molten salts have been proven versatile in modifying the morphology, molecular and electronic structure of g-C_3N_4, the detailed mechanisms how the molten salts influence the property of g-C_3N_4 are still ambiguous. Most of the researches only focus on the LiCl-KCl system and leave two essential questions unexplored: (i) the optimal eutectic temperature of salt mixture and (ii) the optimal chemical composition of salt mixture for g-C_3N_4 synthesis. Because the polycondensation of g-C_3N_4 is a multiple-stage process taking places at discrete temperatures, it is essential to unravel the influences of molten salts at different polycondensation stages of g-C_3N_4 synthesis.

To address the challenges and knowledge gaps mentioned above, in this work, the g-C_3N_4 is for the first time prepared in low-temperature KCl-$ZnCl_2$ eutectic salts with cyanamide, dicyandiamide and melamine as precursors, respectively. During the polycondensation of g-C_3N_4 synthesis, the organic precursors, cyanamide, dicyandiamide and melamine with increasing polycondensation degrees are the three major intermediates representing the three main stages. By comparing the molecular and electronic structures of the prepared g-C_3N_4 from different precursors, the specific roles of melted salts at the different stages of g-C_3N_4 synthesis are unravelled. The optimal g-C_3N_4 synthesized from dicyandiamide (C_3N_4-D) in molten KCl-$ZnCl_2$ shows the significantly enlarged SSA, enhanced MO adsorption and increased photo-oxidation capability. Additionally, a moderate amount of Zn is introduced as the interstitial dopant during the synthesis in KCl-$ZnCl_2$ molten salts and a longer photo-excited carrier lifetime is observed due to the suppressed electron-hole recombination. The photocatalytic MO degradation performance has been significantly promoted on C_3N_4-D comparing with the g-C_3N_4 synthesized via the thermal polycondensation method or in conventionally used LiCl-KCl system.

2. Experimental

2.1. Photocatalysts preparation

To synthesize g-C_3N_4, 3 g of melamine, 5 g of KCl (1.58 g) and $ZnCl_2$ (3.42 g) mixture were fully ground in an agate mortar, and the as-obtained powder was then transferred to a ceramic crucible (20 mL) and covered with a ceramic lid. The crucible was then placed into the centre of a tube furnace. The furnace was firstly vacuumed and then back-filled with N_2 and this process was repeated for 3 times to get rid of O_2. The tube furnace was then heated to 500 °C at a heating ramp of 1 °C min^{-1} and kept at 500 °C for 2 h under N_2 gas flow (100 sccm). The obtained solid was washed with HNO_3 (5%) aqueous solution under reflux condition. After further rinsing with DI-water for several times until the pH = 7 and the powder was dried at 80 °C under vacuum overnight. The as-prepared sample was marked as C_3N_4-M. The other 2 samples were prepared in a similar way, but using cyanamide or dicyandiamide as precursor instead. The samples were denoted as C_3N_4-C and C_3N_4-D, respectively.

The control group g-C_3N_4 sample was prepared via a conventional KCl-LiCl molten salt method. A typical eutectic mixture of 2.79 g KCl and 2.21 g LiCl was used. 3 g of dicyandiamide was fully mixed with the salts by grinding them in a mortar and treated in the same procedure as described above. The as-obtained control group sample was marked as C_3N_4-D-Li. Another important control group sample is the bulk g-C_3N_4 prepared by directly calcinating melamine in static air. 10 g of melamine powder was put into an alumina crucible with a cover. The crucible was then placed into the centre of a muffle furnace, then heated to 500 °C at a ramping rate of 10 °C min^{-1}. After soaking at 500 °C for 2 h, the furnace was cooled down to room temperature naturally. The yellow product was collected and then ground into fine powder in an agate mortar. This sample is denoted as C_3N_4-M-Air. C_3N_4-M-Air was synthesized via the most conventionally used method in literature. Additionally, the semi-closed system during the preparation ensures a self-determined atmosphere derived from the ammonia effluent during the polycondensation of melamine. Therefore, it can be rationally used as a control group and benchmark to evaluate other g-C_3N_4 photocatalysts.

2.2. Photocatalysts characterization

The crystal structures of the prepared photocatalysts were characterized by an X-ray diffractometer (XRD, Brucker Phaser D2) with Cu Kα X-ray source (λ = 1.5406 Å, 40 kV, 20 mA). The prepared samples were ground into fine powder, which was packed into a sample holder for XRD tests. The molecular structure was examined via the vibrational spectroscopy on a Fourier transform infrared spectrometer (FTIR, Shimadzu IRTracer-100). The FTIR characterization followed the standard KBr pellet protocol. ~0.1 mg sample powder was firstly ground with ~200 mg pre-dried KBr powder in an agate mortar to achieve a homogeneous mixture. Then the powder was pressed into a pellet with a hydraulic press with a diameter of 13 mm. The pellet was placed inside the spectrometer chamber and vertical toward the incident IR beam. The spectra were collected within the range of 600–4000 cm^{-1} in a resolution of 4 cm^{-1}. Sixty-four scans were averaged to achieve a good signal to noise ratio. The chemical compositions of prepared g-C_3N_4 samples were analysed with an organic elemental analyser (Carlo Erba NA2500). The chemical environment of the elements inside the sample and the valence band XPS spectra were characterized by an X-ray photoelectron spectrometer (XPS, ThermoFisher K-Alpha) equipped with a monochromatic Al Kα X-ray source (1486.6 eV). The optical response of the samples was tested via ultraviolet–visible diffuse reflectance spectroscopy (UV–Vis DRS) on a UV–Vis spectrometer (Shimadzu, UV3600Plus). The sample powder was firstly ground into the fine powder, which was further packed into the sample holder of a commercially available UV–Vis DRS test accessory (Praying mantis, Harrick Scientific Products, Inc). The background spectrum was collected using the standard Spectralon reference. The steady-state and time-resolved photoluminescence (PL) spectra were conducted on a steady-state spectrofluorometer (Shimadzu RF-6000) and a time-resolved spectrofluorometer (Edinburgh instruments FLS980). For static PL spectra measurements, the excitation wavelength was set to be 325 nm, and emission wavelength range was 350–620 nm. For time-resolved PL measurements, the excitation wavelength was set to the same wavelength of 325 nm. The emission wavelength was chosen as the peak emission wavelength determined by the steady-state PL experiments. The N_2 sorption isotherm was measured at 77 K with an automatic adsorption analyser (Quantachrome Autosorb-iQ). A scanning electron microscope (SEM, Carl Zeiss SIGMA HD VP Field Emission SEM) with X-ray energy dispersive spectrometer (EDS, Oxford AZtecEnergy) was used to analyse the morphologies of the samples and chemical compositions of interesting areas. The g-C_3N_4 powder was dispersed onto the cooper tape and coated with Au to enhance the conductivity before characterization. Thermogravimetric analyses (TGA) and differential scanning calorimetric (DSC) analyses were conducted on a simultaneous thermal analyser (STA, Mettler Toledo, TGA-DSC 3+). Typically, ~5 mg of sample was placed into a 70 μL alumina crucible, and a PTFE rod was used to ensure a dense packing of the powders. An empty crucible was used as the reference for the DSC heat flow measurements. The program was set to ramp from room temperature to 1000 °C with the ramping rate of 10 K min^{-1}. N_2 and synthetic air with the flow rate of 100 sccm were introduced into the STA furnace to provide inert and air atmosphere, respectively.

The photocurrent measurement was conducted in a two-electrode configuration with an electrochemical workstation (Metrohm, Autolab PGSTAT204). 0.1 mol L^{-1} KCl aqueous solution was used as the electrolyte, and a graphite rod as the counter electrode. No potential bias was applied during the experiments. A glassy carbon electrode in 1.5 × 1.5 cm^2 size was used as the substrate for photocatalysts, and an

active area of 0.75 cm^{-2} was defined by covering the rest of the surface with insulation tape. 2 mg powder was firstly dispersed in 0.2 mL ethanol, and 10 μL Nafion 5% solution (Sigma-Aldrich) was added into the mixture. The solution was ultrasonicated for 2 min to achieve a homogeneous dispersion. Then 100 μL of the solution was drop-wisely added on the glassy carbon electrode surface and dried naturally at room temperature. The prepared glassy carbon electrode loaded with photocatalysts was used as the working electrode, which was further wired with a crocodile clamp. A Xenon lamp (SLS401, Thorlabs, Inc) was used to provide the simulated solar light with a built-in optical shutter.

2.3. Catalytic performance evaluation

The photocatalytic performance of as-prepared samples was evaluated by the photocatalytic degradation of MO in aqueous solution. In each photocatalytic reaction, 12 mg of the photocatalyst was added into 60 mL MO solution with a concentration of 10 mg L^{-1}. The photocatalytic degradation of MO was carried out in a jacked Pyrex beaker with water circulation. A 300 W Xenon lamp (PLS-SXE300, Beijing Perfectlight technology co.) was used to provide the simulated solar light from the top to drive the reaction. The light power density was measured to be 720 ± 10 mW cm^{-2} via a thermopile light power meter (PM16-401, Thorlabs, Inc.). This photodegradation reaction starts with a 10-minute sonication and 25-minute stirring in the dark to establish an adsorption-desorption equilibrium. The photocatalytic reaction holds on for 125 min with magnetic stirring (180 rpm). At irradiation time intervals of every 25 min, 3 mL of the mixture was collected and centrifuged (9000 rpm, 7 min) to separate the photocatalyst particles from solution. The concentrations of the MO were monitored using a UV–vis spectrophotometer (Analytik Jena, SPECORD PC 250) by measuring the absorbance peak of MO at ~460 nm.

3. Results and discussion

To elucidate the role of molten salts in the g-C_3N_4 synthesis, it is important to first clarify the relation between salts mixture melting temperature and each polycondensation step. The TGA-DSC characterizations were conducted with cyanamide, dicyandiamide and melamine in flowing N_2, respectively. The results are presented in Fig. 1. As shown in Fig. 1, g-C_3N_4 synthesis from organic precursors is a step-wise process with each step taking places at different temperatures. The details of the peak assignments and discussions are presented in supporting information and Table S1. It is noted that the melting temperature of KCl-$ZnCl_2$ locates between the steps of dicyandiamide and melamine oligomer formations. In contrast, the conventional KCl-LiCl exhibits the melting temperature between the steps of melamine melting and melem oligomer formation.

3.1. Molecular structure of g-C_3N_4 synthesized in KCl-$ZnCl_2$ molten salts

The crystal structure of prepared g-C_3N_4 has been characterized via the XRD. As shown in Fig. 2(a), all the samples prepared in KCl-$ZnCl_2$ molten salts exhibit the typical diffraction pattern of g-C_3N_4 with a prominent peak located at 27°. This peak is attributed to the (0 0 2) facets derived from the stacking of g-C_3N_4 layers [28]. Comparing with the control group samples of C_3N_4-M-Air and C_3N_4-D-Li, the samples prepared in KCl-$ZnCl_2$ molten salts show the lower crystallinity. The peak corresponding to the (1 0 0) facet is only observable in the control group samples C_3N_4-M-Air and C_3N_4-D-Li, whereas this peak is not observed in the XRD patterns of the g-C_3N_4 synthesized in molten KCl-$ZnCl_2$. The absence of (1 0 0) peak indicates the less ordered on-plane heptazine unit repetition ascribed to the doping and structure distortion. The FTIR spectroscopy is used to characterize the molecular structures of the prepared g-C_3N_4 samples and the collected spectra are presented in Fig. 2(b). It can be seen that all the three samples prepared in molten KCl-$ZnCl_2$ show similar IR absorption bands with C_3N_4-M-Air. The peak at 807 cm^{-1} is assigned to the breathing mode of the triazine unit. The peaks from 1621 to 1240 cm^{-1} are attributed to the C-N-C or C-NH-C vibration in the heptazine heterocyclic structure [28,47,48]. And the peak at 2177 cm^{-1} is derived from the vibration of -C≡N group [7,48]. Comparing the FTIR spectra of samples synthesized in eutectic KCl-$ZnCl_2$ salts with the benchmark C_3N_4-M-Air, the C_3N_4-C, C_3N_4-D, C_3N_4-M samples show weaker absorption at the C-N-C heterocycle range (1240–1621 cm^{-1}). It suggests the samples synthesized in eutectic KCl-$ZnCl_2$ salts exhibit a less ordered molecular structure than the C_3N_4-M-Air, which is consistent with XRD results (Fig. 2(a)).

XPS is an effective tool to analyse the molecular structure of the prepared g-C_3N_4. The samples synthesized in eutectic KCl-$ZnCl_2$ with different precursors exhibit similar XPS spectra with the control group samples. As presented in Fig. 3(a), the C 1s spectra can be further deconvoluted into 3 peaks for all 5 samples. Peaks located at 284.6 eV, 286.4 eV and 288.2 eV are ascribed to the adventitious carbon and C-NH_2, N-C=N bonds in the heptazine unit, respectively [49,50]. There is an extra C 1s peak at 287.3 eV in the spectrum of C_3N_4-C, which is attributed to the C=N or C=O [51–53]. Similarly, the N 1s spectra, shown in Fig. 3(b), are further deconvoluted into 3 peaks too. The peak at a binding energy of 398.7 eV is assigned to the sp^2-hybridized aromatic triazine rings (N2C, C-N=C); peak at 399.9 eV is assigned to the tertiary nitrogen (N3C) bonding; peak at 400.8 eV is attributed to the -NH_x functional group [2,50]. The similar assignments of C 1s and N 1s peaks suggest that the samples synthesized in eutectic KCl-$ZnCl_2$ salts are constituted by on-plane repeating heptazine units. The slightly different C 1s spectrum of C_3N_4-C indicates its highly disordered structure and low crystallinity, which is consistent with XRD and FTIR analyses (Fig. 2(a, b)). These experimental results suggest that the precursor with a smaller initial condensation degree results in a more disordered final g-C_3N_4 structure during the molten salts synthesis.

To further examine the possible doping during the synthesis in the molten salts, the Zn 2p, K 2p and Cl 2p spectra are collected and plotted in Fig. 3(c) and Figure S3(a, b). It can be seen that the Zn dopants are only found in C_3N_4-D, C_3N_4-C samples with significant concentration. In C_3N_4-M, the Zn dopant is of trace amount. The Zn $2p_{3/2}$ and $2p_{1/2}$ peaks are located at 1021.6 and 1044.6 eV, respectively, which are assigned to the Zn^{2+} coordinated into the electron-rich heptazine unit [5,17]. Although K and Cl are common dopants for g-C_3N_4 in the literature, the XPS spectra of K 2p and Cl 2p suggest the non-existence of K and Cl dopants in all the 5 g-C_3N_4 samples. Therefore, it can be concluded that Zn is the only dopant in the g-C_3N_4 synthesized in KCl-$ZnCl_2$ molten salts. The Zn doping to g-C_3N_4 is likely to happen before the formation of melamine oligomers because only trace amount of Zn is found when using melamine as the precursor (C_3N_4-M). The Zn doping concentrations are determined by the TGA experiments (Figure S8). By calcinating the Zn doped g-C_3N_4 in flowing air, the remained weights at 1000 °C are ascribed to ZnO. As a result, the Zn doping concentrations are calculated to be 5.39 wt%, 4.34 wt% and 0.19 wt% for C_3N_4-C, C_3N_4-D and C_3N_4-M, respectively (Table S3).

Organic elemental analysis (C, N, H) is an important method to investigate the molecular structures of g-C_3N_4 synthesized in KCl-$ZnCl_2$ molten salts. As summarized in Table S2, the C_3N_4-M-Air shows the C/N atomic ratio of ~0.69, which is close to the theoretical C/N atom ratio in the melon and also in consistence with former reports [2,54,55]. It can be seen that the C/N atomic ratios of C_3N_4-D, C_3N_4-M and C_3N_4-D-Li samples are very similar to the C_3N_4-M-Air reference. This result suggests the molten salts environment for g-C_3N_4 synthesis doesn't affect the C/N ratios, and the Zn atoms are interstitial rather than the substitutional dopants. The only exception is the C_3N_4-C with the significantly reduced C/N atomic ratio of ~0.678. Additionally, the g-C_3N_4 synthesized in molten salts also show higher contents of H atoms. The C_3N_4-C, C_3N_4-D and C_3N_4-M contain the H atoms in the weight percentages of 2.85%, 3.11% and 3.06%, which are remarkably higher than C_3N_4-M-Air of 1.65%. These results are ascribed to the higher

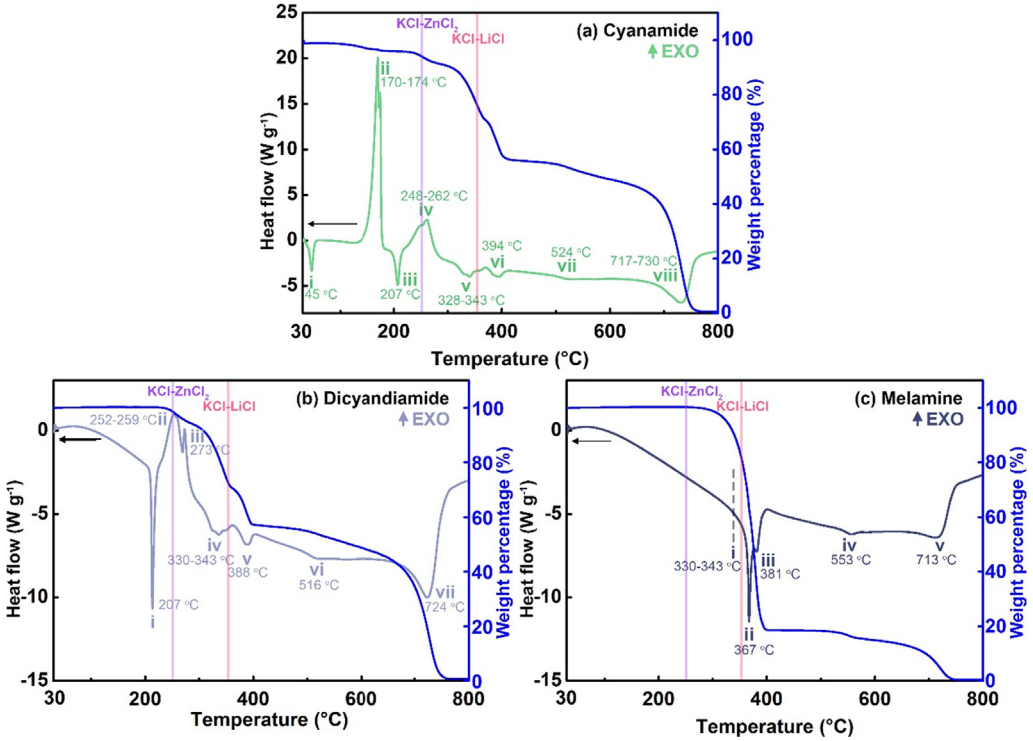

Fig. 1. The TGA and DSC curves of (a) cyanamide (b) dicyandiamide and (c) melamine under flowing N_2 (100 sccm). The peak pointing up represents the exothermal process. The eutectic temperatures of LiCl-KCl (~352 °C) and KCl-$ZnCl_2$ (~250 °C) are annotated using pink and purple solid lines, respectively.

structure distortion and lower polycondensation degree, as also suggested by the XRD, FTIR and XPS analyses (Figs. 2 and 3).

3.2. Electronic structure of g-C_3N_4 synthesized in KCl-$ZnCl_2$ molten salts

Comparing with molecular structures, the electronic structures of g-C_3N_4 samples synthesized in eutectic KCl-$ZnCl_2$ is more important because the VBM and conduction band minimum (CBM) determine the photooxidation and photoreduction potentials of the photocatalysts, respectively. As shown in Figure S4, the VBM (vs. SHE) of C_3N_4-C, C_3N_4-D, C_3N_4-M, C_3N_4-M-Air and C_3N_4-D-Li are calculated to be 0.67, 1.72, 1.86, 1.64, 1.50 eV, respectively. The details of VBM determination are described in the supporting information. The optical bandgaps of the prepared samples are derived from the UV–Vis DR spectroscopy. The optical responses of the samples to the incident light are plotted in the Kubelka-Monk unit, as shown in Figure S5(a). It can be seen that the samples exhibit the typical semiconductor behaviour. The optical bandgaps (E_g) are determined by converting Figure S5(a) to the corresponding Tauc plot, as shown in Figure S5(b). Based on extrapolating the linear range of the curves to the incident light energy axis, the E_g are determined to be 3.07, 3.17, 3.15, 2.65 and 2.90 eV for C_3N_4-C, C_3N_4-D, C_3N_4-M, C_3N_4-M-Air and C_3N_4-D-Li, respectively [28,56]. It is noted that all samples synthesized in the molten salts show broadened E_g than the C_3N_4-M-Air. The wider E_g is likely to be attributed to the decreased size and increased structure distortion of the g-C_3N_4 crystal [1,4,57]. Based on the measured VBM and E_g, the band positions of prepared g-C_3N_4 are summarized and plotted in Fig. 4. It can be seen from the band position alignment plot that the C_3N_4-D and C_3N_4-M show more positive VBM than the control group samples C_3N_4-M-Air and C_3N_4-D-Li, which indicates the higher photooxidation capability of C_3N_4-D and C_3N_4-M. However, it is worth emphasizing that the moderate Zn doping concentration is critical because Zn dopant intends to shift the CBM/VBM to the negative direction.

3.3. Morphology and specific surface area

SSA is a critical parameter for the high-performance photocatalysts since a larger SSA ensures more active sites for reaction. However, low

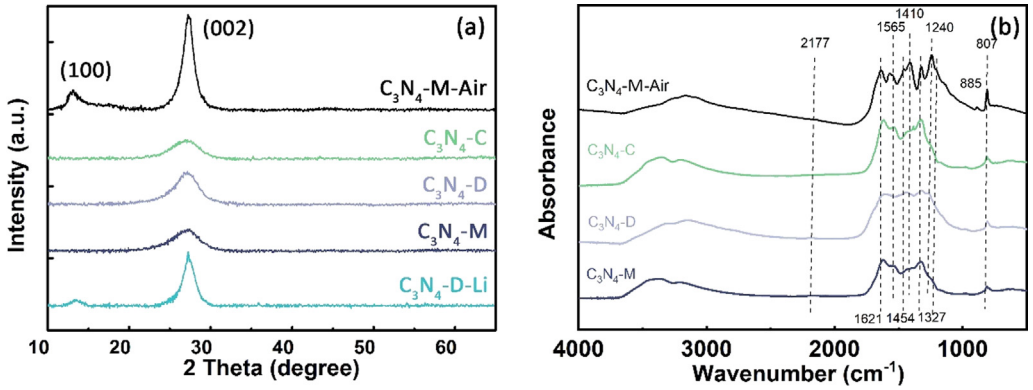

Fig. 2. The (a) XRD patterns and (b) FTIR spectra of C_3N_4-C, C_3N_4-D, C_3N_4-M and control groups of C_3N_4-M-Air and C_3N_4-D-Li.

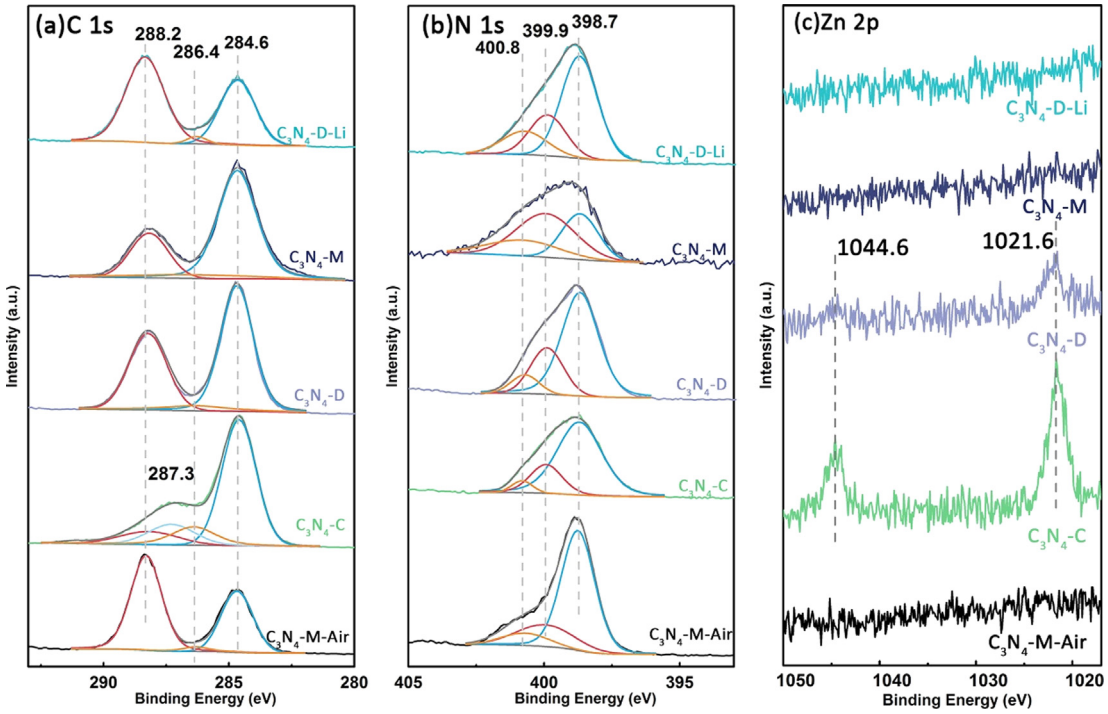

Fig. 3. XPS (a) C 1s, (b) N 1s and (c) Zn 2p spectra of C_3N_4-C, C_3N_4-D, C_3N_4-M and control groups of C_3N_4-M-Air and C_3N_4-D-Li.

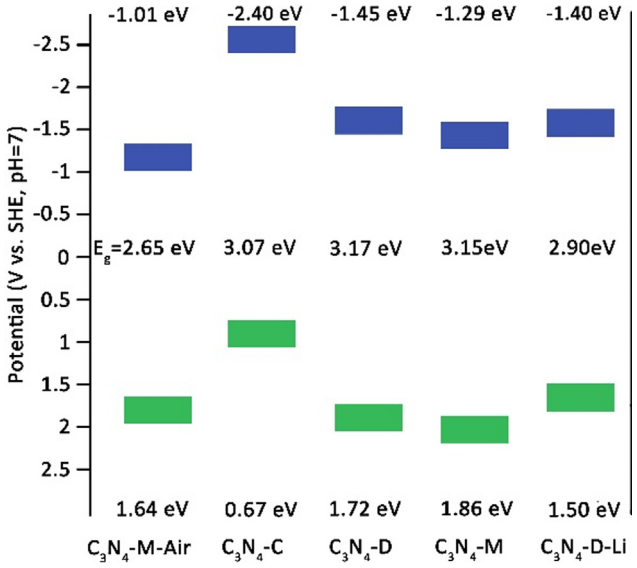

Fig. 4. Band position alignment plot for samples prepared in KCl-$ZnCl_2$: C_3N_4-C, C_3N_4-D, C_3N_4-M and the control group samples C_3N_4-M-Air, C_3N_4-D-Li.

SSA is one of the main drawbacks of g-C_3N_4. For conventional thermal polymerization of melamine or dicyandiamide in the air, the SSA for prepared g-C_3N_4 is usually ~10 $m^2\ g^{-1}$ [28]. Even urea or thiourea is used as the precursor, the reported SSA for two-dimensional or porous g-C_3N_4 is typically ~50–70 $m^2\ g^{-1}$ [58–61]. The SSA of the samples prepared in this work is calculated based on the N_2 sorption isotherm characterized at 77 K using the Brunauer-Emmett-Teller (BET) method (Fig. 5(a)). The derived SSA for C_3N_4-M-Air as the control group is 15 $m^2\ g^{-1}$, which is consistent with the literature [28]. For C_3N_4-D-Li, the g-C_3N_4 synthesized in the conventional KCl-LiCl eutectic system shows an improved SSA of 58 $m^2\ g^{-1}$. Interestingly, this new molten salt synthesis method using KCl-$ZnCl_2$ eutectic salt mixture shows extraordinary enhancement on the SSA. The SSAs for C_3N_4-C, C_3N_4-D and C_3N_4-M are measured to be 110, 139 and 172 $m^2\ g^{-1}$, respectively. They are significantly higher than either of the control group samples. It is worth comparing the pore size distribution curves to unravel the structural differences. As shown in Fig. 5(b), the C_3N_4-M-Air synthesized via thermal condensation of melamine in air shows no obvious peaks, which is ascribed to its non-porous bulk structure. On the contrary, the C_3N_4-C, C_3N_4-D and C_3N_4-M show the peaks corresponding to the pore size of 3–4 nm. These mesopores are likely derived from the stacking of g-C_3N_4 particles. In summary, it is proven that the g-C_3N_4 synthesized in KCl-$ZnCl_2$ molten salts with low melting temperature show larger SSA than the g-C_3N_4 synthesized via the thermal polycondensation in static air or in conventional KCl-LiCl salt mixture.

The morphologies of the prepared samples are presented with SEM images and the corresponding EDS analyses, as shown in Figure S6. Figure S6(a, b) indicates that the control group sample C_3N_4-M-Air exhibit the relatively large particles with the diameter of several microns. The large size of the particles limits the SSA to 15 $m^2\ g^{-1}$. For the sample synthesized in eutectic LiCl-KCl, the C_3N_4-D-Li (Figure S6(m, n)) shows the morphology of smaller particles in submicron size. The reduced particle size induces an enlarged SSA of 58 $m^2\ g^{-1}$. For the samples synthesized in eutectic KCl-$ZnCl_2$, the C_3N_4-C (Figure S6(d, e)), C_3N_4-D (Figure S6(g, h)) and C_3N_4-M (Figure S6(j, k)) exhibit the particles with the smaller diameter and the size decreases in the sequence of C_3N_4-C, C_3N_4-D, C_3N_4-M, which is in consistence with the BET-SSA results (Fig. 5(a)). Based on the SEM images, the particle sizes of g-C_3N_4 are measured and the mean sizes are determined statistically. As shown in Figure S7, the mean particle sizes of C_3N_4-C, C_3N_4-D, C_3N_4-M are 488, 180 and 87 nm, respectively; for the control group samples, the mean particle sizes of C_3N_4-M-Air and C_3N_4-D-Li are ~2.33 and ~0.56 μm, respectively. The EDS is used to identify the possible doping elements in the prepared g-C_3N_4 samples. From Figure S6(c, f, i, l, o), it can be summarized that all the samples are mainly constituted by the C, N, O elements. For the control group sample C_3N_4-M-Air and C_3N_4-D-Li, the EDS spectra suggest that no dopant exists in the crystals. For the samples synthesized in the eutectic KCl-$ZnCl_2$, the EDS results indicate that the Zn is doped in the C_3N_4-C, C_3N_4-D and Cl is negligible. Different from C_3N_4-C and C_3N_4-D, Zn EDS signal is very weak in the C_3N_4-M. The EDS results suggest the g-C_3N_4 synthesized using the cyanamide

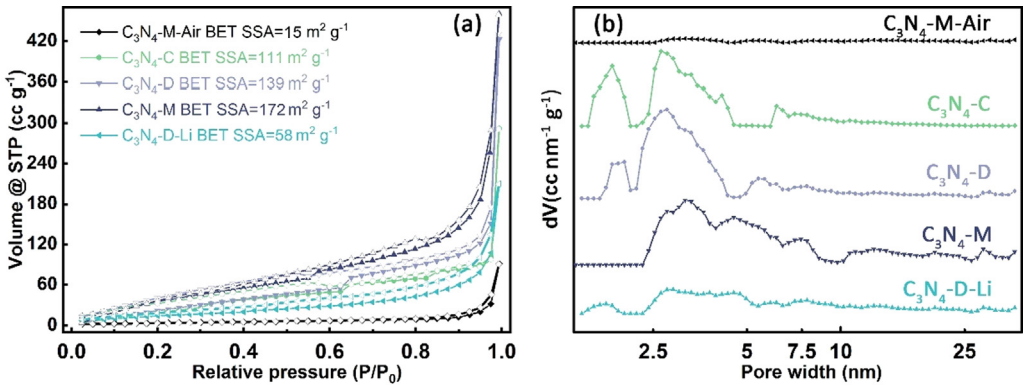

Fig. 5. (a) N_2 sorption isotherms at 77 K and (b) pore size distribution curves (based on the DFT model) of C_3N_4-C, C_3N_4-D, C_3N_4-M and control groups of C_3N_4-M-Air and C_3N_4-D-Li.

with lowest condensation degree exhibits the highest possibility of doping, while the melamine with the highest condensation degree shows the lowest doping possibility.

3.4. Charge carrier separation efficiency

To rationalize the enhanced photocatalytic performance of C_3N_4-D comparing with the counterparts, the charge carrier separation efficiencies of the prepared samples are characterized by the photoluminescence (PL) spectroscopy method. As shown in Fig. 6(a), the steady-state PL spectra of g-C_3N_4 synthesized in KCl-$ZnCl_2$ eutectic salts shows the emission peaks at ~400 nm, which is in consistency with the bandgap analyses. It is important to emphasize that the reduced steady-state PL intensity can be attributed to the higher probability of non-radioactive recombination. Therefore, the charge carrier separation efficiency is further characterized by the time-resolved PL spectroscopy. As presented in Fig. 6(b), the average carrier lifetime of C_3N_4-D is 1.34 ns, which is significantly longer than the 0.61 ns of C_3N_4-M, 0.86 ns of C_3N_4-M-Air and 0.79 ns of C_3N_4-D-Li. The longer carrier lifetime of the C_3N_4-D is attributed to the fact that the Zn dopant energy level can trap the charge carriers temporally before the recombination.

3.5. Photocurrent response experiments

Photocurrent response is an important evidence reflecting the ability of photocatalysts in generating electron-hole pairs under light irradiation. As shown in Fig. 7, the C_3N_4-D shows the highest photocurrent density under irradiation. The photocurrent density generated by C_3N_4-D reaches 370.3nA cm^{-2} on average, which is ~9.8 times as much as the C_3N_4-M-Air (37.9nA cm^{-2}). The C_3N_4-M shows the second-largest photocurrents of 92.9 nA cm^{-2}. The remarkably enhanced photocurrent density of C_3N_4-D proves that the moderate Zn doping

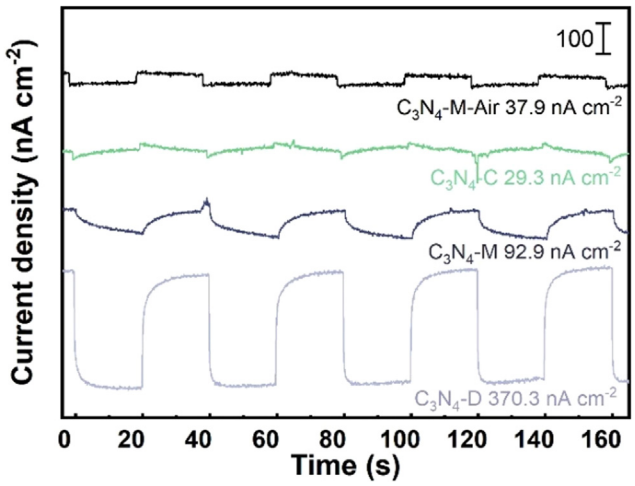

Fig. 7. Transient photocurrent responses for C_3N_4-C, C_3N_4-D, C_3N_4-M and control group C_3N_4-M-Air.

introduced during the KCl-$ZnCl_2$ molten salts synthesis can facilitate the electron/hole separation and increase the carrier lifetime. The slightly inferior current density of C_3N_4-M and C_3N_4-C can be explained by the enlarged bandgap, lower crystallinity and nonoptimal Zn doping concentration.

3.6. Photocatalytic dye-degradation performance

The photocatalytic activities of the g-C_3N_4 prepared in KCl-$ZnCl_2$ molten salts and the control group samples are evaluated via the probe reaction, MO photocatalytic degradation (Fig. 8(a)). The samples were

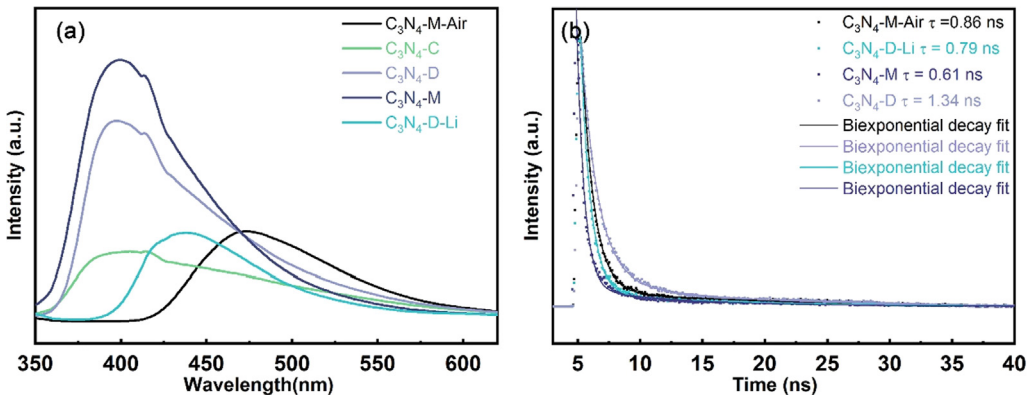

Fig. 6. (a) Steady-state and (b) time-resolved photoluminescence spectra of C_3N_4-D, C_3N_4-M and control group sample C_3N_4-M-Air and C_3N_4-D-Li.

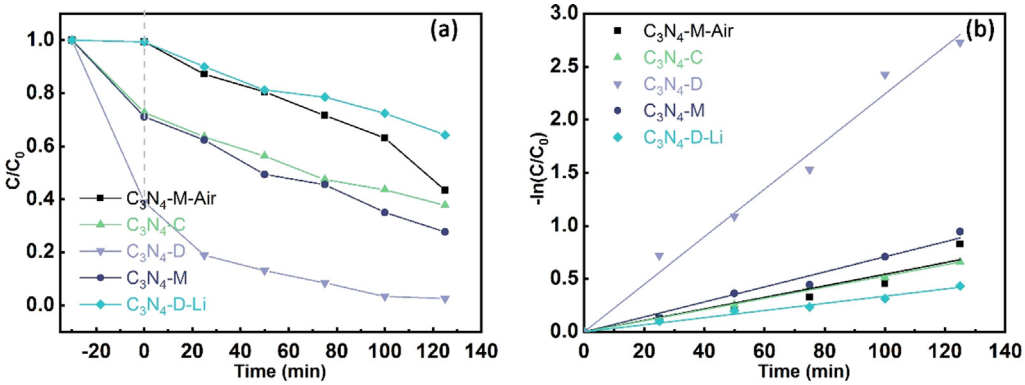

Fig. 8. (a) Photocatalytic MO degradation performance and (b) pseudo-first-order kinetic plot of C_3N_4-C, C_3N_4-D, C_3N_4-M and control group samples C_3N_4-M-Air, C_3N_4-D-Li under simulated solar light irradiation.

firstly kept under darkness for 25 min to compare their adsorption abilities. The photocatalytic reaction was conducted for 125 min, and the MO concentrations were measured every 25 min. After the first 25 min under dark, two control group samples (C_3N_4-M-Air and C_3N_4-D-Li) show negligible adsorption ability, which can be attributed to their poor SSAs (15 and 58 $m^2\ g^{-1}$ respectively). In the case of the samples synthesized in KCl-$ZnCl_2$ molten salts, all the samples exhibit the improved adsorption ability to MO comparing with C_3N_4-D-Li and C_3N_4-M-Air due to the larger SSAs. Among them, the C_3N_4-D exhibits the highest adsorption ability that the MO concentration (C) drops to 72.8% of the initial concentration (C_0). Although the SSA of the g-C_3N_4 synthesized in KCl-$ZnCl_2$ shows the sequence of C_3N_4-M > C_3N_4-D > C_3N_4-C, the sequence of MO adsorption capability is C_3N_4-D > C_3N_4-M ≈ C_3N_4-D. Therefore, the optimal adsorption performance of C_3N_4-D is likely to be explained by the balance achieved between SSA, polycondensation degree and Zn doping: low polycondensation degree and higher Zn doping concentration increase the MO adsorption ability [28,62,63], whereas decrease the SSA. In the photocatalytic MO degradation under simulated solar light, the C_3N_4-D also exhibits the highest photocatalytic activity. After 125 min of photocatalytic reaction, the C_3N_4-D degrades the MO concentration to the 2.5% of the initial concentration (C_0). While C_3N_4-C, C_3N_4-M only reduce the MO concentration to 37.7% and 27.7% of the C_0, respectively. In addition, all the samples synthesized via the KCl-$ZnCl_2$ molten salts method outperform the control group samples C_3N_4-M-Air and C_3N_4-D-Li, which only reduce the MO concentrations to 43.5% and 64.3% of C_0, respectively. To further compare the photocatalytic activity of the photocatalysts, the kinetic reaction rate constants are calculated based on the pseudo-first kinetic model. As shown in Fig. 8(b), the pseudo-first-order reaction kinetic model can be well fitted and the calculated rate constant k is 0.0054, 0.0052, 0.0224, 0.0071, 0.0034 min^{-1} for C_3N_4-M-Air, C_3N_4-C, C_3N_4-D, C_3N_4-M and C_3N_4-D-Li, respectively (Table S4). It is noted that the reaction rate constant k for the optimal sample C_3N_4-D is 415% and 659% of the control group samples C_3N_4-M-Air and C_3N_4-D-Li, respectively. The significantly enhanced photocatalytic activity of C_3N_4-D strongly demonstrates the superiority of this novel g-C_3N_4 synthesis method using KCl-$ZnCl_2$ molten salts comparing with conventional g-C_3N_4 preparation method. To further prove the advantages of this molten salts synthesis method, the MO photodegradation performance of C_3N_4-D is compared with recently reported g-C_3N_4 or ZnO based photocatalysts (Table 1). It can be seen from Table 1 that the C_3N_4-D shows the state-of-the-art MO photodegradation performance under simulated solar light irradiation and even outperforms the recently reported modified g-C_3N_4, ZnO and heterostructure built with g-C_3N_4 (ZnO). The stability of the optimal sample C_3N_4-D was tested by recycling experiments. As shown in Figure S9, after 3 recycles of photodegradation, only a small decrease in activity is observed. It suggests the C_3N_4-D shows good stability during photocatalytic reaction.

3.7. Mechanism underpins the enhanced photocatalytic activity

The enhanced photocatalytic activities of the samples synthesized in KCl-$ZnCl_2$ eutectic salts are reasonably ascribed to the following four reasons: (i) enlarged SSA, (ii) enhanced MO adsorption, (iii) optimized VBM position and (iv) reduced electron-hole recombination due to Zn doping. Firstly, as shown in Fig. 5(a), the SSA is remarkably increased under the assistance of KCl-$ZnCl_2$ molten salts. The SSA of C_3N_4-D is ~9.3 times of the C_3N_4-M-Air synthesized via the conventional thermal polymerization method and ~2.4 times of C_3N_4-D-Li synthesized in conventional KCl-LiCl molten salts. It can be explained by the better dispersion of reaction intermediates in KCl-$ZnCl_2$ molten salts due to its lower melting temperature. The larger SSA provides more active sites for the photocatalytic degradation reaction and the smaller particle size ensures a short transportation length for photo-excited charge carriers. Secondly, the Zn dopants and lower polycondensation degree induce the enhanced MO adsorption. As shown in Fig. 8(a), the C_3N_4-D shows the highest adsorption to MO, whereas its SSA is not the largest. The Zn doping and moderate polycondensation degree are believed as the reasons for the promoted MO adsorption capability. Thirdly, C_3N_4-D shows the enhanced photooxidation capability due to the positively shifted VBM (Fig. 4). Since the photocatalytic degradation is the MO oxidization driven by the photo-excited holes, a more positive VBM is preferred. Lastly, the appropriate amount of Zn dopant can help to suppress the photo-induced charge carrier recombination. It has been reported that a proper amount of dopant can suppress the recombination of photo-excited carriers by trapping them inside dopant energy states, while over-doped g-C_3N_4 exhibits deteriorated recombination due to the dopant acting as the recombination centre [74–77]. As characterized by XPS and TGA, the Zn doping is achieved in a moderate concentration in C_3N_4-D comparing with C_3N_4-C and C_3N_4-M. The appropriate amount of Zn dopant ensures the facilitated electron-hole separation in the semiconductor, which is supported by the photocurrent response experiments (Fig. 7) and time-resolved PL experiments (Fig. 6(b)). It also rationalizes the result that C_3N_4-D shows superior photocatalytic activity to the C_3N_4-M, though the SSA and oxidation potential of C_3N_4-D is inferior to C_3N_4-M.

It is important to emphasize that the four advantages need to be balanced to achieve an optimal photocatalytic MO degradation performance. The low polycondensation degree of g-C_3N_4 benefits the MO adsorption capability and Zn doping suppresses electron-hole recombination. However, the over-doped Zn decreases the SSA, photooxidation capability and enhances recombination; the too low polycondensation degree is detrimental for charge carrier transportation and light absorption. Therefore, it rationalizes the existence of a temperature window in the g-C_3N_4 polycondensation process for the

Table 1
Comparisons of photocatalytic MO degradation performance between C_3N_4-D and typical photocatalysts reported in recent literature.

Photocatalysts	MO solution concentration	Dose (photocatalyst/solution)	Light source (simulated solar light)	Reaction rate constants (10^{-3} min^{-1})	Removal/Time	Ref.
C_3N_4-D	10 ppm	12 mg/60 mL (0.2 g L^{-1})	300 W Xe lamp	22.4	87.1%/50 min 91.7%/75 min 97.5%/125 min	This work
g-C_3N_4-ZnO@graphene aerogel (Z-scheme)	20 ppm	5 mg/25 mL	300 W Hg lamp	n/a	50%/120 min	[62]
2D mesoporous ZnO	~3.3 ppm	100 mg/100 mL	300 W Xe lamp	n/a	85.3%/50 min 98.2%/90 min	[63]
TiO_2/ZnO/rGO	20 ppm	0.5 g L^{-1}	300 W Xe lamp	4.94	63.4%/180 min	[64]
g-C_3N_4/Ag_2WO_4 (Z-scheme)	10 ppm	30 mg/30 mL	300 W Xe lamp	n/a	95%/150 min	[65]
Ppy@Ag/g-C_3N_4	10 ppm	0.1 g/100 mL	300 W Xe lamp	20.4	89%/60 min	[66]
g-C_3N_4@NiAl–LDH	20 ppm	0.2 g/100 mL	500 W Hg lamp	8.4	93%/180 min	[67]
g-C_3N_4/$Bi_2O_2CO_3$	~6.5 ppm	10 mg/40 mL	1000 W Xe lamp	n/a	96.2%/90 min	[68]
O doped mesoporous g-C_3N_4	10 ppm	50 mg/50 mL	500 W Xe lamp	3.81	70%/240 min	[69]
$CuCo_2O_4$/g-C_3N_4	10 ppm	30 mg/50 mL	150 W Xe lamp	1.16	~92.5%/100 min	[70]
g-C_3N_4/Bi_2O_3/$BiPO_4$ (Z-scheme)	10 ppm	15 mg/30 mL	300 W Xe lamp	11.54	~90%/160 min	[71]
β-Fe_2O_3/g-C_3N_4	10 ppm	1.25 g L^{-1}	300 W Xe lamp	8.8	~90%/4h	[72]
TiO_2/g-C_3N_4	5 ppm	0.4 g/400 mL	350 W Xe lamp	n/a	83.3%/80 min	[73]

successful optimization of g-C_3N_4 via molten salts method.

4. Conclusion

In this work, g-C_3N_4 has been prepared for the first time by conducting the thermal polycondensation of organic precursors in KCl-$ZnCl_2$ molten salts with low eutectic temperature. The experimental results suggest that locating the melting temperature of salt mixture within the temperature window between dicyandiamide and melamine formation steps in the polycondensation process is critical to the photocatalytic activity enhancement. The optimal Zn doped g-C_3N_4 (C_3N_4-D) shows ~4.15 times higher pseudo-first reaction rate constant in MO photodegradation than the bulk g-C_3N_4. The advantages of this novel synthesis method using KCl-$ZnCl_2$ molten salts can be summarized into four aspects. Firstly, due to the low eutectic temperature of KCl-$ZnCl_2$ (230 °C), the precursors are better dispersed in the molten salts during the polycondensation process. As a result, the large SSAs of 111, 139 and 172 m^2 g^{-1} are achieved for the prepared g-C_3N_4 using cyanamide, dicyandiamide and melamine precursors, which are at least ~7.4 times as large as the bulk g-C_3N_4 synthesized via the conventional procedure. Secondly, C_3N_4-D exhibits the significantly enhanced MO adsorption capability due to moderate polycondensation degree and Zn doping. Thirdly, C_3N_4-D shows the optimized electronic structure for photocatalytic dye degradation. The VBM is shifted positively, therefore enhancing oxidation capability. Lastly, Zn doping at an appropriate concentration suppresses electron-hole recombination. The photo-excited carrier lifetime of C_3N_4-D is ~1.56 times longer than the bulk g-C_3N_4.

CRediT authorship contribution statement

Mengyu Cao: Conceptualization, Investigation, Formal analysis, Writing - original draft. **Ke Wang:** Conceptualization, Formal analysis, Methodology, Writing - review & editing. **Ignacio Tudela:** Resources, Writing - review & editing. **Xianfeng Fan:** Conceptualization, Funding acquisition, Project administration, Supervision, Writing - review & editing.

Declaration of Competing Interest

There are no conflicts of interest to declare.

Acknowledgements

K. W. thanks the research scholarship provided by the School of Engineering, the University of Edinburgh.

Appendix A. Supplementary data

Supplementary data to this article can be found online at https://doi.org/10.1016/j.apsusc.2020.147429.

References

[1] P. Xia, B. Zhu, J. Yu, S. Cao, M. Jaroniec, Ultra-thin nanosheet assemblies of graphitic carbon nitride for enhanced photocatalytic CO_2 reduction, J. Mater. Chem. A 5 (2017) 3230–3238, https://doi.org/10.1039/c6ta08310b.
[2] K. Wang, J.L. Fu, Y. Zheng, Insights into photocatalytic CO_2 reduction on C_3N_4: strategy of simultaneous B, K Co-doping and enhancement by N vacancies, Appl. Catal., B 254 (2019) 270–282, https://doi.org/10.1016/j.apcatb.2019.05.002.
[3] L.H. Lin, H.H. Ou, Y.F. Zhang, X.C. Wang, Tri-s-triazine-based crystalline graphitic carbon nitrides for highly efficient hydrogen evolution photocatalysis, ACS Catal. 6 (2016) 3921–3931, https://doi.org/10.1021/acscatal.6b00922.
[4] Y. Li, R. Jin, Y. Xing, J. Li, S. Song, X. Liu, M. Li, R. Jin, Macroscopic foam-like holey ultrathin g-C3N4Nanosheets for drastic improvement of visible-light photocatalytic activity, Adv. Energy Mater. 6 (2016) 1601273, https://doi.org/10.1002/aenm.201601273.
[5] Xiangjuan Yuan, Shule Duan, Guangyu Wu, Lei Sun, Gang Cao, Dongya Li, Haiming Xu, Qiang Li, Dongsheng Xia, Enhanced catalytic ozonation performance of highly stabilized mesoporous ZnO doped g-C 3 N 4 composite for efficient water decontamination, Appl. Catal. A 551 (2018) 129–138, https://doi.org/10.1016/j.apcata.2017.12.011.
[6] Z. Lu, L. Zeng, W. Song, Z. Qin, D. Zeng, C. Xie, In situ synthesis of C-TiO_2/g-C_3N_4 heterojunction nanocomposite as highly visible light active photocatalyst originated from effective interfacial charge transfer, Appl. Catal., B 202 (2017) 489–499, https://doi.org/10.1016/j.apcatb.2016.09.052.
[7] H. Yu, R. Shi, Y. Zhao, T. Bian, Y. Zhao, C. Zhou, G.I.N. Waterhouse, L.Z. Wu, C.H. Tung, T. Zhang, Alkali-assisted synthesis of nitrogen deficient graphitic carbon nitride with tunable band structures for efficient visible-light-driven hydrogen evolution, Adv. Mater. 29 (2017) 1605148, https://doi.org/10.1002/adma.201605148.
[8] L. Ruan, G. Xu, L. Gu, C. Li, Y. Zhu, Y. Lu, The physical properties of Li-doped g-C_3N_4 monolayer sheet investigated by the first-principles, Mater. Res. Bull. 66 (2015) 156–162, https://doi.org/10.1016/j.materresbull.2015.02.044.
[9] T. Xiong, W. Cen, Y. Zhang, F. Dong, Bridging the g-C_3N_4 interlayers for enhanced photocatalysis, ACS Catal. 6 (2016) 2462–2472, https://doi.org/10.1021/acscatal.5b02922.
[10] J. Jiang, S. Cao, C. Hu, C. Chen, A comparison study of alkali metal-doped g-C_3N_4 for visible-light photocatalytic hydrogen evolution, Chin. J. Catal. 38 (2017) 1981–1989, https://doi.org/10.1016/s1872-2067(17)62936-x.
[11] Y. Pan, D. Li, H.L. Jiang, Sodium-doped C_3N_4/MOF heterojunction composites with tunable band structures for photocatalysis: interplay between light harvesting and electron transfer, Chem. - Eur. J. 24 (2018) 18403–18407, https://doi.org/10.1002/chem.201803555.
[12] B. Zhu, J. Zhang, C. Jiang, B. Cheng, J. Yu, First principle investigation of halogen-

doped monolayer g-C_3N_4 photocatalyst, Appl. Catal., B 207 (2017) 27–34, https://doi.org/10.1016/j.apcatb.2017.02.020.
[13] Y. Huang, Q. Yan, H. Yan, Y. Tang, S. Chen, Z. Yu, C. Tian, B. Jiang, Layer stacked iodine and phosphorus Co-doped C_3N_4 for enhanced visible-light photocatalytic hydrogen evolution, ChemCatChem 9 (2017) 4083–4089, https://doi.org/10.1002/cctc.201700786.
[14] Z.-A. Lan, G. Zhang, X. Wang, A facile synthesis of Br-modified g-C_3N_4 semiconductors for photoredox water splitting, Appl. Catal., B 192 (2016) 116–125, https://doi.org/10.1016/j.apcatb.2016.03.062.
[15] K. Ding, L. Wen, M. Huang, Y. Zhang, Y. Lu, Z. Chen, How does the B, F-monodoping and B/F-codoping affect the photocatalytic water-splitting performance of g-c3n4? Phys. Chem. Chem. Phys. 18 (2016) 19217–19226, https://doi.org/10.1039/c6cp02169g.
[16] L. Zeng, X. Ding, Z. Sun, W. Hua, W. Song, S. Liu, L. Huang, Enhancement of photocatalytic hydrogen evolution activity of g-C_3N_4 induced by structural distortion via post-fluorination treatment, Appl. Catal., B 227 (2018) 276–284, https://doi.org/10.1016/j.apcatb.2018.01.040.
[17] B. Yue, Q. Li, H. Iwai, T. Kako, J. Ye, Hydrogen production using zinc-doped carbon nitride catalyst irradiated with visible light, Sci. Technol. Adv. Mater. 12 (2011) 034401, , https://doi.org/10.1088/1468-6996/12/3/034401.
[18] Z. Xing, Y. Chen, C. Liu, J. Yang, J. Xu, Y. Situ, H. Huang, Synthesis of core-shell ZnO/oxygen doped g-C_3N_4 visible light driven photocatalyst via hydrothermal method, J. Alloys Compd. 708 (2017) 853–861, https://doi.org/10.1016/j.jallcom.2016.11.295.
[19] X.D. Sun, Y.Y. Li, J. Zhou, C. Hai Ma, Y. Wang, J.H. Zhu, Facile synthesis of high photocatalytic active porous g-C3N4 with ZnCl2 template, J. Colloid Interface Sci. 451 (2015) 108–116, https://doi.org/10.1016/j.jcis.2015.03.059.
[20] W.-D. Oh, V.W.C. Chang, Z.-T. Hu, R. Goei, T.-T. Lim, Enhancing the catalytic activity of g-C_3N_4 through Me doping (Me = Cu, Co and Fe) for selective sulfathiazole degradation via redox-based advanced oxidation process, Chem. Eng. J. 323 (2017) 260–269, https://doi.org/10.1016/j.cej.2017.04.107.
[21] X. Zou, R. Silva, A. Goswami, T. Asefa, Cu-doped carbon nitride: bio-inspired synthesis of H_2-evolving electrocatalysts using graphitic carbon nitride (g-C_3N_4) as a host material, Appl. Surf. Sci. 357 (2015) 221–228, https://doi.org/10.1016/j.apsusc.2015.08.197.
[22] J. Gao, Y. Wang, S. Zhou, W. Lin, Y. Kong, A facile one-step synthesis of Fe-doped g-C_3N_4 nanosheets and their improved visible-light photocatalytic performance, ChemCatChem 9 (2017) 1708–1715, https://doi.org/10.1002/cctc.201700492.
[23] X. Li, W. Bi, L. Zhang, S. Tao, W. Chu, Q. Zhang, Y. Luo, C. Wu, Y. Xie, Single-atom Pt as Co-catalyst for enhanced photocatalytic H_2 evolution, Adv. Mater. 28 (2016) 2427–2431, https://doi.org/10.1002/adma.201505281.
[24] Z. Chen, S. Mitchell, E. Vorobyeva, R.K. Leary, R. Hauert, T. Furnival, Q.M. Ramasse, J.M. Thomas, P.A. Midgley, D. Dontsova, M. Antonietti, S. Pogodin, N. López, J. Pérez-Ramírez, Stabilization of single metal atoms on graphitic carbon nitride, Adv. Funct. Mater. 27 (2017) 1605785, https://doi.org/10.1002/adfm.201605785.
[25] Y. Wang, X. Zhao, D. Cao, Y. Wang, Y. Zhu, Peroxymonosulfate enhanced visible light photocatalytic degradation bisphenol a by single-atom dispersed Ag mesoporous g-C_3N_4 hybrid, Appl. Catal., B 211 (2017) 79–88, https://doi.org/10.1016/j.apcatb.2017.03.079.
[26] G. Gao, Y. Jiao, E.R. Waclawik, A. Du, Single atom (Pd/Pt) supported on graphitic carbon nitride as an efficient photocatalyst for visible-light reduction of carbon dioxide, J. Am. Chem. Soc. 138 (2016) 6292–6297, https://doi.org/10.1021/jacs.6b02692.
[27] X. Huang, Y. Xia, Y. Cao, X. Zheng, H. Pan, J. Zhu, C. Ma, H. Wang, J. Li, R. You, S. Wei, W. Huang, J. Lu, Enhancing both selectivity and coking-resistance of a single-atom Pd1/C_3N_4 catalyst for acetylene hydrogenation, Nano Res. 10 (2017) 1302–1312, https://doi.org/10.1007/s12274-016-1416-z.
[28] S.C. Yan, Z.S. Li, Z.G. Zou, Photodegradation performance of g-C_3N_4 fabricated by directly heating melamine, Langmuir 25 (2009) 10397–10401, https://doi.org/10.1021/la900923z.
[29] G. Liu, P. Niu, C. Sun, S.C. Smith, Z. Chen, G.Q. Lu, H.M. Cheng, Unique electronic structure induced high photoreactivity of sulfur-doped graphitic C_3N_4, J. Am. Chem. Soc. 132 (2010) 11642–11648, https://doi.org/10.1021/ja103798k.
[30] K. Wang, Q. Li, B. Liu, B. Cheng, W. Ho, J. Yu, Sulfur-doped g-C_3N_4 with enhanced photocatalytic CO_2-reduction performance, Appl. Catal., B 176–177 (2015) 44–52, https://doi.org/10.1016/j.apcatb.2015.03.045.
[31] N. Tian, Y. Zhang, X. Li, K. Xiao, X. Du, F. Dong, G.I.N. Waterhouse, T. Zhang, H. Huang, Precursor-reforming protocol to 3D mesoporous g-C_3N_4 established by ultrathin self-doped nanosheets for superior hydrogen evolution, Nano Energy 38 (2017) 72–81, https://doi.org/10.1016/j.nanoen.2017.05.038.
[32] S. Cao, Q. Huang, B. Zhu, J. Yu, Trace-level phosphorus and sodium Co-doping of g-C_3N_4 for enhanced photocatalytic H_2 production, J. Power Sources 351 (2017) 151–159, https://doi.org/10.1016/j.jpowsour.2017.03.089.
[33] J. Fu, B. Zhu, C. Jiang, B. Cheng, W. You, J. Yu, Hierarchical porous O-doped g-C_3N_4 with enhanced photocatalytic CO_2 reduction activity, Small 13 (2017) 1603938, https://doi.org/10.1002/smll.201603938.
[34] F.-Y. Su, C.-Q. Xu, Y.-X. Yu, W.-D. Zhang, Carbon self-doping induced activation of n-π* electronic transitions of g-C_3N_4 nanosheets for efficient photocatalytic H_2 evolution, ChemCatChem 8 (2016) 3527–3535, https://doi.org/10.1002/cctc.201600928.
[35] Y. Li, X. Liu, L. Tan, Z. Cui, X. Yang, Y. Zheng, K.W.K. Yeung, P.K. Chu, S. Wu, Rapid sterilization and accelerated wound healing using Zn^{2+} and graphene oxide modified g-C_3N_4 under dual light irradiation, Adv. Funct. Mater. 28 (2018) 1800299, https://doi.org/10.1002/adfm.201800299.
[36] Z. Qin, W. Fang, J. Liu, Z. Wei, Z. Jiang, W. Shangguan, Zinc-doped g-C_3N_4/$BiVO_4$ as a Z-scheme photocatalyst system for water splitting under visible light, Chin. J. Catal. 39 (2018) 472–478, https://doi.org/10.1016/s1872-2067(17)62961-9.
[37] M. Groenewolt, M. Antonietti, Synthesis of g-C_3N_4 nanoparticles in mesoporous silica host matrices, Adv. Mater. 17 (2005) 1789–1792, https://doi.org/10.1002/adma.200401756.
[38] J. Liu, J. Yan, H. Ji, Y. Xu, L. Huang, Y. Li, Y. Song, Q. Zhang, H. Xu, H. Li, Controlled synthesis of ordered mesoporous g-C_3N_4 with a confined space effect on its photocatalytic activity, Mater. Sci. Semicond. Process. 46 (2016) 59–68, https://doi.org/10.1016/j.mssp.2015.11.013.
[39] W. Zhang, Z. Zhao, F. Dong, Y. Zhang, Solvent-assisted synthesis of porous g-C_3N_4 with efficient visible-light photocatalytic performance for NO removal, Chin. J. Catal. 38 (2017) 372–378, https://doi.org/10.1016/s1872-2067(16)62585-8.
[40] Y. Wang, X. Wang, M. Antonietti, Y. Zhang, Facile one-pot synthesis of nanoporous carbon nitride solids by using soft templates, ChemSusChem 3 (2010) 435–439, https://doi.org/10.1002/cssc.200900284.
[41] M.J. Bojdys, J.-O. Müller, M. Antonietti, A. Thomas, Ionothermal synthesis of crystalline, condensed, graphitic carbon nitride, Chem. - Eur. J. 14 (2008) 8177–8182, https://doi.org/10.1002/chem.200800190.
[42] H. Gao, S. Yan, J. Wang, Y.A. Huang, P. Wang, Z. Li, Z. Zou, Towards efficient solar hydrogen production by intercalated carbon nitride photocatalyst, Phys. Chem. Chem. Phys. 15 (2013) 18077–18084, https://doi.org/10.1039/c3cp53774a.
[43] G. Zhang, G. Li, Z.A. Lan, L. Lin, A. Savateev, T. Heil, S. Zafeiratos, X. Wang, M. Antonietti, Optimizing optical absorption, exciton dissociation, and charge transfer of a polymeric carbon nitride with ultrahigh solar hydrogen production activity, Angew. Chem., Int. Ed. 56 (2017) 13445–13449, https://doi.org/10.1002/anie.201706870.
[44] M.K. Bhunia, K. Yamauchi, K. Takanabe, Harvesting solar light with crystalline carbon nitrides for efficient photocatalytic hydrogen evolution, Angew. Chem., Int. Ed. 53 (2014) 11001–11005, https://doi.org/10.1002/anie.201405161.
[45] G. Algara-Siller, N. Severin, S.Y. Chong, T. Bjorkman, R.G. Palgrave, A. Laybourn, M. Antonietti, Y.Z. Khimyak, A.V. Krasheninnikov, J.P. Rabe, U. Kaiser, A.I. Cooper, A. Thomas, M.J. Bojdys, Triazine-Based Graphitic Carbon Nitride: A Two-Dimensional Semiconductor, Angew. Chem., Int. Ed., 53 (2014) 7450-7455. https://doi.org/10.1002/anie.201402191.
[46] Z. Zeng, H. Yu, X. Quan, S. Chen, S. Zhang, Structuring phase junction between tri-s-triazine and triazine crystalline C_3N_4 for efficient photocatalytic hydrogen evolution, Appl. Catal., B 227 (2018) 153–160, https://doi.org/10.1016/j.apcatb.2018.01.023.
[47] E. Wirnhier, M.B. Mesch, J. Senker, W. Schnick, Formation and characterization of Melam, Melam Hydrate, and a Melam-Melem Adduct, Chem. - Eur. J. 19 (2013) 2041–2049, https://doi.org/10.1002/chem.201203340.
[48] Q. Liu, Y. Guo, Z. Chen, Z. Zhang, X. Fang, Constructing a novel ternary Fe(III)/Graphene/g-C_3N_4 composite photocatalyst with enhanced visible-light driven photocatalytic activity via interfacial charge transfer effect, Appl. Catal., B 183 (2016) 231–241, https://doi.org/10.1016/j.apcatb.2015.10.054.
[49] J. Wang, J. Chen, P. Wang, J. Hou, C. Wang, Y. Ao, Robust photocatalytic hydrogen evolution over amorphous ruthenium phosphide quantum dots modified g-C_3N_4 nanosheet, Appl. Catal., B 239 (2018) 578–585.
[50] J. Wu, N. Li, X.-H. Zhang, H.-B. Fang, Y.-Z. Zheng, X. Tao, Heteroatoms binary-doped hierarchical porous g-C_3N_4 nanobelts for remarkably enhanced visible-light-driven hydrogen evolution, Appl. Catal., B 226 (2018) 61–70.
[51] F. Raziq, M. Humayun, A. Ali, T. Wang, A. Khan, Q. Fu, W. Luo, H. Zeng, Z. Zheng, B. Khan, H. Shen, X. Zu, S. Li, L. Qiao, Synthesis of S-doped porous g-C_3N_4 by using ionic liquids and subsequently coupled With Au-TiO_2 for exceptional cocatalyst-free visible-light catalytic activities, Appl. Catal., B 237 (2018) 1082–1090, https://doi.org/10.1016/j.apcatb.2018.06.009.
[52] X.T. Tian, X.B. Yin, Carbon dots, unconventional preparation strategies, and applications beyond photoluminescence, Small 15 (2019) e1901803, , https://doi.org/10.1002/smll.201901803.
[53] R. Wang, H. Wu, R. Chen, Y. Chi, Strong electrochemiluminescence emission from oxidized multiwalled carbon nanotubes, Small 15 (2019) e1901550, , https://doi.org/10.1002/smll.201901550.
[54] I. Papailias, T. Giannakopoulou, N. Todorova, D. Demotikali, T. Vaimakis, C. Trapalis, Effect of processing temperature on structure and photocatalytic properties of g-C_3N_4, Appl. Surf. Sci. 358 (2015) 278–286, https://doi.org/10.1016/j.apsusc.2015.08.097.
[55] J. Xu, Z. Wang, Y. Zhu, Enhanced visible-light-driven photocatalytic disinfection performance and organic pollutant degradation activity of porous g-C_3N_4 nanosheets, ACS Appl. Mater. Interfaces 9 (2017) 27727–27735, https://doi.org/10.1021/acsami.7b07657.
[56] Z. Hong, B. Shen, Y. Chen, B. Lin, B. Gao, Enhancement of photocatalytic H_2 evolution over nitrogen-deficient graphitic carbon nitride, J. Mater. Chem. A 1 (2013) 11754–11761, https://doi.org/10.1039/c3ta12332d.
[57] J. Xu, L. Zhang, R. Shi, Y. Zhu, Chemical exfoliation of graphitic carbon nitride for efficient heterogeneous photocatalysis, J. Mater. Chem. A 1 (2013) 14766–14772, https://doi.org/10.1039/c3ta13188b.
[58] M. Zhang, J. Xu, R. Zong, Y. Zhu, Enhancement of visible light photocatalytic activities via porous structure of g-C_3N_4, Appl. Catal., B 147 (2014) 229–235, https://doi.org/10.1016/j.apcatb.2013.09.002.
[59] Y. Yang, J. Chen, Z. Mao, N. An, D. Wang, B.D. Fahlman, Ultrathin g-C_3N_4 nanosheets with an extended visible-light-responsive range for significant enhancement of photocatalysis, RSC Adv. 7 (2017) 2333–2341, https://doi.org/10.1039/c6ra26172h.
[60] Y. Yang, L. Geng, Y. Guo, J. Meng, Y. Guo, Easy dispersion and excellent visible-light photocatalytic activity of the ultrathin urea-derived g-C_3N_4 nanosheets, Appl. Surf. Sci. 425 (2017) 535–546, https://doi.org/10.1016/j.apsusc.2017.06.323.

[61] F. Dong, M. Ou, Y. Jiang, S. Guo, Z. Wu, Efficient and durable visible light photocatalytic performance of porous carbon nitride nanosheets for air purification, Ind. Eng. Chem. Res. 53 (2014) 2318–2330, https://doi.org/10.1021/ie4038104.
[62] J.-Y. Zhang, J.-Y. Mei, S.-S. Yi, X.-X. Guan, Constructing of Z-scheme 3D g-C_3N_4-ZnO@graphene aerogel heterojunctions for high-efficient adsorption and photodegradation of organic pollutants, Appl. Surf. Sci. 492 (2019) 808–817, https://doi.org/10.1016/j.apsusc.2019.06.261.
[63] J. Liu, Z.-Y. Hu, Y. Peng, H.-W. Huang, Y. Li, M. Wu, X.-X. Ke, G.V. Tendeloo, B.-L. Su, 2D ZnO mesoporous single-crystal nanosheets with exposed 0001 polar facets for the depollution of cationic dye molecules by highly selective adsorption and photocatalytic decomposition, Appl. Catal., B 181 (2016) 138–145, https://doi.org/10.1016/j.apcatb.2015.07.054.
[64] C.H. Nguyen, M.L. Tran, T.T.V. Tran, R.-S. Juang, Enhanced removal of various dyes from aqueous solutions by UV and simulated solar photocatalysis over TiO_2/ZnO/rGO composites, Sep. Purif. Technol. 232 (2020), https://doi.org/10.1016/j.seppur.2019.115962.
[65] B. Zhu, P. Xia, Y. Li, W. Ho, J. Yu, Fabrication and photocatalytic activity enhanced mechanism of direct Z-scheme g-C_3N_4/Ag_2WO_4 photocatalyst, Appl. Surf. Sci. 391 (2017) 175–183, https://doi.org/10.1016/j.apsusc.2016.07.104.
[66] Z. Zhu, X. Tang, C. Ma, M. Song, N. Gao, Y. Wang, P. Huo, Z. Lu, Y. Yan, Fabrication of conductive and high-dispersed Ppy@Ag/g-C_3N_4 composite photocatalysts for removing various pollutants in water, Appl. Surf. Sci. 387 (2016) 366–374, https://doi.org/10.1016/j.apsusc.2016.06.124.
[67] G. Salehi, R. Abazari, A.R. Mahjoub, Visible-light-induced graphitic-C_3N_4@Nickel-aluminum layered double hydroxide nanocomposites with enhanced photocatalytic activity for removal of dyes in water, Inorg. Chem. 57 (2018) 8681–8691, https://doi.org/10.1021/acs.inorgchem.8b01636.
[68] H. Zhao, G. Li, F. Tian, Q. Jia, Y. Liu, R. Chen, g-C_3N_4 surface-decorated $Bi_2O_2CO_3$ for improved photocatalytic performance: theoretical calculation and photodegradation of antibiotics in actual water matrix, Chem. Eng. J. 366 (2019) 468–479, https://doi.org/10.1016/j.cej.2019.02.088.
[69] B. Zhang, X. Li, Y. Zhao, H. Song, H. Wang, Facile synthesis of oxygen doped mesoporous graphitic carbon nitride with high photocatalytic degradation efficiency under simulated solar irradiation, Colloids Surf., A 580 (2019), https://doi.org/10.1016/j.colsurfa.2019.123736.
[70] S.M.N. Jeghan, J.Y. Do, M. Kang, Fabrication of flower-like copper cobaltite/graphitic-carbon nitride ($CuCo_2O_4$/g-C_3N_4) composite with superior photocatalytic activity, J. Ind. Eng. Chem. 57 (2018) 405–415, https://doi.org/10.1016/j.jiec.2017.08.049.
[71] J. Li, H. Yuan, Z. Zhu, Improved photoelectrochemical performance of Z-scheme g-C_3N_4/Bi_2O_3/$BiPO_4$ heterostructure and degradation property, Appl. Surf. Sci. 385 (2016) 34–41, https://doi.org/10.1016/j.apsusc.2016.05.065.
[72] K.C. Christoforidis, T. Montini, E. Bontempi, S. Zafeiratos, J.J.D. Jaén, P. Fornasiero, Synthesis and photocatalytic application of visible-light active β-Fe_2O_3/g-C_3N_4 hybrid nanocomposites, Appl. Catal., B 187 (2016) 171–180, https://doi.org/10.1016/j.apcatb.2016.01.013.
[73] J. Li, Y. Liu, H. Li, C. Chen, Fabrication of g-C_3N_4/TiO_2 composite photocatalyst with extended absorption wavelength range and enhanced photocatalytic performance, J. Photochem. Photobiol., A 317 (2016) 151–160, https://doi.org/10.1016/j.jphotochem.2015.11.008.
[74] Jonghun Lim, Damián Monllor-Satoca, Jum Suk Jang, Seockheon Lee, Wonyong Choi, Visible light photocatalysis of fullerol-complexed TiO_2 enhanced by Nb doping, Appl. Catal. B 152-153 (2014) 233–240, https://doi.org/10.1016/j.apcatb.2014.01.026.
[75] C. Ye, J. Li, Z. Li, X. Li, X. Fan, L. Zhang, B. Chen, C. Tung, L. Wu, Enhanced driving force and charge separation efficiency of protonated g-C_3N_4 for photocatalytic O_2 evolution, ACS Catal. 5 (2015) 6973–6979, https://doi.org/10.1021/acscatal.5b02185.
[76] W.J. Ong, L.L. Tan, Y.H. Ng, S.T. Yong, S.P. Chai, Graphitic carbon nitride (g-C_3N_4)-based photocatalysts for artificial photosynthesis and environmental remediation: are we a step closer to achieving sustainability? Chem. Rev. 116 (2016) 7159–7329, https://doi.org/10.1021/acs.chemrev.6b00075.
[77] X. Ma, Y. Lv, J. Xu, Y. Liu, R. Zhang, Y. Zhu, A strategy of enhancing the photoactivity of g-C_3N_4 via doping of nonmetal elements: a first-principles study, J. Phys. Chem. C 116 (2012) 23485–23493, https://doi.org/10.1021/jp308334x.

Applied Surface Science 536 (2021) 147784

Contents lists available at ScienceDirect

Applied Surface Science

journal homepage: www.elsevier.com/locate/apsusc

Improve photocatalytic performance of g-C_3N_4 through balancing the interstitial and substitutional chlorine doping

Mengyu Cao, Ke Wang*, Ignacio Tudela, Xianfeng Fan*

Institute for Materials and Processes, School of Engineering, The University of Edinburgh, Edinburgh EH9 3FB, Scotland, UK

ARTICLE INFO

Keywords:
Dopant site control
g-C_3N_4
Photocatalytic degradation
Interstitial Cl dopants
Substitutional Cl dopants

ABSTRACT

Cl doped g-C_3N_4 with controllable doping site is synthesised for the first time via an agitation-assisted solvothermal method. It is found that both the molecular and electronic structure of the prepared g-C_3N_4 correlates strongly with the atomic ratio of interstitial to substitutional Cl dopants (Cl_{int}/Cl_{sub}), which is determined by the agitation rate during the solvothermal synthesis. Due to the different effects of Cl_{int} and Cl_{sub} on the electronic/molecular structure of g-C_3N_4, the photocatalytic activity of g-C_3N_4 can only be optimised by balancing the concentration of Cl_{int} and Cl_{sub} dopants. The optimal synthesis condition for Cl-doped g-C_3N_4 is associated with a moderate agitation rate of 60 rpm (60-C_3N_4). Under 60 rpm agitation during the synthesis, the 60-C_3N_4 exhibits remarkably larger specific surface area, stronger photo-oxidation capability, reduced bandgap and suppressed electron-hole recombination comparing with the control group g-C_3N_4 synthesised via conventional thermal polycondensation method. An outstanding photocatalytic RhB degradation performance is therefore observed for 60-C_3N_4 with ~ 35-fold higher pseudo-first reaction rate constant than the bulk g-C_3N_4 control group sample.

1. Introduction

Water pollution is a severe challenge to human society in the 21st century. Among all the pollutants, organic dyes are a kind of major pollutants due to its wide usage in the industry [1]. Taking advantage of solar light to remove the dyes from water is a sustainable and economically feasible way to address this challenge, and a high-performance photocatalyst is a key to success. Graphitic C_3N_4 (g-C_3N_4) is deemed as a promising candidate for photocatalytic dye degradation due to its low-cost, non-toxicity and free of transition metal-free composition [2–5]. However, the unsatisfactory photocatalytic activity of g-C_3N_4 hinders its practical application. The main shortcomings of g-C_3N_4 are its limited specific surface area (SSA), non-optimised electronic structure and high photo-excited electron-hole recombination rate [6–8]. The development of new strategies to address the shortcomings of g-C_3N_4 and improve its photocatalytic dye degradation performance remains a challenging task.

The strategies to optimise the property of g-C_3N_4 can be classified into two main categories: doping with heteroatoms and vacancy introduction [9,10]. Whereas vacancy introduction is limited to C or N only, heteroatoms doping is more versatile due to the wide variety of dopants. Heteroatom doping has been reported to improve the photocatalytic performance of g-C_3N_4 through different mechanisms: (i) trapping photo-excited electrons or holes and retarding the recombination [10,11]; (ii) optimising the electronic structure by shifting the edge of valence band or conduction band [12,13]; (iii) facilitating the interlayer electron/hole transfer [14] and (iv) enhancing target reactant adsorption and activation [12,15–18]. Among all the potential dopants, the Cl atom is one of the most promising candidates due to its unique features. Cl not only enhances the photocatalytic performance of g-C_3N_4 on its own [19,20], and as a common anion, Cl can also be introduced into g-C_3N_4 along with other dopants [21–24]. Another important feature of Cl as dopants is that Cl can potentially act as both interstitial and substitutional dopants (Cl_{int} and Cl_{sub}). However, no previous work has elucidated the different roles of Cl_{int} and Cl_{sub} on influencing the molecular and electronic structure of g-C_3N_4. The optimal combination of Cl_{int} and Cl_{sub} remain ambiguous.

To optimise the property of pristine g-C_3N_4 for a better photocatalytic activity, one of the most fundamental aspects is to develop a new preparation method. Moreover, the clear understanding of the relationship between preparation parameters and property of the synthesised material is critical. As the most conventional preparation method for g-C_3N_4, thermal polymerisation in a static atmosphere has been comprehensively investigated. Comparing with thermal polymerisation, the solvothermal method possesses unique advantages such as low temperature, controllable morphology, high homogeneity etc.

* Corresponding authors.
E-mail addresses: k.wang@ed.ac.uk (K. Wang), x.fan@ed.ac.uk (X. Fan).

https://doi.org/10.1016/j.apsusc.2020.147784
Received 10 June 2020; Received in revised form 27 August 2020; Accepted 31 August 2020
Available online 09 September 2020

Although the solvothermal synthesis of g-C_3N_4 is still not fully understood as it has not been thoroughly studied yet, synthesis method using dicyandiamide/melamine and cyanuric chloride in acetonitrile have been reported in the literature [25–28]. However, in those works, g-C_3N_4 solvothermal synthesis were all performed in a static condition. The static solvothermal synthesis results in g-C_3N_4 with low SSA, which significantly hinders its photocatalytic performance. For instance, Hu et al. [29] reported the solvothermal synthesis of g-C_3N_4 using cyanuric chloride and sodium azide. Their reported SSA value of 4.4 m^2 g^{-1} showed no obvious advantage comparing with C_3N_4 synthesised via conventional thermal polycondensation method. An SSA value of 34 m^2 g^{-1} was reported by Wang et al. [30] using melamine and cyanuric chloride; Cui et al. [31] synthesised C_3N_4 hollow microspheres with an SSA value of 20 m^2 g^{-1} via the solvothermal method with cyanuric chloride and dicyandiamide. Moreover, in all these studies though, the role of Cl dopants in g-C_3N_4 introduced via cyanuric chloride is either neglected [28–30,32] or largely unexplored [31,33]. Therefore, the correlation between Cl_{int} (Cl_{sub}) doping and the solvothermal synthesis condition remains unknown.

Herein, the Cl doped g-C_3N_4 with controllable Cl doping sites is synthesised for the first time via an agitation-assisted solvothermal method. The effects of agitation rate on the morphology, SSA, Cl doping concentration and their relations with the photocatalytic activity are investigated in detail. By elucidating the different effects of Cl_{int} and Cl_{sub} on electronic/molecular structure of g-C_3N_4, the balance between the Cl_{int} and Cl_{sub} is proven critical to improving the photocatalytic activity of g-C_3N_4. With optimal Cl_{int}/Cl_{sub} atomic ratio, the SSA of Cl doped g-C_3N_4 prepared under 60 rpm agitation (60-C_3N_4) reaches 82.7 m^2 g^{-1}, which is ~6.67 times of the g-C_3N_4 prepared via the conventional thermal polymerisation method. Moreover, the 60-C_3N_4 shows the state-of-the-art RhB photodegradation performance under visible light irradiation and the corresponding pseudo-first reaction rate constant is ~35-fold higher than the conventional g-C_3N_4.

2. Materials and methods

2.1. Materials

All chemicals were of analytical grade and used without any further purification. Cyanuric chloride (1, 3, 5- trichlorotriazine, ≥ 99.5%, ACS reagent), dicyandiamide (99.5+ %, ACS reagent), melamine (99%) and Acetonitrile (99.9+ %, extra dry, AcroSeal) were purchased from ACROS. Deionised (DI) water was used in all the experiments.

2.2. Catalysts preparation

Cl-doped g-C_3N_4 was successfully prepared by a one-step template-free solvothermal method under controlled agitation. To prepare the Cl-doped g-C_3N_4, 15 mmol of cyanuric chloride, 7.5 mmol of dicyandiamide and 60 mL acetonitrile were added into a 150 mL Teflon-lined autoclave (Ø60 mm × 50 mm, ID × H). The temperature of the reactor was monitored via a K-type thermocouple inserted into a blind hole on the wall of a stainless-steel reactor. The heating band tightly surrounding the reactor was used to heat the reactor, and the temperature was controlled by a proportional–integral–derivative (PID) temperature controller. The reaction system was agitated by a Teflon coated round magnetic stirring bar (Ø6mm × 30 mm, D × H) with digital control of the agitation speed. In the synthesis progress, the reactor was heated to 180°C with a ramping rate of 10 °C min^{-1}. During 48 h of soaking at 180 °C, the agitation was maintained constantly. After cooling down to room temperature naturally, the sample was collected and washed by DI water and ethanol (~300 mL) under vigorous stirring for three times. Then, it was dried in a vacuum oven at 80 °C overnight. The g-C_3N_4 samples synthesised via the solvothermal method with different agitation rates of 0 rpm, 60 rpm (minimum speed of magnetic stirrer), 100 rpm, 400 rpm, 750 rpm and 1100 rpm (maximum speed of magnetic stirrer) are denoted as 0-C_3N_4, 60-C_3N_4, 100-C_3N_4, 400-C_3N_4, 750-C_3N_4 and 1100-C_3N_4, respectively, in the rest of this work. Control group sample C_3N_4-M-Air was synthesised via the conventional thermal polycondensation method in static air. 10 g of melamine was packed into an alumina crucible covered with a lid. The crucible was then placed at the centre of a muffle furnace and heated at 500 °C for 2 h with a ramping rate of 10 °C min^{-1}. After cooling to room temperature naturally, the yellowish product was ground to fine powders in an agate mortar and denoted as C_3N_4-M-Air.

2.3. Physical characterisation

Powder X-ray diffraction (XRD) patterns of the prepared samples were characterised using an X-ray diffractometer (Phaser-D2, Bruker) with Cu Kα X-ray source at the voltage of 40 kV and current of 40 mA. Both core-level and valence band (VB) X-ray photoelectron spectra (XPS) were characterised using an X-ray photoelectron spectrometer (ThermoFisher K-Alpha) with an Al Kα X-ray source. The C, H and N chemical compositions of the prepared g-C_3N_4 samples were determined with an organic elemental analyser (Carlo Erba NA2500). The infrared (IR) transmission spectrum was collected on a Fourier transform infrared spectrophotometer (FTIR, Shimadzu IRTracer-100) following the KBr pellet method. The 0.5 mg sample was first mixed with 100 mg pre-dried KBr powder by carefully grinding in a mortar. Then, the mixture was pressed into a pellet in the diameter of 13 mm using a hydraulic press. The prepared KBr pellet was placed inside the FTIR spectrometer vertically to the incident beam. The spectrum within the range of 600–4000 cm^{-1} was collected in the resolution of 4 cm^{-1} by averaging 64 scans. Light adsorption and bandgap determination were conducted by ultraviolet-visible diffuse reflectance spectroscopy (UV–Vis DRS) on a UV–Vis spectrophotometer (UV-3600plus, Shimadzu) equipped with a commercial accessory (Praying Mantis, Harrick). Static photoluminescence (PL) spectra were collected using a spectrofluorometer (Shimazu RF-6000) with a solid sample accessory. 325 nm UV light was used as the excitation source, and the slit width was set to be 3 nm. The time-resolved photoluminescence spectra (time-resolved PL) were collected on a time-resolved fluorescence spectrometer (FLS980, Edinburgh Instruments) by monitoring the fluorescence intensity evolution at the peak wavelength determined from the static PL test. A scanning electron microscope (SEM, Zeiss Sigma VP) was used to obtain the morphological information of the prepared samples. An additional X-ray energy dispersive spectrometer (EDS) installed in the SEM was used to determine the elemental composition of the samples. N_2 sorption experiments were conducted on an automatic sorption analyser (Quantachrome, Autosorb-iQ) at a temperature of 77 K. The specific surface area (SSA) was calculated from the N_2 sorption isotherm using Brunauer-Emmett-Teller (BET) theory.

2.4. Photoelectrochemical experiments

Photoelectrochemical tests were conducted with a typical 3-electrode configuration using a potentiostat (Metrohm, Autolab PGSTAT204). The reference electrode was Ag/AgCl (0.1 M KCl, CHI Instruments); the counter electrode was a Pt-coil electrode (CHI Instruments), and the electrolyte was the 0.1 M KCl aqueous solution. The working electrode was prepared via the following procedure. A 15 × 15 mm^2 indium tin oxide coated glass (ITO glass) was used to support the catalysts as the working electrode. A geometric area of 0.75 cm^2 was kept as an active area on the ITO glass with the rest of the surface insulated by scotch tape. A crocodile clamp with copper lead was used for wiring the working electrode. The whole clamp and wire were kept out of the solution to prevent any side-reaction. (2) mg of catalysts were dispersed into 0.2 mL ethanol by ultrasonication. 10 μL Nafion solution (5 wt%, Sigma-Aldrich) was then added into the solution forming a homogenous mixture. A total amount of 0.1 mL mixture was then dropped on the ITO glass in portions of 20 μL each time. After

drying at room temperature, the working electrode was ready for the photoelectrochemical experiments. During the transient photocurrent response experiments, a Xenon lamp (Thorlabs, SLS 401) equipped with a 420 nm long-pass filter was used to provide the visible light for catalysts excitation. A build-in optical shutter was used to chop the light beam regularly. A bias potential of 0.2 V (vs Ag/AgCl, 0.1 M KCl) was applied to the working electrode during the tests, and the data interval was set to 0.1 s.

2.5. Photocatalytic performance evaluation

The photocatalytic activity of the prepared samples was evaluated by a probe reaction, i.e. photocatalytic RhB degradation under visible light irradiation. A 300 W Xenon lamp (PLS-SXE300, Beijing Perfectlight technology co.) with a 420 nm long-pass filter was used to provide the visible light to drive the reaction. The power density of the light reaching the catalysts was measured to be 508 ± 10 mW cm^{-2} using a thermopile light power meter (Thorlabs, PM16-401). A jacketed glass beaker was used as the reactor with water circulation to keep the solution temperature constant during the photocatalytic experiments. For each degradation experiment, 12 mg of catalyst was dispersed into 60 mL RhB aqueous solution in the concentration of 10 ppm. Before the photocatalytic reaction, the solution was ultrasonicated for 10 min and kept under stirring for another 25 min under dark to achieve a homogeneous catalyst dispersion; this procedure also enables the comparison of the catalyst adsorption capability towards RhB. Then, visible-light-driven photocatalytic RhB degradation experiments were conducted for 125 min under constant stirring. 3 mL aliquots were collected every 25 min for RhB concentration measurements. The aliquots were firstly centrifuged at 9000 rpm for 7 min to separate the catalysts; then the catalyst-free solutions were transferred into a cuvette and tested by a UV-Vis spectrophotometer (Analytik Jena, SPECORD PC 250).

3. Results and discussion

3.1. Molecular structure analysis

As indicated by the plausible g-C_3N_4 synthesis mechanisms via the solvothermal method displayed in Fig. 1, two precursors, cyanuric chloride and dicyandiamide, can be used for the synthesis of g-C_3N_4. Similar to the conventional g-C_3N_4 preparation method (i.e. thermal polycondensation), the solvothermal synthesis undergoes a similar polycondensation process from smaller oligomers to larger ones. The possible reaction intermediates include melamine, melem, melon and the corresponding oligomers with Cl dopants. The resulting g-C_3N_4 crystal is based on the stacking of melon layers with infinite size in theory (in practice, melon layers have a finite size due to the limited crystallisation degree).

The crystal phases of different g-C_3N_4 samples were characterised by XRD (Fig. 2(a)). The results indicate that the crystallisation degree of g-C_3N_4 is remarkably affected by the agitation during the solvothermal preparation. The 0-C_3N_4 synthesised under static solution without agitation exhibits the typical XRD pattern of g-C_3N_4. The main peak at 27.3° refers to the (002) facets of the crystal [34]. It represents the stacking of the layers of repeating melem units via the van der Waals force. The broad peak at ~ 23° can be attributed to the less crystallised g-C_3N_4 structure. The crystallisation degree first drops when agitation is implemented during the synthesis, then increases with the agitation rate rises. An increased crystallisation is achieved for the 1100-C_3N_4 synthesised under the agitation rate of 1100 rpm. The molecular structure of g-C_3N_4 prepared via the solvothermal method was further characterised by FTIR spectroscopy. As shown in Fig. 2(b), all the samples prepared via the solvothermal method exhibit the typical FTIR spectra of g-C_3N_4. All these spectra include the peaks at 812 cm^{-1}, which is characteristic of the existence of NH/NH_2 groups [35,36]. The strong adsorption band from 1269 to 1622 cm^{-1} are the typical vibration modes of C-N heterocycles of heptazine units [25,36,37]. Moreover, the absence of −CH bands at ~3000 cm^{-1} and −CN bands at ~2200 cm^{-1} rules out the possibility of direct involvement of acetonitrile in the g-C_3N_4 syntheses [26].

Organic elemental analysis is a more accurate way to quantitatively determine the chemical compositions of the samples prepared at different agitation rates. The results are summarised in Table 1. As illustrated in Fig. 1, the synthesis of g-C_3N_4 can be described as a polycondensation process. Theoretically, the fully crystallised or polycondensed g-C_3N_4 possesses the atomic C/N, H/N ratios of 0.75 and 0, respectively. Before reaching the full polycondensation, the key intermediates or oligomers are the melamine ($C_3H_6N_6$), melem ($C_6H_6N_{10}$) and melon ($C_{18}N_{27}H_6$). The corresponding atomic C/N ratios of these intermediates are 0.5, 0.6, 0.67 and H/N are 1, 0.6, 0.22, respectively. This indicates that the higher C/N and lower H/N ratios correspond to a higher condensation degree. More importantly, the substitution of N atoms by Cl dopants can significantly increase the C/N atomic ratio, even surpassing the theoretical 0.75 in g-C_3N_4. As summarised in Table 1, the control group sample C_3N_4-M-Air, synthesised via the conventional polycondensation of melamine at 500 °C, comprises N, C, H with weight ratios of 57.61 wt%, 34.10 wt% and 1.65 wt%, respectively. The C/N atomic ratio is 0.691, which is between the melon and fully polycondensed g-C_3N_4, close to the reported values in the literature [38,39]. Additionally, the low H weight percentage (1.65 wt%) and H/N atomic ratio (0.401) indicate a relatively high crystallisation degree of the g-C_3N_4 prepared via this method. Significantly different from the C_3N_4-M-Air, the g-C_3N_4 synthesised via the solvothermal method shows the remarkably different chemical compositions and polycondensation degree. Moreover, the chemical composition and polycondensation are agitation rate-dependent. Different from C_3N_4-M-Air, all the samples synthesised under agitation exhibit the H/N atomic ratios higher than 1.0, which suggests the lower polycondensation degree. The low crystallisation degrees are also proven by the XRD characterisation (Fig. 2(a)). In the case of C/N atomic ratio, for the g-C_3N_4 synthesised under agitation condition with stirring rates of 0, 60, 400, 750 and 1100 rpm, the C/N atomic ratios are 0.772, 0.845, 0.832, 0.818 and 0.760, respectively. The C/N atomic ratio firstly rises with the agitation rate when the agitation rate is relatively low. Then C/N atomic ratio falls back when the agitation rate further increases to 1100 rpm due to the enhanced crystallisation degree. It is important to point out that the C/N atomic ratios are even higher than the theoretical 0.75 of the fully condensed g-C_3N_4. This strongly suggests the Cl dopants substitute the N atoms in the molecular structure of g-C_3N_4, which is further confirmed via the XPS analyses (Fig. 4). The much higher crystallization/polycondensation degree of C_3N_4-M-Air than the solvothermally synthesized g-C_3N_4 can be explained by their different preparation temperature. The C_3N_4-M-Air was prepared at 500 °C; by contrast, the Cl doped g-C_3N_4 was prepared at 180 °C.

The molecular structures of Cl doped g-C_3N_4 prepared via solvothermal method can be determined via XPS analyses. As shown in Fig. 3(a), the C 1s XPS spectra of Cl doped g-C_3N_4 synthesised via the solvothermal method are deconvoluted into 3 peaks, which is in agreement with the control group sample C_3N_4-M-Air. The peak positioned at the binding energy of 284.6 eV is assigned to the adventitious carbon. It is used to calibrate all the XPS spectra for surface charge compensation. The other two peaks with the binding energy of 286.4 and 288.2 eV can be attributed to the C-NH_x and tri-coordinated C in the melem unit, respectively [14,26]. Note that the C-Cl bonds due to Cl_{int} dopants also contributes to the C 1s spectra. However, it is too difficult to accurately assign C-Cl bond due to its low concentration, unknown binding energy and strong overlap with C-NH_x/adventitious C peaks. The N 1s spectra of all the samples are presented in Fig. 3(b). The peaks centred at 398.7, 399.9 and 400.8 eV are assigned to the sp^2-hybridized N (C=N−C), sp^3-hybridized N (N-$(C)_3$) and NH_x functional group, respectively [34,40,41]. The C 1 s and N 1 s spectra of the

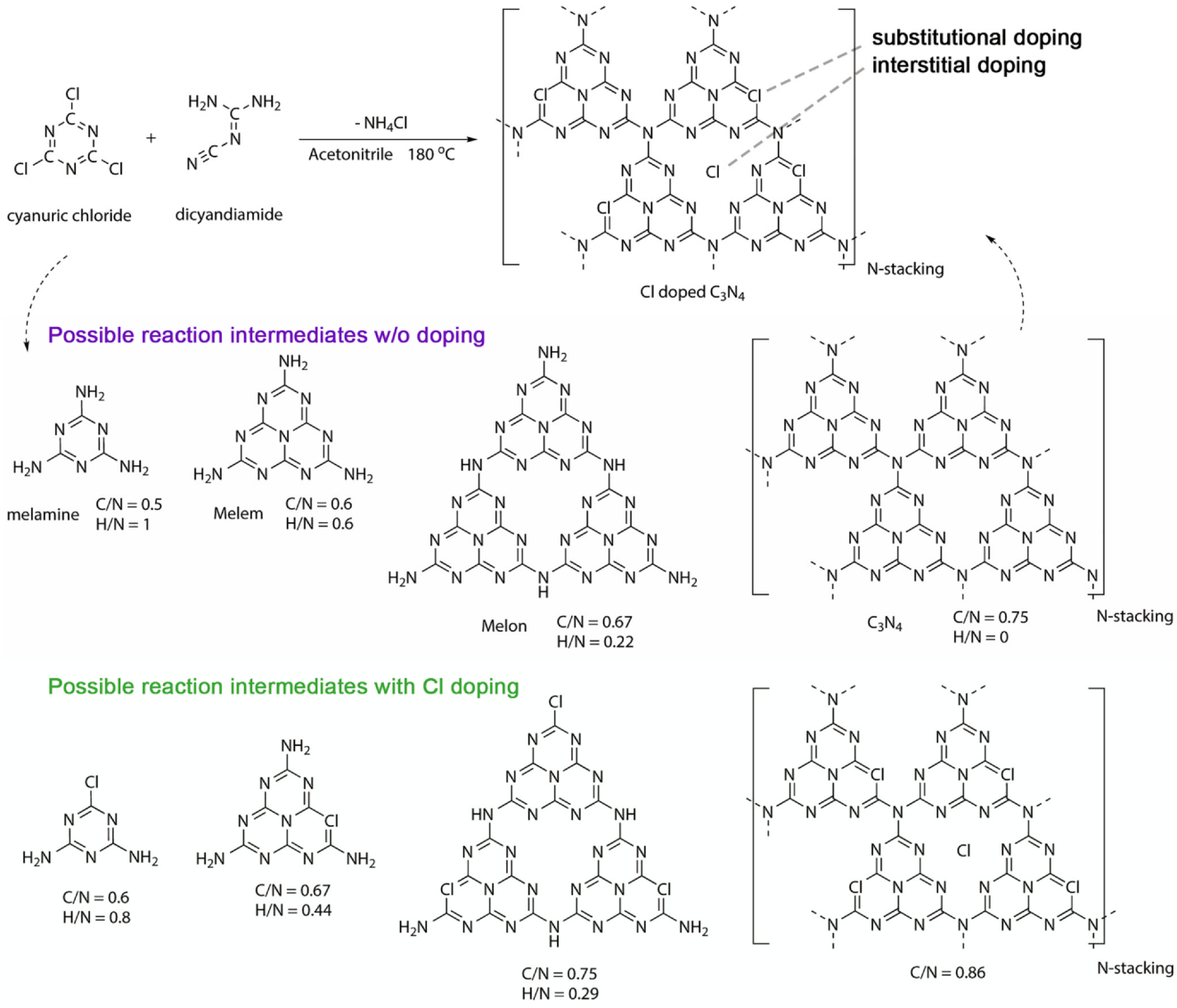

Fig. 1. Scheme of g-C_3N_4 synthesis via solvothermal reaction with the feedstocks of cyanuric chloride and dicyandiamide.

samples prepared via solvothermal method show consistency with C_3N_4-M-Air. It proves that the g-C_3N_4 synthesised via solvothermal method still follows the g-C_3N_4 molecular structure.

In g-C_3N_4, there are two possible sites for Cl doping: substitutional and interstitial sites (Cl_{sub} and Cl_{int}), as schemed in Fig. 1. Since the Cl possesses the moderate electronegativity and atom radius, the possibilities of doping at these two sites are very similar. As being pointed out via the DFT calculation, the formation energy for substitutional (dicoordinated N) and interstitial doping are calculated to be 3.60 and 3.52 eV, respectively [42]. To distinguish the Cl_{int} and Cl_{sub}, the Cl 2p spectra are deconvoluted and presented in Fig. 4. The peak centred at 202.0 and 200.2 eV can be attributed to the $2p_{1/2}$ and $2p_{3/2}$

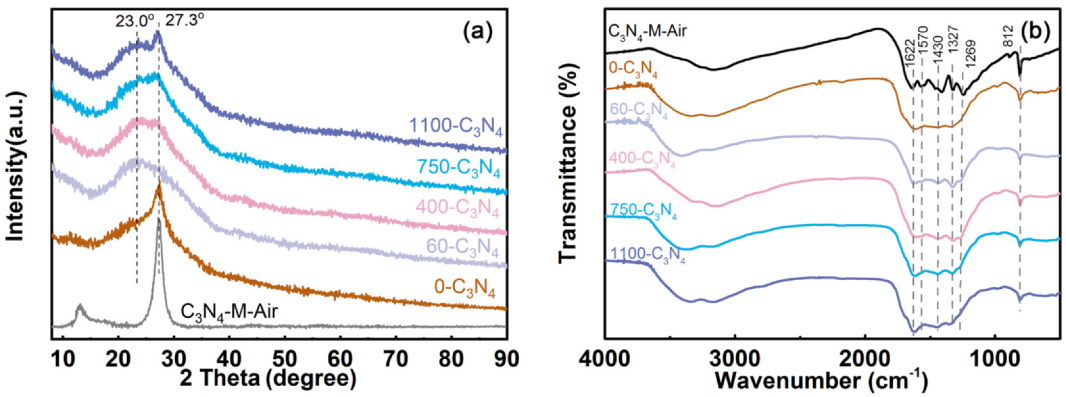

Fig. 2. The XRD patterns (a) and FTIR spectra (b) of the C_3N_4 prepared under different agitation conditions.

Table 1
Chemical compositions of g-C_3N_4 prepared at different agitation conditions determined by organic elemental analyses.

sample	N (wt%)	C (wt%)	H (wt%)	C/N (atomic ratio)	H/N (atomic ratio)
0-C_3N_4	47.74	31.60	2.95	0.772	1.120
60-C_3N_4	45.59	33.02	2.88	0.845	1.048
400-C_3N_4	45.64	32.53	2.79	0.832	1.029
750-C_3N_4	46.42	32.53	2.81	0.818	1.037
1100-C_3N_4	47.65	31.05	3.04	0.760	1.174
C_3N_4-M-Air	57.61	34.10	1.65	0.691	0.401

peaks of Cl_{sub} dopants, which are consistent with the reported binding energy of C-Cl bond in the literature [20,43,44]. And the peaks with the binding energy of 198.2 and 197.2 eV can be assigned to the Cl_{int} dopants derived from the Cl^- ions in the solution. The binding energy matches the typical values of NH_4Cl [45] and the reported value in previous work [46] of Cl-doped g-C_3N_4. The assignments of Cl_{sub} and Cl_{int} are rationalised by their different origins. The Cl_{sub} dopants are brought by the cyanuric chloride (schemed in Fig. 1). In contrast, the Cl_{int} dopants come from the negatively charged Cl^- ions due to the formation of NH_4Cl during the polycondensation for g-C_3N_4 synthesis. Therefore, the Cl_{sub} should exhibit more positive oxidation state than the Cl_{int}, which causes the larger binding energy of Cl_{sub} than Cl_{int} in XPS spectra (Fig. 4). The deconvolution of Cl 2p (Fig. 4) provokes the question why Cl_{int} and Cl_{sub} intend to co-exist. It can be explained from the perspectives of thermodynamics and kinetics. Because the formation energy of Cl_{int} and Cl_{sub} are very similar (3.60 and 3.52 eV, respectively [42]), the equilibrium constant ratio for Cl_{int} over Cl_{sub}, K_{int}/K_{sub}, is calculated to be 1.08. Due to the slow kinetics of the doping process, the dopants are unlikely reaching its equilibrium concentrations. Therefore, the atomic ratio of Cl_{int}/Cl_{sub} can be adjusted by varying the preparation condition.

The effects of agitation on Cl dopants concentration and distribution can be investigated via XPS semi-quantitative analyses of Fig. 4. The atomic and weight percentages of element i (A_i% and W_i%) in Cl doped g-C_3N_4 can be determined based on the peak area S_i, molecular weight m_i, relative sensitivity factor RSF_i and energy compensation factor ECF_i:

$$A_i\% = \frac{S_i/(RSF_i \times ECF_i)}{\sum [S_i/(RSF_i \times ECF_i)]} \times 100\% \quad (1)$$

$$W_i\% = \frac{A_i \times m_i}{\sum (A_i \times m_i)} \times 100\% \quad (2)$$

The total Cl doping concentrations (W_{Cl}%) at different agitation conditions are calculated to be 1.93%, 3.68%, 3.94%, 3.97%, 5.51%, 6.23% for the Cl doped g-C_3N_4 synthesized with agitation rates of 0, 60, 100, 400, 750, 1100 rpm respectively, as summarized in Fig. 5. It is noted that the total Cl doping concentration increases when the agitation rate rises. This can be attributed to the facilitated Cl intercalation derived from agitation during the crystallisation of g-C_3N_4. XPS

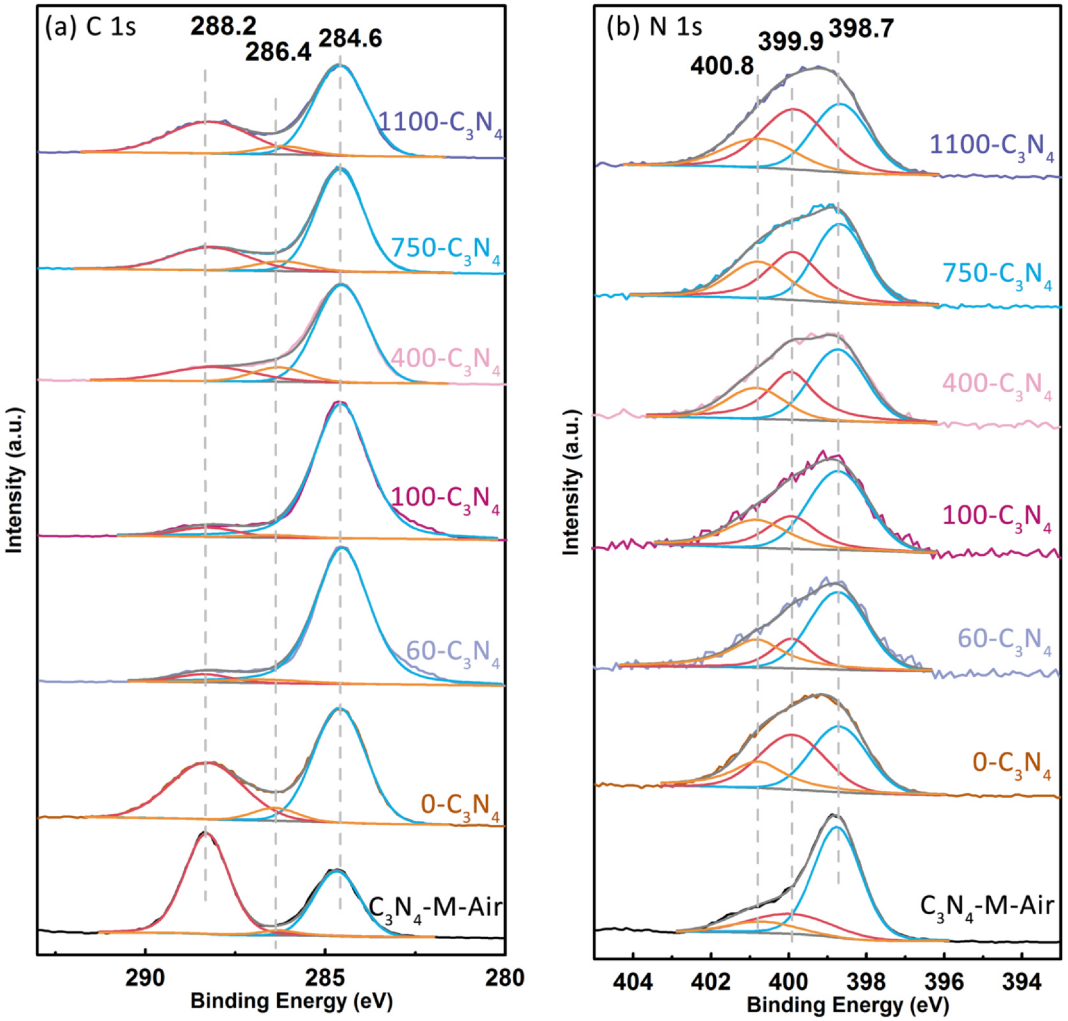

Fig. 3. The XPS (a) C 1s and (b) N 1s spectra of g-C_3N_4 prepared via the solvothermal method with agitation rates of 0, 60, 100, 400, 750 and 1100 rpm respectively. The corresponding spectra of control group sample C_3N_4-M-Air are also presented.

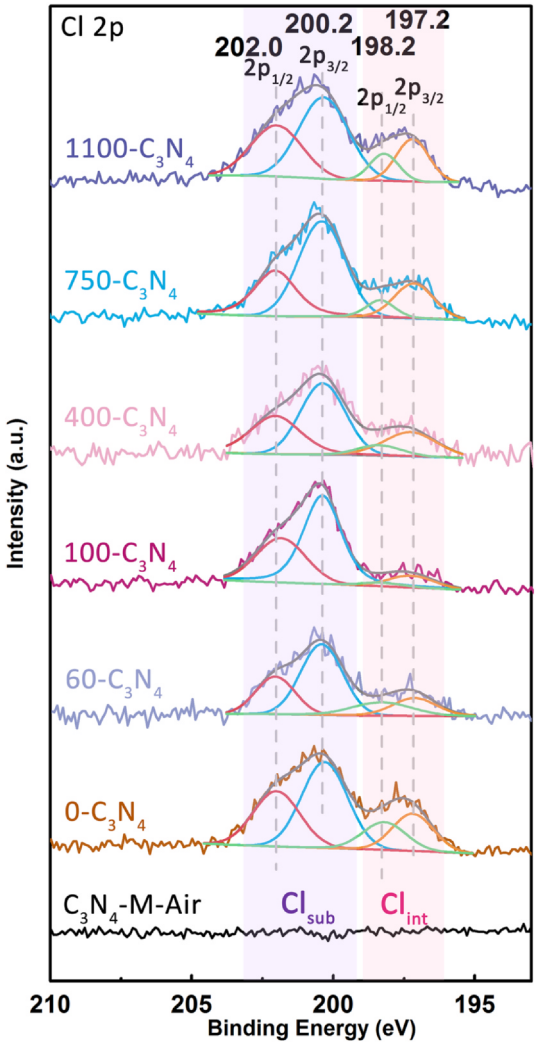

Fig. 4. The XPS Cl 2p spectra of Cl doped g-C_3N_4 prepared via solvothermal method with agitation rates of 0, 60, 100, 400, 750 and 1100 rpm, respectively. The corresponding spectra of control group sample C_3N_4-M-Air are also presented.

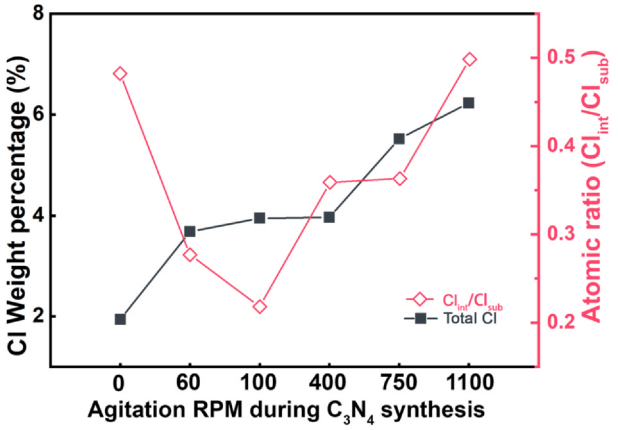

Fig. 5. The concentration of Cl dopants in the samples synthesised via the solvothermal method. And the effects of agitation on the atomic ratio of interstitial over substitutional Cl dopants.

analyses also provide a semi-quantitative understanding of the atomic ratios of Cl_{int} and Cl_{sub} dopants. Due to the same *RSF* and *ECF* for the Cl dopants at different sites, the atomic ratio of Cl_{int} and Cl_{sub} dopants (Cl_{int}/Cl_{sub}) can be directly determined by the comparison of corresponding $2p_{3/2}$ peak areas. As shown in Fig. 5, the calculated atomic Cl_{int}/Cl_{sub} ratios are 0.48, 0.28, 0.22, 0.35, 0.36 and 0.49 for the g-C_3N_4 synthesized with the agitation rates of 0, 60, 100, 400, 750, 1100 rpm, respectively. It is important to emphasise that the Cl_{int}/Cl_{sub} atomic ratio shows a reducing trend when the agitation rate increases from 0 to 100 rpm. However, the Cl_{int}/Cl_{sub} atomic ratio increases when the agitation rate further increases from 100 to 1100 rpm. This U-shape curve describing the correlation between Cl_{int}/Cl_{sub} atomic ratio and agitation rate can be explained by the different dependences of Cl_{int} and Cl_{sub} doping concentrations on agitation rates. In the case of Cl_{int}, the intensified agitation facilitates the Cl_{int} doping due to the enhanced mass transfer. In addition, the shearing force brought by agitation can help Cl^- diffuse into the interlayer site of g-C_3N_4. The similar phenomenon has been observed in other van der Waals crystals such as graphite [47,48], BN [49], MoS_2 [50], etc. Different from Cl_{int}, the correlation between agitation rate and Cl_{sub} concentration is more complicated. Comparing with lower agitation speed, the higher agitation rate can increase the condensation degree of g-C_3N_4 (as suggested by XRD patterns, Fig. 2(a)), which means the larger size of melon unit, more layers stacking and bigger particle size (also confirmed by BET-SSA (Fig. 6) and SEM analyses (Fig. 7)). Since the cyanuric chloride is used as the C, N sources during the polycondensation, it is likely to form Cl_{sub} dopant at the beginning of oligomer formation. In low-rate agitation condition, the Cl_{sub} doped oligomers are added to the edge of the melon unit, which causes the increase of Cl_{sub} concentration. However, at higher agitation rate, the significantly increased crystallisation degree of g-C_3N_4 (Fig. 2(a)) reduces the number of on-plane defects such as the Cl_{sub}. It is consistent with the negative correlation between C/N atomic ratio and agitation rates from 60 to 1100 rpm (Table 1). The explanations proposed here is only the most plausible one based on the observed experimental results. More careful works specifically focusing on this topic are needed to confirm and elucidate the explicit mechanism. In summary, the different agitation dependence of Cl_{int} and Cl_{sub} concentration is responsible for the unique U-shape correlation between the atomic ratio of Cl_{int}/Cl_{sub} and agitation rate.

3.2. The specific surface area (SSA) and surface morphology

The SSA of the g-C_3N_4 synthesised via the solvothermal method was characterised via the N_2 sorption experiments at 77 K. The corresponding isotherms are presented in Fig. 6. The SSAs calculated based on the Brunauer-Emmett-Teller (BET) theory are 12.4, 82.7, 64.7, 43.0, 37.8 and 16.3 $m^2\ g^{-1}$ for 0-C_3N_4, 60-C_3N_4, 100-C_3N_4, 400-C_3N_4, 750-C_3N_4 and 1100-C_3N_4 respectively. All the N_2 sorption isotherms exhibit the characteristic hysteresis of non-porous structure. It is noted that the BET-SSA shows no positive correlation with the concentration of Cl_{int} or total Cl dopants, which rules out the possibility that Cl^- is mainly adsorbed on the surface. The sample synthesised at a static solution without agitation, i.e. 0-C_3N_4, has the SSA of 12.4 $m^2\ g^{-1}$, which is similar to the reported data in the literature [25–27] and the control group C_3N_4-M-Air (14.9 $m^2\ g^{-1}$). It is needed to emphasize that the BET-SSA shows the agitation rate dependence too. When the agitation rate firstly increases to 60 rpm, the SSA of 60-C_3N_4 is enlarged to 82.7 $m^2\ g^{-1}$. However, when the agitation rate further increases, the corresponding SSA reduces accordingly.

The morphologies of the g-C_3N_4 prepared via solvothermal method were examined using SEM, and the corresponding images are shown in Fig. 7. The sample of C_3N_4-M-Air shows the particle sizes of several microns (Fig. 7(a, b)). Though the surface of the particle is relatively rough, the large particle size limits the SSA to be ~14.9 $m^2\ g^{-1}$. The 0-C_3N_4 synthesised in the static solvothermal condition shows the morphology of aggregated large spheres with the size of several microns (Fig. 7(d, e)) and BET-SSA of 12.4 $m^2\ g^{-1}$. When the agitation rate increases to 60 rpm, the size of 60-C_3N_4 primary particles reduce to ~ 200 nm, which further aggregates into sub-micron particles

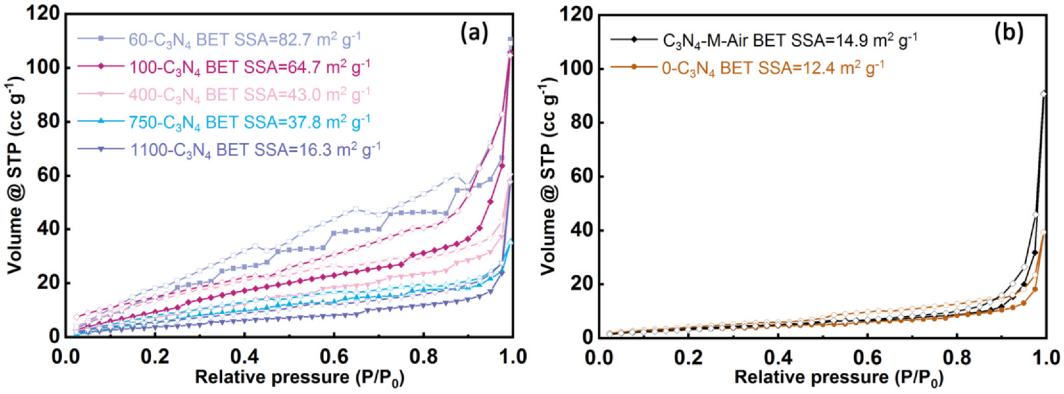

Fig. 6. The isotherms of the N_2 sorption at 77 K for (a) the g-C_3N_4 synthesised in the solvothermal method under different agitation rates and (b) 0-C_3N_4 and control group samples C_3N_4-M-Air.

(Fig. 7(g, h)). The smaller primary particle size of 60-C_3N_4 comparing with 0-C_3N_4 gives a significantly larger SSA of 82.7 m^2 g^{-1}. Further increasing the agitation rate to 400 rpm, the primary particle size starts to increase again, as shown by 400-C_3N_4, 750-C_3N_4 and 1100-C_3N_4 (Fig. 7(j–q)). From the SEM morphology analyses, it can be concluded that the changes in the g-C_3N_4 particle size are responsible for the evolution of SSA at different agitation rates. The EDS spectra were used to unravel the elemental information on all the samples. It can be seen that all the samples are mainly constituted by the C, N. Comparing with the C_3N_4-M-Air, the C_3N_4 synthesised via the solvothermal method all show the existence of Cl dopants.

It is noted that the correlation between SSA and agitation rate in this work is different from the conventional understanding that a more vigorous agitation leads to smaller particle size and larger SSA [51–54]. However, during the solvothermal synthesis of Cl doped g-C_3N_4 under agitation, the correlation between agitation rate and particle size is controlled by a combined effect of crystallisation and Cl_{int} doping. When no agitation is applied, the nucleation rate is slow, which results in large primary particle size (0-C_3N_4). In the case of 60-C_3N_4, the agitation in a relatively slow rate can significantly increase the nucleation rate [54], which results in the smaller primary particle size. At a more intensive agitation rate, the mass transfer is no longer the control factor. Therefore, the larger particle size can be explained by the enhanced crystal growth due to the intensified interparticle interaction [55] or suppressed homogeneous nucleation [56,57]. The rise of interstitial Cl doping inducing g-C_3N_4 interlayer bonding is another reason for the enlarged primary g-C_3N_4 particle size. When higher agitation speed applied, the Cl is inclined to dope at the interstitial sites, as indicated by the XPS analyses (Fig. 5). The higher concentration of Cl_{int} dopants will decrease the BET-SSA because the interstitial dopants can enhance interaction between the g-C_3N_4 layers, which promotes the formation of larger crystallites. This phenomenon can also be observed in many former researches focusing on the interstitially doped g-C_3N_4 [12,14,37,58–60].

3.3. The electronic structure analyses

The bandgap of the samples prepared via solvothermal method was determined via the UV-Vis DR spectroscopy method. As shown in Fig. 8(a), the optical absorption of all g-C_3N_4 show the typical spectra of the semiconductor. The Tauc plots derived from the UV-Vis DR spectra to determine the bandgap are presented in Fig. 8(b). It can be seen that the C_3N_4-M-Air shows much wider bandgap than the samples synthesised via the solvothermal method. Additionally, the samples synthesised in solvothermal method with different agitation rates exhibit similar values. To be specific, the 0-C_3N_4, 60-C_3N_4, 100-C_3N_4, 400-C_3N_4, 750-C_3N_4, 1100-C_3N_4 samples exhibit bandgap energy values of 1.82, 1.78, 1.78, 1.77, 1.82 and 1.87 eV, respectively. The bandgap value of 0-C_3N_4 is close the value reported in the previous work using the same g-C_3N_4 preparation recipe [26]. Comparatively, the control group sample C_3N_4-M-Air presents a bandgap of 2.65 eV, which is in agreement with previous studies in the literature [61,62]. The correlation between bandgap and agitation rate presents a U-shape curve, as displayed in Fig. 9. The mechanism underpins this phenomenon is that the Cl_{sub} shows higher bandgap narrowing capability than Cl_{sub}. It can be rationalised by the stronger electronic interaction, mid-gap state introduction and larger molecular structure distortion brought by Cl_{int}.

The valence band maximum (VBM) is another important parameter affecting the photocatalytic dye degradation performance, because the VBM determines the oxidation capability of photo-excited holes. To calculate the VBM, the XPS VB characterisation was conducted, and results are presented in Fig. 10. VBM binding energy calculated based on the XPS VB spectra are 2.43, 2.91, 3.01, 3.0, 2.82, 2.66 eV for 0-C_3N_4, 60-C_3N_4, 100-C_3N_4, 400-C_3N_4, 750-C_3N_4, 1100-C_3N_4, respectively. The VBM binding energy needs to be further converted to the chemical potential versus standard hydrogen electrode (SHE) using the following equation [38]:

$$\mathrm{VBM(vs.\ SHE)} = \Phi + E_{\mathrm{binding}} - 4.44 \quad (3)$$

where the E_{binding} represents the VBM binding energy achieved from the XPS VB spectra and Φ the work function of the XPS spectrometer (3.83 eV). The 4.44 eV is the potential difference between the SHE and vacuum. The converted VBM (vs. SHE) are calculated to be 1.82, 2.30, 2.40, 2.39, 2.21, 2.05 eV for 0-C_3N_4, 60-C_3N_4, 100-C_3N_4, 400-C_3N_4, 750-C_3N_4, 1100-C_3N_4, respectively. For comparison, the VBM of C_3N_4-M-Air is determined to be 1.64 eV. Combining the optical bandgap determined from the UV–Vis DR spectra (Fig. 8), the conduction band minimum (CBM) of the samples can be calculated by adding CBM and bandgap together. To illustrate the effects of Cl dopants distribution on the electronic structure of g-C_3N_4, the band alignment based on the calculated CBM and VBM is plotted as in Fig. 11. By comparing the electronic structures of samples presented in Fig. 11, it can be seen that all the samples synthesised via the solvothermal method show the lower VBM than the control group C_3N_4-M-Air. It suggests that the higher oxidation capability of the Cl doped g-C_3N_4 synthesised via the solvothermal method than the C_3N_4-M-Air synthesised via conventional thermal polycondensation method. More importantly, the agitation rate during the solvothermal synthesis shows significant influences on the VBM positions and a U-shape correlation is exhibited.

The U-shape correlation between agitation rate and VBM, CBM positions can be explained by the different influences of Cl_{int} and Cl_{sub} on the electronic structure of Cl-doped g-C_3N_4. It is derived from the different coordination environment of the Cl_{int} and Cl_{sub} in the molecule. The Cl_{int} interacts with all the surrounding N atoms in the melem unit (theoretically 6 N atoms) and the Cl_{sub} replacing one N atom forms the strong covalent bonds with 2 adjacent C atoms. On one hand, the

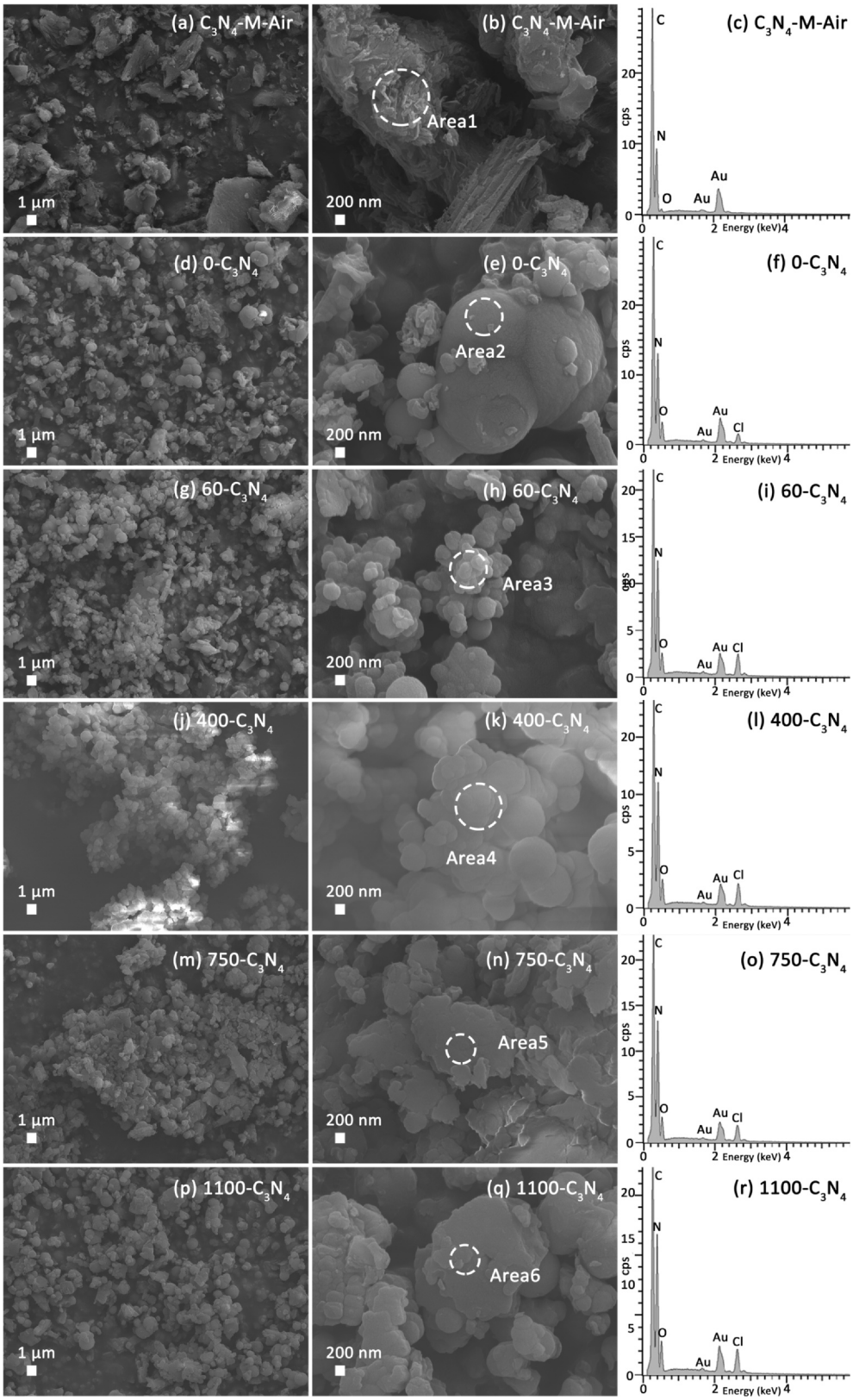

Fig. 7. The SEM images and corresponding EDS spectra of (a-c) C_3N_4-M-Air, (d-f) 0-C_3N_4, (g-i) 60-C_3N_4, (j-l) 400-C_3N_4, (m-o) 750-C_3N_4, (p-r) 1100-C_3N_4.

negatively charged Cl_{int} as the interstitial dopant brings extra electrons to the g-C_3N_4 molecules, which can significantly shift the Fermi energy level (E_F) to the negative direction in the band diagram (Fig. 11) [42,63]. On the other hand, the atomic Mulliken electronegativity (χ) of C, N and Cl is 8.58, 9.77 and 14.06 eV, respectively [64]. The higher electronegativity suggests the Cl_{sub} dopants can shift the VBM to positive direction as described via the approximation from the electronegativity [65–68]:

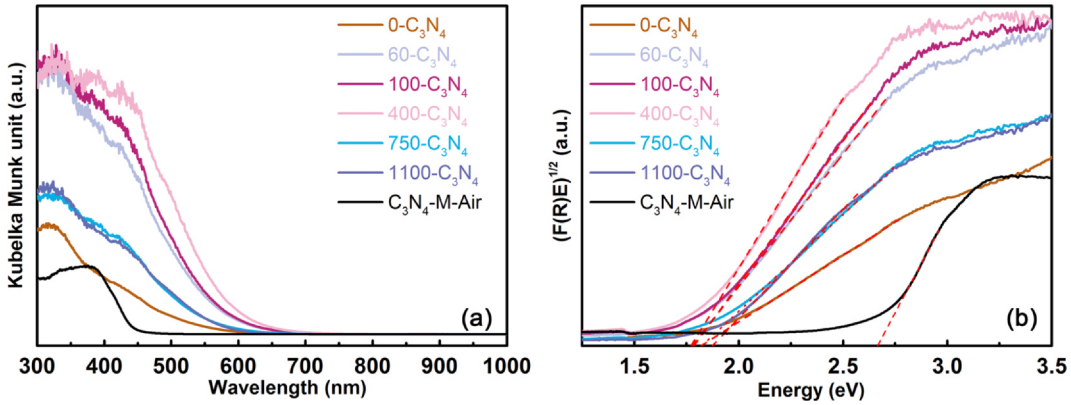

Fig. 8. (a) UV-Vis DRS spectroscopy and (b) Tauc plots of samples prepared via solvothermal method with different agitation rates: 0-C_3N_4, 60-C_3N_4, 100-C_3N_4, 400-C_3N_4, 750-C_3N_4, 1100-C_3N_4 and control group sample C_3N_4-M-Air.

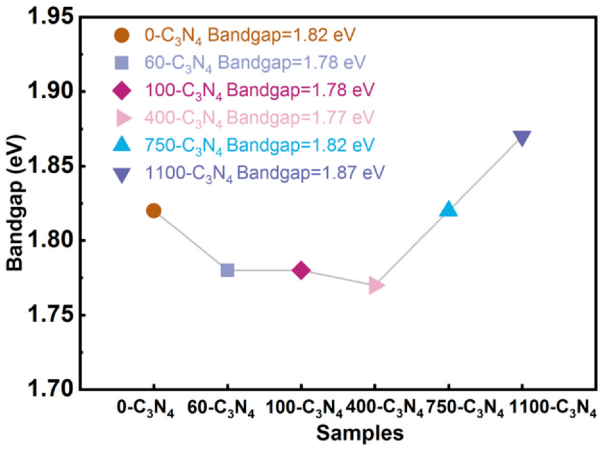

Fig. 9. The calculated bandgap energy of samples prepared via solvothermal method with different agitation rates: 0-C_3N_4, 60-C_3N_4, 100-C_3N_4, 400-C_3N_4, 750-C_3N_4, 1100-C_3N_4.

$$\mathrm{VBM} = -(\chi_A{}^a \chi_B{}^b)^{1/(a+b)} + \frac{1}{2}E_g + E_0 \quad (4)$$

where E_0 is the energy of free electrons on the hydrogen scale (~4.4 eV); E_g is the bandgap energy of the semiconductor; χ is the atomic Mulliken electronegativity in the compound A_aB_b. In summary, the Cl_{int} and Cl_{sub} shift the CBM/VBM to the opposite direction, and the experimentally determined electronic structures are the result of the balance between Cl_{int} and Cl_{sub} influences. As a result, the VBM, CBM positions also show the U-shape correlation with the agitation rate (shown in Fig. 11). It is in consistence with the U-shape correlation between Cl_{int}/Cl_{sub} ratio and agitation rate (Fig. 5).

3.4. Photoluminescence (PL) analyses

PL analyses are the methods to investigate the efficiency of photo-excited electron/hole radiative recombination. As shown in Fig. 12(a), the C_3N_4-M-Air synthesised via conventional thermal condensation method shows a significantly strong steady-state PL emission spectrum, which is at least two orders of magnitude larger than the g-C_3N_4 synthesised via the solvothermal method. It suggests the remarkable photo-excited electron/hole recombination in conventional g-C_3N_4, as already pointed out in the literature [24,69,70]. Different from the C_3N_4-M-Air, the g-C_3N_4 synthesised via the solvothermal method exhibits greatly reduced PL intensity due to Cl doping. The PL emission intensity decreases in the sequence of 0-C_3N_4 > 1100-C_3N_4 > 750-C_3N_4 > 60-C_3N_4, 100-C_3N_4 > 400-C_3N_4. From the PL intensity sequence, it can be seen that the reduction of PL intensity not only relates to the total amount of Cl dopants but also Cl doping sites dependent. As illustrated in Fig. 5, the total Cl doping concentration increases monotonically along with the agitation rate rise, while the heaviest total Cl doping

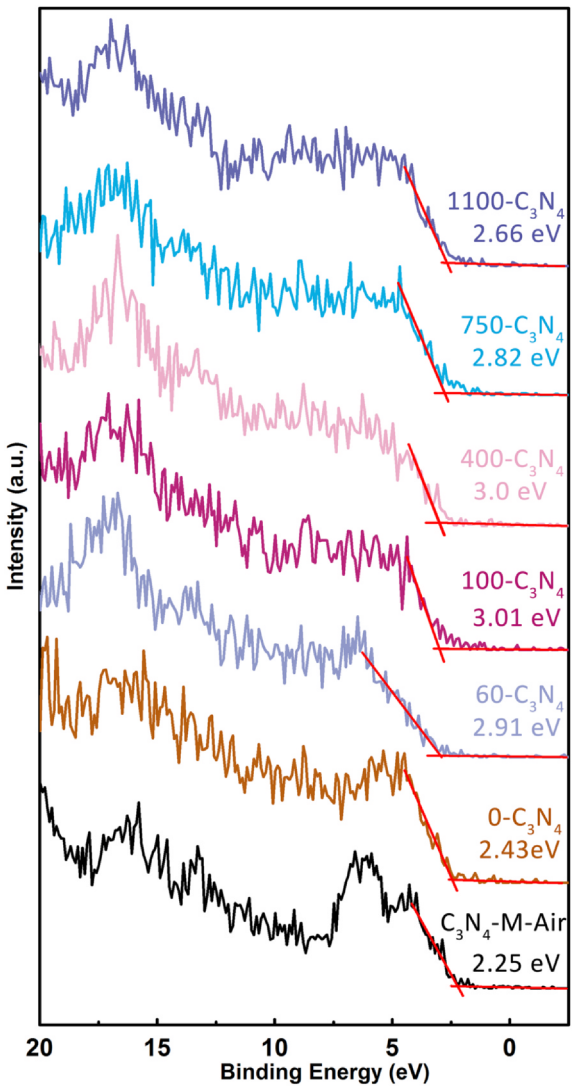

Fig. 10. The XPS valence band (VB) spectra of samples prepared via solvothermal method with different agitation rates: 0-C_3N_4, 60-C_3N_4, 100-C_3N_4, 400-C_3N_4, 750-C_3N_4, 1100-C_3N_4. The C_3N_4-M-Air as a control group is also presented.

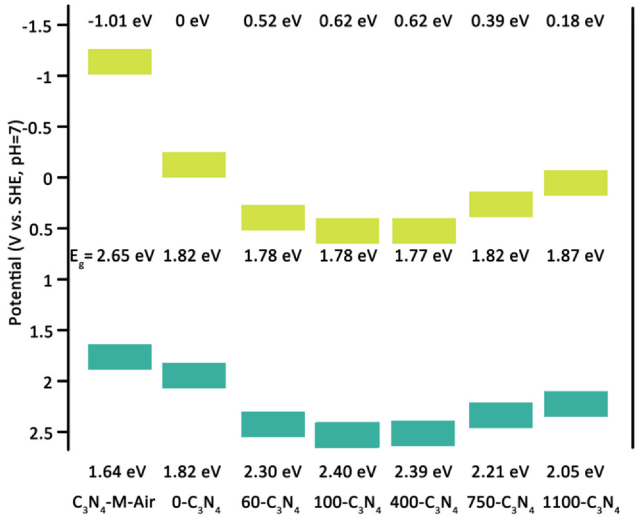

Fig. 11. Band alignment diagram of Cl-doped C_3N_4 prepared via solvothermal method with different agitation rates: 0-C_3N_4, 60-C_3N_4, 100-C_3N_4, 400-C_3N_4, 750-C_3N_4, 1100-C_3N_4. The C_3N_4-M-Air synthesised via the conventional thermal polycondensation in static air is presented for comparison.

doesn't guarantee the lowest PL intensity. To more explicitly unravel the roles of Cl at different doping sites in the photo-excited electron/hole separation, time-resolved PL spectroscopy experiments were conducted on the 4 most important samples: 0-C_3N_4, 60-C_3N_4, 1100-C_3N_4 and the benchmark C_3N_4-M-Air. As shown in Fig. 12(b), the average carrier lifetime of 0-C_3N_4, 60-C_3N_4, 1100-C_3N_4 and C_3N_4-M-Air are 0.39, 0.95, 1.15 and 0.86 ns, respectively. It is noted that the 1100-C_3N_4 with the highest concentration of Cl_{int} shows the longest average lifetime of photo-excited carriers. On the contrary, the 0-C_3N_4 with lowest Cl_{int} doping concentration exhibits the shortest average lifetime of photo-excited carriers. These results suggest the Cl_{int} dopants are mainly ascribed to the enhanced charge carrier separation by acting as the bridge for inter-layer charge transfer. The reduced steady-state PL intensities of solvothermally synthesised samples are attributed to the facilitated non-radiative recombination. It is also worth mentioning that the 60-C_3N_4 still shows longer carrier lifetime than C_3N_4-M-Air, which indicates the more efficient suppression of recombination of charge carriers.

3.5. Photocurrent measurements

Transient photocurrent experiments can elucidate the efficiency of electron/hole generation and transportation of catalysts under light irradiation. As shown in Fig. 13, all the g-C_3N_4 synthesised via the solvothermal method shows significantly larger transient photocurrent density than that of control group sample C_3N_4-M-Air (34.2nA cm^{-2}). The remarkable enhancement of the transient photocurrent density for the g-C_3N_4 synthesised via the solvothermal method can be mainly explained by the reduced bandgap attributed to Cl dopants (Fig. 8). The smaller bandgap can induce broader adsorption of incident light and produce larger photocurrent density. For Cl doped g-C_3N_4 synthesised

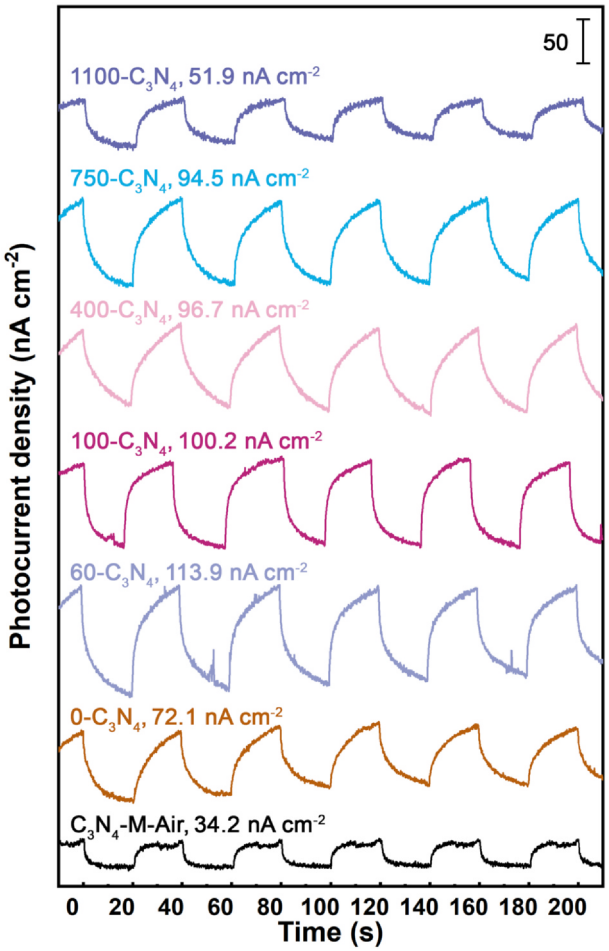

Fig. 13. Transient photocurrent responses of 0-C_3N_4, 60-C_3N_4, 100-C_3N_4, 400-C_3N_4, 750-C_3N_4, 1100-C_3N_4 and C_3N_4-M-Air as control group under visible light ($\lambda > 420$ nm) on-off irradiation condition.

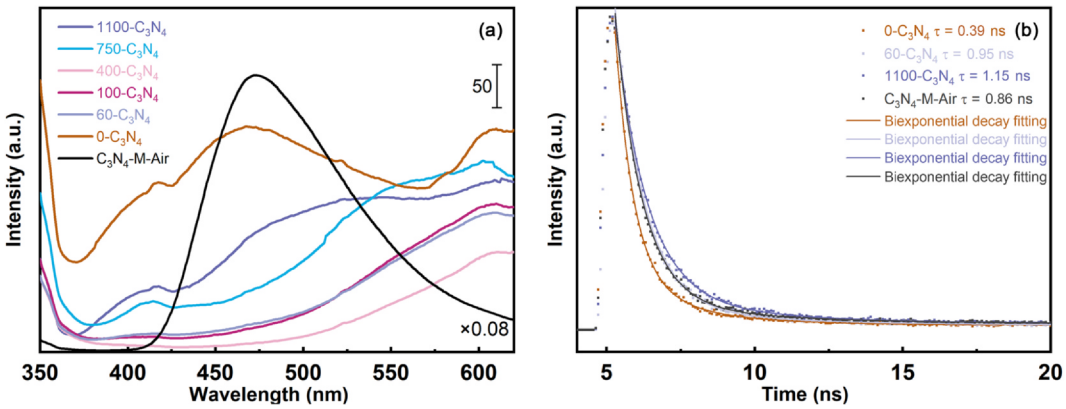

Fig. 12. (a) Steady-state photoluminescence (PL) spectra of 0-C_3N_4, 60-C_3N_4, 100-C_3N_4, 400-C_3N_4, 750-C_3N_4, 1100-C_3N_4 and C_3N_4-M-Air as control group under 325 nm UV light excitation. The intensity of C_3N_4-M-Air PL spectrum is multiplied by 0.08 to improve legibility. (b) Time-resolved PL spectra of 0-C_3N_4, 60-C_3N_4, 1100-C_3N_4 and C_3N_4-M-Air.

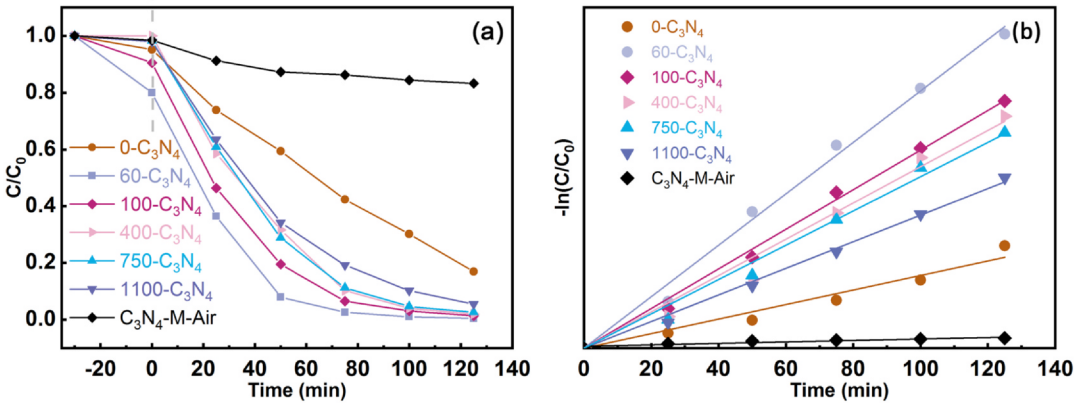

Fig. 14. (a) The photocatalytic RhB degradation performance under visible light irradiation (λ ≥ 420 nm) and (b) the corresponding pseudo-first-order kinetics plot of 0-C_3N_4, 60-C_3N_4, 100-C_3N_4, 400-C_3N_4, 750-C_3N_4, 1100-C_3N_4 and control group sample C_3N_4-M-Air.

via solvothermal method, the transient photocurrent densities under visible light (λ > 420 nm) irradiation for 0-C_3N_4, 60-C_3N_4, 100-C_3N_4, 400-C_3N_4, 750 C_3N_4 and 1100-C_3N_4 are 72.1, 113.9, 100.2, 96.7 and 94.5nA cm^{-2}, respectively. The 60-C_3N_4 exhibits the highest transient photocurrent density suggesting its more robust photocatalytic activity. It is noticed that the reduced bandgap is not sufficient to explain the dependence of transient photocurrent density on agitation rate since the bandgaps are very similar for all these 6 samples (Fig. 11). The higher photocurrent density can only be attributed to the suppressed electron/hole recombination and enlarged SSA (Fig. 6 and Fig. 12).

3.6. The photocatalytic activity of RhB degradation

The photocatalytic activities of the Cl-doped g-C_3N_4 samples were characterised via the probe reaction, visible-light-driven photocatalytic RhB degradation, to unravel the effects of Cl doping and agitation on photocatalytic activity. The control group sample of C_3N_4-M-Air prepared via conventional thermal polycondensation in static air is also tested in the identical condition for comparison. Fig. 14(a) presents the RhB concentration evolution during the photocatalytic reaction. At the first 25 min, the solution with catalysts was kept in the dark under the stirring condition to demonstrate the adsorption capabilities of the samples. The 60-C_3N_4 and 100-C_3N_4 show good RhB adsorption ability that reduce the RhB concentration (C) to 80.0% and 90.5% of the original concentration (C_0). The rest samples only reduce C by less than 5%. This result is in consistence with the BET-SSA results characterised via the N_2 sorption experiments (Fig. 6). After 25 min of RhB adsorption in the dark, the catalysts were further exposed to the visible light provided by a Xenon lamp with 420 nm cut-off filter. After 125 min of photocatalytic reaction, the 0-C_3N_4, 60-C_3N_4, 100-C_3N_4, 400-C_3N_4, 750-C_3N_4, 1100-C_3N_4 can degrade 82.23%, 99.60%, 98.60%, 98.00%, 97.41%, 94.38% of RhB after adsorption respectively. By comparison, the C_3N_4-M-Air only decomposes 16.75% of the RhB after the same 125 min photocatalytic degradation. It can be seen that all the samples prepared via the solvothermal method show the superior photocatalytic RhB degradation performance than the C_3N_4-M-Air. It demonstrates the advantages of the solvothermal g-C_3N_4 preparation method. In addition, the photocatalytic activities of Cl-doped g-C_3N_4 synthesised via solvothermal method are largely affected by the agitation condition. To further compare the photocatalytic RhB degradation performances of the Cl doped g-C_3N_4 synthesised via solvothermal method, the corresponding kinetic curves are plotted in Fig. 14(b). All the data can appropriately fit with the pseudo-first-order kinetic model, which is described by the following equation:

$$\ln\left(\frac{C_0}{C}\right) = kt \quad (5)$$

where the C and C_0 are the initial and current concentration of RhB solution after adsorption in dark, respectively; the k represents the apparent reaction rate constant; the t is the reaction time. Based on the linear fitting of the data in Fig. 14(b), the k is determined to be 12.2, 43.4, 33.4, 30.6, 28.9, 22.5 (10^{-3} min^{-1}) for 0-C_3N_4, 60-C_3N_4, 100-C_3N_4, 400-C_3N_4, 750-C_3N_4, 1100-C_3N_4, respectively. By comparison, the C_3N_4-M-Air shows a much smaller k value of 1.24 (10^{-3} min^{-1}). The kinetic parameters derived from fitting are summarised in Table 2. The 60-C_3N_4 exhibits the highest photocatalytic RhB degradation performance. To further prove the advantage of prepared Cl-doped g-C_3N_4 with balanced Cl_{int}/Cl_{sub}, the optimal 60-C_3N_4 is compared with the reported g-C_3N_4 photocatalysts in recent literature on the RhB photodegradation performance (Table 3). It can be seen from Table 3 that the 60-C_3N_4 not only outperforms the recently reported single-phase heteroatom doped g-C_3N_4 but also shows superior performance to the state-of-the-art heterostructures constituted by g-C_3N_4.

3.7. Mechanism underpins photocatalytic activity enhancement

The sequence of photocatalytic activity is in high consistency with the transient photocurrent density experiments (Fig. 13), which indicates the high photocatalytic activity is derived from the efficient generation and transportation of charge carriers under light excitation. Moreover, it can be seen that the photocatalytic activity associates with the atomic ratio of Cl_{int}/Cl_{sub} with a negative correlation. As shown in Fig. 5, the Cl_{int}/Cl_{sub} values shows a U-shape correlation with agitation rate. The 60-C_3N_4 and 100-C_3N_4 with the lowest Cl_{int}/Cl_{sub} values (the bottom of the U-shape curve) show the highest photocatalytic activity. On the contrary, the 0-C_3N_4 and 1100-C_3N_4 with the highest Cl_{int}/Cl_{sub} values (the two ends of the U-shape curve) exhibit the lowest photocatalytic activity. The atomic ratio of Cl_{int}/Cl_{sub} is emphasised as a descriptor here, because Cl_{int} and Cl_{sub} function differently or even oppositely on influencing the properties of g-C_3N_4. The enhanced photocatalytic activity can be attributed to 3 reasons: (i) enlarged SSA (Fig. 6), (ii) higher oxidation capability brought by the positively

Table 2
The summary of photocatalytic RhB degradation performance under visible light (λ ≥ 420 nm).

Photocatalyst	Rate constant k (min^{-1}) (10^{-3})	R^2	SSA (m^2 g^{-1})
C_3N_4-M-Air	1.24	0.9381	14.9
0-C_3N_4	12.2	0.9847	12.3
60-C_3N_4	43.4	0.9976	82.7
100-C_3N_4	33.4	0.9983	64.7
400-C_3N_4	30.6	0.9929	43.0
750-C_3N_4	28.9	0.9955	37.8
1100-C_3N_4	22.5	0.9983	16.3

Table 3
Comparison of g-C_3N_4 prepared in this work with the reported catalysts in recent literature.

Photocatalysts	RhB solution concentration	Catalyst dose (catalyst/solution)	Light source	Reaction rate constants (10^{-3} min^{-1})	Removal/Time	Ref.
60-C_3N_4	10 ppm	12 mg/60 mL (0.2 g L^{-1})	300 W Xe lamp ($\lambda \geq 420$ nm)	43.4	90.3%/50 min 97.4%/75 min 99.6%/125 min	this work
C/Ce co-doped g-C_3N_4	5 ppm	50 mg/100 mL	300 W Xe lamp, ($\lambda \geq 420$ nm)	24.96	90.1%/60 min	[4]
Fe doped g-C_3N_4	50 ppm	60 mg/30 mL	500 W Xe lamp, ($\lambda \geq 420$ nm)	37.8	~97%/100 min	[71]
P doped g-C_3N_4	10 ppm	0.5 g L^{-1}	300 W Xe lamp ($\lambda \geq 400$ nm)	15.8	~62.1/60 min	[72]
P doped g-C_3N_4/g-C_3N_4	10 ppm	0.5 g L^{-1}	300 W Xe lamp ($\lambda \geq 400$ nm)	43.9	89.7%/60 min	[72]
PCN-222/g-C_3N_4	20 ppm	100 mg/100 mL	300 W Xe lamp ($\lambda \geq 400$ nm)	28.27	97.9%/120 min	[5]
ultrathin BiOCl/g-C_3N_4	10 ppm	30 mg/30 mL	300 W Xe lamp ($\lambda \geq 420$ nm)	41.0	95.93%/80 min	[73]
$Bi_{12}TiO_{20}$/g-C_3N_4	10 ppm	200 mg/80 mL	500 W Xe lamp ($\lambda \geq 420$ nm)	53.8	97%/50 min	[74]
$SrZnTiO_3$/g-C_3N_4	5 ppm	20 mg/200 mL	500 W Xe lamp ($\lambda \geq 420$ nm)	8.27	82.2%/180 min	[75]
TiO_2/C/$BiVO_4$	10 ppm	60 mg/60 mL	500 W Xe Lamp ($\lambda \geq 420$ nm)	13.7	93.3%/125 min	[76]
Ag/g-C_3N_4/$NaTaO_3$	20 ppm	1 g L^{-1}	300 W Xe lamp ($\lambda \geq 420$ nm)	n/a	~85.5%/60 min	[77]
g-heptazine-C_3N_4/triazine-g-C_3N_4	10 ppm	30 mg/200 mL	300 W Xe lamp ($\lambda \geq 400$ nm)	17.7	93.3%/150 min	[78]
graphene quantum dots/mpg-C_3N_4	10 ppm	25 mg/50 mL	300 W Xe lamp ($\lambda \geq 400$ nm)	n/a	97%/120 min	[79]
WO_3/Ag/g-C_3N_4	10 ppm	100 mg/300 mL	500 W Xe lamp ($\lambda \geq 400$ nm)	53	96.2%/40 min	[80]

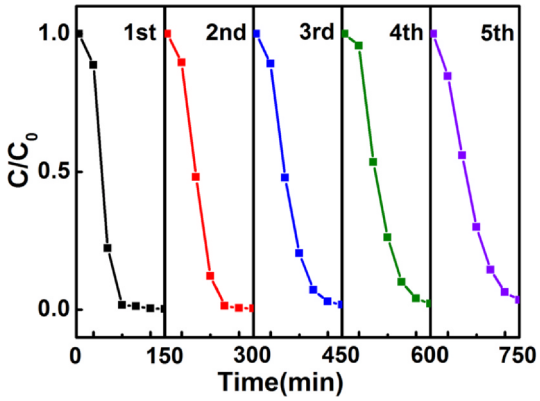

Fig. 15. Photocatalytic degradation of RhB performances for recycled 60-C_3N_4 under visible light irradiation ($\lambda > 420$ nm).

shifted VBM (Fig. 11) and (iii) suppressed photo-excited electron-hole recombination (Fig. 12). As a summary of the previous sections, Cl_{int} results in the smaller SSA, lower oxidation capability but suppressed electron-hole recombination; in contrast, the Cl_{sub} corresponds to the larger SSA, higher oxidation capability, while shows insignificant effects on recombination. The different roles of Cl_{int} and Cl_{sub} rationalise the importance of balancing the Cl_{int} and Cl_{sub} doping in optimising the photocatalytic pollutants degradation performance of g-C_3N_4.

3.8. Recycling tests

The stability of the prepared catalysts is an important criterion for performance evaluation. The optimal 60-C_3N_4 catalyst was chosen to perform the recycling experiments. The fresh 60-C_3N_4 was firstly conducted a photocatalytic RhB degradation and recycled from the solution via centrifuging. After rinsing with DI-water for 10 times and drying under vacuum, the recycled 60-C_3N_4 was used to conduct another photocatalytic RhB degradation experiment following the same procedure. The photocatalytic RhB degradation performances of the 5 recycling experiments are presented in Fig. 15. It can be seen that the 60-C_3N_4 shows no apparent deactivation after 5 successive photocatalytic degradations. The RhB can be completely photocatalytically degraded within 125 min in all 5 recycling runs. The morphologies of 60-C_3N_4 before and after the 5-round recycling experiment were characterised with SEM; the corresponding images are shown in Figure S1 in the supporting information. It can be seen that the morphology and crystal size are not changed after the stability test. These results indicate that the Cl doped g-C_3N_4 synthesised via the solvothermal method exhibit good stability in working condition.

4. Conclusion

In this work, Cl doped g-C_3N_4 is synthesised for the first time via an agitation-assisted solvothermal method and the atomic ratio of Cl_{int}/Cl_{sub} dopants is controlled by the agitation rate. The significantly improved RhB photodegradation performance of Cl doped g-C_3N_4 is attributed to the larger SSA, stronger photo-oxidation capability and suppressed electron/hole recombination. A U-shape relation is found between agitation rate and molecular/electronic structure of prepared g-C_3N_4. The mechanism underpins this phenomenon is that the Cl_{sub} and Cl_{int} function differently and even oppositely on influencing the molecular/electronic structure of g-C_3N_4, which determines the photocatalytic activity. To be specific, the Cl_{int} dopants between the g-C_3N_4 layers can prolong the lifetime of the charge carriers but result in the smaller SSA and lower photo-oxidation capability. By contrast, the in-plane Cl_{sub} dopants can enhance the photo-oxidation capability, while only exhibit insignificant influence on charge separation efficiency. The optimal photocatalytic dye-degradation performance can only be

achieved by balancing the Cl_{int}/Cl_{sub} ratios and synthesising under a moderate agitation rate.

CRediT authorship contribution statement

Mengyu Cao: Conceptualization, Investigation, Formal analysis, Writing - original draft. **Ke Wang:** Conceptualization, Formal analysis, Methodology, Writing - review & editing. **Ignacio Tudela:** Resources, Writing - review & editing. **Xianfeng Fan:** Conceptualization, Funding acquisition, Project administration, Supervision, Writing - review & editing.

Declaration of Competing Interest

The authors declare that they have no known competing financial interests or personal relationships that could have appeared to influence the work reported in this paper.

Acknowledgements

K.W. thanks the research scholarship from the School of Engineering, the University of Edinburgh.

Appendix A. Supplementary material

Supplementary data to this article can be found online at https://doi.org/10.1016/j.apsusc.2020.147784.

References

[1] A. Kumar, S. Kumar, A. Bahuguna, A. Kumar, V. Sharma, V. Krishnan, Recyclable, bifunctional composites of perovskite type N-CaTiO3 and reduced graphene oxide as an efficient adsorptive photocatalyst for environmental remediation, Mater. Chem. Front. 1 (2017) 2391–2404, https://doi.org/10.1039/c7qm00362e.
[2] X. Wang, K. Maeda, A. Thomas, K. Takanabe, G. Xin, J.M. Carlsson, K. Domen, M. Antonietti, A metal-free polymeric photocatalyst for hydrogen production from water under visible light, Nat. Mater. 8 (2009) 76–80, https://doi.org/10.1038/nmat2317.
[3] L. Lin, Z. Yu, X. Wang, Crystalline Carbon Nitride Semiconductors for Photocatalytic Water Splitting, Angew. Chem. Int. Ed. 58 (2019) 6164–6175, https://doi.org/10.1002/anie.201809897.
[4] K. Wu, D. Chen, S. Lu, J. Fang, X. Zhu, F. Yang, T. Pan, Z. Fang, Supramolecular self-assembly synthesis of noble-metal-free (C, Ce) co-doped g-C3N4 with porous structure for highly efficient photocatalytic degradation of organic pollutants, J. Hazard. Mater. 382 (2020) 121027, , https://doi.org/10.1016/j.jhazmat.2019.121027.
[5] H. Jia, D. Ma, S. Zhong, L. Li, L. Li, L. Xu, B. Li, Boosting photocatalytic activity under visible-light by creation of PCN-222/g-C3N4 heterojunctions, Chem. Eng. J. 368 (2019) 165–174, https://doi.org/10.1016/j.cej.2019.02.147.
[6] G. Algara-Siller, N. Severin, S.Y. Chong, T. Bjorkman, R.G. Palgrave, A. Laybourn, M. Antonietti, Y.Z. Khimyak, A.V. Krasheninnikov, J.P. Rabe, U. Kaiser, A.I. Cooper, A. Thomas, M.J. Bojdys, Triazine-based graphitic carbon nitride: a two-dimensional semiconductor, Angew. Chem. Int. Ed. 53 (2014) 7450–7455, https://doi.org/10.1002/anie.201402191.
[7] Y. Wang, X. Wang, M. Antonietti, Polymeric Graphitic Carbon Nitride as a Heterogeneous Organocatalyst: From Photochemistry to Multipurpose Catalysis to Sustainable Chemistry, Angew. Chem. Int. Ed. 51 (2012) 68–89, https://doi.org/10.1002/anie.201101182.
[8] R. Zhang, T. Ran, Y. Cao, L. Ye, F. Dong, Q. Zhang, L. Yuan, Y. Zhou, Oxygen activation of noble-metal-free g-C_3N_4/α-$Ni(OH)_2$ to control the toxic byproduct of photocatalytic nitric oxide removal, Chem. Eng. J. 382 (2020), https://doi.org/10.1016/j.cej.2019.123029.
[9] P. Yang, H. Zhuzhang, R. Wang, W. Lin, X. Wang, Carbon Vacancies in a Melon Polymeric Matrix Promote Photocatalytic Carbon Dioxide Conversion, Angew. Chem. Int. Ed. 58 (2019) 1134–1137, https://doi.org/10.1002/anie.201810648.
[10] K. Wang, Q. Li, B. Liu, B. Cheng, W. Ho, J. Yu, Sulfur-doped g-C3N4 with enhanced photocatalytic CO2-reduction performance, Appl. Catal. B 176-177 (2015) 44–52, https://doi.org/10.1016/j.apcatb.2015.03.045.
[11] Y. Wang, S. Zhao, Y. Zhang, J. Fang, Y. Zhou, S. Yuan, C. Zhang, W. Chen, One-pot Synthesis of K-doped g-C_3N_4 Nanosheets With Enhanced Photocatalytic Hydrogen Production Under Visible-Light Irradiation, Appl. Surf. Sci. 440 (2018) 258–265, https://doi.org/10.1016/j.apsusc.2018.01.091.
[12] K. Wang, J.L. Fu, Y. Zheng, Insights into Photocatalytic CO2 Reduction on C3N4: Strategy of Simultaneous B, K co-Doping and Enhancement by N Vacancies, Appl. Catal. B 254 (2019) 270–282, https://doi.org/10.1016/j.apcatb.2019.05.002.
[13] D. Masih, Y. Ma, S. Rohani, Graphitic C_3N_4 Based Noble-Metal-Free Photocatalyst Systems: A Review, Appl. Catal. B 206 (2017) 556–588, https://doi.org/10.1016/j.apcatb.2017.01.061.
[14] T. Xiong, W. Cen, Y. Zhang, F. Dong, Bridging the g-C_3N_4 Interlayers for Enhanced Photocatalysis, ACS Catal. 6 (2016) 2462–2472, https://doi.org/10.1021/acscatal.5b02922.
[15] J.-Y. Tang, W.-G. Zhou, R.-T. Guo, C.-Y. Huang, W.-G. Pan, Enhancement of Photocatalytic Performance In CO_2 Reduction over Mg/g-C_3N_4 Catalysts Under Visible Light Irradiation, Catal. Commun. 107 (2018) 92–95, https://doi.org/10.1016/j.catcom.2018.01.006.
[16] S. Hu, X. Chen, Q. Li, F. Li, Z. Fan, H. Wang, Y. Wang, B. Zheng, G. Wu, Fe3 + doping promoted N2 photofixation ability of honeycombed graphitic carbon nitride: The experimental and density functional theory simulation analysis, Appl. Catal. B 201 (2017) 58–69, https://doi.org/10.1016/j.apcatb.2016.08.002.
[17] S. Hu, X. Qu, J. Bai, P. Li, Q. Li, F. Wang, L. Song, Effect of Cu(I)–N Active Sites on the N2 Photofixation Ability over Flowerlike Copper-Doped g-C3N4 Prepared via a Novel Molten Salt-Assisted Microwave Process: The Experimental and Density Functional Theory Simulation Analysis, ACS Sustain. Chem. Eng. 5 (2017) 6863–6872, https://doi.org/10.1021/acssuschemeng.7b01089.
[18] S. Hu, X. Qu, P. Li, F. Wang, Q. Li, L. Song, Y. Zhao, X. Kang, Photocatalytic oxygen reduction to hydrogen peroxide over copper doped graphitic carbon nitride hollow microsphere: The effect of Cu(I)-N active sites, Chem. Eng. J. 334 (2018) 410–418, https://doi.org/10.1016/j.cej.2017.10.016.
[19] C. Liu, Y. Zhang, F. Dong, A.H. Reshak, L. Ye, N. Pinna, C. Zeng, T. Zhang, H. Huang, Chlorine Intercalation in Graphitic Carbon Nitride for Efficient Photocatalysis, Appl. Catal. B 203 (2017) 465–474, https://doi.org/10.1016/j.apcatb.2016.10.002.
[20] F. Yi, H. Gan, H. Jin, W. Zhao, K. Zhang, H. Jin, H. Zhang, Y. Qian, J. Ma, Sulfur- and chlorine-co-doped g-C3N4 nanosheets with enhanced active species generation for boosting visible-light photodegradation activity, Sep. Purif. Technol. 233 (2020), https://doi.org/10.1016/j.seppur.2019.115997.
[21] X.D. Sun, Y.Y. Li, J. Zhou, C.H. Ma, Y. Wang, J.H. Zhu, Facile Synthesis of High Photocatalytic Active Porous g-C_3N_4 with $ZnCl_2$ Template, J. Colloid Interf. Sci. 451 (2015) 108–116, https://doi.org/10.1016/j.jcis.2015.03.059.
[22] J. Liu, W. Fang, Z. Wei, Z. Qin, Z. Jiang, W. Shangguan, Efficient photocatalytic hydrogen evolution on N-deficient g-C3N4 achieved by a molten salt post-treatment approach, Appl. Catal. B 238 (2018) 465–470, https://doi.org/10.1016/j.apcatb.2018.07.021.
[23] J. Gao, Y. Wang, S. Zhou, W. Lin, Y. Kong, A Facile One-Step Synthesis of Fe-doped g-C_3N_4 Nanosheets and Their Improved Visible-Light Photocatalytic Performance, ChemCatChem 9 (2017) 1708–1715, https://doi.org/10.1002/cctc.201700492.
[24] X. Wu, D. Gao, P. Wang, H. Yu, J. Yu, NH4Cl-induced low-temperature formation of nitrogen-rich g-C3N4 nanosheets with improved photocatalytic hydrogen evolution, Carbon 153 (2019) 757–766, https://doi.org/10.1016/j.carbon.2019.07.083.
[25] Q. Gu, Y. Liao, L. Yin, J. Long, X. Wang, C. Xue, Template-Free Synthesis of Porous Graphitic Carbon Nitride Microspheres for Enhanced Photocatalytic Hydrogen Generation With High Stability, Appl. Catal. B 165 (2015) 503–510, https://doi.org/10.1016/j.apcatb.2014.10.045.
[26] Y. Cui, Z. Ding, X. Fu, X. Wang, Construction of Conjugated Carbon Nitride Nanoarchitectures in Solution at Low Temperatures for Photoredox Catalysis, Angew. Chem. Int. Ed. 51 (2012) 11814–11818, https://doi.org/10.1002/anie.201206534.
[27] Y. Cui, Y. Tang, X. Wang, Template-Free Synthesis of Graphitic Carbon Nitride Hollow Spheres for Photocatalytic Degradation of Organic Pollutants, Mater. Lett. 161 (2015) 197–200, https://doi.org/10.1016/j.matlet.2015.08.106.
[28] H. Montigaud, B. Tanguy, G. Demazeau, I. Alves, S. Courjault, C_3N_4: Dream or Reality? Solvothermal Synthesis as Macroscopic Samples of the C_3N_4 Graphitic Form, J. Mater. Sci. 35 (2000) 2547–2552, https://doi.org/10.1023/a:1004798509417.
[29] C. Hu, Y. Chu, M. Wang, X. Wu, Rapid Synthesis of g-C_3N_4 Spheres Using Microwave-Assisted Solvothermal Method for Enhanced Photocatalytic Activity, J. Photochem. Photobiol. A 348 (2017) 8–17, https://doi.org/10.1016/j.jphotochem.2017.08.006.
[30] L. Wang, M. Yu, C. Wu, N. Deng, C. Wang, X. Yao, Synthesis of Ag/g-C_3N_4 Composite as Highly Efficient Visible-Light Photocatalyst for Oxidative Amidation of Aromatic Aldehydes, Adv. Synth. Catal. 358 (2016) 2631–2641, https://doi.org/10.1002/adsc.201600138.
[31] Y. Wang, H. Wang, F. Chen, F. Cao, X. Zhao, S. Meng, Y. Cui, Facile Synthesis of Oxygen Doped Carbon Nitride Hollow Microsphere for Photocatalysis, Appl. Catal. B 206 (2017) 417–425, https://doi.org/10.1016/j.apcatb.2017.01.041.
[32] X. Li, Y. Yuan, X. Pan, L. Zhang, J. Gong, Boosted Photoelectrochemical Immunosensing of Metronidazole in Tablet Using Coral-Like g-C_3N_4 Nanoarchitectures, Biosens. Bioelectron. 123 (2019) 7–13, https://doi.org/10.1016/j.bios.2018.09.084.
[33] Q. Gu, Z. Gao, C. Xue, Self-Sensitized Carbon Nitride Microspheres for Long-Lasting Visible-Light-Driven Hydrogen Generation, Small 12 (2016) 3543–3549, https://doi.org/10.1002/smll.201600181.
[34] L. Lin, H. Ou, Y. Zhang, X. Wang, Tri-s-triazine-Based Crystalline Graphitic Carbon Nitrides for Highly Efficient Hydrogen Evolution Photocatalysis, ACS Catal. 6 (2016) 3921–3931, https://doi.org/10.1021/acscatal.6b00922.
[35] I. Papailias, T. Giannakopoulou, N. Todorova, D. Demotikali, T. Vaimakis, C. Trapalis, Effect of Processing Temperature on Structure and Photocatalytic Properties of g-C_3N_4, Appl. Surf. Sci. 358 (2015) 278–286, https://doi.org/10.1016/j.apsusc.2015.08.097.
[36] Z. Hong, B. Shen, Y. Chen, B. Lin, B. Gao, Enhancement of photocatalytic H_2 evolution over nitrogen-deficient graphitic carbon nitride, J. Mater. Chem. A 1 (2013) 11754–11761, https://doi.org/10.1039/c3ta12332d.

[37] Z.-A. Lan, G. Zhang, X. Wang, A facile synthesis of Br-modified g-C3N4 semiconductors for photoredox water splitting, Appl. Catal. B 192 (2016) 116–125, https://doi.org/10.1016/j.apcatb.2016.03.062.

[38] H. Yu, R. Shi, Y. Zhao, T. Bian, Y. Zhao, C. Zhou, G.I.N. Waterhouse, L.Z. Wu, C.H. Tung, T. Zhang, Alkali-Assisted Synthesis of Nitrogen Deficient Graphitic Carbon Nitride with Tunable Band Structures for Efficient Visible-Light-Driven Hydrogen Evolution, Adv. Mater. 29 (2017) 1605148, https://doi.org/10.1002/adma.201605148.

[39] Q. Tay, P. Kanhere, C.F. Ng, S. Chen, S. Chakraborty, A.C.H. Huan, T.C. Sum, R. Ahuja, Z. Chen, Defect Engineered g-C_3N_4 for Efficient Visible Light Photocatalytic Hydrogen Production, Chem. Mater. 27 (2015) 4930–4933, https://doi.org/10.1021/acs.chemmater.5b02344.

[40] C. Ye, J. Li, Z. Li, X. Li, X. Fan, L. Zhang, B. Chen, C. Tung, L. Wu, Enhanced Driving Force and Charge Separation Efficiency of Protonated g-C_3N_4 for Photocatalytic O_2 Evolution, ACS Catal. 5 (2015) 6973–6979, https://doi.org/10.1021/acscatal.5b02185.

[41] J. Duan, S. Chen, M. Jaroniec, S.Z. Qiao, Porous C3N4 nanolayers@N-graphene films as catalyst electrodes for highly efficient hydrogen evolution, ACS Nano 9 (2015) 931–940, https://doi.org/10.1021/nn506701x.

[42] B. Zhu, J. Zhang, C. Jiang, B. Cheng, J. Yu, First Principle Investigation of Halogen-Doped Monolayer g-C_3N_4 Photocatalyst, Appl. Catal. B 207 (2017) 27–34, https://doi.org/10.1016/j.apcatb.2017.02.020.

[43] X. Zhang, A. Hsu, H. Wang, Y. Song, J. Kong, M.S. Dresselhaus, T. Palacios, Impact of Chlorine Functionalization on High-Mobility Chemical Vapor Deposition Grown Graphene, ACS Nano 7 (2013) 7262–7270, https://doi.org/10.1021/nn4026756.

[44] L. Fan, H. Zhang, P. Zhang, X. Sun, One-Step Synthesis of Chlorinated Graphene by Plasma Enhanced Chemical Vapor Deposition, Appl. Surf. Sci. 347 (2015) 632–635, https://doi.org/10.1016/j.apsusc.2015.04.147.

[45] E.W. Kauffman, XPS and Carbon-13 NMR Spectroscopic Analysis of Composite Rocket Propellants, Virginia Polytechnic, Institute and State University, 1983.

[46] L. Liang, Y. Cong, L. Yao, F. Wang, L. Shi, One Step to Prepare Cl Doped Porous Defect Modified g-C_3N_4 With Improved Visible-Light Photocatalytic Performance for H_2 Production and Rhodamine B Degradation, Mater. Res. Express 5 (2018), https://doi.org/10.1088/2053-1591/aade38.

[47] Q. Xu, W. Zhao, J. Zhi, J. Yin, Exfoliation of Graphite in CO_2 Expanded Organic Solvents Combined With Low Speed Shear Mixing, Carbon 135 (2018) 180–186, https://doi.org/10.1016/j.carbon.2018.03.040.

[48] T.-R. Lee, Quantitative Correlation Between Interlayer Distance and Shear Rate in Liquid-Based Exfoliation of Graphene Layers, Carbon 129 (2018) 661–666, https://doi.org/10.1016/j.carbon.2017.12.068.

[49] R. Rizvi, E.P. Nguyen, M.D. Kowal, W.H. Mak, S. Rasel, M.A. Islam, A. Abdelaal, A.S. Joshi, S. Zekriardehani, M.R. Coleman, R.B. Kaner, High-Throughput Continuous Production of Shear-Exfoliated 2D Layered Materials using Compressible Flows, Adv. Mater. 30 (2018) 1800200, https://doi.org/10.1002/adma.201800200.

[50] Y. Li, X. Yin, W. Wu, Preparation of Few-Layer MoS_2 Nanosheets via an Efficient Shearing Exfoliation Method, Ind. Eng. Chem. Res. 57 (2018) 2838–2846, https://doi.org/10.1021/acs.iecr.7b04087.

[51] F. Di Renzo, Zeolites as Tailor-Made Catalysts: Control of the Crystal Size, Catal. Today 41 (1998) 37–40, https://doi.org/10.1016/s0920-5861(98)00036-4.

[52] W.R. Wilcox, Transport Phenomena in Crystal Growth From Solution, Prog. Cryst. Growth Charact. Mater. 26 (1993) 153–194, https://doi.org/10.1016/0960-8974(93)90014-u.

[53] Z.Q. Yu, R.B.H. Tan, P.S. Chow, Effects of Operating Conditions on Agglomeration and Habit of Paracetamol Crystals in Anti-Solvent Crystallization, J. Cryst. Growth 279 (2005) 477–488, https://doi.org/10.1016/j.jcrysgro.2005.02.050.

[54] J. Liu, Å.C. Rasmuson, Influence of Agitation and Fluid Shear on Primary Nucleation in Solution, Cryst. Growth Des. 13 (2013) 4385–4394, https://doi.org/10.1021/cg4007636.

[55] N. Nakamura, K. Inayama, T. Okuno, H. Ogi, M. Hirao, Accelerated crystallization of colloidal glass by mechanical oscillation, Sci. Rep. 7 (2017) 1369, https://doi.org/10.1038/s41598-017-01484-y.

[56] J.W. Mullin, K.D. Raven, Nucleation in Agitated Solutions, 251 251, Nature 190 (1961), https://doi.org/10.1038/190251a0.

[57] D. Richard, T. Speck, The role of shear in crystallization kinetics: From suppression to enhancement, Sci. Rep. 5 (2015) 14610, https://doi.org/10.1038/srep14610.

[58] S. Zhao, Y. Zhang, Y. Wang, Y. Zhou, K. Qiu, C. Zhang, J. Fang, X. Sheng, Ionic Liquid-Assisted Synthesis of Br-Modified g-C_3N_4 Semiconductors With High Surface Area and Highly Porous Structure for Photoredox Water Splitting, J. Power Sources 370 (2017) 106–113, https://doi.org/10.1016/j.jpowsour.2017.10.023.

[59] M. Bellardita, E.I. García-López, G. Marcì, I. Krivtsov, J.R. García, L. Palmisano, Selective Photocatalytic Oxidation of Aromatic Alcohols in Water by Using P-doped g-C_3N_4, Appl. Catal. B 220 (2018) 222–233, https://doi.org/10.1016/j.apcatb.2017.08.033.

[60] J.C. Wang, C.X. Cui, Y. Li, L. Liu, Y.P. Zhang, W. Shi, Porous Mn Doped g-C_3N_4 Photocatalysts for Enhanced Synergetic Degradation Under Visible-Light Illumination, J. Hazard. Mater. 339 (2017) 43–53, https://doi.org/10.1016/j.jhazmat.2017.06.011.

[61] P. Niu, L.C. Yin, Y.Q. Yang, G. Liu, H.M. Cheng, Increasing the visible light absorption of graphitic carbon nitride (melon) photocatalysts by homogeneous self-modification with nitrogen vacancies, Adv. Mater. 26 (2014) 8046–8052, https://doi.org/10.1002/adma.201404057.

[62] G. Zhang, G. Li, Z.A. Lan, L. Lin, A. Savateev, T. Heil, S. Zafeiratos, X. Wang, M. Antonietti, Optimizing Optical Absorption, Exciton Dissociation, and Charge Transfer of a Polymeric Carbon Nitride with Ultrahigh Solar Hydrogen Production Activity, Angew. Chem. Int. Ed. 56 (2017) 13445–13449, https://doi.org/10.1002/anie.201706870.

[63] S. Lu, C. Li, H.H. Li, Y.F. Zhao, Y.Y. Gong, L.Y. Niu, X.J. Liu, T. Wang, The Effects of Nonmetal Dopants on the Electronic, Optical and Chemical Performances of Monolayer g-C_3N_4 by First-principles Study, Appl. Surf. Sci. 392 (2017) 966–974, https://doi.org/10.1016/j.apsusc.2016.09.136.

[64] M.V. Putz, N. Russo, E. Sicilia, About the Mulliken Electronegativity in DFT, Theor. Chem. Acc. 114 (2005) 38–45, https://doi.org/10.1007/s00214-005-0641-4.

[65] M.A. Butler, Prediction of Flatband Potentials at Semiconductor-Electrolyte Interfaces from Atomic Electronegativities, J. Electrochem. Soc. 125 (1978), https://doi.org/10.1149/1.2131419.

[66] Y. Xu, M.A.A. Schoonen, The Absolute Energy Positions of Conduction and Valence Bands of Selected Semiconducting Minerals, Am. Mineral. 85 (2000) 543–556, https://doi.org/10.2138/am-2000-0416.

[67] K. Ding, L. Wen, M. Huang, Y. Zhang, Y. Lu, Z. Chen, How does the B, F-mono-doping and B/F-codoping affect the photocatalytic water-splitting performance of g-C3N4? PCCP 18 (2016) 19217–19226, https://doi.org/10.1039/c6cp02169g.

[68] Y.I. Kim, S.J. Atherton, E.S. Brigham, T.E. Mallouk, Sensitized layered metal oxide semiconductor particles for photochemical hydrogen evolution from nonsacrificial electron donors, J. Phys. Chem. 97 (1993) 11802–11810, https://doi.org/10.1021/j100147a038.

[69] X. Wu, D. Gao, H. Yu, J. Yu, High-Yield Lactic Acid-Mediated Route for a g-C_3N_4 Nanosheet Photocatalyst With Enhanced H_2-Evolution Performance, Nanoscale 11 (2019) 9608–9616, https://doi.org/10.1039/c9nr00887j.

[70] H. Tang, R. Wang, C. Zhao, Z. Chen, X. Yang, D. Bukhvalov, Z. Lin, Q. Liu, Oxamide-modified g-C_3N_4 Nanostructures: Tailoring Surface Topography for High-Performance Visible Light Photocatalysis, Chem. Eng. J. 374 (2019) 1064–1075, https://doi.org/10.1016/j.cej.2019.06.029.

[71] W. Miao, Y. Liu, X. Chen, Y. Zhao, S. Mao, Tuning layered Fe-doped g-C3N4 structure through pyrolysis for enhanced Fenton and photo-Fenton activities, Carbon 159 (2020) 461–470, https://doi.org/10.1016/j.carbon.2019.12.056.

[72] L. Jiang, X. Yuan, G. Zeng, J. Liang, Z. Wu, H. Wang, J. Zhang, T. Xiong, H. Li, A facile band alignment of polymeric carbon nitride isotype heterojunctions for enhanced photocatalytic tetracycline degradation, Environ. Sci. Nano 5 (2018) 2604–2617, https://doi.org/10.1039/c8en00807h.

[73] X. Zhang, D. An, D. Feng, F. Liang, Z. Chen, W. Liu, Z. Yang, M. Xian, In situ surfactant-free synthesis of ultrathin BiOCl/g-C3N4 nanosheets for enhanced visible-light photodegradation of rhodamine B, Appl. Surf. Sci. 476 (2019) 706–715, https://doi.org/10.1016/j.apsusc.2019.01.147.

[74] L. Cao, Y.F. Li, Y. Tong, R. Yang, L. Sun, Q. Cao, R. Chen, A novel Bi12TiO20/g-C3N4 hybrid catalyst with a bionic granum configuration for enhanced photocatalytic degradation of organic pollutants, J. Hazard. Mater. 379 (2019) 120808, https://doi.org/10.1016/j.jhazmat.2019.120808.

[75] D.J. Kim, W.-K. Jo, Sustainable treatment of harmful dyeing industry pollutants using SrZnTiO3/g-C3N4 heterostructure with a light source-dependent charge transfer mechanism, Appl. Catal. B 242 (2019) 171–177, https://doi.org/10.1016/j.apcatb.2018.10.001.

[76] L. Shi, C. Xu, D. Jiang, X. Sun, X. Wang, Q. Wang, Y. Zhang, X. Qu, F. Du, Enhanced interaction in TiO2/BiVO4 heterostructures via MXene Ti3C2-derived 2D-carbon for highly efficient visible-light photocatalysis, Nanotechnology 30 (2019) 075601, https://doi.org/10.1088/1361-6528/aaf313.

[77] L. Tang, C. Feng, Y. Deng, G. Zeng, J. Wang, Y. Liu, H. Feng, J. Wang, Enhanced photocatalytic activity of ternary Ag/g-C3N4/NaTaO3 photocatalysts under wide spectrum light radiation: The high potential band protection mechanism, Appl. Catal. B 230 (2018) 102–114, https://doi.org/10.1016/j.apcatb.2018.02.031.

[78] Q. Liang, Z. Li, Y. Bai, Z.H. Huang, F. Kang, Q.H. Yang, A Composite Polymeric Carbon Nitride with In Situ Formed Isotype Heterojunctions for Highly Improved Photocatalysis under Visible Light, Small 13 (2017), https://doi.org/10.1002/smll.201603182.

[79] J. Liu, H. Xu, Y. Xu, Y. Song, J. Lian, Y. Zhao, L. Wang, L. Huang, H. Ji, H. Li, Graphene quantum dots modified mesoporous graphite carbon nitride with significant enhancement of photocatalytic activity, Appl. Catal. B 207 (2017) 429–437, https://doi.org/10.1016/j.apcatb.2017.01.071.

[80] J. Chen, X. Xiao, Y. Wang, Z. Ye, Ag nanoparticles decorated WO3/g-C3N4 2D/2D heterostructure with enhanced photocatalytic activity for organic pollutants degradation, Appl. Surf. Sci. 467–468 (2019) 1000–1010, https://doi.org/10.1016/j.apsusc.2018.10.236.